JUSTUS-LIEBIG-
UNIVERSITÄT
GIESSEN

Investigating Substitutional Point Defects in Nickel-Rich Layered Oxides through Ion Exchange Synthesis

Leonhard Ferdinand Paul Karger

Vollständiger Abdruck der vom
Fachbereich Biologie und Chemie
der Justus-Liebig-Universität Gießen
zur Erlangung des akademischen Grades eines

Doktor der Naturwissenschaften (Dr. rer. nat.)

genehmigten Dissertation.

Vorsitz: Prof. Maren Lepple
Erster Gutachter: Prof. Jürgen Janek
Zweiter Gutachter: Prof. Bernd Smarsly
Prüfer: Prof. Derck Schlettwein

Diese Dissertation wurde am 20.02.2024 beim Fachbereich Biologie und Chemie
der Justus-Liebig-Universität eingereicht und am 03.05.2024 angenommen.

Dekan/Dean

Prof. Dr. Thomas Wilke

1. Gutachter / 1st Examiner

Prof Dr. Dr. (hc.) Jürgen Janek

2. Gutachter / 2nd Examiner

Prof. Dr. Bernd Smarsly

Eidesstattliche Versicherung

Hiermit versichere ich an Eides statt, dass es sich bei der vorliegenden Arbeit mit dem Titel „Investigating Substitutional Point Defects in Nickel-Rich Layered Oxides through Ion Exchange Synthesis“, um mein eigenständig erstelltes Werk handelt, welches den Regeln guter wissenschaftlicher Praxis entspricht. Ich habe nur die angegeben Quellen und Hilfsmittel verwendet und mich keiner unzulässigen Hilfe durch Dritte bedient. Alle wörtlichen und nicht wörtlichen Zitate aus anderen Werken sind als solche kenntlich gemacht. Die vorliegende Arbeit oder Teile der Arbeit habe ich bislang nicht an einer Hochschule des In- oder Auslandes als Bestandteil einer Qualifikations- oder Prüfungsleistung vorgelegt. Die Richtigkeit dieser Erklärung bestätige ich. Ich kenne die Bedeutung der eidesstattlichen Erklärung und die strafrechtlichen Folgen einer unrichtigen oder unvollständigen eidesstattlichen Erklärung. Ich bin damit einverstanden, dass die vorliegende Arbeit zum Zwecke des Plagiatsabgleichs in elektronischer Form versendet, gespeichert und verarbeitet wird.

Declaration in Lieu of Oath

I hereby declare in lieu of oath, that the following thesis with the title: “Investigating Substitutional Point Defects in Nickel-Rich Layered Oxides through Ion Exchange Synthesis”, is my own work and to the rules of proper scientific conduct. In writing the thesis I did not seek unauthorized assistance of a third party and I have employed no other means except the ones listed. I clearly marked any direct or indirect quotations derived from the work of others. I have not as of yet presented this work to any other institution of higher education in Germany or abroad. I hereby confirm the accuracy of the affirmation above. I am aware of the significance of this affirmation and the legal ramifications in case of untrue or incomplete statements. I affirm in lieu of oath that the statements above are to the best of my knowledge true and complete. I agree that for the purpose of assessing plagiarism the dissertation may be electronically forwarded, stored and processed.

Danksagung

An der Entstehung dieser Arbeit waren viele Menschen beteiligt. Einige mit hilfreichen Diskussionen, sei es über wissenschaftliche, gesellschaftliche, literarische und persönliche Themen, andere mit Beistand, Unterstützung, Wohlwollen und sicherlich noch einigem mehr. Zunächst möchte ich mich bei meinem Doktorvater, Professor Janek, bedanken, der mir die Möglichkeit gegeben hat, in seiner erweiterten Arbeitsgruppe zu forschen und der immer Wert auf den Austausch zwischen den Gruppen in Karlsruhe und Gießen, sowie auch zu anderen Forschungsgruppen und Kulturen, nicht zuletzt im Rahmen der deutsch-israelischen Batterieschule, gesorgt hat. Ich möchte mich sehr herzlich bei Torsten Brezesinski und Aleksandr Kondrakov bedanken, die mit viel Geduld, Begeisterung, Offenheit für neue Ideen, Enthusiasmus und Hilfsbereitschaft eine ideale Arbeitsatmosphäre geschaffen und mich dazu motiviert haben, gute Forschung zu betreiben. Weiterhin möchte ich mich bei Andreas Fischer und Matteo Bianchini bedanken, die durch ihr Engagement seitens der BASF eine gute Grundlage für die Forschung am BELLA geschaffen haben. Außerdem bedanke ich mich bei meinen wissenschaftlichen Betreuern aus Bachelor und Master, die mich durch Abschlussarbeiten, Praktika und Auslandsaufenthalte begleitet haben.

Ich bin Daniel Weber zutiefst dankbar, dass er mich in der Anfangszeit am BELLA unter seine Fittiche genommen hat und mir durch seine fundierte Herangehensweise geholfen hat, in die Themen Strukturchemie und Festkörpersynthese einzusteigen. Weiterhin möchte ich mich bei meinen Arbeitskollegen und Freunden, David, Wessel, Siyu, Kumar, Flo, Sören, Nikolai, Ruizhuo, Jing, Philip, Miriam, Barbara, Fatih, Wengao, Jingui, Eduardo, Damian, Marie, Arash, Yuan und Teo, am BELLA bedanken, mit denen ich eine wunderbare Zeit verbringen konnte und die mich sowohl beim Forschen, als auch bei gutem Essen und Trinken, Skifahren, Tanzen, zur Arbeit fahren, Wandern und Rätsel lösen begleitet haben.

Besonderer Dank gilt außerdem Victor und Rui, die mir dabei geholfen haben, Experimentideen auch während des Schreibens zu verfolgen und deren Einsatz im Labor sicherlich interessante Forschungsergebnisse generieren wird.

Außerdem möchte ich mich bei meinen Freunden bedanken, die sich, obwohl nur ein paar von Ihnen Chemiker sind, mit großem Interesse meinen Berichten aus dem Labor gewidmet haben und mir damit die Doktorarbeitszeit versüßt haben. Vielen Dank, Julian, Johannes, Alex, Alexandra, Tobi, Benedikt, Jonas, Alessia, Nils, Lisa, Patrick, Joel, Fabi, Sara, Julia, Andreas, Niklas und außerdem noch vielen Freunden aus dem Jazz-Chor am KIT. Besonders bin ich auch meiner Familie dankbar, die mich immer unterstützt und ermutigt hat und mir mit Rat und Tat zur Seite steht. Zu guter Letzt möchte ich mich bei meiner Partnerin Chiara bedanken! Vielen Dank, dass du dich immer wieder für mehr oder weniger anschauliche Erklärungen von meinen Laborspinnereien begeistern kannst, so viel Interesse an meiner Arbeit zeigst und mich auf meinem Weg begleitest. Mit dir ist es tausendmal schöner!

The prize is in the pleasure of finding the thing out, the kick in the discovery, the observation that other people use it - those are the real things.

Richard Feynman

Kurzfassung

Das Ziel dieser Doktorarbeit war es, den Kapazitätsverlust von $LiNiO_2$ (LNO) und verwandten $LiNi_aCo_bMn_cO_2$ (NCM) Kathodenmaterialien mit Schichtstruktur im ersten Lade-/Entladezyklus zu verstehen und die spezifischen Einflüsse der Materialeigenschaften, wie Partikelgröße, Zusammensetzung und Defektdichte, zu entschlüsseln. Das Projekt führte zur Entwicklung einer neuartigen Herstellung von LNO und nickelreichem NCM, die von der üblicherweise verwendeten Festkörpersynthese abweicht, da mit diesem Ansatz $Ni_{Li}^{\bullet}$-Substitutionsdefekte vollständig vermieden werden. Zunächst wurden Natriumanaloga von LNO und nickelreichem NCM, $NaNiO_2$ und $NaNi_aCo_bMn_cO_2$, mittels Festkörpersynthese hergestellt. Der größere Ionenradius von Na^+- im Vergleich zu Li^+-Ionen führt zu vollständig ausgebildeten Nickel- und Natriumschichten in diesen Phasen. Daraufhin wurden Na^+- gegen Li^+-Ionen ausgetauscht, wobei perfekt geschichtetes LNO und NCM entstand. Dieser Ansatz ermöglicht erstmalig die elektrochemische Untersuchung von $Ni_{Li}^{\bullet}$-freiem LNO und nickelreichem NCM.

Mithilfe der entwickelten Methode wurden Serien monolithischer LNO-Partikel mit unterschiedlicher Kristallitgröße synthetisiert. Dies ermöglicht die selektive Untersuchung des Einflusses der Partikelgröße auf den anfänglichen Kapazitätsverlust ohne Beiträge von $Ni_{Li}^{\bullet}$-Defekten. Weiterhin wurde der Einfluss von $Ni_{Li}^{\bullet}$ auf herkömmliches LNO rekonstruiert und die Ergebnisse durch ein neuartiges duales Ionenaustauschverfahren validiert. Die Vermeidung von $Ni_{Li}^{\bullet}$-Defekten führte zu einer schnelleren Lithiumdiffusion, resultierte aber auch in Destabilisierung bei hohen Ladezuständen. Dies verdeutlicht die ambivalente Rolle von $Ni_{Li}^{\bullet}$-Substitutionsdefekten. Einerseits stabilisieren sie LNO, behindern aber andererseits die Lithiumdiffusion, wodurch die vollständige Entladung des Materials erschwert wird. Darüber hinaus wurde der Einfluss des Nickelgehalts auf den anfänglichen Kapazitätsverlust geprüft. Eine Serie von ionenausgetauschten, nickelreichen NCM-Materialien ohne $Ni_{Li}^{\bullet}$-Defekte wurde synthetisiert und elektrochemisch untersucht. Ziel der Studie war es, den Einfluss des Nickelgehalts auf den anfänglichen Kapazitätsverlust zu untersuchen. Ähnlich wie bei den $Ni_{Li}^{\bullet}$-Defekten zeigten die Ergebnisse ein Zusammenspiel aus Stabilität und Diffusion in Bezug auf die Übergangsmetallzusammensetzung. Ein verringerter Nickelgehalt stabilisiert das Aktivmaterial im delithiierten Zustand, wohingegen ein höherer Nickelgehalt die Lithiummobilität verbessert.

Die gesamte Untersuchung verdeutlicht die Gratwanderung zwischen verbesserter Materialstabilität (Thermodynamik) und schnellerer Lithiumdiffusion (Kinetik). Materialien mit schnellerer Diffusion waren tendenziell weniger stabil und umgekehrt. Die signifikant stabilisierende Wirkung von $Ni_{Li}^{\bullet}$, selbst bei niedrigen Ladeschlussspannungen von 4,3 V gegenüber Li^+/Li, wurde zum ersten Mal in defektfreien Materialien beobachtet, da literaturbekannte Materialien inhärent defekt-stabilisiert sind. Dies wirft die Frage nach der optimalen Konzentration und den Eigenschaften von Lithium-Substitutionsdefekten auf.

Abstract

The primary aim of this doctoral project was to comprehensively understand the capacity loss in the initial charge/discharge cycle of layered $LiNiO_2$ (LNO) and related $LiNi_aCo_bMn_cO_2$ (NCM) cathode materials and to untangle the specific influences of material characteristics, such as particle size, composition and defect density. The project led to an innovative method of synthesizing LNO and Ni-rich NCM, diverging from the commonly used solid-state synthesis. This method produces layered oxides devoid of $Ni_{Li}^{\bullet}$ substitutional defects by creating sodium analogs of LNO and Ni-rich NCM, namely $NaNiO_2$ and $NaNi_aCo_bMn_cO_2$. The larger size of sodium ions, compared to lithium ions, facilitates the formation of perfectly layered phases in these sodium analogs. Subsequently, such phases can be transformed into well layered LNO and NCM through an exchange of sodium ions with lithium ions. This approach enabled the examination of perfectly layered LNO and Ni-rich NCM for the first time.

Three sets of monolithic LNO particles with differing grain sizes were synthesized using the developed ion exchange method, allowing the selective study of the impact of particle size on the initial capacity loss without contributions from $Ni_{Li}^{\bullet}$ defects. The study reconstructed the influence of $Ni_{Li}^{\bullet}$ substitutional defects on conventional LNO and validated the findings by introducing magnesium to the lithium site using a unique dual ion exchange approach. The absence of $Ni_{Li}^{\bullet}$ defects led to faster lithium diffusion, but resulted in material degradation at high potentials, thus highlighting the ambivalent role of $Ni_{Li}^{\bullet}$ substitutional defects, which contribute to stabilization at high states of charge, but also hinder diffusion. Additionally, the role of nickel content in the initial capacity loss was studied on ion-exchanged NCM materials with variable nickel content. Similar to the effects observed for $Ni_{Li}^{\bullet}$ defects, the study revealed a complex interplay between stability (thermodynamics) and diffusion (kinetics). Lower nickel contents were found to stabilize the material at high potentials, whereas higher nickel contents mitigated polarization during discharge.

Throughout the investigation, a trade-off between material stability and lithium diffusion was observed. Materials with enhanced diffusion tended to be less stable and vice versa. The significant instability of LNO, even at low cut-off potentials of 4.3 V vs. Li^+/Li, was observed in ion-exchanged materials for the first time. Literature known material was inherently stabilized due to the presence of $Ni_{Li}^{\bullet}$, which obscured this property. This raises the question what the optimal concentration and the ideal properties of lithium ion substituents are.

List of Abbreviations

CAM	cathode active material
DEMS	differential electrochemical mass spectrometry
DFT	density functional theory
EDS	energy dispersive X-ray spectroscopy
EV	electric vehicle
GITT	galvanostatic intermittent titration technique
H	hexagonal
FCCL	first-cycle capacity loss
ICP-OES	inductively coupled plasma optical emission spectroscopy
IE	ion exchange(d)
JT	Jahn-Teller
KH	kinetic hindrance
LCO	lithium cobalt oxide ($LiCoO_2$)
LFP	lithium iron phosphate ($LiFePO_4$)
LIB	lithium-ion battery
LNO	lithium nickel oxide ($LiNiO_2$)
LS	low-spin
M	monoclinic
MAS	magic-angle spinning
Na-NCM	sodium nickel cobalt manganese oxide ($NaNi_aCo_bMn_cO_2$)
NCA	lithium nickel cobalt aluminium oxide ($LiNi_aCo_bAl_cO_2$)
NCM	litihum nickel cobalt manganese oxide ($LiNi_aCo_bMn_cO_2$)
NMP	N-methyl pyrrolidone
NMR	nuclear magnetic resonance
NNO	sodium nickel oxide ($NaNiO_2$)
O	octahedral
P	prismatic

PC	polycrystalline
PVDF	polyvinylidene difluoride
(P)XRD	(Powder) X-ray diffraction
SC	single crystalline
SEM	scanning electron microscopy
SIB	sodium-ion-battery
SOC	state of charge
sst	solid-state synthesis/synthesized
STEM	scanning transmission electron microscopy
TEM	transmission electron microscopy
TOF-SIMS	time-of-flight secondary ion mass spectrometry

Contents

1 Introduction

Since their inception in the 1970s and introduction to market in 1991, secondary batteries based on the lithium-ion technology, also called lithium-ion batteries (LIBs), have become ubiquitous in everyday live as power sources of mobile devices. Their development has been honored with the Nobel Prize in Chemistry in 2019.[1–5] While portable electronic devices were successfully powered with the initial design of a lithium cobalt oxide (LCO) cathode and graphite anode,[6] the recent emphasis on an all-encompassing energy transition towards a more sustainable supply generates new demand for battery technologies that have to go beyond the initial LCO/graphite design.[7,8] Therefore, great efforts have been invested in improving battery technology with regards to volumetric and gravimetric energy density, power density, cost-effectiveness, long-term stability, sustainability and safety, although the prioritization of certain aspects can vary depending on the intended application.[9] While there are numerous fields in which batteries can and will be applied, the main sectors are stationary storage and transportation in the form of electric vehicles (EVs).[10] Consequently, most of the development has been devoted to construct batteries for either one of these applications. In the case of EVs, high energy density, stability, low price and safety are paramount, which are also desirable properties for long-term storage, although the emphasis shifts from energy density to stability and price. For the latter application, non-electrochemical means of energy storage, such as pumped hydro energy storage, are competing technologies.[11] Some authors argue, however, that by 2030, second life use of EV batteries will be sufficient to satisfy the short-term stationary storage needs.[12] Either way, the development of high-performance batteries for the EV sector sits at the heart of decarbonization of the economy, and the development of improved batteries is therefore a viable goal.

Regarding improved cell designs, for the negative electrode side, lithium-metal anodes, ideally generated *in situ*, provide the maximal possible energy density.[13,14] Therefore, several strategies have been proposed to make lithium-metal anodes industrially viable, such as protective surface layers,[15] structured current collectors,[16] solid-state batteries,[17] almost solid-state batteries[18] and electrolyte additives.[19] Another approach is to improve upon the commercialized graphite anodes through refined processing and morphology.[20] The use of silicon as an anode material,[21–23] either pure or blended with graphite is also promising to improve energy density, but is plagued by extreme volume variations during cycling.[24] Similarly, for the positive electrode side, new compositions have been introduced to the market and are being developed continuously. Some promising examples include solid solutions of various combinations of nickel, manganese, aluminum and cobalt in the layered lithium metal oxide structure,[25–29] which when used in conjunction yield the $LiNi_aCo_bMn_cO_2$ (NCM or NMC)[30–33] and $LiNi_aCo_bAl_cO_2$ (NCA)[34] material families. Alternatives are the olivine type $LiFePO_4$ (LFP) and related structures,[35,36] $LiMn_2O_4$ spinel[37] and so-called “high-voltage” spinel,[38] lithium-rich disordered rock-salt materials,[39,40] lithium sulfide,[41] lithium vanadates,[42,43] and lithium- and manganese-rich layered oxides.[44–47] Beyond lithium, other ions have been proposed as the shuttling agent, which aim to lower overall material cost and

environmental impact.[48,49] Among these, sodium-ion-battery (SIB) technology was one of the first to find commercial application in an EV.[50]

However, for long-range and high-power demand in EVs, energy density and power density are key parameters. To fulfil these demands, typically LIBs are used.[51] State-of-the-art cells feature (i) a graphite or blended silicon anode, (ii) a carbonate-based liquid electrolyte and (iii) for the cathode side, either NCM/NCA or LFP.[8,51] While LFP has the advantage of lower processing cost and material prices, as well as good long-term stability, NCM or NCA cells have higher theoretical and practical volumetric and gravimetric energy densities.[52] Nevertheless, the theoretical specific capacity of ~275 mAh/g_{CAM} of the latter cathode active materials (CAMs) cannot be harnessed yet experimentally.[53,54] While all NCM and NCA materials can, in principle, deliver similar specific capacities, the upper cut-off voltage limits the amount of lithium that is extracted and thus cycled.[53,54] Upon charging to high cut-off voltages the commonly used carbonate electrolytes undergo parasitic side reactions and form the so-called cathode solid-electrolyte-interphase, causing an increase in cell impedance.[55] Furthermore, high cut-off voltages can cause loss of active material due to its degradation.[55,56] Lastly, some of the capacity of NCM is lost during the first charge/discharge cycle due to incomplete relithiation.[55,56] With an increase in nickel content, the average charge and discharge voltages decrease, which increases the specific capacities achievable within the stability window of common liquid electrolytes.[53] Therefore, for NCM and NCA materials with higher nickel contents, so-called “high-nickel” or “Ni-rich” materials, which is commonly defined as a nickel content of ≥ 80 mol%, the gap between theoretical and experimental specific charge capacity decreases. If this trend is pushed to its extreme, the pure nickel compound, $LiNiO_2$ (LNO), can routinely be charged to 260 mAh/g at just 4.3 V vs. Li^+/Li, which is 95% of the theoretical specific capacity and corresponds to a residual lithium content of 5%.[57]

Upon discharge, about ~90% of the first-cycle charge capacity is reached.[57] This discrepancy between charge and discharge capacity is commonly referred to as first-cycle capacity loss (FCCL). In LNO, the FCCL was shown to be mainly a result of slow lithium diffusion at the end of discharge, such that 0% FCCL can, in principle, be achieved with extremely slow cycling.[58] Therefore, investigating the cause of this first-cycle loss is warranted to improve the utilization of lithium ions in Ni-rich NCM and NCA materials. Several structural aspects were correlated with the FCCL. As mentioned above, parasitic side reactions play a role if materials are cycled to high cut-off voltages, but do not seem to be a major factor with lower cut-off voltages.[55,58] Particle size also has a direct impact on the lithium diffusion path length and could clearly be correlated with FCCL.[57,59,60] Lastly, $Ni_{Li}^{\bullet}$ substitutional point defects, which are inherently present in Ni-rich cathodes, as a residual from their solid-state-synthesis (sst), also show correlation with the FCCL.[56]

The objective of this doctoral work was to develop a deeper understanding of the FCCL phenomenon and to disentangle the individual contributions of material properties, such as

particle size, transition-metal substitution and defect density. The project resulted in a novel synthesis method for LNO and Ni-rich NCM, which, contrary to the widely employed sst, yields materials void of $Ni_{Li}^{\bullet}$ substitutional defects. This is achieved by synthesizing the sodium analogs of LNO and Ni-rich NCM, which are $NaNiO_2$ (NNO) and $NaNi_aCo_bMn_cO_2$ (Na-NCM). Due to the larger size of Na^+ ions ($r(Na^+)$ = 1.0 Å), compared to Li^+ ions ($r(Li^+)$ = 0.76 Å),[61] these sodium analogs form perfectly layered materials, which can be transformed into well layered LNO and NCM by means of sodium to lithium ion exchange (IE). This methodology enabled the investigation of perfectly layered LNO for the first time. Three series of monolithic LNO particles with differing particle sizes were synthesized and the impact of particle size on the FCCL was studied in the absence of $Ni_{Li}^{\bullet}$ defects. An optimized IE-LNO was compared in detail to a reference material, and the results were validated with an artificial lithium-site defect through a novel dual-ion-exchange approach. In the absence of $Ni_{Li}^{\bullet}$ defects, lithium diffusion at the end of discharge became faster, while material degradation was observed at high potentials. Thus, the results indicate an ambivalence of $Ni_{Li}^{\bullet}$ defects, which on the one hand help to stabilize LNO, while on the other hand they impede diffusion and do not allow complete discharge of the material. Furthermore, the role of nickel content on the FCCL was also studied by synthesizing a series of IE-NCM materials without $Ni_{Li}^{\bullet}$ defects. Similar to the impact of $Ni_{Li}^{\bullet}$ defects described above, a trade-off between thermodynamicas and kinetics was observed when altering the nickel content. Lower nickel contents were shown to stabilize the material at high SOC, but higher nickel contents were observed to lead to more complete discharge.

The substantial stabilization achieved by the presence of $Ni_{Li}^{\bullet}$ defects, even at low cut-off potentials of 4.3 V vs. Li^+/Li, was found in defect-free materials for the first time, as all materials previously described in the literature are inherently sufficiently pillared to obscure this property, as a result of their synthesis history. This raises the question of an optimal defect, or pillar ion, concentration, as well as the optimal properties of such pillar ions, to improve the performance of Ni-rich CAMs. Additionally, a novel coating strategy for cathode materials to be used in solid-state-batteries was developed and tested during the duration of this doctoral project. The results of this project have been submitted to a peer-reviewed journal, and the submitted draft can be found in the Appendix in chapter 6.2.1. Since the topic of this initial investigation deviates somewhat from the main theme of this doctoral thesis, it was not included in the main text.

2 Fundamentals

2.1 Structure of Lithium Nickel Oxide

$LiNiO_2$ owes its properties as a promising CAM to its layered crystal structure, which allows for simultaneous redox activity and electronic/ionic transport. In the following chapters, the crystal structure of LNO is described, and the presence and role of different defect types is discussed.

2.1.1 Crystal Structure

Analogous to its predecessor (LCO) for LIB application, LNO forms a layered structure of the α-$NaFeO_2$ type, wherein nickel is sandwiched between two layers of oxygen in octahedral coordination.[62,63] The spaces in between these nickel oxide layers are filled with lithium, which is also coordinated in octahedral sites. Experimentally, LNO adopts the rhombohedral *R*–3*m* space group, as shown in Figure 1c. The oxygen stacking in this structure repeats after three layers (AB CA BC), which corresponds to an O3 (repetition after three layers) structure according to the nomenclature for layered metal oxides introduced by Delmas.[64]

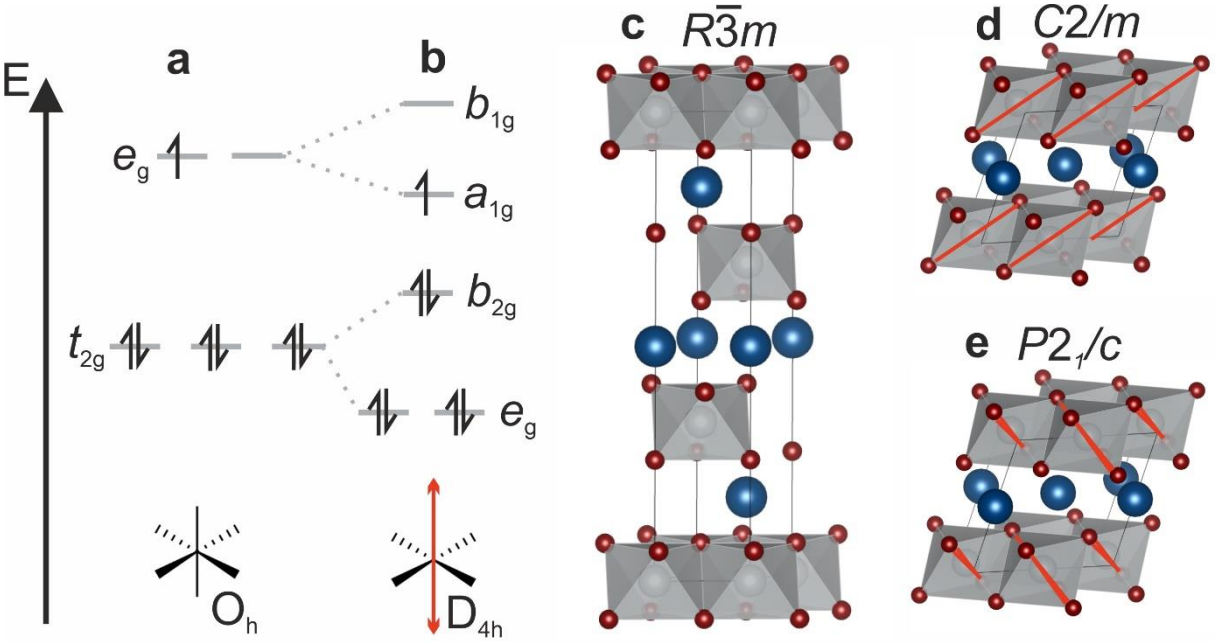

Figure 1. (a) Molecular orbital scheme of a LS-Ni^{3+} octahedral complex. (b) Molecular orbital scheme of a LS-Ni^{3+} JT-distorted complex. Unit-cell of LNO in the hexagonal phase (*R*–3*m* space group) with nickel in gray, lithium in blue and oxygen in burgundy (diameters of the spheres do not correspond to the ion radii) (c). Unit-cell of LNO with collinear JT-distortion (*C*2/*m* space group) with elongated bond axes in red (d). Unit-cell of LNO with zigzag JT-distortion ($P2_1/c$ space group) with elongated bond axes in red (e).

Contrary to LCO, however, the low-spin (LS) Ni^{3+} in LNO should be Jahn-Teller (JT) active. JT-distortion describes the instability of non-linear molecular systems with degenerate

electronic states, causing a distortion that lowers symmetry and splits the degenerate energetic states, allowing the system to adopt an overall lower energetic state. Figure 1a, b shows the JT effect in the molecular-orbital schemes of an octahedral complex and its elongated JT-distorted state.

Since the ideal structure of LNO contains Ni^{3+}, the 3d orbitals are occupied by seven electrons. In this case, energetic stabilization is achieved by elongation along the *z*-axis, which lowers the energy of the d_{z^2} orbital (a_{1g}) and destabilizes the $d_{x^2-y^2}$ orbital (b_{1g}). Density functional theory (DFT) calculations validate this picture and find that ideal LNO should adopt a JT-distorted structure. Several crystal structures would fit the axial elongation of the nickel to oxygen bonds, as the elongated bonds can adopt several ordered states.[65] One of these configurations is the collinear JT distortion, wherein all elongated bonds are oriented in the same direction, as is shown in Figure 1d, which corresponds to the *C*2/*m* space group. A second configuration is the so-called "zigzag" JT-distorted structure, which corresponds to the $P2_1/c$ space group, as can be seen in Figure 1e. Thirdly, a disproportionate structure exists, which features random orientation of all elongated bonds. DFT calculations have shown that the energetically most favorable state would be the zigzag JT distortion.[65]

Experimentally, no cooperative long-range JT distortion is observed when LNO is probed by X-ray diffraction (XRD). Instead, the rhombohedral non-JT-distorted $R\bar{3}m$ structure is observed, as stated above. The JT distortion is nevertheless present and causes dynamic local distortions with domain sizes of ~10 nm and the presence of three sublattices, due to the threefold symmetry of $R\bar{3}m$, as was confirmed by extended X-ray absorption fine structure (EXAFS) measurements and atomic pair-density function (PDF) studies.[65–70] The lack of cooperative JT ordering is explained by fast interconversion through pseudo-rotations of the three possible directions of JT-based octahedral elongation.[65] However, one should also keep in mind that truly stoichiometric $Li_1Ni_1O_2$ is, as of yet, not experimentally accessible and thus the discrepancy between theoretically predicted and experimentally observed structure may be caused by a defective sample.

2.1.2 Defects in Lithium Nickel Oxide

In principle, a plethora of structural defects can occur in Ni-rich cathodes, such as LNO. However, the main defects typically studied are either planar defects (2D) or point defects (0D).[71] Among the planar defects, twin boundaries,[72] antiphase boundaries,[73] edge-dislocations[73] and free surfaces resulting in impurity phase formation[74,75] are known to occur in pristine (uncycled) LNO. Of these defects, the most intensively studied is most likely the free surface, as it is highly reactive and its presence obvious. The surface reacts spontaneously with moisture under ambient conditions, which leads to intercalation of protons near the particle surface, as well as formation of lithium residues, which are quickly converted to lithium carbonate on the surface.[76,77] The free particle surface is further prone to reduction, which is accompanied by release of lattice oxygen.[78] While the other planar defects are less

studied, their impact on electrochemical performance is generally negative, and their implications are an active area of study.[72,73]

As to the point defects, vacancies,[79–81] anti-site defects[82] and substitutional defects[62,63,83,84] are the commonly described intrinsic defects in layered oxide cathodes, that is not intentionally synthesized through foreign ion addition etc. Within the group of point defects, only $Ni_{Li}^{\bullet}$ substitutional defects, accompanied by Ni_{Ni}' defects for charge compensation, can be observed in LNO close to stoichiometric conditions (when $z < 0.15$ in $Li_{1-z}Ni_{1+z}O_2$), as was shown by combined refinement of synchrotron and neutron diffraction data, the latter of which is more sensitive to the lithium sub-lattice.[82,85–87] The formation of this defect pair causes the average oxidation state within the transition-metal slab to decrease,[84,86,88] thus causing the nickel slab size to increase, while the lithium slab size decreases due to the presence of smaller Ni^{2+} ions ($r(Ni^{2+}, LS) = 0.69$ Å) compared to Li^{+} ($r(Li^{+}) = 0.76$ Å).[61] Consequently, the Li-O bond length decreases while the Ni-O bond length increases which results in an increase in the lattice parameters *a* and *c*, as well as the unit-cell volume *V*.[74,86,88–93] Regarding the potential JT distortion of LNO, such defects were shown to act as non-distorted centers, disrupting the long-range JT distortion.[94]

For simplicity, within this thesis, the presence of $Ni_{Li}^{\bullet}$ and Ni_{Ni}' defects is referred to as only $Ni_{Li}^{\bullet}$, while the co-presence of Ni_{Ni}' is implied. The role of these defects is vital to the properties of LNO, as well as those of Ni-rich CAMs.[62,95] A truly defect-free LNO was in this regard likely never synthesized, which is due to the experimentally challenging requirements of highly oxidizing conditions, which benefit from low temperatures, paired with sufficiently high temperatures needed for reactant interdiffusion in solid-state reactions. To sum up, the ever-present $Ni_{Li}^{\bullet}$ substitutional point defects affect almost every property of LNO. In the pristine material, $Ni_{Li}^{\bullet}$ defects change the magnetic properties, the structural parameters and the JT-activity play a role.

2.2 Synthesis Methods and Resulting Properties

The interest in LNO is driven by its potential application as a high-energy CAM for LIBs. The electrochemical performance of materials is contingent on a variety of factors across different length scales, which are dependent on the synthesis history. In the following chapters, an overview of the relevant processes for the synthesis of LNO is given.

2.2.1 Solid-State Synthesis

The first synthesis of LNO was reported in 1954, simultaneous with its sodium analog NNO, as the reaction product of nickel metal tubes with LiOH and NaOH, respectively, at 650-850 °C under oxygen flow.[96] While a similar approach is still being investigated,[97] the commercial interest in lithium layered oxide materials of high purity has spurred the pursuit of other synthesis methods, and by now a plethora of synthesis options is available.

State-of-the-art synthesis of Ni-rich CAMs relies on solid-state-synthesis with precursors of transition metals and lithium, which are mixed as powders and annealed at elevated temperatures in a flowing oxidizing atmosphere.[62] Atmospheric flow is needed for mass transport, because byproducts have to be removed from the reaction.[98,99] In the case of LNO, Ni^{2+} has to be oxidized to Ni^{3+}, for which an oxygen atmosphere, compared to air, yields higher quality material.[62] The reaction temperature is typically in the range of 650-750 °C, as too high temperatures lead to volatilization of the lithium precursor and decomposition of LNO, while too low temperatures cause incomplete reaction and overlithiation of LNO to form Li_2NiO_3 domains.[100,101]

While several synthesis techniques share the calcination conditions mentioned above, the choice of precursors, as well as the means to mix the precursors, is crucial and distinguishes several synthetic approaches to LNO. The simplest reaction scheme is the mechanical mixing of nickel oxide with lithium oxide, hydroxide, nitride or carbonate in a mortar, mixer or ball mill.[84,102,103] Depending on the precursor morphology, too large domains of nickel precursor lead to incomplete reaction, due to slow reaction, even if the temperature is chosen correctly, as was the case in the initial synthesis of LNO from large pieces of metal.[63,96] Therefore, small nickel oxide grains, which remain in a solid state at the calcination temperature, are beneficial to decrease the reaction time, which is directly associated with the processing cost. With regard to the molar ratios, lithium is typically used in excess to compensate for its loss due to volatilization.[62]

Some industrial processes for Ni-rich materials rely on a nanoporous transition metal precursor (pCAM), which is synthesized by co-precipitation in a batch feed reactor.[104] In the case of LNO, precipitation of $Ni(OH)_2$ is achieved by addition of alkaline solutions to aqueous nickel salt solutions.[105] The obtained particles possess a refined morphology consisting of secondary particle agglomerates in the micrometer range, which are each comprised of nanoscale $Ni(OH)_2$ grains.[73,105] This method allows for facile inclusion of dopants with intimate contact between all reaction partners and is thus very attractive for the synthesis of Ni-rich

NCM and NCA CAMs.[106] Furthermore, gradient distributions can be achieved, which allow to design particles with core-shell type morphology.[107] Due to the retention of the secondary particle morphology, which is beneficial for lithiation reactions, as well as the materials' electrochemical properties,[108] precipitated $Ni(OH)_2$ is often used as precursor for LNO.[57,59,109–111]

Another method to ensure intimate contact between the reaction partners is sol-gel synthesis. Typically water- or ethanol soluble salts of lithium and nickel, such as nitrates, hydroxides and acetates, are dissolved in water or mixtures of water and ethanol.[62,112,113] The use of additional chelating agents has been reported, but sol-gel synthesis can also be carried out without chelating agents.[114] The obtained sols are dried until a gel is formed, which is then calcined in air to relieve the anions as gasses. The obtained precursor mixture is then typically calcined as outlined above.

Furthermore, mechanochemical synthesis of LNO has been attempted, which yields only the rock-salt-type $Li_{1-z}Ni_{1+z}O_2$ material and not layered LNO.[102] However, when this material is subjected to annealing conditions, as outlined above, a well-layered LNO is formed.[102] Therefore, one could consider mechanochemical mixing another method to combine the respective precursors intimately.

2.2.3 The Relationship between Calcination Conditions, Particle Size and Microstructure

Key factors that govern the electrochemical performance of LNO are the crystal structure and the microstructure/morphology. Both features are directly linked to the calcination conditions and, in particular, to the calcination temperature. As established by the first systematic investigations,[103,115] and as mentioned in the previous chapter, LNO is typically synthesized at a reaction temperature of ~700 °C in an oxygen atmosphere. Too low temperatures cause incomplete reaction, which is most likely related to slower interdiffusion.[74] This is not the only reason for impurities in low-temperature synthesis, because the oxygen activity also increases as the temperature is lowered. Such conditions favor, in sufficient supply of lithium, the formation of overlithiated CAM, with Li_2NiO_3 being the most oxidized structure that can be formed, in which nickel is formally present as Ni^{4+}.[100,116] The full solid solution of $Li_{1+z}NiO_{2+z}$ down to LNO exists, but if lithium is supplied in exactly one equivalent to nickel, the reaction product still differs from LNO synthesized at 700 °C.[100] An obvious difference is the much smaller particle size, due to the mentioned slower interdiffusion of reactants and reduced sintering. A second difference is the presence of Li''_{Ni} defects, which typically only occur in LNO far from stoichiometric conditions.[100] As outlined in 2.1.2, such intermixing effects normally occur only for samples with high off-stoichiometry, but apparently the higher oxidation potential at 550 °C is sufficient to drive full oxidation of nickel to induce true cation intermixing. Another reason for this observation could be incomplete layer formation from rock-salt type $Li_yNi_{1-y}O_2$ due to the lower calcination temperature, which is the

intermediate structure formed during calcination of LNO, with residual impurities being misinterpreted as intermixing defects.[101]

The mechanism of LNO formation was studied in detail by *in situ* synchrotron XRD and neutron powder diffraction.[101,117,118] After initial dehydration of the precursors to yield NiO and partially dehydrated LiOH, the solid-state reaction between the nickel and lithium precursors can be separated into three regions.[101,117] The first region is the gradual lithiation of rock-salt type NiO, which crystallizes in the *Fm*–3*m* space group, to yield $Li_yNi_{1-y}O$ up to $y \leq 0.4$.[101,117] Region II defines the onset of the layering transition to yield a defective layered phase that is rich in Li/Ni intermixing, opposed to $Ni_{Li}^{\bullet}$ substitutional defects.[101,117] As the reaction progresses, the defects in this phase heal out further until a fully layered state is reached in region III, which may be when intermixing disappears, below $x \geq 0.15$ in $Li_{1-x}Ni_{1+x}O_2$, as described by Weber and co-workers.[82,101,117] The temperatures at which these phases are observed are related to the specific parameters chosen to study the reaction and may therefore vary, *e.g.* depending on the temperature ramp speed, but judging from systematic analyses of the annealing temperature, the desired low-defect LNO phase is likely only formed above 650 °C.[74,75] As described above, LNO can also be synthesized at lower temperatures, but then contains defects due to overlithiation of the material.[100]

Too high calcination temperatures also result in several structural defects, which are ultimately detrimental to the materials' performance as CAM. With an increase in calcination temperature or too long reaction times, the crystal structure of LNO proves unstable and decomposes to lithium-deficient states.[119,120] This could be due to the decrease of oxygen activity, μ_{O_2}, with rising temperatures, which can be expressed by the following formulas:

$$\mu_{O_2}(p_0, T) = \mu_0(p_0, T) + k_B T \ln\left(\frac{p_{O_2}}{p_0}\right) \quad (1)$$

$$\mu_{O_2}(p_0, T) = h_{O_2}(p_0, T) - T s_{O_2}(p_0, T) + k_B T \ln\left(\frac{p_{O_2}}{p_0}\right) \quad (2)$$

with the oxygen partial pressure p_{O_2}, a reference oxygen partial pressure p_0, Boltzmann's constant k_B, the specific entropy s_{O_2} and the specific enthalpy h_{O_2} of oxygen, and the temperature T.[100,121] Therefore, as T increases, the entropic term becomes more relevant and favors the formation of Ni^{2+} and the release of molecular oxygen. The decrease of oxygen activity is likely not the only reason for LNO decomposition. Several authors describe a loss of lithium due to the volatilization of Li_2O in an environment of pure oxygen, which is suspected to sublimate as the peroxide, Li_2O_2, at high calcination temperatures.[120,122] For this reason lithium carbonate, which is otherwise a common precursor for NCM-type material synthesis, is not commonly used for LNO synthesis, as it only decomposes and fully reacts above 720 °C, which is sub-optimal for LNO synthesis with regards to crystallinity, as well as lithium loss.[84,103] Therefore, solid-state synthesis of LNO should ideally be carried out at temperatures of around 700 °C in an oxygen atmosphere, where lower temperatures yield more oxidizing conditions and thus should result in less substitutional defects and smaller

primary grains, while an increase in temperature favors the growth of a coarse-grained material while sacrificing low $Ni_{Li}^{\bullet}$ defect concentration.[57,59,111]

When attempting to synthesize much larger grain sizes, up to single crystal (SC) morphology of several microns in size by high-temperature sintering, the thermal instability becomes more problematic, and the obtained materials are off-stoichiometric.[123,124] An alternative to this is to use fluxes to grow larger grain materials, which can either protect the sample from decomposition or assist in low-temperature (~700 °C) sintering to obtain micron-sized, ideally isolated grains.[125–128] These salt melts have an inherent drawback, as they have to be washed off the CAM particles after sintering, ultimately causing degradation of the surface, as outlined in the next chapter.

2.2.3 Lithium Residuals, Washing and Surface Stability

Depending on the synthesis method, some LNO can directly be used after synthesis, whereas other techniques, *e.g.* flux-assisted single-crystal growth, require a post washing step.[126–128] Industrially, washing steps are implemented, because they help to remove residual lithium.[129] Excess salt has to be removed, because it can otherwise cause gelation in the preparation of an electrode slurry,[130] as well as clogging the particles pores, which decreases the specific surface area for electrochemical intercalation reactions.[131–134] Washing helps to remove such residues, which are often present in the form of carbonates and cause gas evolution during cycling.[135,136] The presence of carbonates can be explained by the high reactivity of free surfaces, even at ambient conditions, in the presence of moisture and CO_2, which is why such materials should be handled in dry or inert gas conditions.[77,137–139] Next to conversion of lithium oxide to lithium carbonate, ambient moisture can also leach lithium from the lattice *via* lithium to proton ion exchange near the surface, as is depicted in Figure 4b.[76,140] This reaction also occurs during washing with water, forming a partially protonated surface layer.[141] Depending on the subsequent processing, the surface layer either still contains protons during cell assembly, if the material is not heat treated, or it transforms into a decomposed rock-salt type structure when increasing the drying temperature from 80 °C to 300 °C.[141] Upon further increase of the drying temperature to the calcination temperature (~700 °C), the decomposed surface layer undergoes a solid-state reaction with lithium from the bulk material, thus partially recovering the layered structure.[142] Another method to avoid the formation of rock-salt type NiO while also removing intercalated protons, is the addition of dopants, such as boric acid or certain transition metals, to the washing solution or the freshly washed material to obtain a lithium-conductive surface layer.[143–145] It should be noted that the conversion of residual lithium into coatings or additional electrochemically active phases, to avoid water exposure and the associated pitfalls, is an active area of research as well.[146,147]

2.2.4 Other Synthesis Methods

Alternative to the controlled synthesis by high-temperature annealing, the combustion method, also referred to as self-propagating heat treatment, is appealing, as it is usually faster than solid-state calcination and provides the heat needed for LNO formation directly from the combustion fuel, which can be urea, starch, hydrazine, gelatin or glycine.[148–151] In some instances, the combustion product is used directly as a CAM,[148,152] while other authors use the combustion to obtain a precursor mixture, which is then further calcined, similar to what is described for the sol-gel method in 2.2.2.[149–151] When the combustion products are used directly as a CAM, the performance is worse than the materials obtained from solid-state synthesis in terms of capacity and capacity retention.[149] This is likely related to the small particle size, poor crystallinity and residues from the combustion reaction. Therefore, the combustion method does not represent a promising alternative to the solid-state reaction.

Another alternative is the use of microwaves as the energy source for LNO formation. The advantage is again faster reaction, while control over the synthesis parameters is lost. Two types of microwave-assisted synthesis were reported, of which one investigates the product obtained directly from microwave irradiation,[153] while the other method employs a high-temperature calcination after microwave treatment.[152,154] While the direct microwave synthesis product is shown to work extremely well as a CAM (q_{dis} > 260 mAh/g), this is ambiguous as the phase evolution described does not allow for this capacity to be achieved, even theoretically,[155] and is therefore likely a measurement error. When compared to the other synthesis methods, solution-based combustion is found to yield the overall best results, but since the date of publication, better results have been achieved with the solid-state synthesis approach.[57,59,152]

Autoclave synthesis under hydrothermal conditions has also been used to obtain LNO.[156–159] In one instance, the solid solution of LNO with LCO was investigated, but particularly for the synthesis of LNO from $NiCl_2$ the pure product could not be obtained.[156] When instead of Ni^{2+} precursors, Ni^{3+} in the form of nickel oxy-hydroxide is used, phase-pure LNO can be obtained, even without annealing. Sun and co-workers use this precursor and the hydrothermal method as a means for reaction mixture preparation and calcine the material in air to obtain a well-layered structure.[158] Nickel oxy-hydroxide can also be used directly as a hydrothermal precursor for phase-pure LNO.[157,159] Contrary to layered β-$Ni(OH)_2$, β- or γ-NiO(OH) contain nickel in the same oxidation state as LNO, which is Ni^{3+}. This is achieved by oxidizing β-$Ni(OH)_2$, *e.g.* with hypochlorite salts in highly basic conditions, which yields two forms of NiO(OH) with smaller (β) or larger (γ) interlayer spacing, as a result of interstitial water and potassium ions in the latter case.[157,159] One method to obtain NiO(OH) is the ion-exchange reaction from sodium to protons, which is a spontaneous reaction of NNO under aqueous conditions, which depending on the pH can be used to obtain NiO(OH) with

tailored interlayer spacing in either variety.[160] Under high-pressure hydrothermal conditions, NiO(OH) can then be transformed into crystalline LNO.[157,159] The capacity achieved with these materials is consistently lower than that of sst-LNO and also lower than LNO obtained from the hydrothermal approach paired with annealing, as utilized by Sun and coworkers.[157–159] One method to improve the performance of LNO obtained from direct hydrothermal synthesis is the inclusion of cobalt, which likely helps to reduce the water affinity of the structure and thus drives the reaction towards full lithiation.[159] Indeed, for LCO, the hydrothermal method yields high-capacity material, which is comparable to sst-LCO.[159] Apart from the hydrothermal proton to lithium ion exchange, sodium to lithium ion exchange can also be conducted under a variety of conditions,[161–164] but for LNO synthesis, no results were reported prior to this doctoral project. By now, one paper has been reported on the molten-salt-based ion exchange of a Ni-rich NCM, with capacities that are overall lower than the materials studied during this doctoral project.[161] Depending on the ion exchange conditions, the material has to be washed after synthesis, particularly in the molten-salt-based ion exchange. This makes the ion-exchange technique challenging for the synthesis of LNO, which is known to be sensitive to water exposure. This may be the reason why the literature reported performance of Ni-rich IE-NCM has been lower than its sst-analogs.

Finally, several synthesis techniques exist that are specific to the formation of thin films of LNO, rather than bulk material. Some of these techniques are adaptions of bulk syntheses, such as the hydrothermal approach, which can either be conducted as a direct adaption of the hydrothermal bulk synthesis[165] or coupled with electrochemical deposition to promote film growth.[166] Alternatively, pulsed laser deposition (PLD), chemical vapor deposition (CVD) and sputtering have been used to obtain thin films of LNO.[167–169]

While several alternatives to the solid-state synthesis were proposed and tested, to date no true contester has emerged that can deliver similar capacity to sst-LNO. Indeed, of all the alternative techniques described here, the techniques involving a final annealing step have always shown the best capacity. At least to some degree, this is caused by the decreasing stability when moving to high nickel contents, which puts tight constraints on the synthesis window of high-performance Ni-rich CAMs.

2.3 Electrochemistry of Lithium Nickel Oxide

While LNO delivers remarkably high reversible capacity, outperforming all other NCM- and NCA-type materials, it still loses about 10% of capacity due to kinetic limitations. Additionally, the introduction of LNO as a commercial CAM is hampered by its intrinsic instability. The following chapter aims to give an overview of the electrochemistry and degradation of LNO.

2.3.1 Phase Evolution

Upon electrochemical lithium de-intercalation, LNO undergoes a cascade of phase transitions, which can be tracked *via ex situ* or *operando* XRD and correlated with the charge/discharge curves.[57,74,89,155,170,171] If these curves are transformed to differential capacity plots, the phase transformations appear as positive peaks during charge and as negative peaks during discharge, while the single-phase regions appear as troughs. The typical phase evolution of LNO is shown in Figure 2a, b. The first change in space group, corresponding to the second peak during charge (H1-M), is the emergence of cooperative (collinear) JT-distortion, which results in formation of the monoclinic $C2/m$ space group, due to oxidation of nickel as well as lithium/vacancy orderings that stabilize the elongated octahedra.[155,172] The next change in crystallographic phase is the loss of monoclinic distortion, corresponding to the fifth peak (M-H2), which yields a hexagonal phase that crystallizes in the $R\bar{3}m$ space group with α-$NaFeO_2$-type structure. This phase is commonly labeled H2 (second hexagonal phase) and corresponds to an O3 (AB CA BC) structure type. Upon further charging, another phase with the same space group and structure is formed, however, which does feature a much smaller interlayer spacing due to the so-called interlayer collapse upon sufficient delithiation. This phase is commonly labeled H3 (third hexagonal phase). Upon further delithiation, transformation to yet another hexagonal phase, labeled H4 (fourth hexagonal phase) is observed, which adopts an O1 (AB AB) structure in a distorted CdI_2-type structure in the $C2/m$ space group.[62,173,174] This phase forms upon approximating the fully delithiated state, which is NiO_2, and features the smallest interlayer spacing during cycling of LNO.[173,175] Reversible (de-)intercalation was reported for all phases described above, if the material is cycled to moderate cut-off voltages.[175] However, when keeping the material at high SOC, over hundreds of hours, some authors argue that slow decomposition by means of nickel migration from the nickel to the lithium slab can occur.[173,176] Other authors reject the notion of nickel migration due to the highly destabilized state of nickel in face sharing tetrahedral sites, which would be the intermediate migration state, as well as due to complete reversibility of the de-intercalation reaction, even with cut-off voltages that allow H4 formation.[175] It should be noted that, while the H4 phase represents the highest degree of delithiation, the phase propagation outlined above does not imply a full conversion from one phase to the other. Instead for the last transition one could also describe the simultaneous formation of H3 and H4 from H2.[175] Therefore, the phase sequence may be noted as: H2-

H3-(H3-H4)-H4[177] or H2-H3+H4[175], depending on the assumed formation mechanism of H4.

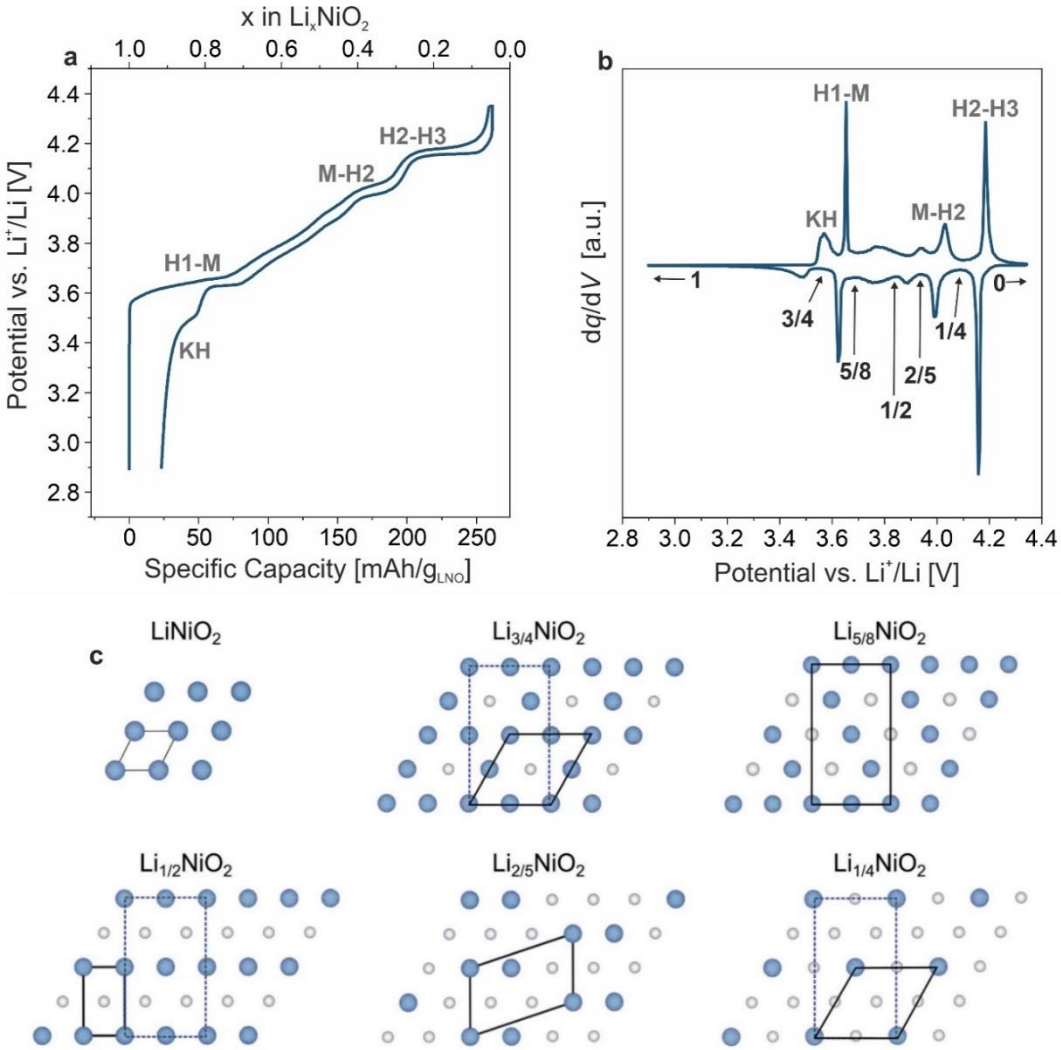

Figure 2. First-cycle charge/discharge curve of LNO in the potential range of 2.9 to 4.35 vs. Li^+/Li, with crystal phase changes and kinetic hindrance region indicated in gray (a). Second-cycle charge/discharge differential capacity plot, with lithium content of ordered phases presented in bold letters (b). Lithium/vacancy ordered phases reproduced with permission from reference [155] (c).

Due to the change from O3 to O1 stacking during the H3 to H4 transition, the NiO_2 layers have to glide, in a threefold degenerate direction, to accommodate for the change in oxygen stacking. The change in stacking fold is driven by dislocations, such as screw dislocations, which LNO can accommodate better than, *e.g.* LCO, due its JT activity.[178] Such dislocation cores can act as lithium-vacancy sinks, which is why they were hypothesized to cause degradation of the material.[178] In LNO with a low defect concentration, the H3 phase is the main phase formed after charging to 4.3 V vs. Li^+/Li, while only small fractions of H4 are observed within the H3 layered structure.[175] The co-existence of these two phases with different oxygen stacking causes strain, which can be visualized as bending of the NiO_2

sheets.[177,179] At sufficiently high $Ni_{Li}^{\bullet}$ defect concentration (> 7 mol%), the H3-H4 transition is not observed anymore.[173] This may be explained by the pillaring effect of these intrinsic defects, which prevent dislocation of the NiO_2 layers, as schematically shown in Figure 5b, similar to the pillaring strategies developed for LCO.[173,180,181] Upon discharge, the H3 phase is re-lithiated faster than the H4 phase, which is the remaining phase at the cusp of transforming to the expanded H2 phase.[175] This could be related to slower re-lithiation of the NiO_2 phase because of its smaller interlayer spacing when compared to H3 or because of the additional energy required to cause slab gliding from O1 to O3, which is the stacking sequence in the H2 state.[175]

Apart from the phase changes according to the pattern H1-M-H2-H3(+H4), several other, less intense peaks are also visible in the differential capacity curve shown in Figure 2b. These transitions are suspected to correspond to the two-phase regions between lithium/vacancy ordered states. From simulating stoichiometric LNO at 0 K, Mock and co-workers predict ordered phases for Li_xNiO_2 at x = 0.25 (1/4), 0.4 (2/5), 0.5 (1/2), 0.625 (5/8) and 0.75 (3/4),[155] which are shown in Figure 2c, while other authors predict additional stable phases at x = 0.33, 0.6 and 0.83[182] and x = 0.125, 0.33, 0.5, 0.6, 0.67, 0.83 and 0.875.[183] When increasing the temperature, some of the miscibility gaps in the models close and solid solutions appear in the range from 0.5 to 0.75.[155] Experimentally, these lithium orderings can be observed by magic-angle spinning (MAS) nuclear magnetic resonance (NMR) spectroscopy[184,185] and electron diffraction.[186] The NMR measurements show the presence of the ordered states of x = 0.25 and 0.5,[187] as well as x = 0.4, 0.6 and 0.75[184], while no close agreement between predicted and observed NMR shifts was found for x = 0.33. From electron diffraction patterns, Delmas and co-workers identified the ordered states of x = 0.63, which lies in the predicted monoclinic region from 0.5 to 0.75,[186] and of x = 0.25, 0.33 and 0.65.[188]

The above described orderings found by Mock and co-workers, 1/4, 2/5, 1/2, 5/8, 3/4, coincide with the single-phase regions (minima) observed in the differential capacity curve shown in Figure 2b, to which the trivial states of x = 1 and 0 were added. The labels added in Figure 2b do not perfectly correspond to the lithium content found electrochemically, but rather are tentative correspondences between the predictions for stoichiometric LNO and the charge/discharge curves of LNO produced by solid-state synthesis. As outlined in the synthesis section, LNO prepared in this way is inherently defective, and the $Ni_{Li}^{\bullet}$ point defects may change the position in the charge profile and the energetic stabilization of lithium/vacancy ordered states. In close proximity to such defects, up to six lithium vacancies may be trapped energetically, as the local strain induced by $Ni_{Li}^{\bullet}$ substitutional defects raises the zero-point energy of re-lithiation.[189] This, in turn, decreases the effective vacancy concentration in the perfectly layered regions of the crystal lattices, thus moving the observed ordered states to higher degrees of de-lithiation (lower x values). In the presence of lithium

pinning substituents, the opposite effect should be observed, because in this case the effective lithium concentration available for formation of lithium/vacancy ordered states would be lower. The presence of either pinning feature also decreases the domain sizes that are available to establish fully ordered phases, as the pinning sites force lithium or lithium vacancies into specific positions in the crystal lattice, thus destabilizing the ordered states and smoothing the obtained voltage profile. Therefore, an increase in $\mathrm{Ni}_{\mathrm{Li}}^{\bullet}$ defects results in smoothed voltage profiles, shifts of phase positions and promotes solid-solution behavior, as observed experimentally and in simulation (schematically depicted in Figure 5a, d).[56,155] In addition to these effects, the first peak observed during charge is particularly affected by the $\mathrm{Ni}_{\mathrm{Li}}^{\bullet}$ defect fraction, due to the importance of lithium diffusion for the deep discharge of LNO. The impact of $\mathrm{Ni}_{\mathrm{Li}}^{\bullet}$ defects on the presence or absence of this particular feature is discussed in the next chapter.

2.3.2 Lithium Diffusion in Lithium Nickel Oxide

The movement of lithium in the α-$NaFeO_2$-type structures Li_xNiO_2, Li_xCO_2 and Li_xTiS_2 with octahedral lithium environment is similar.[190,191] Lithium jumps to a neighboring interstitial tetrahedral site, from which it jumps again to an adjacent octahedral site, as depicted in Figure 3a.[191] The chemical diffusion coefficient, $\widetilde{D}_{\mathrm{Li}}$, can therefore be expressed as the product of the jumping coefficient, D_{J}, and a thermodynamic factor, Θ, according to the following formulas:

$$D_{\mathrm{C}} = D_{\mathrm{J}}\Theta \tag{3}$$

$$\Theta = \frac{\partial \frac{\mu_{\mathrm{Li}}}{k_{\mathrm{B}}T}}{\partial \ln(x)} \tag{4}$$

$$D_{\mathrm{J}} = \lim_{t\to\infty}\left[\frac{1}{4t}\left\langle\frac{1}{N}\left(\sum_{i=1}^{N}\vec{r}_i(t)\right)^2\right\rangle\right] \tag{5}$$

with the chemical potential of lithium μ_{Li}, the lithium content in Li_xMO_2 *x*, the number of diffusing lithium ions *N*, the time *t* and the *i*-th displacement after time *t* labeled $\vec{r}_i(t)$.[191] According to transition-state theory, the rate *R* with which lithium ions jump to neighboring sites can therefore be calculated as:

$$R = v\exp\left(\frac{\Delta E_{\mathrm{A}}}{k_{\mathrm{B}}T}\right) \tag{6}$$

with v being an effective vibration frequency and ΔE_{A} the activation barrier, which is the difference between the transition state and the ground state from which diffusion begins.[191] Diffusion of lithium ions thus depends on the temperature of the system, the chemical potential of lithium and the activation barrier.

When cycling Ni-rich CAMs, the region of 20-70% SOC (delithiation) is usually unproblematic with regards to stability and lithium diffusion.[192] However, below and above this regime, diffusion plays a crucial role as rate-limiting.[185,192] In the low-potential regime at the end of

discharge, the lithium content in the material increases. The activation barrier depends on the lithium content, as the barrier to diffusion increases with increasing lithiation, which is caused by filled lithium sites adjacent to the tetrahedral jumping site, which raises the energy level of lithium in tetrahedral coordination, as is shown in Figure 3b, c.[190] This causes sluggish diffusion at the very end of discharge, which can be measured as increasing polarization.[58] Capacity is lost in the so-called kinetic hindrance (KH) region, depending on discharge rate. Upon slow cycling, a plateau (peak in dq/dV) will be visible in that region (3.4-3.6 V), which is named KH peak, as shown in Figure 2a, b, which does, however, only partially recover under slow cycling (C/10) and even under extremely slow cycling (C/50) does not lead to full lithiation.[58]

The degree of polarization (capacity loss) is dependent on the fraction of $\mathrm{Ni}_{\mathrm{Li}}^{\bullet}$ substitutional defects.[56] Through a combination of experimental and theoretical work, Xiao and co-workers conclusively showed that an increase in $\mathrm{Ni}_{\mathrm{Li}}^{\bullet}$ affects the reversible capacity obtained at the end of discharge. They argue that this is, as outlined above, caused by occupation of the neighboring octahedral lithium site (gate site) and its respective neighbors, which dictate the diffusion properties, because the average occupation of the gate site depends on its respective surroundings.[56] The presence of $\mathrm{Ni}_{\mathrm{Li}}^{\bullet}$ in these gate sites increases the energetic barrier to diffusion, and the defects are completely immobile, thus exhibiting roughly the same effect as three additional lithium ions on adjacent diffusion paths.[56] While this may be true, $\mathrm{Ni}_{\mathrm{Li}}^{\bullet}$ defects can affect the end of discharge through another mechanism. As demonstrated by Sicolo and co-workers, the free lithium-vacancy content cannot simply be calculated from the lithium content x (and the occupied $\mathrm{Ni}_{\mathrm{Li}}^{\bullet}$ sites), as the $\mathrm{Ni}_{\mathrm{Li}}^{\bullet}$ point defects themselves alter the density of free vacancies through trapping, as described in the previous chapter and shown in Figure 5f.[189] Each point defect can, in this fashion, remove six lithium vacancies from the defect-free regions, causing an earlier onset of the low diffusion regime due to high lithium concentrations. Lithium/vacancy ordered states may further complicate the picture, as they can alter the energetic state of the initial diffusion position and thus change the activation energy.

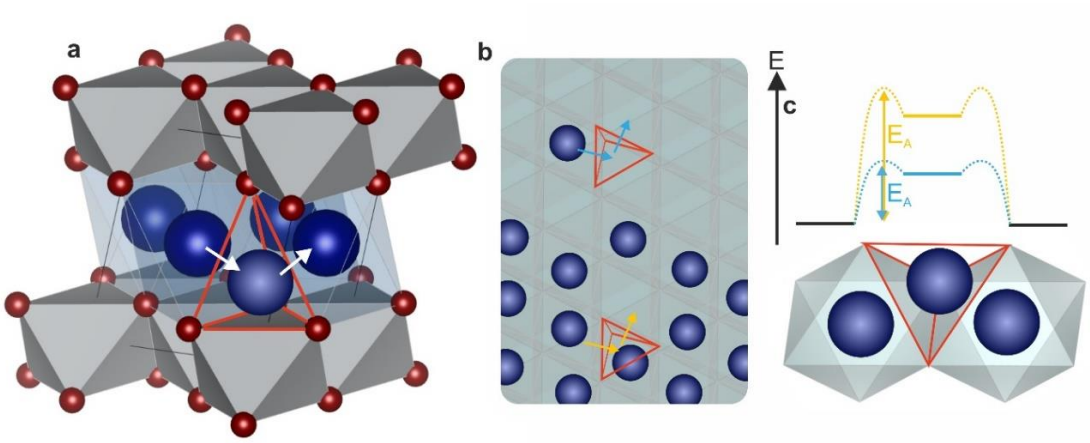

Figure 3. Scheme of lithium diffusion through tetrahedral sites in a lithium layered oxide (a). Comparison between lithium diffusion in dilute (blue) and non-dilute (orange) conditions (b). Energy diagram and scheme of lithium diffusion through tetrahedral sites using the color code from panel b (c).

At high SOC, increasing polarization during charge is observed, which is commonly associated with the decreased interlayer spacing in H3 compared to H2 and thus slower lithium diffusion.[56] Contrary to this, Xiao and co-workers recently proposed that the diffusion of lithium from H2 to H3 phase is the limiting step, while lithium diffusion within the H3 phase has similar energy barriers to the diffusion in the expanded H2 state. Moreover, they argue that defects may help in disturbing attractive Li-Li interactions that exist in the transition regime from H2 to H3, thereby increasing the conversion rate and thus facilitating the charge process. A similar effect is proposed to occur at the free particle surface, which helps to transform H2 to H3 phase.[56] This would explain the observation that SC-LNO typically charges to significantly lower capacities (< 240 mAh/g),[126] even at high temperatures, compared to its polycrystalline (PC) analogs (> 260 mAh/g).[57] During discharge on the other hand, the re-intercalating lithium ions can stay at the H2 phase boundary and thus convert the H3 phase back to H2 without diffusing into the H3 phase, which makes the discharge process in this regime much faster.[56] The predicted asymmetry between charge and discharge has also been observed experimentally as polarization at the end of charge.[175] The authors argue that a surface phase formed by the decomposition of LNO, which itself is redox active, is responsible for the observed behavior.[175] While rock-salt type impurities undoubtedly increase the overall impedance of CAM, it is yet to be seen whether they also feature varying ionic conductivities depending on the electrochemical potential, as proposed by Delmas and co-workers.[175] Similar to these surface impurities, twin boundaries between primary grains can also impede diffusion through the particles, having an overall negative effect on the cycling performance.[72]

At both ends of the voltage range, diffusion of lithium becomes slow. In the high-voltage regime, the charge process is slower, while the re-lithiation at low voltage is slower during

discharge. Particularly for the larger SC-CAMs, these processes lead to worse electrochemistry when compared to their PC counterparts. [193] Nevertheless, the PC materials also suffer from diffusion limitations, particularly at high current rates.[194]

2.3.3 Degradation of Lithium Nickel Oxide

After delithiation, LNO becomes less stable, evident from the lowering decomposition temperature.[174,195,196] For example, when LNO is kept at high SOC (4.5 V vs. C_6/Li_xC_6) for 18 h at 80 °C, it partially decomposes to rock-salt type NiO.[174] During this reaction, oxygen has to be released from the structure, either as a gas or in a direct reaction with the electrolyte. Gas evolution from electrodes can be measured *via* differential electrochemical mass spectrometry (DEMS, also labeled on-line electrochemical mass spectrometry, OEMS).[197–199] In the case of Ni-rich CAMs cycled in LIBs, CO_2 is the gas that is observed in highest quantities.[170,200] There are three distinct pathways through which CO_2 may form in a battery cell.[201,202] Firstly, as mentioned in chapter 2.2.3, lithium residuals, such as lithium carbonate, are present on the surface of Ni-rich materials, which decompose (either chemically or electrochemically) and form CO_2 mostly during the initial cycle.[202] Secondly, the Ni-rich NCM and LNO lattice can release reactive oxygen during cycling, [203] which can also be monitored directly by DEMS, but mostly reacts with the carbonate-based electrolyte to yield CO_2.[203–205] Lastly, the electrolyte solvent can decompose electrochemically, which for a typical solvent, such as ethylene carbonate, occurs at potentials of > 4.6 V vs. Li^+/Li.[206–208] Therefore, the latter process is not expected to contribute in the study of Ni-rich materials, which are typically cycled to lower cut-off potentials.[53] Only the second process is thus directly related to the structural properties of Ni-rich materials, although washing, which is typically used to remove lithium residuals and which also is relevant to the first gas evolution process, can also affect the behavior of the altered surface states in LNO due to degradation.[202,204,209]

Upon oxygen evolution, the material surface undergoes reconstruction due to the simultaneous reduction of transition-metal atoms.[205,210,211] In LNO, typically more oxygen is evolved than in Ni-rich NCM, and the degradation causes spinel-type and ultimately rock-salt type NiO formation on the particle surface.[200,212–217] Gas evolution is observed in the solid-solution regions of H2 and H3, but not during their interconversion according to one study.[170] The bulk, by which the inside of the primary grains is meant within the context of this thesis, was not conclusively found to participate in the high-voltage degradation *via* oxygen release,[213] although, as outlined in the previous chapter, some authors suspect nickel migration as a bulk decomposition pathway at elevated temperatures, which would also require oxygen release. The released oxygen would then have to diffuse through the lithium layer to the particle surface.[218] Therefore, the bulk structure of Ni-rich materials is most likely not degrading and surface phenomena, as well as possibly defect-centered decomposition reactions, are the primary cause of degradation, at least with moderate cut-off voltages and at low or moderate cycling temperatures.

One aspect that may consolidate the conflicting viewpoints of stable bulk, but long-term instability and rock-salt type formation, is the transformation of bulk material to free surface by consecutive exposure of new particle surfaces through operation in electrochemical cells. Continuous surface exposure can happen in various ways, and while some mechanisms are relevant for all morphologies, this so-called "cracking behavior" is different for PC and SC morphologies.

Irrespective of the particle morphology, the CAM surface may be attacked by leaching agents formed from the electrolyte, as schematically shown in Figure 4g. An example of this mechanism is the formation of HF from the commonly used $LiPF_6$ salt and residual moisture in the electrolyte, according to the following reactions:

$$LiPF_6 + H_2O \leftrightarrow LiF_{(s)} + 2HF + POF_3 \quad (7)$$

$$LiPF_6 \leftrightarrow LiF_{(s)} + PF_5 \quad (8)$$

$$PF_5 + H_2O \leftrightarrow +2HF + POF_3.^{[219]} \quad (9)$$

Apart from residual water in the electrolyte, the leaching agents may also form during cycling, *e.g.* from carbonate decomposition on the surface, or moisture adsorbed onto the CAM surface.[220] Furthermore, hydrofluoric acid is likely also formed from other fluorine-bearing electrolyte salts, such as $LiBF_4$.[220] Once formed, it readily attacks the particle surface and dissolves transition metal ions, which can then be observed in deposits on the anode side.[220–222] Hydrofluoric acid is not the only cause of transition-metal leaching, and the formation of β-diketones,[223] acetates[221] and even cycling in thiophosphate solid electrolytes[224] have all been associated with transition-metal dissolution. The leached surface is again exposed to the electrolyte and likely undergoes oxygen loss and surface densification, as outlined above.[220]

Intergranular cracking is another process by which pristine surfaces are exposed continuously during cycling. Ni-rich cathodes are known to undergo anisotropic volume change upon charge and discharge,[54,170,171] which causes severe strain between the individual agglomerated grains, which are present in a secondary particle structure, ultimately leading to pulverization.[109,225–227] This process exposes the surface of individual primary grains, which were initially protected by the surrounding grains.[228,229] The freshly exposed surface then undergoes the same side reactions that the pristine outer surface of the secondary particle structure underwent in the first cycle, ultimately converting a substantial amount of active material to inactive rock-salt type NiO in the case of LNO. Additionally, the pulverization leads to loss of active material due to delamination of the electrodes, as depicted in Figure 4a.[230] Therefore, volume-change-induced intergranular cracking is one of the main degradation pathways for PC Ni-rich materials, by exposing more pristine surface to degradation and due to pulverization-induced contact loss. [231]

Recently, the direct correlation of cycling-induced volume change to particle cracking has been questioned, as several studies reported novel reactive electrolytes to suppress intragranular cracking, thereby stabilizing the active material.[232–235] Manthiram and co-workers hypothesized that cracking is merely a result of detrimental surface reaction, which could be mitigated by coating or change of electrolyte, and that increased cracking is not directly related to more volume change in Ni-rich CAMs.[236] The apparent correlation originates from increasing nickel contents allowing for higher SOC at a given cut-off voltage and therefore more reactive phases to form, paired with the increased proclivity of Ni-rich CAM surfaces to release oxygen.[53,54] If this hypothesis is correct, the efforts to stabilize LNO should focus on the secondary particle surface, rather than bulk doping to mitigate volume change and phase transformations. However, most likely a an interplay between the discussed effects describes the situation best. Surface coatings help to protect against detrimental side reactions, as well as mechanically stabilize the surface.

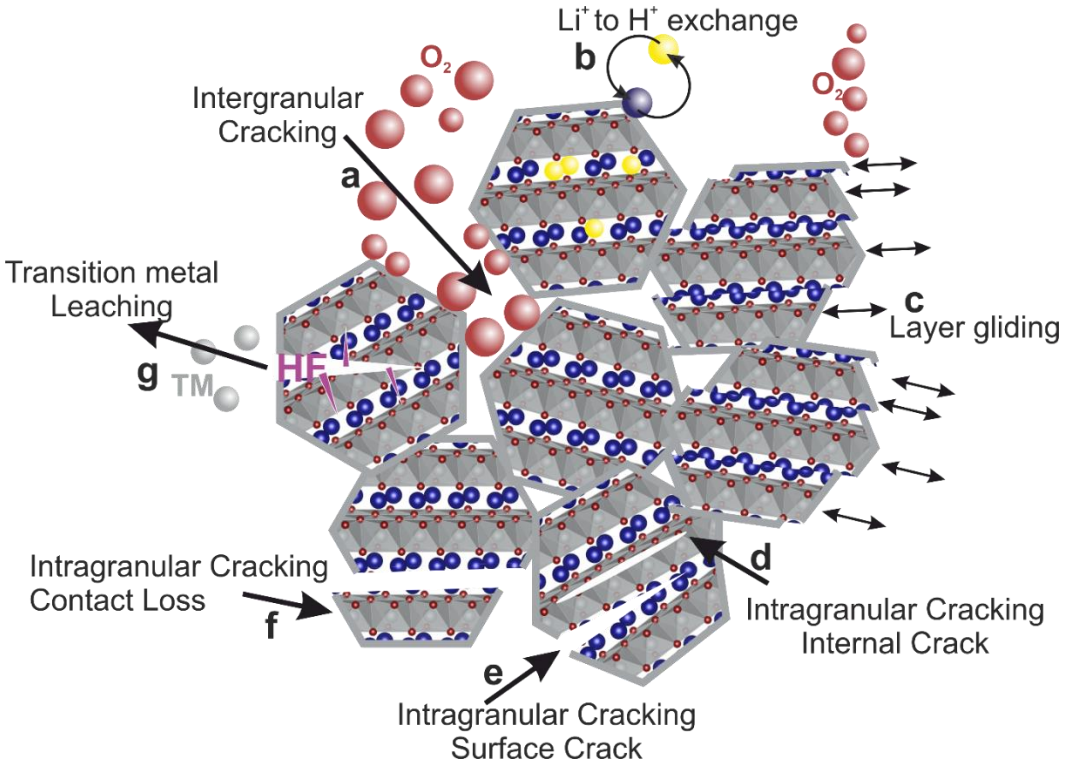

Figure 4. Schematic representation of degradation mechanisms in Ni-rich CAMs.

SC Ni-rich CAMs consist of single isolated grains. In such systems, intergranular cracking is per definition not possible and the growth of large primary particles is thus an attractive stabilization strategy for Ni-rich CAMs.[60,123,237] The larger grains still exhibit intragranular cracks, which can reach from microcrack formation to splitting of the whole grain, as is shown in Figure 4e, f.[80,238] Similar to other microcracks, intragranular cracks are visible after charging to high cut-off potentials and/or prolonged cycling.[80,239] This process also occurs in PC CAMs and was correlated with oxygen release, but it is challenging to discern the contributions of each degradation mode to the overall fading in PC materials.[240] One cause

of intragranular crack formation, which would favor their presence in SC material, is inhomogeneous lithium distribution and subsequent microstrain.[238] Once formed, intragranular cracks also lead to renewed surface reactivity, as described above, but only if the crack is connected to the particle surface, as otherwise the electrolyte has no access to the exposed surface, as is shown in Figure 4d. An internal crack, which results in the formation of a void that grows and shrinks with the so-called "breathing" of the particle upon consecutive cycles, should thus not cause side reactions and capacity loss. For this reason, interior cracks are deemed stabilized and could be the key to stable operation of SC CAMs.[80,241]

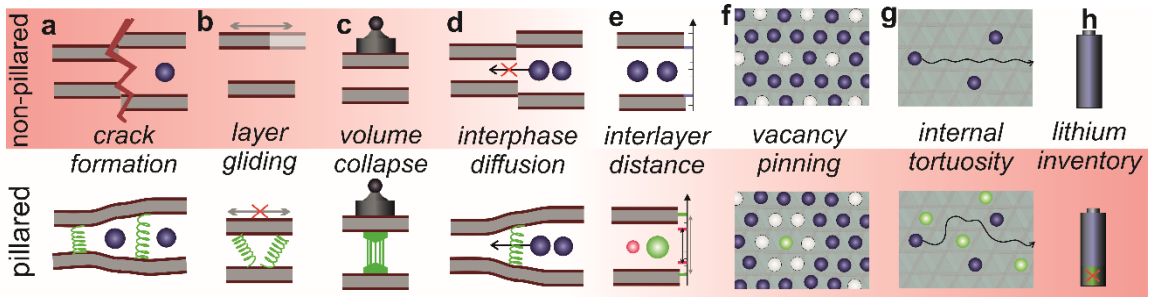

Figure 5. Schematic representation of the discussed impacts of lithium-site doping. Diffusion enhancement at phase boundaries (a). Inducing solid-solution behavior (b). Mitigating interlayer collapse (c). Hindering layer gliding (d). Change of interlayer separation distance (e). Vacancy trapping and ordering disruption (f). Increasing diffusion path length due to physical barrier (g). Lowering the overall intercalate inventory (h).

Apart from microcrack formation, gliding of the transition-metal oxide sheets, which is schematically shown in Figure 4c, can also expose reactive surfaces to the electrolyte at high SOC. Upon reaching a high SOC, the oxygen stacking sequence tends to change from O3 to O1, as described in the previous chapter. This causes a shearing movement between individual sheets, which can be expressed in three directions, due to the threefold symmetry in the *R*–3*m* structure.[178] While such gliding motions are mostly reversible, not all layers return to their original position, leaving a slightly defective discharged state, which can cause microcrack formation at the surface. Each cycle exposes fresh surfaces on the particles, which were described for SC but presumably also exist in PC CAMs. The conditions under which gliding, rather than cracking, occurs are not yet conclusively understood. Bi and co-workers hypothesize that oxygen vacancies are key to the in-plane diffusion of transition-metal species, which is necessary for reversible gliding.[79] They validate these finding by cycling oxygen-deficient and oxygen-rich SC-NCMs at different temperatures.[79] At low temperatures, more cracking is observed in both materials, while the oxygen-deficient material undergoes reversible gliding at elevated temperatures.[79] For LNO, oxygen-deficient structures with true oxygen vacancies are, however, not known in the pristine state and may only form as a surface-degradation product.[82,85,86] On the other hand, simulations by Sadowski and co-workers identify screw dislocations as possible transition states for layer gliding at high SOC.[178] In this case, the stiffness of the material is an important metric, and softer materials favor gliding, whereas more stiff materials tend to crack.[178] This could also

explain the observation, that cycling at low temperatures is correlated with increased crack formation, because the materials can be expected to be stiffer. When comparing LNO to LCO, they find that LNO favors gliding and can adopt the distorted transition state more easily due its JT-distorted microstructure.[178] Another aspect that needs to be taken into account when judging the reversibility of gliding, is the stability of the newly formed O1-stacked domain, which may require more activation energy for its lithiation than the O3-stacked H3 phase.[175] In fact, in the closely related sodium analog of LNO, NNO, layer gliding occurs as an irreversible process and is one of the causes of capacity loss. This further stresses the difficulty of re-intercalation into the O1-stacked H4 phase, which is likely even more energetically unfavorable when larger sodium ions have to be intercalated.[242] Another hypothesis would be the degradation of the H4 phase, *e.g.* to a defective spinel structure and subsequent prevention of gliding back to the original layer position in the discharge cycle. However, the electrochemistry and properties of NNO are not fully understood, not least because of less interest in NNO due its significantly lower specific capacity, as is discussed in chapter 2.5.

The degradation mechanisms of Ni-rich CAMs all seem to center around the free particle surfaces as the driver of degradation. Such surfaces are very reactive, particularly at high SOC, and undergo redox reactions with their environment by gassing and/or direct reaction. During cycling, the bulk material can be exposed as fresh surfaces *via* transition-metal leaching, intergranular cracking, intragranular cracking and layer gliding. Of these mechanisms, gliding and intragranular cracking are the only mechanisms that might affect the bulk material in a negative way, if the material undergoes irreversible gliding, which may result in intragranular cracks.

2.4 Chemical Modification of Lithium Nickel Oxide

The Ni-rich NCM and NCA material families can be considered as chemically modified LNO. Each dopant thereby adds specific properties to the obtained CAM. Apart from the established dopants, manganese, cobalt and aluminum, other elements have also been used to alter the electrochemistry of LNO. The following chapters highlight commonly used dopants, their corresponding position in Ni-rich CAMs and their impact on the electrochemical behavior.

2.4.1 Substitution on the Nickel Site

Historically the interest in layered metal oxide cathodes started with the material LCO, which crystallizes in the same space group as LNO.[3] As such, it comes as no surprise that the full solid solution $LiNi_aCo_{1-a}O_2$ can by synthesized,[243–245] wherein cobalt and nickel occupy the same crystallographic site, as shown in Figure 6, although cobalt atoms tend to cluster according to NMR results.[246] Due to the smaller LS-Co^{3+} ions ($r(Co^{3+}, LS) = 0.545$ Å vs. $r(Ni^{3+}, LS) = 0.56$ Å), which are also thermodynamically more stable, the layering improves with cobalt substitution and for $a \leq 0.8$, $Ni_{Li}^{\bullet}$ defects are fully suppressed.[243,244,247,248] Cobalt-doped LNO delivers a specific discharge capacity of up to 210 mAh/g with 4.3 V vs. Li^+/Li cut-off and 26 mol% Co content, but suffers from similar instability issues as LNO.[249] Cobalt introduction was further reported to enhance lithium diffusion, but the results could not clearly be separated from the reduction in $Ni_{Li}^{\bullet}$ substitutional defect concentration.[250]

Manganese, on the other hand, increases the $Ni_{Li}^{\bullet}$ defect density and can induce Li_{Ni}'' formation in the transition-metal layer.[95] However, contrary to LCO, the layered $LiMnO_2$ competes with the formation of other lithium manganese oxide phases and is only formed under careful reduction of MnO_2 or ion-exchange reaction and decomposes upon electrochemical cycling.[251,252] Therefore, the solid solution $LiNi_bMn_{1-b}O_2$ only exists for $b \geq 0.5$. With the introduction of excess lithium, layered phases are observed for $b < 0.5$ due to the mixing of LNO with $Li_2Mn^{IV}O_3$, rather than $LiMn^{III}O_2$.[25,253] The favored formation of overlithiated phases, when working with considerable Mn contents, is exploited in the so-called lithium-manganese-rich layered oxides, which promise reversible capacities beyond those of the NCM and NCA material families.[95] When Mn contents are limited to $b = 0.75$-0.95, good capacities can be obtained, and the materials show more isotropic volume change (meaning that $\Delta c / \Delta a$ is closer to 1).[254,255] Adding manganese also decreases the average nickel oxidation state, by being oxidized to Mn^{4+}, and may allow to synthesize high-energy cathode materials in air, rather than pure oxygen, which is normally needed to fully oxidize nickel.[256]

The last dopant to complete the industrially relevant NCM and NCA series is aluminum. Aluminum can substitute nickel in LNO without changing its oxidation state, but is contrary to manganese and cobalt, redox inactive.[103] Substitution results in materials with lower capacity and higher FCCL, although aluminum is lighter than nickel and improves the cycling stability slightly, thus compensating for some of the energy loss.[257–261] The introduction of

aluminum is usually only achieved with co-precipitation, and even in this case, it segregates within the slabs.[262] The $Ni_{Li}^{\bullet}$ substitutional point defects are not improved by aluminum introduction and the FCCL increases.[257] The main advantage of aluminum seems to be its beneficial effect on surface stability, resulting in less gas evolution.[250]

When used in conjunction, these dopants yield NCM- and NCA-type materials. Upon increasing the nickel content, the average redox potential is lowered, which allows to cycle to higher SOC at a given cut-off potential.[53,54,254] Therefore, Ni-rich materials were long thought to be less stable,[263] but more recent results suggest higher stability of Ni-rich CAMs if capacity-limited cycling is used.[53,54,254] However, this comparison also has its drawbacks if one considers the redox inactivity of certain dopants, such as aluminum, and the higher cut-off potentials that likely induce more undesirable side reactions, resulting in a false sense of instability of low-Ni NCMs.

Other nickel site dopants, such as Ti,[255,264,265] Fe[266–268] or Cu,[269] have also been tested for the transition-metal sites and are actively pursued in conjunction with manganese and aluminum in an effort to make cobalt-free NCM inspired CAMs.[270] While synergetic effects of multi-constituent doping might be exploited,[271] single dopant effect studies are likely a better way to delve into the effect each individual constituent offers.

2.4.2 Substitution on the Lithium Site

Modification of the lithium site occupation through introduction of so-called “pillar” ions, which are introduced to prevent extreme interlayer collapse, as schematically shown in Figure 5c, has been investigated. A classic example of this approach is magnesium doping. Magnesium is stable in the 2+ oxidation state and is slightly smaller than lithium ($r(Mg^{2+})$ = 0.74 Å vs. $r(Li^{+})$ = 0.76 Å).[61] Therefore, its addition to the synthesis of LNO is commonly accepted to lead to occupation of the lithium sites.[272–274] Upon closer inspection of the substitution pattern, it was observed that only after the magnesium content exceeds 1.7 mol%, it is added to the lithium site as $Mg_{Li}^{\bullet}$, while the first 1.7 mol% end up in the transition-metal site as $Mg_{Ni}^{\prime}$. This finding elucidates the complex substitution patterns that can emerge with such dopants and that careful evaluation of the crystal structure is necessary to judge the position of any dopant in Ni-rich CAMs. The addition of magnesium was shown to slightly suppress $Ni_{Li}^{\bullet}$ formation from 2.4 mol% to 2.0 mol%, while the overall lithium-site content ($Mg_{Li}^{\bullet}$ + $Ni_{Li}^{\bullet}$) was 3.2 mol% and 5.2 mol%. A characteristic sign of inclusion of $Mg_{Li}^{\bullet}$ formation was the improvement of the *c*/*a* lattice parameter ratio, sometimes referred to as a layering parameter.[275] Gallium, which is smaller than Mg^{2+} ($r(Ga^{3+})$ = 0.62 Å)[61] was originally intended as a nickel-site dopant, but was found to also exhibit a complex substitution pattern, similar to Mg-doping of LNO.[261,276] For dopants that are larger than lithium, such as lanthanides and calcium, several reports exist that either claim successful pillar-

ing[277–280] or surface segregation,[281,282] as shown in Figure 6. However, a clear understanding as to what the maximal size for a dopant to enter the material bulk, rather than segregating on the surface during solid-state synthesis, is does not yet exist.

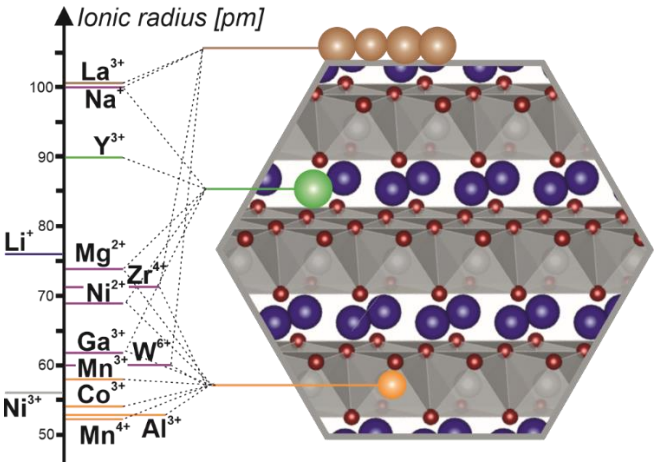

Figure 6. Ionic radii in octahedral coordination and low-spin configuration[61] and reported location within the LNO structure of common additives.

Conceptually, $Ni_{Li}^{\bullet}$ defects also fall under the category of lithium-site dopants and have many parallels to the functionality of the above described Mg and Ga modification strategies. For example, substitution with $Ni_{Li}^{\bullet}$, magnesium or gallium always causes a decrease in charge and discharge capacity,[83,119,275,276,283] due to a combination of lower lithium inventory and slower lithium diffusion at the end of discharge, as schematically shown in Figure 5g, h.[56] The latter point could be related to the smaller ionic radius of LS-Ni^{2+}, Mg^{2+} and Ga^{3+} compared to Li^{+} and may change for dopants larger than lithium, which could expand the interlayer distance and thus facilitate diffusion, as schematically shown in Figure 5e.

2.4.3 Coating and Surface Modification

Particle surface modification helps to stabilize Ni-rich CAMs.[132] For this reason, coatings are often applied to the secondary particles, which is good for protecting the surface initially, but only represents a viable strategy if the PC morphology is maintained, either through cycling to lower cut-off potentials or through mechanical stabilization by the coating. Otherwise, consecutive cracking of the particle structure will likely cause degradation, irrespective of the surface protection layer. One way to still protect the material is through doping the surface of each primary grain. Dopants that segregate at the primary particle surface, rather than occupying crystallographic sites, fulfill this purpose. Examples of these modifications are the incorporation of Zr or W, which can either be added during the co-precipitation process or during the precursor mixing.[110,125,284] One function such dopants can serve is stabilizing the particle surface, *e.g.* by stabilizing a favorable intermediate spinel phase in the degradation cascade, or preferentially forming lithium-conducting rock-salt type structures.[285,286]

Another aspect of surface-segregating dopants can be the selective enhancement or inhibition of the growth of particular crystal facets, thereby influencing the overall morphology and stability of the particles.[287] This facet engineering not only imparts unique structural features, but also opens avenues for optimizing material performance in diverse scenarios, *e.g.* to optimize for stability or rate performance with specific exposed crystal facets. Moreover, surface-segregating dopants play a pivotal role in dictating grain growth within the material. Their influence can either promote or hinder grain growth, offering a mechanism to control the structural evolution of the material during synthesis and subsequent processing.[125,127,284,288] This level of control is instrumental in tailoring the material's microstructure to meet specific performance requirements, making surface-segregating dopants valuable tools in the realm of advanced CAM design. Next to the surface-segregation approach, grain surface modifications can also be made after the CAM has been synthesized. One such strategy is surface doping with specific dopants that either occupy transition-metal or lithium sites, as outlined in 2.4.1 and 2.4.2.[289,290] A common example for transition-metal site surface doping is post treatment by cobalt dry coating and subsequent annealing, which generates a cobalt-rich surface of the CAM, featuring higher stability against oxygen release and surface densification.[291] In the same fashion, doping of the lithium site, *e.g.* by ion exchange or by high-temperature annealing, has been reported.[292–295]

In summary, the strategic incorporation of surface dopants, either through segregation or post-processing, adds another dimension to the design and synthesis of materials like LNO. This approach not only diversifies the range of dopants available for modification, but also provides a nuanced control over crystal facets and grain growth, thus paving the way for tailored materials with enhanced and customized properties.

2.5 Sodium Nickel Oxide

2.5.1 Synthesis and Structure

The synthesis of NNO was first reported with the synthesis of LNO, as mentioned in chapter 2.2.1.[96] In more recent studies on NNO, the material is typically produced *via* solid-state synthesis from NiO and a sodium source, such as Na_2O_2, Na_2O or mixtures thereof under oxidizing conditions and elevated temperatures, similar to the LNO synthesis temperature.[160,296–299] In some instances, the reactants were pelletized,[242] while other authors calcined the mixed powders directly.[299] Depending on the intended application, shorter (3-12 h)[299] or longer (3-83 days)[300,301] annealing times are used, to synthesize cathode active material or in order to synthesize NNO to research its magnetic properties.[302]

Similar to LNO, NNO also crystallizes in discrete layers of nickel oxide and sodium, in which both nickel and sodium are coordinated by octahedra of oxygen. Therefore, NNO is a so-called O3-stacked material (sodium in octahedral coordination, repetition of layering after three stacks). This separates NNO from many other sodium materials, which adopt a P-type structure with prismatic alkali-ion environment.[64,303] Compared to LNO, the interlayer spacing increases, because of the larger sodium ions (r_{Na^+} = 1.00 Å) compared to lithium (r_{Li^+} = 0.76 Å).[61] Another key difference is that sodium ions are large enough to prevent the formation of any nickel substitutional defects, and the anti-site defect reaction energy was calculated to be 2.84 eV, which makes formation unlikely.[301,304] For this reason, NNO is well suited as a precursor for the synthesis of perfectly layered LNO.

As outlined above, LS-Ni^{3+} in an octahedral oxygen environment is JT-active, and in NNO, this causes the crystal structure to be distorted collinearly, which results in crystallization in the *C*2/*m* space group at ambient conditions. However, at 220 °C, NNO undergoes a structural transition and forms the non-JT-distorted hexagonal *R*–3*m* phase, which is O3 layered and has higher electronic conductivity.[305] The JT distortion in NNO can also be relieved by substitution of nickel with JT-inactive species or by changing the oxidation state of nickel into the non-JT-active Ni^{2+} or Ni^{4+} states, such as in NNO substituted with 22 mol% cobalt or the structurally closely related sodium analogs of NCM.[305] For stoichiometries close to the transition towards a monoclinic distorted structure, such as the sodiated NCA, $NaNi_{0.8}Co_{0.15}Al_{0.05}O_2$, an effect of the cooling rate on the obtained crystal structure was observed, whereby slow cooling gave the monoclinic phase, while quenching yielded an overall hexagonal material, likely as a kinetic product.[306]

When substituting the sodium site with lithium, Holzapfel and co-workers also observed a relieve of monoclinic distortion in NNO containing 21 mol% lithium, but the material also only contained 91 mol% of combined Na^++Li^+-ions, which is less than what is formally needed to form either NNO or LNO.[297] Therefore, the origin of the reduced monoclinic distortion is unclear, as both the smaller interlayer spacing caused by lithium addition or the oxidation of Ni^{3+} due to charge compensation for the missing sodium could cause the loss

of JT activity. Also, lithium addition to layered sodium oxides can force lithium into the transition-metal site, causing further oxidation of the transition-metal ions for charge compensation, which would also relieve JT distortion. However, in the material studied by Holzapfel and co-workers,[297] the average transition metal to oxygen bond length decreased with lithium addition, which points to lithium addition to the sodium site and not into the transition-metal slab, which further agrees with the elemental analysis results. Therefore, the most likely explanation of reduced JT distortion is the smaller interlayer spacing due to inclusion of lithium ions, as well as the reduction of alkali-ion content and subsequent oxidation of the transition-metal slab. If the lithium content is increased further, two-phase materials are obtained, segregating into NNO and LNO until reaching complete LNO formation at sodium contents of 5% or lower.[272,307]

2.5.2 Properties of Sodium Nickel Oxide

NNO has been tested as a potential CAM for sodium-ion batteries. When cycled in the potential range of 1.5-4.0 vs. Na^+/Na and with a liquid electrolyte comprising either $NaPF_6$ or $NaClO_4$ in mixed carbonate solvents, NNO was found to undergo a cascade of phase transformations. The structural evolution of NNO can be denoted as O'3→P'3↔P"3↔O"3↔O'"3→O'""3, wherein according to the nomenclature established by Delmas, O represents an octahedral sodium coordination, P a prismatic sodium coordination and the apostrophe denotes the presence of a distorted phase.[160] Note that the first phase transition is written as an irreversible reaction of NNO, because during discharge only 91 mol% sodium are intercalated.[299] Furthermore, when charged above 4.0 V vs. Na^+/Na, irreversible capacity loss is observed due to formation of a phase labeled O""3, which is not sodiated upon discharge.[242]

The voltage plateaus of NNO are much flatter than what is typically observed in LNO, for which a number of reasons can be given.[299] Firstly, NNO is naturally void of intercalation site defects, whereas LNO would contain $Ni_{Li}^{\bullet}$ defects, which smoothen the voltage profile.[56] Secondly, the sodium/vacancy ordered phases in NNO can be expected to be thermodynamically more stable, since *e.g.* the energetic stabilization of ordered Na_xCrO_2 phases is about 2.5 times higher than those found in LNO.[155,308] Lastly the differences in oxygen stacking from octahedral to prismatic, which is absent in LNO, prevents solid solution of these two phases. The specific capacity that can be achieved with NNO is much lower than that delivered by LNO and typically lies in the range of q_{dis} = 110-150 mAh/g, much lower than what is accessible with other layered SIB cathodes, such as Na-NCMs which easily supply up to 180 mAh/g.[242,299,306,309] Some of the difference may lie in the enhanced reactivity of pure nickel compounds, but to some extent, monoclinic distortion also contributes to the lower capacity. Indeed, when the same $NaNi_{0.8}Co_{0.15}Al_{0.05}O_2$ is synthesized with and without monoclinic distortion, by changing the cooling rate after calcination, a capacity increase by 12 mAh/g is observed, while the monoclinic material delivered virtually the same capacity as NNO.

Pure NNO has not received much attention as a potential CAM, although Li and co-workers modeled the effects of titanium substitution.[310] During the course of this doctoral thesis, doping of NNO, particularly with titanium, which was previously predicted as a promising dopant,[310] was investigated as a precursor for the ion-exchanged material, but also as a SIB cathode (patent no. 3, chapter 6.3.2). Interestingly, this material delivered a high specific capacity of q_{dis} = 180 mAh/g, likely due to the suppression of monoclinic distortion upon introduction of titanium, as well as changes in oxidation state.

NNO has also been of some interest to solid-state physics because of its quasi 2D structure and metamagnetic behavior, changing from paramagnetic to antiferromagnetic below the Néel temperature of 20 K.[300,302] As briefly mentioned in chapter 2.2.4, NNO can also be used as a precursor for the formation of oxyhydroxides, which is particularly useful to obtain mixed-metal oxyhydroxide materials.[160]

3 Results

3.1 Publication I: Low-Temperature Ion Exchange Synthesis of Layered $LiNiO_2$ Single Crystals with High Ordering

Publication I describes the development of an ion exchange synthesis for LNO and validates the absence of otherwise intrinsic $Ni_{Li}^{\bullet}$ point defects in the obtained IE-LNO. The parent NNO phase is prepared *via* solid-state reaction from secondary particles of $Ni(OH)_2$ and sodium hydroxide. The temperature range that can be used for this synthesis is broader than that of LNO and allows for preparation at calcination temperatures as low as 450 °C. With a change in calcination temperature, the primary particle (grain) size can be tailored, an aspect which was studied in some more detail in Publication II. The absence of $Ni_{Li}^{\bullet}$ substitutional defects was probed by a combination of PXRD, MAS NMR spectroscopy and (*operando*) electrochemical analysis.

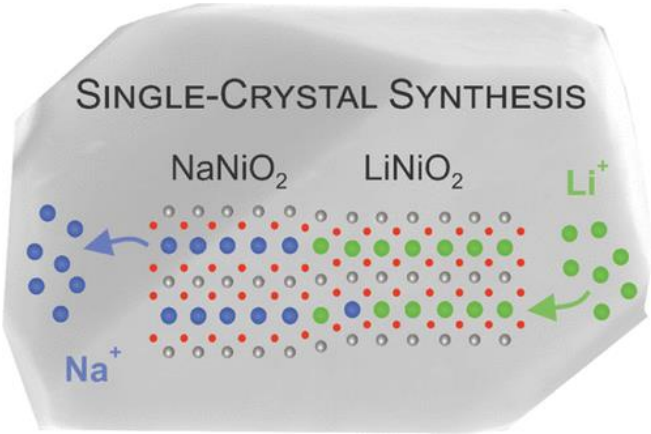

Figure 7. Graphical table of content of publication I. Reprinted from reference [311].

The experiments were planned and designed by the first author under the supervision of D. Weber, A. Kondrakov, J. Janek and T. Brezesinski. The first author developed and optimized the synthesis method for NNO, developed the described ion exchange procedures and optimized the process to obtain IE-LNO. The first author carried out electrochemical experiments and data analysis. A. Mazilkin performed the (S)TEM investigation and interpreted the corresponding results together with the first author. Y. Ma and R. Zhang conducted the SEM experiments, and the data were analyzed by the first author. D. Goonetilleke analyzed the *operando* XRD data together with the first author, and H. Li as well as S. Indris carried out the MAS NMR spectroscopy experiments, while the results were analyzed together with the first author. The manuscript was written by the first author and edited by all coauthors.

Publication I - reprinted from [311]

CHEMISTRY OF MATERIALS

pubs.acs.org/cm Article

Low-Temperature Ion Exchange Synthesis of Layered $LiNiO_2$ Single Crystals with High Ordering

Leonhard Karger, Daniel Weber,* Damian Goonetilleke, Andrey Mazilkin, Hang Li, Ruizhuo Zhang, Yuan Ma, Sylvio Indris, Aleksandr Kondrakov, Jürgen Janek,* and Torsten Brezesinski*

Cite This: *Chem. Mater.* 2023, 35, 648−657 Read Online

ACCESS | Metrics & More | Article Recommendations | Supporting Information

ABSTRACT: Layered Ni-rich oxide cathode materials are being explored in an effort to boost the energy density of lithium-ion batteries, especially for automotive applications. Among them, the ternary-phase $LiNiO_2$ (LNO) is a promising candidate but brings along various issues, such as poor structural stability. The material is prone to disordering (Li off-stoichiometry) when prepared by conventional solid-state synthesis, leading to the presence of Ni^{2+} in the Li layer. These point defects negatively affect the utilization of the Li inventory, thereby limiting the practical specific capacity. In this work, we report on a two-step synthesis approach that avoids the formation of nickel substitutional defects. First, $NaNiO_2$ (NNO) is prepared, showing no such defects due to larger differences in ionic radii between Ni^{2+}/Ni^{3+} and Na^+. NNO is then subjected to Na^+/Li^+ exchange under mild conditions. In so doing, monolithic LNO particles free of $Ni_{Li}^{\bullet}$ defects can be produced at relatively low temperatures. Notably, this route allows for tailoring of the grain size, a strategy that may be used to gain insights into the structure−size−property relations in single-crystalline LNO.

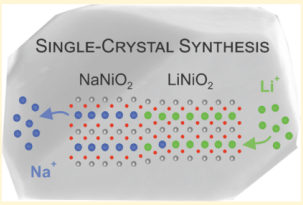

INTRODUCTION

Cathode active materials (CAMs) from the $LiNi_xCo_yMn_zO_2$ (NCM) and $LiNi_xCo_yAl_zO_2$ (NCA) material families (solid solutions based on layered ternary compounds) have been widely employed in commercial high-energy-density Li-ion batteries (LIBs).[1,2] In an effort to boost the specific energy, compositions with increasing Ni content have been adopted. The substitution of cobalt with nickel is also desirable owing to its higher abundance and lower cost while retaining high theoretical specific capacity. However, increasing the Ni content [i.e., development of so-called Ni-rich CAMs (>80% Ni) and especially $LiNiO_2$ (LNO)] has been linked to lower cycling stability. The latter is usually attributed to unfavorable structural transitions at high levels of delithiation (high states of charge).[3,4] Nickel substitutional defects on the Li site ($Ni_{Li}^{\bullet}$) represent another detrimental factor kinetically hindering the occupation of neighboring Li sites during discharge.

LNO adopts a rhombohedral structure with space group $R\bar{3}m$, in which ideally Li^+ and Ni^{3+} cations separate into different layers within a cubic close-packed lattice of O^{2-} anions. When prepared by solid-state synthesis, $Ni_{Li}^{\bullet}$ defects (Ni^{2+} ions present on the crystallographic Li site) are formed. These defects may originate from incomplete transition of the cubic, 3D-isotropic $Ni_{1-x}Li_xO_{1-\delta}$ intermediate[5,6] into the layered, anisotropic 2D-type structure of LNO due to Li off-stoichiometry and/or insufficient oxygen activity.[7] Experimentally, the oxidation of Ni^{2+} from the reactant to Ni^{3+} requires high temperatures of at least 600 °C for kinetic reasons, which typically leads to lithium losses (LiOH is commonly used as a Li precursor).[8] This competition between minimum temperature and lithium loss is inherent to the solid-state synthesis of LNO,[9] with even the least defective samples having more than 1 to 2% of Ni^{2+} on the Li site.[10] This is related to the similar ionic radii of Ni^{2+} (r = 0.69 Å) and Li^+ (r = 0.76 Å) and thus reduced driving force for oxidation and separation into discrete Ni^{3+} and Li^+ layers.[11]

Because the point defects affect the material properties, especially the electrochemical behavior, various characterization techniques have been utilized for the study of Li off-stoichiometry in LNO, including X-ray diffraction (XRD), magnetometry, magic-angle spinning nuclear magnetic resonance (MAS NMR) spectroscopy, and empiric correlations (e.g., voltage range at which characteristic phase transitions occur).[10,12−14] Doping with Mg^{2+}, for example, has been investigated as a means to decrease off-stoichiometry, yet the effects observed can also be interpreted via complex substitution patterns.[15,16] Despite this toolbox, full suppression of Li off-stoichiometry remains elusive in LNO synthesized at elevated temperatures, and thorough defect analysis is experimentally very challenging.[10,17,18]

Received: October 21, 2022
Revised: December 15, 2022
Published: January 4, 2023

https://doi.org/10.1021/acs.chemmater.2c03203
Chem. Mater. 2023, 35, 648−657

Table 1. Rietveld Refinement Results for Reference NNO and Samples Prepared from $Ni(OH)_2$ and NaOH at Temperatures of 450 °C (6 h), 600 °C (6 h and 12 h*), and 700 °C (6 h)

material	a [Å]	b [Å]	c [Å]	β [deg]	V [Å^3]	R_{Bragg} [%]
ref. NNO	5.3187(1)	2.8428(1)	5.5790(1)	110.449(1)	79.040(3)	2.91
NNO-450	5.3140(2)	2.8421(1)	5.5770(2)	110.441(2)	78.924(5)	3.12
NNO-600	5.3158(1)	2.8419(1)	5.5779(2)	110.482(2)	78.938(5)	3.19
NNO-600*	5.3183(1)	2.8432(1)	5.5796(1)	110.474(1)	79.041(3)	2.36
NNO-700	5.3173(2)	2.8424(1)	5.5789(1)	110.485(1)	78.987(3)	2.67

Another approach toward electrochemically active LNO with low point-defect concentration relies on low-temperature and/or ion exchange reactions, generally aiming at the exchange of H^+ for Li^+ in NiOOH. When NiOOH and $LiOH{\cdot}H_2O$ react under hydrothermal or low-temperature (<200 °C) conditions, as reported by Tarascon and coworkers,[19−21] the resulting LNO delivers a specific charge capacity of $q_{ch} \approx 120$ mA h g^{-1}, much lower than the theoretical one ($q_{th} = 275$ mA h g^{-1}). The decreased capacity originates from the presence of NiOOH and NiO impurity phases, which have been shown to form as decomposition products in water.[22,23] Consequently, water-based synthesis appears less suited for the preparation of high-capacity LNO. In an alternative route, LNO was produced from NiOOH and $LiOH{\cdot}H_2O$ in the temperature range from 450 to 600 °C by Sun et al. The material obtained at 550 °C delivered specific charge and discharge capacities of $q_{ch} \approx 183$ mA h g^{-1} and $q_{dis} \approx 170$ mA h g^{-1}, respectively, falling short of achieving the goal of >200 mA h g^{-1} that can be expected for LNO obtained from the solid-state reaction.[24] While these investigations focused on the exchange of the smaller H^+ for Li^+, a parent material having a larger monovalent cation might be capable of more readily establishing layers as a structural motif. One such example is $NaNiO_2$ (NNO), a material that crystallizes in the space group $C2/m$ and exhibits well-separated layers of Na^+ and Ni^{3+}.[25] NNO is typically produced from NiO and Na_2O_2 or Na_2O at elevated temperatures under oxidizing conditions[25−28] for studying its magnetic and electrochemical properties.[29−33] Because of the large size difference between Na^+ ($r = 1.02$ Å) and Ni^{2+}/Ni^{3+} [$r(Ni^{2+}) = 0.69$ Å, $r(Ni^{3+}) = 0.56$ Å], they separate readily into different layers, without formation of interlayer occupancy defects. Overall, NNO represents an attractive parent compound for topotactic ion exchange (Na^+ vs Li^+), which has already been demonstrated for other layered materials.[34−42]

Herein, we examine the synthesis of LNO with high ordering by means of ion exchange from NNO for application in LIB cells. Monolithic material is prepared from commercially available polycrystalline $Ni(OH)_2$ and NaOH in the first step. These reactants allow for control over grain size by varying the annealing temperature. In a second step, Na^+ is exchanged for Li^+ in molten $LiNO_3$ at temperatures below the formation temperature of $Ni^{\bullet}_{Li}$ defects. The structural and electrochemical results indicate the absence of Ni^{2+} substitutional defects in the interlayer space of the single-crystalline LNO CAM.

■ RESULTS AND DISCUSSION

$NaNiO_2$ Synthesis. NNO was prepared from polycrystalline $Ni(OH)_2$ and NaOH by heating powder mixtures at temperatures between 450 and 700 °C under O_2 gas flow for 6 to 12 h, as described in the Experimental Section. The corresponding samples are referred to as NNO-ϑ. The observed XRD reflections match those of single-phase NNO (see Figure S1). Elemental analysis confirms the expected composition but points to the presence of an amorphous, Na^+-rich side phase, which is likely residual NaOH (see Table S1). Calcination at temperatures lower than 450 °C or higher than 750 °C yields a material with a rocksalt-type phase, in addition to layered NNO. Rietveld refinement analysis was performed based on a model of the NNO structure in the $C2/m$ space group with lattice parameters of $a \approx 5.32$ Å, $b \approx 2.84$ Å, $c \approx 5.58$ Å, and $\beta \approx 110.4°$. The refined parameters agree with those reported in the literature and of a reference sample synthesized by the solid-state reaction from Na_2O_2 and NiO (see the Supporting Information for experimental details).[31] The lattice parameters are shown in Table 1. Models assuming the presence of Ni^{2+} on the interlayer Na site were tested too. However, the fraction of $Ni^{\bullet}_{Na}$ converged to zero in the refinements. Accordingly, NNO prepared from $Ni(OH)_2$ and NaOH consists of well-separated layers of sodium and nickel and appears to be free of substitutional defects.

Synthesis of $LiNiO_2$ from $NaNiO_2$ via Ion Exchange. The exchange of Na^+ for Li^+ ions was studied in some detail for NNO-600 heated for 12 h in an O_2 atmosphere (see XRD patterns and electron microscopy images in Figure 1a−f) using a 20 mol % excess of molten $LiNO_3$ as a lithium source. The product (IE-LNO) was washed repeatedly with deionized water and finally vacuum dried. XRD (see Figures 1f and S1) suggests that the material is single phase. However, elemental analysis revealed the presence of residual sodium at about 10% (see Table S1). From the absence of additional reflections, we conclude that a significant fraction of Na^+ resides in the IE-LNO structure.

As the described route requires an aqueous washing step that is known to be detrimental to the LNO (surface structure and constitution), alternative reaction pathways were examined too. However, all other solvents and low-melting Li salts tested for $LiNO_3$ removal and/or ion exchange partially or violently reacted with the LNO and/or NNO (see the Supporting Information for details). Overall, the ion exchange reaction with $LiNO_3$ yielded the most promising results. Additionally, reference LNO was prepared by conventional solid-state synthesis (SS-LNO) at 700 °C, following the description provided in the Supporting Information.

Both IE-LNO and SS-LNO crystallize in the $R\bar{3}m$ space group, and the refined structural parameters are in agreement with literature data (see Tables 2 and S2). Although the XRD pattern collected from the IE-LNO CAM indicates structural similarity to SS-LNO, subtle differences can be observed. Except for 003, all other reflections are broadened. This is likely due to strain introduced by the residual Na^+ ions. There are also distinct differences in lattice parameter-derived variables used to characterize the degree of layering and the $Ni^{\bullet}_{Li}$ defect concentration in LNO, namely, the c/a ratio and unit cell volume. For $Li_{1-z}Ni_{1+z}O_2$ with $z = 0.38$, the c/a ratio

https://doi.org/10.1021/acs.chemmater.2c03203
Chem. Mater. 2023, 35, 648−657

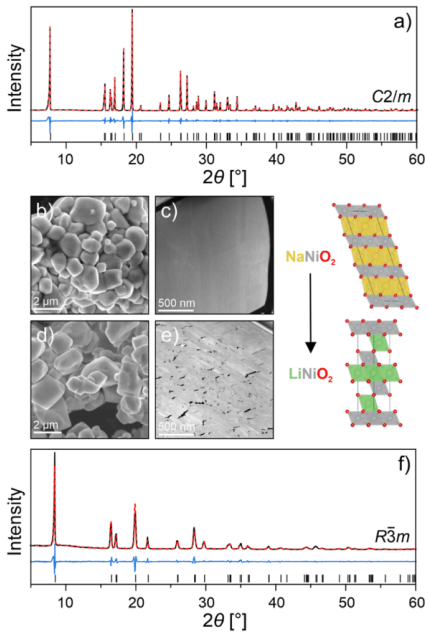

Figure 1. (a,f) XRD pattern and corresponding Rietveld refinement profile for NNO-600 and IE-LNO, respectively. (b,d) SEM images and (c,e) FIB-cut STEM images. Schematic structures of the unit cell for $NaNiO_2$ and $LiNiO_2$ are shown on the right.

equals 4.899 and increases toward 4.95 with decreasing z, while $V \approx 104.1$ Å^3 and decreases toward 101.5(1) Å^3 with $z \rightarrow 0$.[10] For SS-LNO, these metrics agree well with the literature for low-z LNO within the experimental error [c/a = 4.937, V = 101.420(3) Å^3]. For IE-LNO, on the other hand, the c/a ratio (4.940) is slightly higher than that of SS-LNO, indicating some improvement in the degree of layering and low cation disorder. However, this is in contrast to the larger unit cell volume [V = 101.634(9) Å^3] found for IE-LNO, suggesting an increased amount of substitutional defects. The deviation from the known correlations can be rationalized by the presence of Na^{x}_{Li} rather than $Ni^{\bullet}_{Li}$. In the case of Li off-stoichiometry (deficiency), Ni'_{Ni} defects are generated for charge compensation. This leads to an increase in unit cell volume since Ni^{2+} is larger in size than Ni^{3+}. The c/a ratio in turn decreases (increase in lattice parameter a). By contrast, no charge compensation is required upon Na^{x}_{Li} formation, leading to the observation of increased unit cell volume. The latter is enhanced by the larger size of Na^{+} than that of Ni^{2+} while maintaining a high c/a ratio.[11] For NNO, both the unit cell volume (with $V' = 3/2 \cdot V_m \approx 118.6$ Å^3) and pseudohexagonal c'/a' ratio (with $c'/a' = 3 \cdot c_m \cdot \sin\beta/(1/2 \cdot (a_m^2 + b_m^2)^{1/2}) \approx$ 5.201) are larger than those of LNO. In addition, Rietveld refinement indicates the presence of electron density on the crystallographic site of lithium for both IE- and SS-LNO. This electron density can be refined to 1.7(2)% $Ni^{\bullet}_{Li}$ for SS-LNO. For IE-LNO, it can be either interpreted as 5.0(8)% Na^{x}_{Li} or 1.6(2)% $Ni^{\bullet}_{Li}$. Based on the above results, we assign the excess electron density to Na^{x}_{Li} point defects. According to previous studies, the solubility limit of Na^{+} is $\lesssim$5% relative to lithium.[25,43] This is consistent with our refinement data. It should be noted that Na-doped SS-LNO reported in the literature and reference samples prepared in the present work (see the Supporting Information for experimental details and Figure S2) show cycling behaviors similar to that of undoped LNO.[25,43] We therefore assume that the residual sodium in the IE-LNO CAM has no major effect on the electrochemical properties. Minor differences in structural parameters were found for a sample that was subjected to a second ion exchange step (see Table S2). While helping to slightly decrease the Na^{x}_{Li} defect concentration, this approach was not pursued further considering the detrimental effect of washing.

^{7}Li and ^{23}Na MAS NMR Spectroscopy. ^{7}Li MAS NMR spectroscopy measurements were conducted on the IE-LNO sample for probing both the local Li^{+} environment and the presence of Ni^{2+} (S = 1) in the Li layer. The data were compared to NMR results obtained on a series of $Li_{1-z}Ni_{1+z}O_2$ CAMs (referred to as LNO-set1), for which z was varied from about 0.03 to 0.08 using different amounts of $LiOH \cdot H_2O$ in the synthesis [n(Ni)/n(Li) = 1:(0.95−1.05)]. The measured NMR spectra are shown in Figure 2a. For all samples, the main

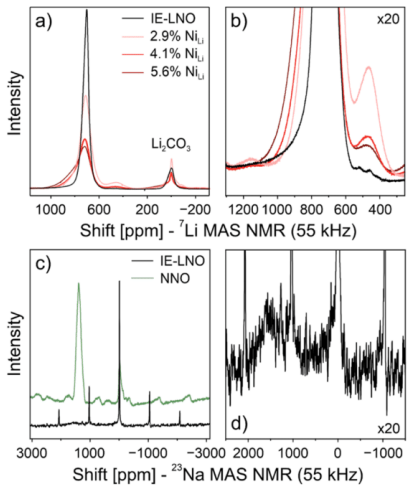

Figure 2. (a) ^{7}Li MAS NMR spectra of LNO-set1 (red) and IE-LNO (black). (b) Zoomed-in region of interest. (c) ^{23}Na MAS NMR spectra collected prior to (green) and after ion exchange (black). (d) Zoomed-in region of interest for IE-LNO.

Table 2. Rietveld Refinement Results for Water-Washed IE-LNO and SS-LNO

material	a [Å]	c [Å]	V [Å^3]	substitutional defects [%]	R_{Bragg} [%]
SS-LNO	2.8732(3)	14.1853(3)	101.420(3)	1.7(2) Ni_{Li}	1.83
IE-LNO	2.8748(2)	14.2001(2)	101.634(9)	5.0(8) Na_{Li}	1.75

https://doi.org/10.1021/acs.chemmater.2c03203
Chem. Mater. 2023, 35, 648−657

peak is observed at 704−723 ppm, with a decreasing paramagnetic shift as z decreases and the samples become less defective. The observation of this signal is consistent with previous findings.[13,44] It is caused by the transfer of unpaired electron spin density from Ni^{3+} to Li^{+} via six 90° and six 180° oxygen-bridged bonds from 12 surrounding nickel ions.[13,45,46] A shoulder peak appears at ∼850 ppm with increasing Li off-stoichiometry (see Figure 2b), which has been attributed previously to an intrinsic anisotropy of the NMR signal of LNO.[13] However, this apparent anisotropy is not visible in the spectrum of IE-LNO. Therefore, we assign it to Ni^{2+} states,[47] present for charge neutrality reasons (formation of two Ni^{2+}, on the defect site and in the Ni layer). The point defects interact with lithium via a 90° oxygen-bridged bond.[48] With decreasing Li off-stoichiometry, the shoulder peak diminishes in intensity, while the main paramagnetic peak becomes more prominent and shifts to a lower parts per million value. In the extreme case of IE-LNO, it is not observed, which is in good agreement with the XRD data, indicating the lack of (nickel) substitutional defects, as expected for "perfectly" layered LNO. A second peak is detected at ∼460 ppm. A lower chemical shift should be caused by a less paramagnetic Li^{+} environment. Interestingly, the peak intensity increases with decreasing Li off-stoichiometry in the SS-LNO reference samples or, in other words, with increasing lithium excess in the synthesis, but it is not observed for IE-LNO. The signal could be related to the presence of Ni^{4+} due to the formation of slightly overlithiated SS-LNO. In this case, lithium atoms would occupy the Ni site and induce the formation of Ni^{4+} for charge balancing. The appearance of the peak could also be caused by lithium-containing NiO with a rocksalt-type structure. Additional peaks in the range from 200 to 400 ppm have been assigned to Li^{+} in the Ni layer by Bianchini et al.[45]

The structural information obtained from ^{7}Li MAS NMR spectroscopy, represented by the narrow peak at 720 ppm and the absence of additional peaks, hints at a uniform magnetic environment in IE-LNO. This agrees with our hypothesis of "perfect" layering achieved by low-temperature ion exchange synthesis. The Li slabs may still contain a few percent of Na^{+} ions, as found by Rietveld refinement. However, they do not induce paramagnetic shifts in the Li^{+} environment. Furthermore, the structural information presented here is limited to the close proximity of lithium and therefore does not account for the presence of impurity phases, such as NiO. Nevertheless, considering only the main phase, we can conclude that no Ni^{2+} ions are occupying the crystallographic Li site.

^{23}Na NMR spectroscopy measurements were conducted on the IE-LNO and NNO-600 samples to probe the presence of Na^{+} ions in the layered structure after ion exchange. The corresponding spectra are shown in Figure 2c. The most intense peak in the NNO-600 spectrum is observed at ∼1400 ppm, stemming from Na^{+} in the NNO structure. The 12 surrounding Ni^{3+} ions interact with sodium and cause a paramagnetic shift through 90 and 180° oxygen-bridged bonds. A second peak is visible around 0 ppm, which can be attributed to Na residues that are not part of the NNO structure. This signal is most likely caused by unreacted NaOH [note that n(Ni)/n(Na) = 1:1.1 in the synthesis]. After ion exchange, the main peak is located at 0 ppm, corresponding to the presence of Na-containing impurities, such as $NaNO_3$. A broad peak appears between 1400 and 1600 ppm, as can be seen in Figure 2d. After background subtraction and peak integration, the signal is found to be ∼4.2% relative to NNO-600. Because it shows a paramagnetic shift, we assume this amount of Na^{+} to be present in the Li layer of IE-LNO. The complementary results from XRD and elemental analysis thus lead to the conclusion that ∼5% Na^{+} ions are left in the structure after the first ion exchange step.

Particle Size Control and Microstructure. While point defects determine properties at the atomic level, it is also important to understand the effect that the microstructure and particle morphology (on the nm to μm scale) have in general. In addition to improvements in the degree of layering over the SS-LNO sample, the synthesis procedure employed in the present work allows for the preparation of monolithic particles of controlled size. The ion exchange reaction proceeds in a topotactic manner, leading to the formation of intact (nonagglomerated) monolithic grains, as highlighted in Figure 3a. The particle size distribution was analyzed via scanning

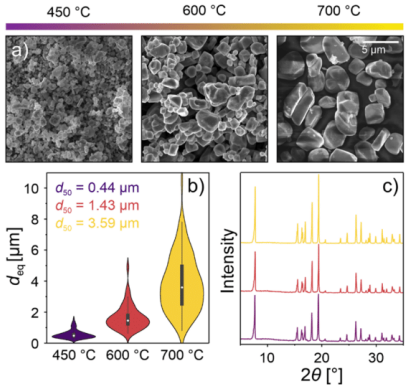

Figure 3. (a) SEM images of IE-LNO particles derived from NNO prepared at temperatures of 450, 600, and 700 °C (6 h). (b) Corresponding particle size distributions and (c) XRD patterns (see Table 1 for Rietveld refinement results).

electron microscopy (SEM) image processing (see the Supporting Information for details). The equivalent diameter d_{eq} of ion-exchanged samples from NNO prepared at different temperatures (6 h) increased by about an order of magnitude from ∼0.4 μm for 450 °C to ∼3.6 μm for 700 °C (d_{50}, see Figure 3b). This corresponds to an increase in mass and volume per particle by a factor of ∼500. As can be seen, the particle size distribution is multimodal, which may help increase packing density (tap density). The correlation between the particle size distribution of NNO-600 (12 h) and that of IE-LNO was also examined (see Figure S3 for violin and box-plot analyses). A small increase in the d_{eq} of IE-LNO is evident from the data, which we attribute to selective removal of "small" particles during the washing step and the sampling size. Overall, the ion exchange route allows for tailoring of the particle size from the typical primary particle level of polycrystalline CAMs to micrometer-sized single crystals. Contrary to conventional single-crystalline materials prepared *via* solid-state synthesis, minimal agglomeration of the individual particles/grains is observed after ion exchange, rendering post deagglomeration procedures moot.

The morphology of the obtained LNO particles is largely inherited from the NNO precursor, as can be seen from

https://doi.org/10.1021/acs.chemmater.2c03203
Chem. Mater. 2023, 35, 648−657

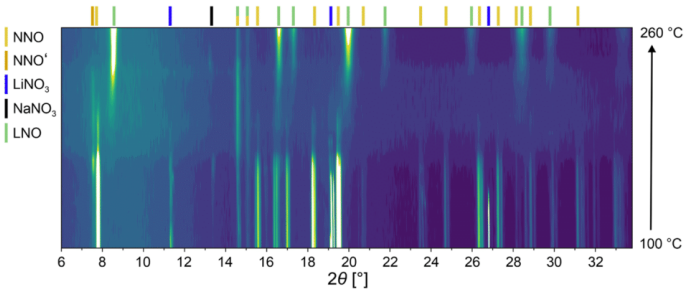

Figure 4. Contour plot of in situ XRD data collected during heating of a 1:1 wt mixture of NNO-600 and $LiNO_3$ in an O_2 atmosphere at 1 K min^{-1}.

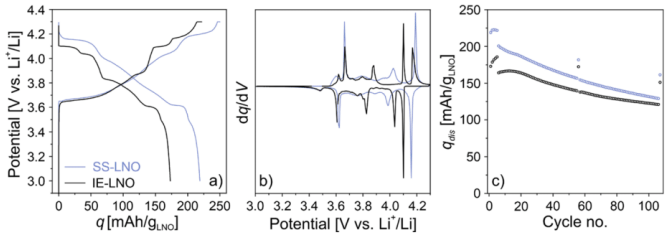

Figure 5. (a) Initial-cycle charge/discharge curves, (b) second-cycle differential capacity curves, and (c) capacity retention for water-washed IE-LNO (black) and SS-LNO (blue). The first five cycles were performed at a rate of 0.1 C, followed by 0.5 C charge and 1 C discharge cycling (0.1 C after 55 and 106 cycles).

Figures 1b–e, 3a, and S4. Microstructural analysis via scanning transmission electron microscopy (STEM) imaging revealed microcracking throughout the particles and the presence of rocksalt-type NiO surrounding the cracks (see Figure 1e). The NiO domains are not visible in the XRD patterns (see Figures 1a,f and 3c), suggesting a low mass fraction of ≤1–2 wt %. Comparing the change in the microstructure from NNO to IE-LNO, the crack formation appears to be a result of the ion exchange reaction itself. We expect it to negatively impact the cycling performance by hindering lithium diffusion. The surface of the water-washed IE-LNO was probed using electron energy loss spectroscopy (EELS, see Figure S5). EELS mapping revealed a two-layer structure of ∼12 nm thickness, with the top layer containing primarily Ni^{2+} ions. The layer underneath shows mixed oxidation states (2+/3+) for Ni (similar observations are made for cracks), probably owing to the ion exchange and washing procedures.

The size distribution, microstructure, and shape of the particles are the result of a complex interplay between processes occurring during NNO synthesis, Na^+/Li^+ exchange, and subsequent washing, all of which potentially affect the electrochemical performance of the LNO CAM.

Kinetic Pathway of Na^+/Li^+ Exchange. To better understand the kinetics of the ion exchange reaction, in situ XRD data were collected during heating of a mixture of NNO-600 and $LiNO_3$, see the contour plot in Figure 4. Initially, the reflections can be indexed to NNO and $LiNO_3$. At ∼140 °C, the reflections of $LiNO_3$ start to decrease in intensity, while a weak $NaNO_3$ signal is detected, which increases with increasing temperature. At ∼180 °C, the background becomes diffuse (with increasing intensity) and the reflections of $LiNO_3$ and $NaNO_3$ disappear. This could be indicative of the formation of a liquid $LiNO_3/NaNO_3$ eutectic, which has a melting point of ∼190 °C.[49] The NNO reflections start to decrease in intensity at 170 °C, suggesting the onset of a reaction below the melting point of $LiNO_3$. A second peak at lower diffraction angles is observed in the temperature range from 150 to 230 °C, herein denoted as NNO′. This peak probably stems from a Na-deficient (oxidized) structure, as is known for chemical deintercalation of Na^+ from NNO materials.[28] The formation of layered LNO occurs at ∼190 °C, evident from the presence of broad reflections that become narrower with increasing temperature (their intensity continues to increase until the temperature of the mixture reaches 260 °C). These findings point to a (complex) multistep reaction: (i) 140 °C ≤ ϑ ≤ 170 °C: oxidation of NNO toward NNO′ accompanied by Na^+/Li^+ ion migration; (ii) 170 °C < ϑ ≤ 210 °C: formation of LNO via the NNO → NNO′ pathway in an eutectic melt of $LiNO_3/NaNO_3$; (iii) 210 °C < ϑ ≤ 230 °C: disappearance of the NNO (full conversion) and LNO crystallization; and (iv) ϑ > 230 °C: disappearance of the NNO′, further crystallization of LNO, and solidification of the nitrate salt melt.

Taken together, the in situ XRD results indicate a fast and atomically efficient mechanism for the ion exchange with $LiNO_3$. Notably, the reaction yields single-phase LNO, even when using a relatively small excess of $LiNO_3$ [here, $n(LiNO_3)/n(NNO)$ = 1.2:1].

Electrochemistry and Operando XRD. To investigate the electrochemical behavior and the structural changes during cycling, the CAMs were incorporated into electrodes and cycled against Li metal in coin cells in the potential range

https://doi.org/10.1021/acs.chemmater.2c03203
Chem. Mater. 2023, 35, 648–657

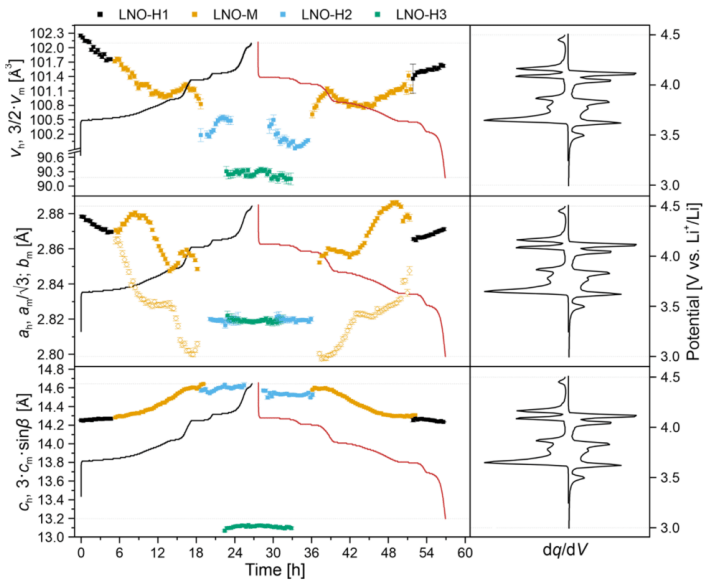

Figure 6. Refinement results for the lattice parameters and cell volume of the hexagonal (H) and monoclinic (M) phases. Operando XRD was conducted on the IE-LNO cathode in half-cells cycled at a C/30 rate in the potential range of 3.0−4.5 V vs Li^+/Li.

between 3.0 and 4.3 V versus Li^+/Li. Interestingly, the voltage profiles differ to some degree from the charge/discharge curves observed for SS-LNO, see Figure 5a,b. The choice of the exchange salt/washing solvent is found to have a strong effect on the capacity, with the best results achieved for $LiNO_3/H_2O$ (see Figure S2). Thus, in the following, the cycling performance of the latter IE-LNO is compared to that of the SS-LNO reference CAM with a relatively low Li off-stoichiometry [1.7(2)% $Ni^{\bullet}_{Li}$]. However, the positions of the phase transitions are similar for all ion-exchanged materials. This is indicative of the same structure for the electrochemically active fraction of CAMs, with a similar electrochemical behavior of the bulk material (independent of the synthesis/postprocessing conditions). The residual Na is apparently not playing a major role. Note that Na-doped SS-LNO cathodes show the same dq/dV peaks as those of the SS-LNO sample (see Figure S2).[25,43] The specific discharge capacity increases from ∼173 to ∼185 mA h g^{-1} (∼1.3 mA h cm^{-2}) over the first five cycles at 0.1 C rate, which is probably related to opening of pores. A similar effect is observed for the SS-LNO reference CAM (see Figure 5c). However, the latter material is capable of delivering capacities that are larger by up to 40 mA h g^{-1}. As expected, the fading is somewhat lower for the IE-LNO, with specific discharge capacities of ∼161 and ∼151 mA h g^{-1} at 0.1 C for SS-LNO and IE-LNO, respectively, after 100 additional cycles at 0.5 C charge and 1 C discharge (plus a 0.1 C testing after 55 cycles).

During electrochemical delithiation, LNO is expected to undergo transitions between several hexagonal and monoclinic phases, commonly denoted as H1 ↔ M ↔ H2 ↔ H3. These transitions have been well characterized previously.[50−52] To examine whether the preparation of LNO via ion exchange affects the structural transitions, operando XRD was conducted on the IE-LNO. As discussed above, the CAM presents different features in the differential capacity curve compared to SS-LNO.[51] Figure 6 shows the refined structural parameters for the initial cycle at a C/30 rate (3.0−4.5 V vs Li^+/Li) together with the potential. An example of the typical quality of fit is provided in Figure S6. An extended voltage window up to 4.5 V was used for operando XRD, whereas electrochemical testing was performed with a cutoff potential of 4.3 V, resulting in overall slightly lower capacities but higher cycling stability. In the experiment, the material delivered specific charge and discharge capacities of 215.9 and 201.5 mA h g^{-1}, respectively, and was found to transition through the expected phases upon delithiation. From OCV to ∼3.7 V, the material retains the initial hexagonal structure (H1). Afterward, it undergoes a transition toward the monoclinic phase (M1), which is characterized by the splitting of selected reflections; for example, the 101_h reflection splits into the $20\bar{1}_m$ and 110_m reflections, as can be seen in the 16.0° < 2θ < 16.8° region in Figure S6. The transition from M′ to M″ is found as a peak in the differential capacity curve and can be tracked by two regions, in which a maximum difference between the a and b lattice parameters is observed. This behavior indicates full conversion to M′ and M″, separated by a clear convergence of the two parameters at ∼3.9 V. The transition back to hexagonal (H2) is observed at ∼4.1 V, followed by the H2 to H3 phase transition at 4.2 V. During the monoclinic regime, the c lattice parameter increases gradually from 14.284(4) Å (∼3.7 V) to a maximum of 14.604(3) Å (∼4.07 V). Beyond 4.1 V, a small decrease is observed as the material transitions toward the H2 phase, with c = 14.552(9) Å at 4.2 V. The transition to the H3 phase results in a drastic reduction, from ∼14.552(9) to ∼13.115(7) Å, the latter being much lower than typically reported for LNO.[51,52] The overall behavior is

https://doi.org/10.1021/acs.chemmater.2c03203
Chem. Mater. 2023, 35, 648−657

consistent with previous findings, suggesting that the exchange reaction does not adversely affect the structural evolution of the system. As the potential approaches 4.5 V, another peak appears in the differential capacity curve, which is not seen in the discharge curve. We attribute it to the H3 to H4 transition, which occurs upon full delithiation of LNO and apparently is only visible at very low current rates.[10] Since this phase transition is impeded by Li off-stoichiometry, preventing sheet gliding at 7%,[53,54] we expect it to be more pronounced in a sample with no substitutional defects as there is no Ni^{2+} present in the Li slab. This observation agrees with the data described above.

The aforementioned phase transitions are typical of LNO CAMs, but the potential ranges at which they occur are somewhat shifted for the IE-LNO sample studied here. In general, the potential of the H2−H3 transition is found to shift to higher values with increasing Li off-stoichiometry.[12] This is caused by increasing destabilization of the H3 phase due to Ni^{2+} occupying the Li site.[9] In Figure 7, the mean H2−H3

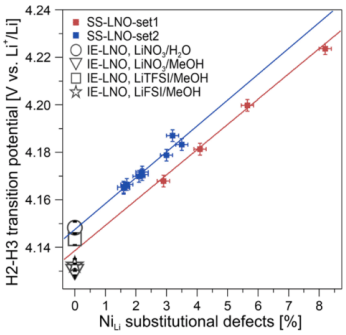

Figure 7. H2−H3 transition potential for LNO-set1, LNO-set2, and various IE-LNO samples from differential capacity curves as a function of the Li off-stoichiometry (from XRD for LNO-set1 and LNO-set2). The peak potentials shown are average values from charge and discharge.

(peak) potential for various IE-LNO CAMs is compared to that of the LNO-set1 reference samples (see the Supporting Information for details on the dq/dV peak analysis). A linear regression was applied to the data in accordance with the procedure reported by Kurzhals and coworkers.[12] From this, the mean potential of the H2−H3 transition for "perfectly" layered LNO (0% $Ni_{Li}^{\bullet}$) is estimated at 4.138(5) V versus Li^+/Li. The results of Kurzhals et al. are also reproduced in Figure 7 (referred to as LNO-set2). From the analysis of these data, a potential of 4.148(3) V is determined. As can be seen, both data sets follow a linear relationship but are slightly offset with respect to each other. The reason is likely a systematic error in the determination of the Li off-stoichiometry by XRD. We attribute the H2−H3 transition potential of 4.13−4.15 V to the lack of off-stoichiometry and therefore intrinsic stabilization of the H3 phase (i.e., the absence of nickel substitutional defects strongly affects the mean potential of the phase transitions).

Taken together, the structural information from ^{7}Li MAS NMR spectroscopy and XRD agrees well with the empirical electrochemical evidence, indicating high ordering of the ion-exchanged LNO. However, the specific capacity delivered by the obtained material is lower than that of the reference material. We believe that the main reasons for this are the formation of cracks and rocksalt-type NiO domains during ion exchange. An additional annealing step in the presence of a lithium source might help produce a high-capacity material. An alternative strategy could be doping of the parent NNO compound for increasing structural integrity in the exchange reaction. Lastly, we consider coating of the particles an interesting approach to prevent unwanted surface side reactions with the washing solvent.

■ CONCLUSIONS

In summary, we have successfully developed a novel two-step calcination process followed by facile ion exchange for the preparation of LNO single crystals. The layered structure of the parent NNO phase is maintained during Na^+/Li^+ exchange, leading to a material that is free of Ni^{2+} substitutional defects on the Li site. This is confirmed by XRD and solid-state NMR spectroscopy measurements, the latter indicating a very uniform Li^+ environment. The synthesis procedure further allows for size tailoring of the monolithic LNO grains. The absence of $Ni_{Li}^{\bullet}$ point defects is found to directly affect the charge/discharge behavior of ion-exchanged LNO by altering the voltage at which the characteristic phase transitions occur. The changes are neither associated with electrochemical reactivity to a specific lithium salt used for ion exchange or washing solvent nor residual Na present in the structure. We believe that this methodology, once optimized for battery performance by suppressing NiO formation and cracking, is applicable to study size effects in LNO (fracture behavior, charge-storage kinetics, interfacial degradation, etc.) and related single-crystalline materials and may help us better understand the electrochemical implications of Li off-stoichiometry in layered oxide cathodes.

■ EXPERIMENTAL SECTION

Materials Synthesis. $NaNiO_2$ was synthesized by the solid-state reaction from $Ni(OH)_2$ ($d_{50} \approx 4$ μm, BASF SE) and NaOH (Sigma-Aldrich). The reactants were homogenized under an Ar atmosphere for 5 min with 10 mol % excess of NaOH, that is, $n(Ni)/n(Na)$ = 1:1.1, using a laboratory blender (Kinematica). The blended precursor mixture was heated in an alumina crucible under O_2 flow (2 atm h^{-1}) in a tube furnace (Nabertherm P330) at 300 °C for 10 h with 3 K min^{-1} heating and cooling rates. After cooling to room temperature, it was homogenized again for 5 min, and the resulting mixture was transferred to an alumina crucible for calcination at temperatures ranging from 450 to 700 °C for 6−12 h using the above-mentioned conditions.

$LiNiO_2$ was synthesized via ion exchange by mixing $NaNiO_2$ with 20 mol % excess of $LiNO_3$ and heating to 320 °C under an Ar atmosphere. After cooling to room temperature, the mixture was washed twice with water under stirring. The resulting powder was dried in a vacuum at 120 °C (see the Supporting Information for water-free washing procedures and alternative lithium salts for ion exchange).

Electrochemical Testing. Electrodes were prepared by casting an *N*-methyl-pyrrolidone (NMP)-based slurry with 94 wt % CAM, 3 wt % Super C65 carbon, and 3 wt % polyvinylidene difluoride (PVDF, Solef 5130; Solvay) onto an Al foil current collector. The slurry was prepared by combining all constituents with 20 wt % additional NMP in a planetary centrifuge mixer (ARE250, Thinky) and stirring applying a two-step program (3 min at 2000 rpm and 3 min at 400 rpm). The slurry was spread onto 0.03 mm Al foil using an Erichsen Coatmaster 510 film applicator at a rate of 5 mm s^{-1}. The as-made

https://doi.org/10.1021/acs.chemmater.2c03203
Chem. Mater. 2023, 35, 648−657

tapes were dried overnight in a vacuum at 120 °C and then calendered at 14 N mm^{-1} (Sumet Messtechnik). Cathodes of 13 mm diameter and 7−10 mg_{CAM} cm^{-2} areal loading were punched out, and half-cells with LP57 electrolyte (1 M $LiPF_6$ in a 3:7 weight ratio mixture of ethylene and ethyl methyl carbonate), a GF/D separator, and Li metal assembled in an Ar glovebox. Electrochemical testing was performed in the potential range of 3.0−4.3 V versus Li^+/Li. The first five cycles were carried out at a rate of 0.1 C (1 C = 220 mA g^{-1}), followed by 100 cycles at 0.5 C charge and 1 C discharge (0.1 C after 55 and 106 cycles), with constant voltage charging until the specific current decayed to 0.02 C.

X-ray Diffraction. XRD patterns were collected on a STADI P (STOE) diffractometer in Debye−Scherrer geometry utilizing monochromatic Mo $K\alpha_1$ radiation (λ = 0.7093 Å, 50 kV, 40 mA) and a Mythen 1 K detector (Dectris). The diffraction data sets were analyzed using TOPAS Academic v7. A LeBail fit was performed first, in which background correction was peformed by applying a Chebyshev polynomial function with 10 terms. Lattice parameters, zero-shift, axial divergence, and crystallite size were extracted as Gaussian and Lorentzian contributions. The phenomenological model by Stephens was used to refine *hkl*-dependent microstrain.[55] During Rietveld refinement, the parameters from the LeBail fit were first fixed, and the oxygen coordinate(s) z_O (LNO) and z_{O_1} and z_{O_2} (NNO), site occupancies, and Debye−Waller factors were refined while applying an absorption correction. Lastly, all parameters were refined in parallel until convergence was achieved. The confidence intervals are 3 times the estimated standard deviations as obtained from TOPAS Academic v7. The errors of cell volumes were estimated to be higher than the errors obtained directly from refinement and therefore rounded to the first significant digit after the comma when given in cubic angstrom.

Operando XRD. The positive caps, negative caps, and spacers of the coin-cell casings were modified by electro-erosion for operando XRD experiments to have a central hole of 5 mm diameter and sealed with glass windows of 6 mm diameter and 160 μm thickness using a surface-treated polyethylene foil. Cells were cycled at a rate of C/30 using a Gamry Interface 1000 potentiostat, while XRD patterns were collected simultaneously using a STOE Stadi-P diffractometer with a Mo anode. Diffraction data were collected in the range of $5° < 2\theta < 37°$ with a collection time of 21 min per pattern. Rietveld refinement was carried out sequentially on the diffraction data using GSAS-II.[56] The zero offset and instrumental contribution to peak broadening were determined by measurement of a LaB_6 660b reference material.

In Situ XRD. The exchange reaction was studied by in situ XRD using a custom-built diffractometer, the specifics of which were reported previously.[57] For sample preparation, a 1:1 wt mixture of NNO-600 and $LiNO_3$ was ground in a mortar and filled into a sapphire capillary. The mixture was then heated at a rate of 1 K min^{-1} under an O_2 atmosphere, with each XRD pattern being the accumulated signal over 5 min. Temperature calibration was performed by comparison with the cell volume of Al_2O_3 powder, which was measured in a separate heating experiment.

7Li and ^{23}Na Nuclear Magnetic Resonance Spectroscopy. ^{7}Li and ^{23}Na MAS NMR experiments were conducted on a Bruker Avance 200 MHz spectrometer at a magnetic field of 4.7 T. Spectra were acquired at Larmor frequency values of 77.8 and 52.9 MHz for ^{7}Li and ^{23}Na, respectively, with 1.3 mm rotors and spinning at 55 kHz. A rotor-synchronized Hahn-echo pulse sequence (90°-τ-180°-τ-acquisition) was used with a recycle delay of 1 s and 90° pulse lengths of 0.85 μs for ^{7}Li and 0.80 μs for ^{23}Na. The NMR shifts were referenced using aqueous 1 M LiCl and NaCl solutions (0 ppm). All spectra are normalized with respect to sample mass and the number of scans.

Inductively Coupled Plasma−Optical Emission Spectroscopy. The elemental composition was determined by inductively coupled plasma (ICP)−optical emission spectroscopy (OES) using a Thermo Fischer Scientific ICAP 7600 DUO. Powder samples were dissolved in an acid digester in a graphite furnace. The mass fraction values were obtained from three independent measurements for each sample. About 10 mg was dissolved in 6 mL of hydrochloric acid and 2 mL of nitric acid at 353 K for 4 h. The digested samples were diluted, and analysis of elements was conducted with four different calibration solutions and an internal standard (Sc). Two/three wavelengths of elements were used. The O content was analyzed by carrier gas hot extraction using a commercial oxygen/nitrogen analyzer TC600 (LECO). It was calibrated using the certified standard KED 1025 (ALPHA). The measurements were conducted at 5800 W.

Electron Microscopy. Morphological and compositional information about the as-prepared samples was obtained from field-emission SEM and energy-dispersive X-ray spectroscopy using a LEO-1530 microscope (Carl Zeiss AG). Specimens for transmission electron microscopy (TEM) investigation were prepared by the lift-out technique using a Ga FIB on a STRATA dual-beam system. They were milled at 30 kV, followed by final polishing at 2 kV to reduce surface damage. Sample preparation was immediately followed by TEM investigation to reduce the risk of oxidation during storage and handling. TEM was performed on a Themis Z (Thermo Fisher Scientific) double-corrected transmission electron microscope at 300 kV. STEM images were collected using a high-angle annular dark field detector. EELS data were acquired with an energy resolution of ∼1 eV. Spectra were collected in the dual EELS mode, allowing us to lock the ZLP and use it as a reference for accurate determination of the edge position for each element. Analysis was carried out using the multiple linear least squares fitting method integrated in Gatan Digital Micrograph.

■ ASSOCIATED CONTENT

Supporting Information

The Supporting Information is available free of charge at https://pubs.acs.org/doi/10.1021/acs.chemmater.2c03203.

Experimental section including synthesis of reference materials and details on alternative ion exchange procedures, structural characterization via XRD and Rietveld refinement, particle size analysis, ICP−OES results, and additional data from electrochemical cycling and TEM analysis (PDF)

■ AUTHOR INFORMATION

Corresponding Authors

Daniel Weber − *Battery and Electrochemistry Laboratory (BELLA), Institute of Nanotechnology, Karlsruhe Institute of Technology (KIT), 76344 Eggenstein-Leopoldshafen, Germany; Institute for Applied Materials-Energy Storage Systems (IAM-ESS), Karlsruhe Institute of Technology (KIT), 76344 Eggenstein-Leopoldshafen, Germany;* orcid.org/0000-0003-4175-9278; Email: daniel.weber3@kit.edu

Jürgen Janek − *Battery and Electrochemistry Laboratory (BELLA), Institute of Nanotechnology, Karlsruhe Institute of Technology (KIT), 76344 Eggenstein-Leopoldshafen, Germany; Institute of Physical Chemistry & Center for Materials Research (ZfM/LaMa), Justus-Liebig-University Giessen, 35392 Giessen, Germany;* orcid.org/0000-0002-9221-4756; Email: juergen.janek@phys.chemie.uni-giessen.de

Torsten Brezesinski − *Battery and Electrochemistry Laboratory (BELLA), Institute of Nanotechnology, Karlsruhe Institute of Technology (KIT), 76344 Eggenstein-Leopoldshafen, Germany;* orcid.org/0000-0002-4336-263X; Email: torsten.brezesinski@kit.edu

Authors

Leonhard Karger − *Battery and Electrochemistry Laboratory (BELLA), Institute of Nanotechnology, Karlsruhe Institute of*

https://doi.org/10.1021/acs.chemmater.2c03203
Chem. Mater. 2023, 35, 648−657

Technology (KIT), 76344 Eggenstein-Leopoldshafen, Germany

Damian Goonetilleke − *Battery and Electrochemistry Laboratory (BELLA), Institute of Nanotechnology, Karlsruhe Institute of Technology (KIT), 76344 Eggenstein-Leopoldshafen, Germany;* orcid.org/0000-0003-1033-4787

Andrey Mazilkin − *Battery and Electrochemistry Laboratory (BELLA), Institute of Nanotechnology, Karlsruhe Institute of Technology (KIT), 76344 Eggenstein-Leopoldshafen, Germany*

Hang Li − *Institute for Applied Materials-Energy Storage Systems (IAM-ESS), Karlsruhe Institute of Technology (KIT), 76344 Eggenstein-Leopoldshafen, Germany*

Ruizhuo Zhang − *Battery and Electrochemistry Laboratory (BELLA), Institute of Nanotechnology, Karlsruhe Institute of Technology (KIT), 76344 Eggenstein-Leopoldshafen, Germany*

Yuan Ma − *Battery and Electrochemistry Laboratory (BELLA), Institute of Nanotechnology, Karlsruhe Institute of Technology (KIT), 76344 Eggenstein-Leopoldshafen, Germany;* orcid.org/0000-0003-4369-9520

Sylvio Indris − *Institute for Applied Materials-Energy Storage Systems (IAM-ESS), Karlsruhe Institute of Technology (KIT), 76344 Eggenstein-Leopoldshafen, Germany; Helmholtz Institute Ulm (HIU) Electrochemical Energy Storage, 89081 Ulm, Germany;* orcid.org/0000-0002-5100-113X

Aleksandr Kondrakov − *Battery and Electrochemistry Laboratory (BELLA), Institute of Nanotechnology, Karlsruhe Institute of Technology (KIT), 76344 Eggenstein-Leopoldshafen, Germany; BASF SE, 67056 Ludwigshafen, Germany*

Complete contact information is available at: https://pubs.acs.org/10.1021/acs.chemmater.2c03203

Notes

The authors declare no competing financial interest.

■ ACKNOWLEDGMENTS

This work was partially supported by the BASF SE. Thomas Bergfeldt is acknowledged for conducting the ICP−OES analysis and Svetlana Korneychuk and Philipp Müller for TEM analysis of IE-LNO and NNO, respectively. We thank Nikolai Bartnick and Holger Geßwein for experimental support as well as Philipp Kurzhals and Felix Riewald for sharing electrochemical data on LNO, denoted as LNO-set2 herein. We are also grateful to Marie Duffiet and Matteo Bianchini for helpful discussions regarding NMR spectroscopy and Na doping of LNO.

■ REFERENCES

(1) Nitta, N.; Wu, F.; Lee, J. T.; Yushin, G. Li-Ion Battery Materials: Present and Future. *Mater. Today* **2015**, *18*, 252−264.

(2) Blomgren, G. E. The Development and Future of Lithium Ion Batteries. *J. Electrochem. Soc.* **2017**, *164*, A5019−A5025.

(3) Noh, H.-J.; Youn, S.; Yoon, C. S.; Sun, Y.-K. Comparison of the Structural and Electrochemical Properties of Layered $Li[Ni_xCo_yMn_z]O_2$ (x = 1/3, 0.5, 0.6, 0.7, 0.8 and 0.85) Cathode Material for Lithium-Ion Batteries. *J. Power Sources* **2013**, *233*, 121−130.

(4) Kim, J.-H.; Ryu, H.-H.; Kim, S. J.; Yoon, C. S.; Sun, Y.-K. Degradation Mechanism of Highly Ni-Rich $Li[Ni_xCo_yMn_{1-x-y}]O_2$ Cathodes with x > 0.9. *ACS Appl. Mater. Interfaces* **2019**, *11*, 30936−30942.

(5) Li, W.; Reimers, J. N.; Dahn, J. R. Crystal Structure of $Li_xNi_{2-x}O_2$ and a Lattice-Gas Model for the Order-Disorder Transition. *Phys. Rev. B* **1992**, *46*, 3236−3246.

(6) Reimers, J. N.; Li, W.; Dahn, J. R. Short-Range Cation Ordering in $Li_xNi_{2-x}O_2$. *Phys. Rev. B* **1993**, *47*, 8486−8493.

(7) Bianchini, M.; Fauth, F.; Hartmann, P.; Brezesinski, T.; Janek, J. An In Situ Structural Study on the Synthesis and Decomposition of $LiNiO_2$. *J. Mater. Chem. A* **2020**, *8*, 1808−1820.

(8) Lin, S. P.; Fung, K. Z.; Hon, Y. M.; Hon, M. H. Crystallization Kinetics and Mechanism of the $Li_xNi_{2-x}O_2$ ($0<x\leq1$) from Li_2CO_3 and NiO. *J. Cryst. Growth* **2002**, *234*, 176−183.

(9) Riewald, F.; Kurzhals, P.; Bianchini, M.; Sommer, H.; Janek, J.; Gasteiger, H. A. The LiNiO2 Cathode Active Material: A Comprehensive Study of Calcination Conditions and their Correlation with Physicochemical Properties Part II. Morphology. *J. Electrochem. Soc.* **2022**, *169*, 020529.

(10) Bianchini, M.; Roca-Ayats, M.; Hartmann, P.; Brezesinski, T.; Janek, J. There and Back Again—The Journey of $LiNiO_2$ as a Cathode Active.Material. *Angew. Chem., Int. Ed.* **2019**, *58*, 10434−10458.

(11) Shannon, R. D. Revised Effective Ionic Radii and Systematic Studies of Interatomie Distances in Halides and Chaleogenides. *Acta Crystallogr.* **1976**, *32*, 751−767.

(12) Kurzhals, P.; Riewald, F.; Bianchini, M.; Sommer, H.; Gasteiger, H. A.; Janek, J. The $LiNiO_2$ Cathode Active Material: A Comprehensive Study of Calcination Conditions and Their Correlation with Physicochemical Properties. Part I. Structural Chemistry. *J. Electrochem. Soc.* **2021**, *168*, 110518.

(13) Chazel, C.; Ménétrier, M.; Croguennec, L.; Delmas, C. $^{6/7}$Li NMR Study of the $Li_{1-z}Ni_{1+z}O_2$ Phases. *Magn. Reson. Chem.* **2005**, *43*, 849−857.

(14) Rougier, A.; Gravereau, P.; Delmas, C. Optimization of the Composition of the $Li_{1-z}Ni_{1+z}O_2$ Electrode Materials: Structural, Magnetic, and Electrochemical Studies. *J. Electrochem. Soc.* **1996**, *143*, 1168−1175.

(15) Pouillerie, C.; Croguennec, L.; Biensan, Ph.; Willmann, P.; Delmas, C. Synthesis and Characterization of New $LiNi_{1-y}Mg_yO_2$ Positive Electrode Materials for Lithium-Ion Batteries. *J. Electrochem. Soc.* **2000**, *147*, 2061−2069.

(16) Weber, D.; Lin, J.; Pokle, A.; Volz, K.; Janek, J.; Brezesinski, T.; Bianchini, M. Tracing Low Amounts of Mg in the Doped Cathode Active Material $LiNiO_2$. *J. Electrochem. Soc.* **2022**, *169*, 030540.

(17) Yabuuchi, N.; Ohzuku, T. Novel Lithium Insertion Material of $LiCo_{1/3}Ni_{1/3}Mn_{1/3}O_2$ for Advanced Lithium-Ion Batteries. *J. Power Sources* **2003**, *119−121*, 171−174.

(18) MacNeil, D. D.; Lu, Z.; Dahn, J. R. Structure and Electrochemistry of $Li[Ni_xCo_{1-2x}Mn_x]O_2$ ($0\leq x\leq1/2$). *J. Electrochem. Soc.* **2002**, *149*, A1332−A1336.

(19) Amatucci, G. G.; Tarascon, J.-M.; Larcher, D.; Klein, L. C. Synthesis of Electrochemically Active $LiCoO_2$ and $LiNiO_2$ at 100 °C. *Solid State Ionics* **1996**, *84*, 169−180.

(20) Palacín, M. R.; Larcher, D.; Audemer, A.; Sac-Épée, N.; Amatucci, G. G.; Tarascon, J.-M. Low-Temperature Synthesis of $LiNiO_2$: Reaction Mechanism, Stability, and Electrochemical Properties. *J. Electrochem. Soc.* **1997**, *144*, 4226−4236.

(21) Larcher, D.; Palacin, M. R.; Amatucci, G. G.; Tarascon, J.-M. Electrochemically Active $LiCoO_2$ and $LiNiO_2$ Made by Cationic Exchange under Hydrothermal Conditions. *J. Electrochem. Soc.* **1997**, *144*, 408−417.

(22) Pritzl, D.; Teufl, T.; Freiberg, A. T. S.; Strehle, B.; Sicklinger, J.; Sommer, H.; Hartmann, P.; Gasteiger, H. A. Editors' Choice—Washing of Nickel-Rich Cathode Materials for Lithium-Ion Batteries: Towards a Mechanistic Understanding. *J. Electrochem. Soc.* **2019**, *166*, A4056−A4066.

(23) Toma, T.; Maezono, R.; Hongo, K. Electrochemical Properties and Crystal Structure of Li^+/H^+ Cation-Exchanged $LiNiO_2$. *ACS Appl. Energy Mater.* **2020**, *3*, 4078−4087.

(24) Sun, Y.; Wan, P.; Pan, J.; Xu, C.; Liu, X. Low Temperature Synthesis of Layered $LiNiO_2$ Cathode Material in Air Atmosphere by Ion Exchange Reaction. *Solid State Ionics* **2006**, *177*, 1173−1177.
(25) Holzapfel, M.; Darie, C.; Bordet, P.; Chappel, E.; Núñez-Regueiro, M.-D.; Diaz, S.; de Brion, S.; Chouteau, G.; Strobel, P. Mixed Layered Oxide Phases $Na_xLi_{1-x}NiO_2$: A Detailed Description of Their Preparation and Structural and Magnetic Identification. *Solid State Sci.* **2005**, *7*, 497−506.
(26) Matsumura, T.; Kanno, R.; Gover, R.; Kawamoto, Y.; Kamiyama, T.; Mitchell, B. J. Synthesis, Structure and Physical Properties of $Li_xNa_{1-x}NiO_2$. *Solid State Ionics* **2002**, *152*−*153*, 303−309.
(27) Vassilaras, P.; Ma, X.; Li, X.; Ceder, G. Electrochemical Properties of Monoclinic $NaNiO_2$. *J. Electrochem. Soc.* **2013**, *160*, A207−A211.
(28) Han, M. H.; Gonzalo, E.; Casas-Cabanas, M.; Rojo, T. Structural Evolution and Electrochemistry of Monoclinic $NaNiO_2$ upon the First Cycling Process. *J. Power Sources* **2014**, *258*, 266−271.
(29) Dyer, L. D.; Borie, B. S., Jr.; Smith, G. P. Alkali Metal-Nickel Oxides of the Type $MNiO_2$. *J. Am. Chem. Soc.* **1954**, *76*, 1499−1503.
(30) Wang, L.; Wang, J.; Zhang, X.; Ren, Y.; Zuo, P.; Yin, G.; Wang, J. Unravelling the Origin of Irreversible Capacity Loss in $NaNiO_2$ for High Voltage Sodium Ion Batteries. *Nano Energy* **2017**, *34*, 215−223.
(31) Chappel, E.; Núñez-Regueiro, M. D.; Dupont, F.; Chouteau, G.; Darie, C.; Sulpice, A. Antiferromagnetic Resonance and High Magnetic Field Properties of $NaNiO_2$. *Eur. Phys. J. B* **2000**, *17*, 609−614.
(32) Chappel, E.; Núñez-Regueiro, M. D.; Chouteau, G.; Isnard, O.; Darie, C. Study of the Ferrodistorsive Orbital Ordering in $NaNiO_2$ by Neutron Diffraction and Submillimeter Wave ESR. *Eur. Phys. J. B* **2000**, *17*, 615−622.
(33) Delmas, C.; Borthomieu, Y.; Faure, C.; Delahaye, A.; Figlarz, M. Nickel Hydroxide and Derived Phases Obtained by Chimie Douce from $NaNiO_2$. *Solid State Ionics* **1989**, *32*−*33*, 104−111.
(34) Tsuda, M.; Arai, H.; Takahashi, M.; Ohtsuka, H.; Sakurai, Y.; Sumitomo, K.; Kageshima, H. Electrode performance of layered LiNi0.5Ti0.5O2 prepared by ion exchange. *J. Power Sources* **2005**, *144*, 183−190.
(35) Cao, X.; Qiao, Y.; Jia, M.; He, P.; Zhou, H. Ion-Exchange: A Promising Strategy to Design Li-Rich and Li-Excess Layered Cathode Materials for Li-Ion Batteries. *Adv. Energy Mater.* **2022**, *12*, 2003972.
(36) Wu, E. J.; Tepesch, P. D.; Ceder, G. Size and Charge Effects on the Structural Stability of $LiMO_2$ (M = Transition Metal) Compounds. *Philos. Mag. B* **1998**, *77*, 1039−1047.
(37) Tournadre, F.; Croguennec, L.; Saadoune, I.; Carlier, D.; Shao-Horn, Y.; Willmann, P.; Delmas, C. On the Mechanism of the P2-$Na_{0.70}CoO_2$→O2- $LiCoO_2$ Exchange Reaction—Part I: Proposition of a Model to Describe the P2-O2 Transition. *J. Solid State Chem.* **2004**, *177*, 2790−2802.
(38) Kadoma, Y.; Oshitari, S.; Ui, K.; Kumagai, N. Synthesis of Hollandite-Type Li_xMnO_2 by Li^+ Ion-Exchange in Molten Salt and Lithium Insertion Characteristics. *Electrochim. Acta* **2007**, *53*, 1697−1702.
(39) Hua, W.; Wang, S.; Wang, K.; Missyul, A.; Fu, Q.; Dewi Darma, M. S.; Li, H.; Baran, V.; Liu, L.; Kübel, C.; Binder, J. R.; Knapp, M.; Ehrenberg, H.; Indris, S. Li^+/Na^+ Ion Exchange in Layered $Na_{2/3}(Ni_{0.25}Mn_{0.75})O_2$: A Simple and Fast Way to Synthesize O3/O2-Type Layered Oxides. *Chem. Mater.* **2021**, *33*, 5606−5617.
(40) Luo, Y.-h.; Pan, Q.-l.; Wei, H.-x.; Huang, Y.-d.; Tang, L.-b.; Wang, Z.-y.; He, Z.-j.; Yan, C.; Mao, J.; Dai, K.-h.; Zhang, X.-h.; Zheng, J.-c. Towards Ni-Rich Layered Oxides Cathodes with Low Li/Ni Intermixing by Mild Molten-Salt Ion Exchange for Lithium-Ion Batteries. *Nano Energy* **2022**, *102*, 107626.
(41) Kang, B.; Ceder, G. Battery Materials for Ultrafast Charging and Discharging. *Nature* **2009**, *458*, 190−193.
(42) Kang, K.; Meng, Y. S.; Bréger, J.; Grey, C. P.; Ceder, G. Electrodes with High Power and High Capacity for Rechargeable Lithium Batteries. *Science* **2006**, *311*, 977−980.
(43) Kim, H.; Choi, A.; Doo, S. W.; Lim, J.; Kim, Y.; Lee, K. T. Role of Na^+ in the Cation Disorder of $[Li_{1-x}Na_x]NiO_2$ as a Cathode for Lithium-Ion Batteries. *J. Electrochem. Soc.* **2018**, *165*, A201−A205.
(44) Li, H.; Hua, W.; Liu-Théato, X.; Fu, Q.; Desmau, M.; Missyul, A.; Knapp, M.; Ehrenberg, H.; Indris, S. New Insights into Lithium Hopping and Ordering in $LiNiO_2$ Cathodes during Li (De)-Intercalation. *Chem. Mater.* **2021**, *33*, 9546−9559.
(45) Bianchini, M.; Schiele, A.; Schweidler, S.; Sicolo, S.; Fauth, F.; Suard, E.; Indris, S.; Mazilkin, A.; Nagel, P.; Schuppler, S.; Merz, M.; Hartmann, P.; Brezesinski, T.; Janek, J. From $LiNiO_2$ to Li_2NiO_3: Synthesis, Structures and Electrochemical Mechanisms in Li-Rich Nickel Oxides. *Chem. Mater.* **2020**, *32*, 9211−9227.
(46) Grey, C. P.; Dupré, N. NMR Studies of Cathode Materials for Lithium-Ion Rechargeable Batteries. *Chem. Rev.* **2004**, *104*, 4493−4512.
(47) Li, H.; Hua, W.; Schwarz, B.; Etter, M.; Mangold, S.; Melinte, G.; Casati, N. P. M.; Ehrenberg, H.; Indris, S. Investigation of Structural and Electronic Changes Induced by Postsynthesis Thermal Treatment of $LiNiO_2$. *Chem. Mater.* **2022**, *34*, 8163−8177.
(48) Marker, K.; Reeves, P. J.; Xu, C.; Griffith, K. J.; Grey, C. P. Evolution of Structure and Lithium Dynamics in $LiNi_{0.8}Mn_{0.1}Co_{0.1}O_2$ (NMC811) Cathodes during Electrochemical Cycling. *Chem. Mater.* **2019**, *31*, 2545−2554.
(49) Maeso, M. J.; Largo, J. The Phase Diagrams of $LiNO_3$-$NaNO_3$ and $LiNO_3$-KNO_3: The Behaviour of Liquid Mixtures. *Thermochim. Acta* **1993**, *223*, 145−156.
(50) Delmas, C.; Pérès, J. P.; Rougier, A.; Demourgues, A.; Weill, F.; Chadwick, A.; Broussely, M.; Perton, F.; Biensan, Ph.; Willmann, P. On the Behavior of the Li_xNiO_2 System: An Electrochemical and Structural Overview. *J. Power Sources* **1997**, *68*, 120−125.
(51) Li, H.; Zhang, N.; Li, J.; Dahn, J. R. Updating the Structure and Electrochemistry of Li_xNiO_2 for $0 \leq x \leq 1$. *J. Electrochem. Soc.* **2018**, *165*, A2985−A2993.
(52) de Biasi, L.; Schiele, A.; Roca-Ayats, M.; Garcia, G.; Brezesinski, T.; Hartmann, P.; Janek, J. Phase Transformation Behavior and Stability of $LiNiO_2$ Cathode Material for Li-Ion Batteries Obtained from In Situ Gas Analysis and Operando X-Ray Diffraction. *ChemSusChem* **2019**, *12*, 2240−2250.
(53) Croguennec, L.; Pouillerie, C.; Delmas, C. Structural Characterisation of New Metastable NiO_2 Phases. *Solid State Ionics* **2000**, *135*, 259−266.
(54) Croguennec, L.; Pouillerie, C.; Mansour, A. N.; Delmas, C. Structural Characterisation of the Highly Deintercalated $Li_xNi_{1.02}O_2$ Phases (with $x \leq 0.30$). *J. Mater. Chem.* **2001**, *11*, 131−141.
(55) Stephens, P. W. Phenomenological Model of Anisotropic Peak Broadening in Powder Diffraction. *J. Appl. Crystallogr.* **1999**, *32*, 281−289.
(56) Toby, B. H.; Von Dreele, R. B. GSAS-II: The Genesis of a Modern Open-Source All Purpose Crystallography Software Package. *J. Appl. Crystallogr.* **2013**, *46*, 544−549.
(57) Geßwein, H.; Stüble, P.; Weber, D.; Binder, J. R.; Mönig, R. A Multipurpose Laboratory Diffractometer for Operando Powder X-Ray Diffraction Investigations of Energy Materials. *J. Appl. Crystallogr.* **2022**, *55*, 503−514.

https://doi.org/10.1021/acs.chemmater.2c03203
Chem. Mater. 2023, 35, 648−657

3.2 Publication II: Seesaw Effect of Substitutional Point Defects on the Electrochemical Performance of Single-Crystal $LiNiO_2$ Cathodes

Publication II describes the analysis of three series of size-tailored IE-LNOs, in an effort to separate the contributions of grain size and defect concentration to the overall performance. The grain size of the parent NNO phase was tailored by changing the calcination temperature, ball-milling and by introducing surface segregating species preventing sintering. For each size series, a clear correlation between grain size and FCCL is observed. The capacity loss is separated into degradation induced losses and KH losses. While the KH losses are clearly related to the particle size, the degradation losses occurred irrespective of particle size and thus particle surface. The kinetic hindrance observed in the ion-exchanged materials is, however, much lower than in the reference material. During cycling, IE-LNO releases much more oxygen than the reference sst-LNO, which is accompanied by harsher collapse of interlayer spacing at high SOC. The results point towards an ambivalent effect of $Ni_{Li}^{\bullet}$ substitutional defects, which help to stabilize the material at high SOC while inducing KH losses.

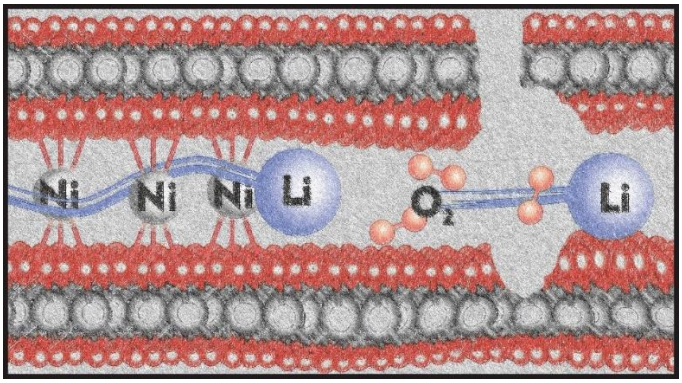

Figure 8. Graphical table of content of publication II. Reprinted from reference [312].

The experiments were planned and designed by the first author under the supervision of A. Kondrakov, J. Janek and T. Brezesinski. The first author developed and optimized the size-tailoring methods for NNO and carried out the ion-exchange procedures. W. van den Bergh carried out some preliminary NNO synthesis, which is not included in the publication, and further helped with discussions. The first author carried out electrochemical experiments and data analysis. S. Korneychuk performed the TEM investigation and interpreted the corresponding results together with the first author. R. Zhang conducted the SEM experiments and the data was analyzed by the first author. S. Dreyer conducted the DEMS experiments, analyzed the data and discussed the results with the first author. The manuscript was written by the first author and edited by all coauthors.

Publication II - Reprinted from [312]

CHEMISTRY OF MATERIALS

pubs.acs.org/cm Article

Seesaw Effect of Substitutional Point Defects on the Electrochemical Performance of Single-Crystal $LiNiO_2$ Cathodes

Leonhard Karger, Svetlana Korneychuk, Wessel van den Bergh, Sören L. Dreyer, Ruizhuo Zhang, Aleksandr Kondrakov, Jürgen Janek,* and Torsten Brezesinski*

Cite This: https://doi.org/10.1021/acs.chemmater.3c02727 Read Online

ACCESS | Metrics & More | Article Recommendations | Supporting Information

ABSTRACT: Layered oxide cathode materials, such as $LiNi_aCo_bMn_cO_2$ or $LiNi_aCo_bAl_cO_2$, are sought after mainly because of their high theoretical specific capacity. Especially those with a high nickel content are being pursued to increase capacity and lower costs. In these materials, substitutional defects are a common feature and are typically associated with poor overall quality. Herein, we employ a sodium-to-lithium ion exchange to produce $LiNiO_2$ (LNO) without such characteristic defects. Three different methods are used to tailor the primary particle (grain) size over a broad range, and each material is subjected to electrochemical testing. By analyzing the initial charge/discharge profiles, we separate kinetic hindrance and structural degradation as two independent contributions to the first-cycle capacity loss. We find that the $Ni_{Li}^{\bullet}$ point defects stabilize LNO at high potentials and help mitigate material degradation while leading to incomplete discharge. The kinetic hindrance at the end of discharge vanishes upon their removal, but the degradation at high states of charge becomes more pronounced. We examine the cause of material degradation and corroborate the results by artificially introducing pillaring Mg^{2+} ions through a novel dual-ion exchange as a model system for nickel substitutional defects. This methodology may be exploited to identify an optimal concentration of pillar ions, especially in a range of defect densities that are inaccessible by conventional solid-state synthesis.

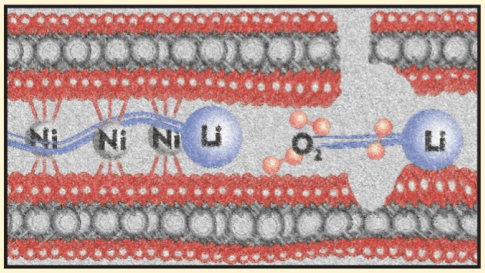

INTRODUCTION

Substitutional defects are present in cathode materials of the $LiNi_aCo_bMn_cO_2$ (NCM or NMC) and $LiNi_aCo_bAl_cO_2$ (NCA) solid solutions.[1−3] Especially the 100% nickel endmember, $LiNiO_2$ (LNO), is prone to off-stoichiometry, which strongly affects its electrochemical behavior.[4] Typically, LNO is made through solid-state synthesis under an oxygen atmosphere at high temperatures. This thermal process leads to an inherently "lithium-deficient" or "off-stoichiometric" LNO of the general formula $Li_{1-z}Ni_{1+z}O_2$.[4−6] Depending on the relative ratio of nickel to lithium as well as the calcination temperature, different types of defects can emerge. For example, Ni/Li antisite defects, which refer to Li_{Ni}'' and $Ni_{Li}^{\bullet\bullet}$ point defects (Kroeger−Vink notation), are only observed for large off-stoichiometries of $z \geq 0.15$.[7] For the close-to-stoichiometric LNO, which is the material of interest for lithium-ion battery (LIB) application, only $Ni_{Li}^{\bullet}$ defects, accompanied by Ni_{Ni}' for charge compensation, are the prevailing defects and should be considered for understanding the electrochemistry of LNO.[7] In the context of this study, for simplicity, we only mention the $Ni_{Li}^{\bullet}$ defects when referring to the combination of $Ni_{Li}^{\bullet}$ and Ni_{Ni}'.[2] Note that these substitutional defects are a result of both incomplete oxidation of Ni^{2+} to Ni^{3+} and the similar ionic radii of Ni^{2+} and Li^{+} and are as such inherent to LNO prepared by solid-state synthesis.[8−10]

Optimized calcination protocols and careful stoichiometric control can achieve defect concentrations of no lower than 1.6 mol % of $Ni_{Li}^{\bullet}$ with respect to nickel.[11,12] Furthermore, only the annealing step seems to be crucial for the fraction of $Ni_{Li}^{\bullet}$ as no signs of nickel migration in the bulk are found during cycling in the stable electrochemical window of LNO in recent studies, although this is still a subject of debate.[10,13] This is not the least caused by the experimentally challenging characterization and quantification of point defects. Common ways to probe $Ni_{Li}^{\bullet}$ are a combination of powder X-ray diffraction (PXRD) and neutron diffraction, magic-angle spinning nuclear magnetic resonance (MAS NMR) spectroscopy, and magnetometry.[4,12,14]

Received: October 24, 2023
Revised: December 6, 2023
Accepted: December 8, 2023

https://doi.org/10.1021/acs.chemmater.3c02727
Chem. Mater. XXXX, XXX, XXX−XXX

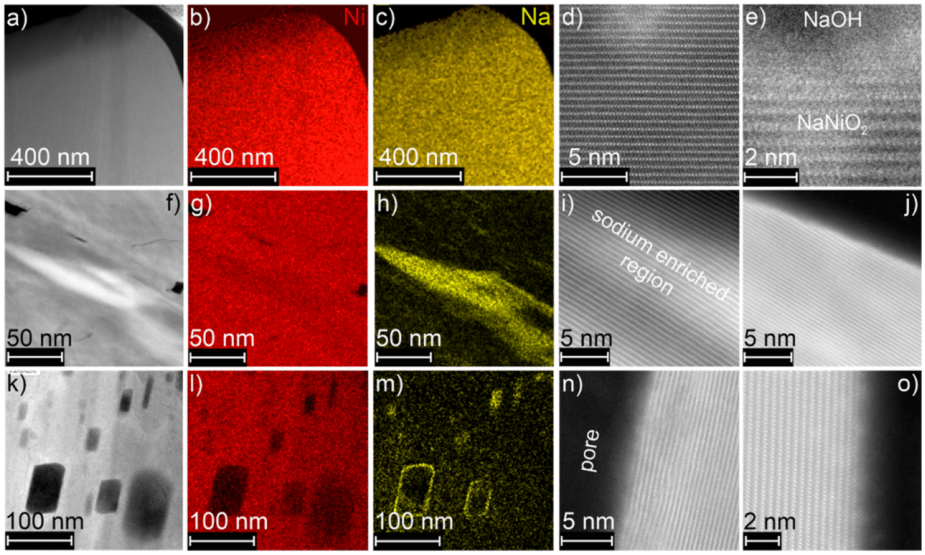

Figure 1. (a) STEM and (b,c) EDXS results for FIB-cut NNO. HRTEM of (d) NNO bulk and (e) particle edge. (f) STEM and (g,h) EDXS results for FIB-cut IE-LNO. HRTEM of (i) IE-LNO bulk and (j) particle edge. (k) STEM and (l,m) EDXS results for FIB-cut IE-LNO + LiOH-40 h. HRTEM of (n) IE-LNO + LiOH-40 h bulk and (o) particle edge.

Achieving a low $Ni_{Li}^{\bullet}$ defect density is considered desirable as the specific charge and discharge capacities increase due to facilitated lithium diffusion, but other effects have been reported too.[15] Increasing the fraction of the nickel substitutional defects increases the potential at which the so-called H3 phase forms (the last reversible transition during the LNO charge/discharge).[12] When going beyond this transition, the H4 phase forms, which is associated with oxygen release and irreversibility.[16,17] High defect concentrations of ≥7.2 mol % suppress this phase transition completely, which may be indicative of the stabilizing properties of the $Ni_{Li}^{\bullet}$ defects.[18] Another aspect is their relation to the first-cycle capacity loss, as reported by Arai et al., Delmas et al., and Bianchi et al. In particular, they emphasized the need for lowering the defect density for decreasing the first-cycle loss.[19−21] Subsequent studies did not find this correlation and instead proposed a direct link between the first-cycle loss and primary particle size of the active material.[11,12,22] However, since the $Ni_{Li}^{\bullet}$ defects affect the lithium transport properties through vacancy trapping and by acting as a diffusion barrier, it is difficult to distinguish between the influence of the point defects and size effects, which arise at different calcination temperatures.[23] This intrinsic convolution of particle size and defect density contributions to the electrochemical performance demands further study, as diffusion-induced capacity loss can be substantial particularly for single-crystalline morphologies.[22,24]

Recently, we have developed a method to prepare LNO that is free of $Ni_{Li}^{\bullet}$ defects by synthesizing perfectly layered $NaNiO_2$ (NNO) and then conducting sodium-to-lithium ion exchange in molten salts (yielding ion-exchanged LNO, referred to as IE-LNO).[14] In this study, we report on the particle-size-dependent electrochemistry of single-crystal IE-LNO cathodes and correlate capacity loss and stability to grain (primary particle) size and $Ni_{Li}^{\bullet}$ defects being present or absent. We stress the ambivalent character of the $Ni_{Li}^{\bullet}$ defects, which act similarly to (stabilizing) pillar ions but impede lithium diffusion at the same time. Upon their removal, these effects are reversed. This means that the charge transport improves while material stability decreases, tilting the seesaw-like behavior to the other extreme.

■ RESULTS AND DISCUSSION

Optimization of LNO Synthesis. Solid-state synthesis of NNO leads to single-crystalline particles with a uniform distribution of sodium and nickel, as can be seen from the scanning transmission electron microscopy (STEM) image and energy-dispersive X-ray spectroscopy (EDXS) maps in Figure 1a−c. High-resolution TEM (HRTEM) imaging of focused ion beam (FIB) cross-sections indicates that there is little strain or bending of individual nickel oxide slabs in the as-made NNO (Figure 1d), and the surface is covered by an amorphous layer, likely residual NaOH (Figure 1e). When this material is subjected to ion exchange and washed with water, the overall morphology is retained, but the internal structure exhibits abundant intragranular cracks and domains with high sodium content (Figure 1f−j). These sodium-rich domains may be caused by sluggish diffusion because of crack formation or inhibition of ion exchange at the lithium-rich surface.

As shown in our preceding work, postannealing of the IE-LNO at elevated temperatures produces a material with ≥5 mol % $Ni_{Li}^{\bullet}$ defects, which seems to be due to sodium diffusing out of the structure and being replaced by Ni^{2+}. For this reason, it was tested whether additional lithium can prevent structural degradation upon heating in order to preserve a low- or ideally a zero-defect state. To this end, the IE-LNO was combined with 10 mol % $LiOH{\cdot}H_2O$ and annealed at 700 °C

https://doi.org/10.1021/acs.chemmater.3c02727
Chem. Mater. XXXX, XXX, XXX−XXX

Table 1. Results from Rietveld Analysis of the PC-LNO and IE-LNO Samples before and after Annealing in the Presence of $LiOH{\cdot}H_2O$

sample	R_{wp} [%]	R_{Bragg} [%]	a [Å]	c [Å]	V [Å^3]	defects [mol %]
PC-LNO	11.0	2.1	2.8733(1)	14.1854(6)	101.42(1)	$Ni^{\bullet}_{Li}$ 1.7(2)
IE-LNO	11.5	1.8	2.8746(6)	14.1968(54)	101.70(2)	$Ni^{\bullet}_{Li}$ 0 $Na^{\times}_{Li}$ 5.0(8)[a]
IE-LNO + LiOH-6 h	15.6	2.0	2.8758(1)	14.1781(12)	101.55(1)	$Ni^{\bullet}_{Li}$ 2.5(3)
IE-LNO + LiOH-40 h	10.3	1.7	2.8750(1)	14.1765(12)	101.48(1)	$Ni^{\bullet}_{Li}$ 1.6(2)

[a]From PXRD and NMR spectroscopy.[14]

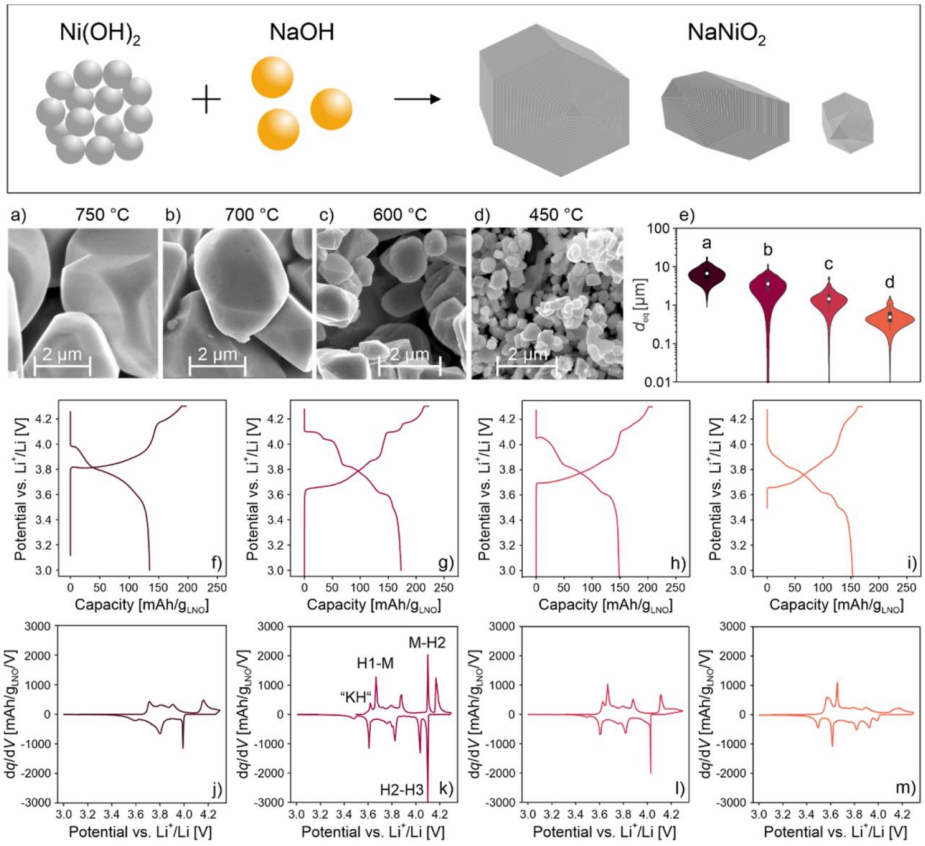

Figure 2. Analysis of the temperature-based size tailoring of IE-LNO. SEM images of (a) IE-LNO-750, (b) IE-LNO-700, (c) IE-LNO-600, and (d) IE-LNO-450. (e) Corresponding particle size distribution. (f–i) First-cycle charge/discharge and (j–m) second-cycle differential capacity curves at C/10 rate (3.0–4.3 V vs Li^+/Li). The electrochemical data are in the same order as in panels (a–d).

for 6 h (referred to as IE-LNO + LiOH-6 h). Rietveld analysis of PXRD data collected from this material reveals a defect concentration of 2.5(3) mol % $Ni^{\bullet}_{Li}$ (Table 1). When the material is annealed at the same temperature for 40 h (referred to as IE-LNO + LiOH-40 h), a decrease in defect concentration to 1.6(2) mol % is observed, which is comparable to that of the polycrystalline reference LNO (referred to as PC-LNO). Electron microscopy images of this annealed material indicate the presence of rhombohedral voids (Figure 1k–o) containing sodium on the inner surfaces. Apparently, the cracks heal and rearrange to form the said voids, and the residual sodium diffuses toward the surfaces, where it is deposited as an oxide. In the remaining bulk structure, no sodium is detected by EDXS. Therefore, annealing seems to be effective at removing sodium from the layered phase but also leads to the formation of voids and $Ni^{\bullet}_{Li}$ defects. The voids are believed to still hinder lithium diffusion, similar to the cracks that are present prior to heating. In addition, postannealing reintroduces the point defects and is therefore not suited for retaining the initially $Ni^{\bullet}_{Li}$-free nature.

https://doi.org/10.1021/acs.chemmater.3c02727
Chem. Mater. XXXX, XXX, XXX–XXX

Table 2. Results from Rietveld Analysis of the Temperature-Based, Size-Tailored IE-LNO Samples

sample	R_{wp} [%]	R_{Bragg} [%]	a [Å]	c [Å]	V [Å^3]	$Na_{Li}^{\times}$ [mol %]
IE-LNO-450	15.7	4.3	2.8731(12)	14.1876(90)	101.42(12)	0
IE-LNO-600	14.9	4.8	2.8747(9)	14.1854(30)	101.51(3)	0.7(2)
IE-LNO-700	11.5	1.8	2.8746(6)	14.1968(54)	101.70(2)	5.0(8)
IE-LNO-750	14.0	3.2	2.8816(6)	14.1647(41)	101.86(2)	7.8(8)

Instead, sodium should be removed completely in a temperature range, where substitutional defects do not form. Nevertheless, the IE-LNO + LiOH-40 h material exhibits improved capacity over that of IE-LNO annealed in the absence of $LiOH{\cdot}H_2O$ (Figure S1, Supporting Information).

A promising strategy to avoid the aforementioned problem of incomplete ion exchange is the application of sufficiently small crystallites that allow for short sodium diffusion path lengths. Control over the NNO particle (grain) size can be achieved by varying the annealing temperature in the range of 450−750 °C.[14] Furthermore, using NaOH instead of Na_2O_2 as a precursor (sodium source) leads to a decrease in the primary particle size.

Temperature-Based Particle Size Tailoring. A series of NNO samples with different particle sizes were synthesized by heating NaOH with $Ni(OH)_2$ at 450, 600, and 700 °C, as well as by heating NiO nanoparticles with Na_2O_2 at 750 °C (referred to as NNO-ϑ, with ϑ being the temperature). These NNO samples were then subjected to ion exchange (referred to as IE-LNO-ϑ; see the Experimental section for details). As can be seen from the scanning electron microscopy (SEM) images in Figure 2a−d, the particle size increases with increasing temperature. The size distribution is relatively broad, with d_{50} values ranging from 480 nm for IE-LNO-450 to 6.67 μm for IE-LNO-750 (Figure 2e). With regard to faceting, no obvious correlation to the particle shape is apparent, even though they are not completely spherical. After ion exchange, the crystallites appear to be well separated, and virtually no agglomeration of the monolithic particles is observed. As expected, the materials crystallize in the $R\bar{3}m$ space group, and Rietveld analysis reveals similar lattice parameters for all samples (Table 2), in good agreement with literature results.[6] Therefore, we assert that the particles are of a single-phase nature. However, particularly, the larger particles may still contain residual sodium, as is evident from the decrease of $Na_{Li}^{\times}$ to 0 mol % with decreasing particle size. This is confirmed by the EDXS measurements conducted on IE-LNO-700; the small particles do not contain sodium, but the larger particles exhibit the presence of sodium-rich domains described above (Figure S2, Supporting Information). The evolution of lattice parameters corroborates this finding with decreasing values for a and V with decreasing grain size. IE-LNO-750 shows a smaller c-parameter, which might be related to the different (more oxidizing) sodium precursor used in the synthesis. Nevertheless, a clear trend of increasing cell volume and lattice parameters with increasing temperature is found for the parent NNO samples (Table S1, Supporting Information). Overall, controlling the annealing temperature yields the desired materials, namely, a size-tailored IE-LNO series.

The IE-LNO samples were then subjected to electrochemical testing at C/10 rate in LIB half-cells (3.0−4.3 V vs Li^+/Li). As shown in Figure 2f−i, the first-cycle specific discharge capacities are rather low, with the highest achieved with IE-LNO-700 and IE-LNO-450 with q_{dis} = 173 and 152 mA h/g_{LNO}, respectively. No clear trend between the particle size and capacity is found. However, the first-cycle capacity loss does show a distinct trend and decreases from about 31 to 8% with decreasing particle size. Furthermore, the differential capacity curves for the second cycle in Figure 2j−m reveal differences for the different IE-LNO samples. The observed dq/dV peaks have been previously assigned to structural transitions that are well-known for LNO produced by solid-state synthesis.[14,25−28] In short, when charging the material, a peak that is associated with high diffusivity or small particle size (strongly dependent on the lithium intercalation at the end of discharge; in a region of the discharge profile, where lithium diffusion is hindered), commonly referred to as kinetic hindrance (KH), is observed first.[29,30] The following peaks are typically labeled as H1-M, M-H2, and H2-H3, as shown in Figure 2k. The largest particles (IE-LNO-750) exhibit a high overpotential, and the phase transitions appear broadened compared to those of IE-LNO-700. Upon moving to smaller particle sizes, the high-voltage transitions, M-H2 and H2-H3, become less intense and broadened and shift outside the operating potential window. Also, the onset of the H3-H2 transition during discharge shifts to lower potentials with decreasing particle size, while the other peaks do not show a similar shift. By the same token, the low-voltage peaks, especially the KH peak, become more pronounced. This could be the reason why the first-cycle loss decreases with decreasing particle size as the relithiation of the material becomes more effective. At the same time, these smaller particles cannot be fully charged due to voltage hysteresis, which is increased at high states of charge (high degrees of delithiation) and has been linked to surface densification.[13] Indeed, if the cells are operated at 4.8 V vs Li^+/Li, the specific discharge capacity increases significantly, e.g., from q_{dis} = 152 mA h/g_{LNO} to 191 mA h/g_{LNO} for IE-LNO-450 (Figure S3, Supporting Information). Also, the smaller particles are likely to undergo more side reactions (surface degradation) due to their higher relative surface area.[31] For example, the particles need to be subjected to water washing in order to get rid of the salt used for ion exchange, which is known to cause lithium-to-proton exchange and subsequent formation of surface impurities, potentially lowering the fraction of active material.[32] In essence, two counteracting effects are observed in IE-LNO: (i) destabilization of high states of charge and (ii) faster diffusion and therefore improved capacity retention in the first cycle when moving to smaller particles. One can visualize these opposing effects as the two sides of a seesaw, with the optimal balance of both resulting in minimal first-cycle capacity loss.

Ball-Milling-Assisted Particle Size Tailoring. To test whether the effects observed with temperature-based size control are of a more general nature, two other methods for tailoring the grain size of the parent NNO phase were applied. One of these is high-energy milling. Ball milling is an effective method to decrease particle size, with higher energy input and longer milling times leading to smaller particles. We specifically focused on the largest NNO particles, namely, NNO-750. The latter material was milled at 300, 400, and 600 rpm for 10 min,

https://doi.org/10.1021/acs.chemmater.3c02727
Chem. Mater. XXXX, XXX, XXX−XXX

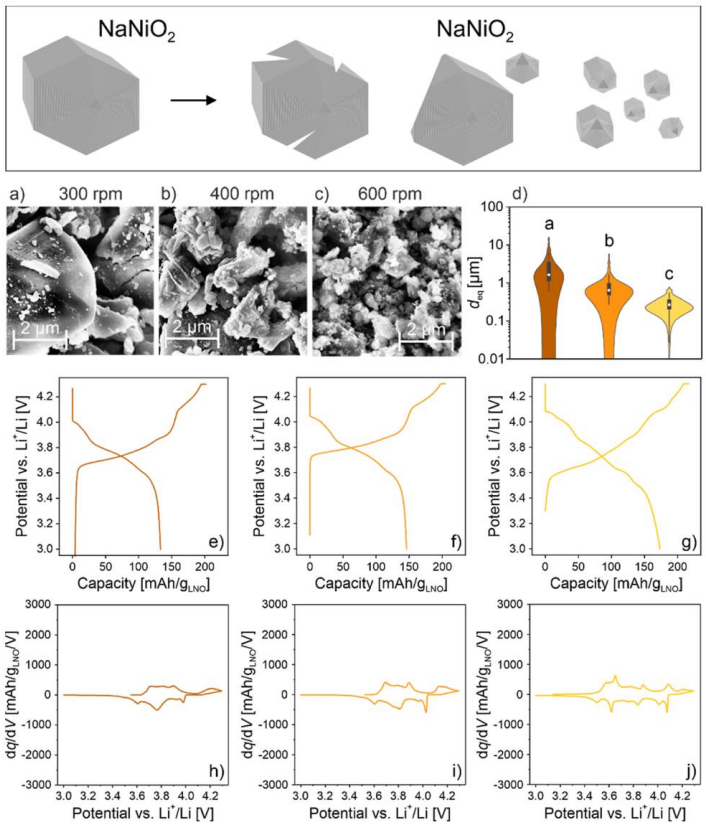

Figure 3. Analysis of the ball-milling-assisted size tailoring of IE-LNO. SEM images of (a) IE-LNO-300 rpm, (b) IE-LNO-400 rpm, and (c) IE-LNO-600 rpm. (d) Corresponding particle size distribution. (e–g) First-cycle charge/discharge and (h–j) second-cycle differential capacity curves at *C*/10 rate (3.0–4.3 V vs Li^+/Li). The electrochemical data are in the same order as in panels (a–c).

Table 3. Results from Rietveld Analysis of the Ball-Milling-Assisted, Size-Tailored IE-LNO Samples

sample	R_{wp} [%]	R_{Bragg} [%]	a [Å]	c [Å]	V [Å^3]	$Na_{Li}^{\times}$ [mol %]
IE-LNO-300 rpm	14.8	2.9	2.8746(9)	14.2166(90)	101.740(96)	0.1(4)
IE-LNO-400 rpm	15.3	3.6	2.8761(4)	14.2075(90)	101.78(4)	0.6(2)
IE-LNO-600 rpm	15.1	3.4	2.8805(12)	14.2215(120)	102.193(120)	2.8(6)

and the as-made powders were then subjected to ion exchange (products are referred to as IE-LNO-*X* rpm). With increasing rotational speed, particles with sizes ranging from d_{50} = 1.64 μm for IE-LNO-300 rpm to 268 nm for IE-LNO-600 rpm are obtained, as shown in Figure 3a–d. The size distributions are broader than those of the IE-LNO-ϑ samples. After milling at 300 rpm, nanoscale particles are present, which likely originate from the chipping of NNO-750, while the large particles remain mostly intact. This is also visible from the size analysis in Figure 3d, revealing a broad tail toward very small particles. Furthermore, the larger particles appear to be partially cracked, thus evidencing high mechanical stress. Structural analysis confirms all ion-exchanged materials to conform to the $R\bar{3}m$ space group. We find increased *c*-parameter values and decreased $Na_{Li}^{\times}$ defect concentrations for the ball-milled materials (Table 3). However, even for the smallest particles, IE-LNO-600 rpm, substitutional defects are observed by PXRD. The presence of sodium is further corroborated by EDXS (Figure S2, Supporting Information). The latter could be the result of severe damage to the layered structure, leading to sodium trapping within the bulk. Indeed, the particle core of IE-LNO-600 rpm is found by STEM to be nonuniform.

The materials were also electrochemically tested in LIB half-cells at C/10 rate. As mentioned above, IE-LNO-750 exhibits poor performance, which is due in part to the presence of large particles and a high overpotential. Upon decreasing the particle size by milling, the specific charge and discharge capacities increase. Furthermore, the first-cycle capacity loss decreases

https://doi.org/10.1021/acs.chemmater.3c02727
Chem. Mater. XXXX, XXX, XXX–XXX

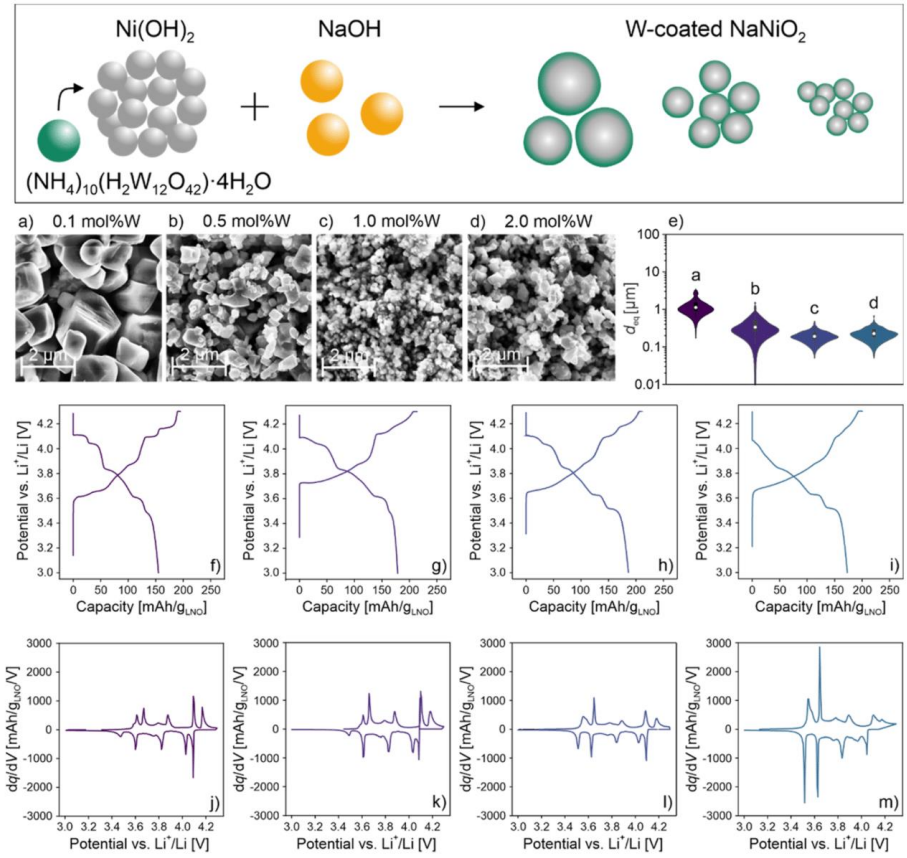

Figure 4. Analysis of the anti-sintering size tailoring of IE-LNO. SEM images of (a) IE-LNO-0.1W, (b) IE-LNO-0.5W, (c) IE-LNO-1.0W, and (d) IE-LNO-2.0W. (e) Corresponding particle size distribution. (f–i) First-cycle charge/discharge and (j–m) second-cycle differential capacity curves at C/10 rate (3.0–4.3 V vs Li^+/Li). The electrochemical data are in the same order as in panels (a–d).

from about 31 to 12% (Figure 3e–g), similar to the observations made for the temperature-based size tailoring. The relithiation is rendered more effective with decreasing particle size (i.e., the KH peak intensity increases with decreasing particle size). However, for the high-voltage region, no clear trend is observed with these samples as the M-H2 and H2-H3 transitions appear broadened and are partially shifted outside the potential window (Figure 3h–j). Overall, the results point to better cycling of the smaller particles, which is likely due to improved diffusion during ion exchange and battery operation. While being effective at reducing the overall grain size, ball milling does not seem promising for obtaining narrow size ranges of particles. Apart from that, sodium remains trapped within the structure irrespective of the grain size, likely due to some loss of long-range order because of a mechanically introduced disorder. This in turn reduces the specific capacity to such an extent that this method was not pursued further.

Anti-Sintering Particle Size Tailoring. The third method to tailor the particle size relies on controlling the sintering of the NNO grains during calcination. For LNO, ammonium paratungstate (APT) addition has been shown to prevent growth by acting as an anti-sintering agent.[33] Inspired by this finding, we tested whether a similar growth inhibition would be observed in the preparation of NNO. To this end, syntheses with 0.1, 0.5, 1.0, and 2.0 mol % tungsten from APT were performed, and the as-made materials were probed using PXRD. All samples conform to the monoclinic structure of NNO ($C2/m$ space group), with minor differences in cell volume and lattice parameters among them (Table S1, Supporting Information). Note that larger differences would be indicative of tungsten inclusion. However, small amounts of rock-salt-type NiO are observed, except for the sample containing 0.5 mol % tungsten, which likely originates from experimental variation during calcination (Figure S4, Supporting Information). Additionally, WO_3 residues are detected for the sample containing 2 mol % tungsten. The NNO particles

https://doi.org/10.1021/acs.chemmater.3c02727
Chem. Mater. XXXX, XXX, XXX–XXX

Table 4. Results from Rietveld Analysis and ICP-OES of the Anti-Sintering, Size-Tailored IE-LNO Samples

sample	R_{wp} [%]	R_{Bragg} [%]	a [Å]	c [Å]	V [Å^3]	$Na_{Li}^{\times}$ [mol %]
IE-LNO-0.1W	15.2	3.4	2.8750(12)	14.2009(120)	101.65(12)	0.6(7)
IE-LNO-0.5W	17.7	4.7	2.8760(6)	14.1889(66)	101.65(7)	0
IE-LNO-1.0W	14.9	3.5	2.8766(4)	14.2012(41)	101.77(2)	1.8(10)
IE-LNO-2.0W	16.3	3.7	2.8775(12)	14.1768(156)	101.65(15)	2.4(21)
sample	Li [%]	Na [%]	Ni [%]	W [%]	O [%]	
IE-LNO-0.1W	95.2	3.1	100	0.07	215.2	
IE-LNO-0.5W	108.7	2.6	100	0.25	261.4	
IE-LNO-1.0W	91.6	2.1	100	0.43	206.3	
IE-LNO-2.0W	93.1	1.2	100	0.40	208.5	

were also subjected to ion exchange, and the resulting materials (Figure 4a–d) are referred to as IE-LNO-*Y*W hereafter (*Y* being the nominal mol % of tungsten from APT with respect to nickel). Structural analysis by Rietveld refinement suggests that all products are phase-pure LNO (Table 4). Yet, they still contain NiO impurities as they are carried over from the respective NNO materials. For the smaller particles, the presence of $Na_{Li}^{\times}$ defects is also apparent, while inductively coupled plasma-optical emission spectroscopy (ICP-OES) reveals a decreasing trend in the overall sodium content with decreasing particle size (Table 4), similar to that in the temperature-based size tailoring. Therefore, the higher $Na_{Li}^{\times}$ concentration seen for the smallest particles is likely caused by the rock-salt-type NiO (or partially decomposed LNO), which forms because of the increase in the specific surface area (higher tungsten content) combined with water washing and drying and can be misinterpreted in Rietveld analysis as excess electron density in the lithium slab. The smaller particles also give rise to broader and less intense reflections, a sign of their nanoscale nature and/or presence of strain, rendering pattern refinements more challenging. The particle sizes are found to be similar for the IE-LNO-1.0W and IE-LNO-2.0W samples, with d_{50} = 191 and 226 nm, respectively (Figure 4e). Hence, APT addition of 1.0 mol % is sufficient to prevent sintering of the NNO grains. ICP-OES measurements also reveal the presence of tungsten in the samples, yet in lower levels than nominally used. This could be related to tungsten being located on the particle surface from which it can be removed, especially during water washing, if soluble or readily suspendable species are present.

Eventually, the IE-LNO-*Y*W cathode materials were cycled in LIB half-cells. A trend similar to that observed with the temperature-based and ball-milling-assisted size-tailored samples is found. With decreasing particle size, the capacity increases (Figure 4f–i). IE-LNO-1.0W delivers the highest first-cycle specific discharge capacity of q_{dis} = 186 mA h/g_{LNO}. Again, the KH region becomes more pronounced, and the high-voltage transitions are muted with decreasing particle size (Figure 4j–m), perfectly following the trends outlined by the size-tailoring methods described above.

When the tungsten source is added after the preannealing step during the NNO synthesis, a different particle morphology is obtained than that with tungsten addition to the initial hydroxide precursor mixture prior to heating. After ion exchange, the primary particle agglomerates (secondary particle morphology) remain mostly intact, as shown in Figure 5a. For that reason, the resulting material is termed polycrystalline IE-LNO (here, IE-LNO-2.0W-PC). PXRD analysis of this sample reveals the presence of trace amounts of WO_3 impurities (Figure S4, Supporting Information). However, the main phase crystallizes in the $R\bar{3}m$ space group; the refined lattice parameters and results from ICP-OES are given in Table 5. The size distribution of the primary particles, which are visible on the surface of the secondary particles, is similar to that of IE-LNO-2.0W, although some larger grains can be observed, and the median size decreases from d_{50} = 226 to 166 nm (Figure 5b). The STEM/EDXS results in Figure 5e–g indicate that the interior of the secondary particles also consists primarily of nanoscale grains. As can be seen from the mapping results in Figure 5h–k, no clear accumulation of tungsten at the grain boundaries is found. In HRTEM (Figure 5l,n) of the areas marked in Figure 5m, a well-layered structure without strain in the nickel slabs and the presence of minor amounts of rock-salt-type NiO toward the particle surface are evident.

Interestingly, this material is capable of delivering much higher capacities than those with single-crystalline particles (Figure 5c). A first-cycle specific discharge capacity of q_{dis} = 204 mA h/g_{LNO} is achieved with IE-LNO-2.0W-PC, compared to 172 mA h/g_{LNO} for IE-LNO-2.0W and 186 mA h/g_{LNO} for IE-LNO-1.0W. The preservation of the secondary particle morphology seems to help protect the IE-LNO (free) surface from degradation during ion exchange, washing, and cycling. The corresponding differential capacity curve (Figure 5d) reveals the same transitions observed in the IE-LNO materials discussed previously. The peak ratios closely resemble those of IE-LNO-1.0W and IE-LNO-2.0W while showing distinct features in the KH and high-voltage regions. Consequently, this route represents the best way for preparing a competitive material and was further used in a comparison with PC-LNO.

In summary, three different particle-size-tailoring methods were tested to gain insight into the electrochemistry of $Ni_{Li}^{\bullet}$-free LNO particles. All of them generated phase-pure IE-LNO materials, with minor amounts of rock-salt-type NiO for the tungsten-based anti-sintering approach. The specific capacities differ substantially among the samples from the different methods, but within each set, clear size trends are observed. The reasons for the differences in performance are described above. In short, even the smallest temperature-tailored particles, IE-LNO-450 (d_{50} = 480 nm), are much larger in size than the smallest particles from the other two series, namely, IE-LNO-600 rpm and IE-LNO-1.0W with d_{50} = 268 and 191 nm, respectively. The best performance in all IE-LNOs is achieved with IE-LNO-2.0W-PC, which exhibits the smallest primary particle size (d_{50} = 166 nm) and benefits from a secondary particle morphology.

Individual Contributions to First-Cycle Capacity Loss. To further study the effect of the particle size on electrochemical performance, the relative capacity loss on the initial cycle, commonly known as first-cycle loss, was examined in

https://doi.org/10.1021/acs.chemmater.3c02727
Chem. Mater. XXXX, XXX, XXX−XXX

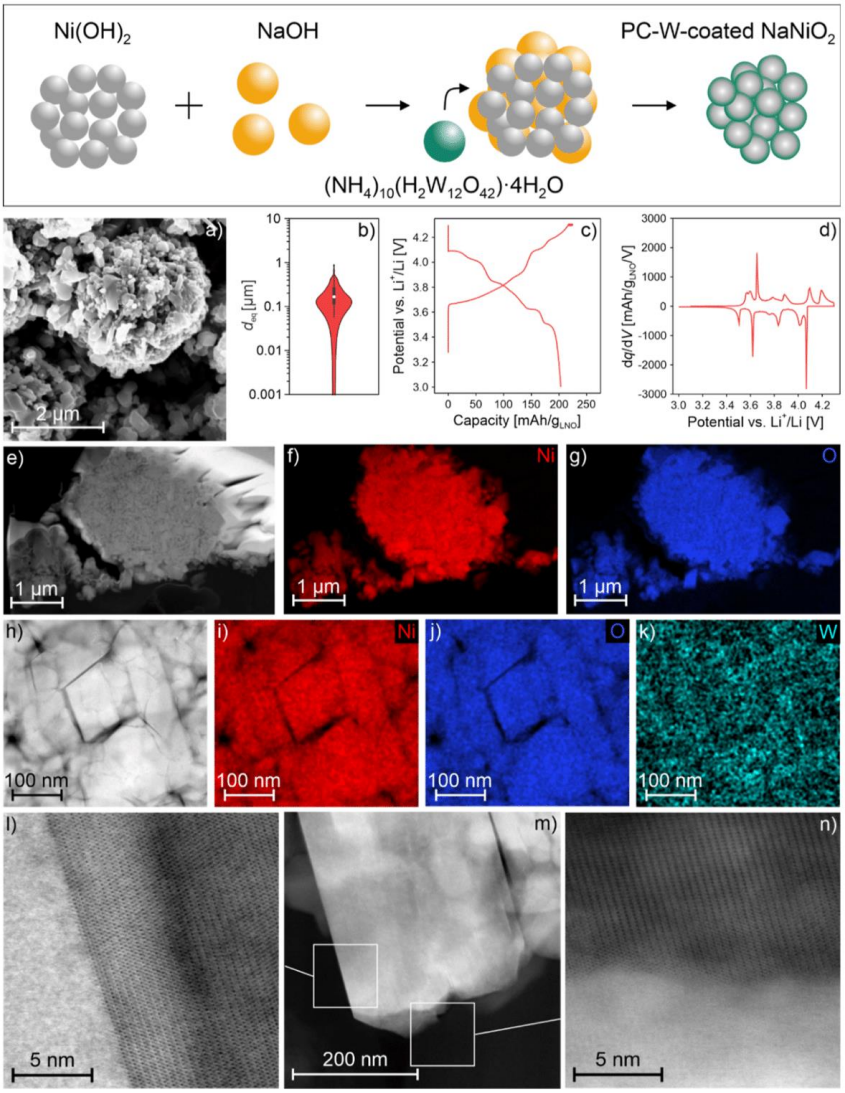

Figure 5. Structural and electrochemical analysis of IE-LNO-2.0W-PC. (a) SEM image, (b) particle size distribution, and (c) first-cycle charge/discharge and (d) second-cycle differential capacity curves at *C*/10 rate (3.0−4.3 V vs Li^+/Li). (e−k) STEM/EDXS results. (l,n) HRTEM of the particle edges [parallel (l) and perpendicular (n) to the layering direction], with the respective areas indicated in the STEM image in panel (m).

Table 5. Results from Le Bail Analysis and ICP-OES of the IE-LNO-2.0W-PC and IE-LNO-2.0W-PC-Mg Samples

sample	R_{wp} [%]	R_{Bragg} [%]	a [Å]	c [Å]	V [Å^3]
IE-LNO-2.0W-PC	16.9	3.8	2.8734(2)	14.1677(300)	101.31(24)
IE-LNO-2.0W-PC-Mg	18.2	3.7	2.8790(15)	14.1943(810)	101.887(162)

sample	Li [%]	Na [%]	Mg [%]	Ni [%]	W [%]	O [%]
IE-LNO-2.0W-PC	92.8	2.1		100	0.38	211.5
IE-LNO-2.0W-PC-Mg	91.0	0.4	1.49	100	0.41	201.5

https://doi.org/10.1021/acs.chemmater.3c02727
Chem. Mater. XXXX, XXX, XXX−XXX

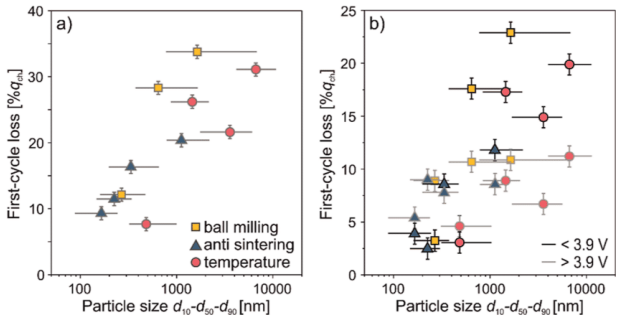

Figure 6. (a) First-cycle capacity loss as a function of particle size distribution (d_{50} is represented by symbols) for the different IE-LNO samples. (b) Corresponding separation of contributions to the capacity loss above and below 3.9 V vs Li^+/Li.

some more detail. The corresponding results are shown in Figure 6a. A correlation between grain size and first-cycle loss is found for all size-tailoring methods, and an even closer correlation is observed within each set of samples. For the temperature-tailored materials, the lowest loss at a given particle size is found, while the relative losses are similar for ball milling and anti-sintering. This could be related to the surface degradation upon milling and tungsten addition, which negatively affects diffusion (charge transport) in these particles. To determine the individual contributions to the first-cycle loss, a separation of capacity loss from KH at low potentials versus that at high states of charge was attempted. To this end, the charge curves were aligned in what we deem a noncritical region of good stability and maximum diffusion, namely, the monoclinic phase at ~4.0 V during charge and ~3.9 V during discharge (Figure S5, Supporting Information). This allows separating contributions to the first-cycle loss from features above and below 3.9 V, which we assume can be attributed to KH at <3.9 V and structural degradation at >3.9 V.

If this analysis is carried out on the reference material (PC-LNO), capacity losses of about 1% at high states of charge and 12% due to KH are found. From this result, we conclude that in conventional LNO, the first-cycle loss is dominated by KH, and degradation at high potentials plays a minor role, as already reported for NCMs and LNO.[13,34,35] For IE-LNO, on the other hand, a much larger loss at high states of charge of ~5−10% is observed, as shown in Figure 6b. This loss is slightly increased for the larger particles and is therefore most likely not directly connected to surface degradation, as in this case, an increase with decreasing particle size would be expected.[12] This raises the question of origin in the bulk material. A possible explanation is layer gliding (note that intragranular cracking has been linked to planar slipping in monolithic particles),[36] with the pillaring defects likely preventing the translational movement of NiO_2 slabs and rather causing the formation of stacking faults.[28] However, because of the presence of microcracks in the uncycled materials, this hypothesis could not be validated. By contrast, the KH loss is strongly correlated with the particle size and can be decreased from about 23% to almost 2% by decreasing the grain size. Regarding KH, IE-LNO seems to be superior to PC-LNO, even if the size of the single-crystalline particles is larger than that of the primary grains, as is the case for IE-LNO-450.[12]

The effects of avoiding $Ni_{Li}^{\bullet}$ defect formation seem to be 2-fold. On the one hand, diffusion is markedly facilitated, which helps mitigate the KH loss. However, a second loss feature at high states of charge becomes apparent that is usually not observed as it is weak enough to be ignored in reference LNO. It is well-known that defective LNO is unstable at high potentials and tends to form warped layers and release oxygen.[4,13,27] We therefore liken the effects of the substitutional point defects to a seesaw, balancing between improved diffusion and deteriorated stability as the $Ni_{Li}^{\bullet}$ concentration approaches 0 mol %.

Further electrochemical analysis was performed to shed more light on high-voltage degradation. To confirm that the reported effects originate from the lack of the pillaring $Ni_{Li}^{\bullet}$ defects, Mg^{2+} ions were introduced into the lithium site (for mimicking point defects, considering the same oxidation state and similar size of Mg^{2+} and Ni^{2+} in octahedral coordination).[37] First, it was attempted to introduce Mg^{2+} during the synthesis of NNO. Here, the increasing doping levels are accompanied by decreasing monoclinic distortion (Figure S6, Supporting Information), typically present in NNO due to Jahn-Teller distortion of Ni^{3+}. This leads us to the conclusion that Mg^{2+} likely occupies the nickel site in NNO and will maintain its position upon ion exchange. Indeed, even in solid-state syntheses of LNO, Mg^{2+} is found to occupy the lithium and nickel sites in a complex substitution pattern.[38] Hence, with the larger Na^+ ions being present, Mg^{2+} and other similar-sized ions, such as Zn^{2+}, preferentially occupy the transition-metal site.[37] To still introduce Mg^{2+} into the lithium site in IE-LNO, a dual-ion exchange method was devised. Here, sodium ions are simultaneously replaced with lithium and magnesium ions from a molten salt mixture of lithium and magnesium nitrates. In this example, a salt melt containing 1 mol % magnesium nitrate was prepared and used in the ion exchange of polycrystalline NNO containing 2 mol % tungsten from the anti-sintering approach. The magnesium concentration was found to be 1.49 mol % by ICP-OES (Table 5). Compared with IE-LNO-2.0W-PC, this material (termed IE-LNO-2.0W-PC-Mg) shows a larger *c*-parameter and cell volume, which is indicative of successful pillaring through dual-ion exchange. It was then used to re-establish the conclusions from the preceding analyses while having the same synthesis history as that of the unpillared IE-LNO samples.

To fully address the reversible capacity, the potential window was slightly widened from 3.0 to 4.3 to 2.9−4.35 V

https://doi.org/10.1021/acs.chemmater.3c02727
Chem. Mater. XXXX, XXX, XXX−XXX

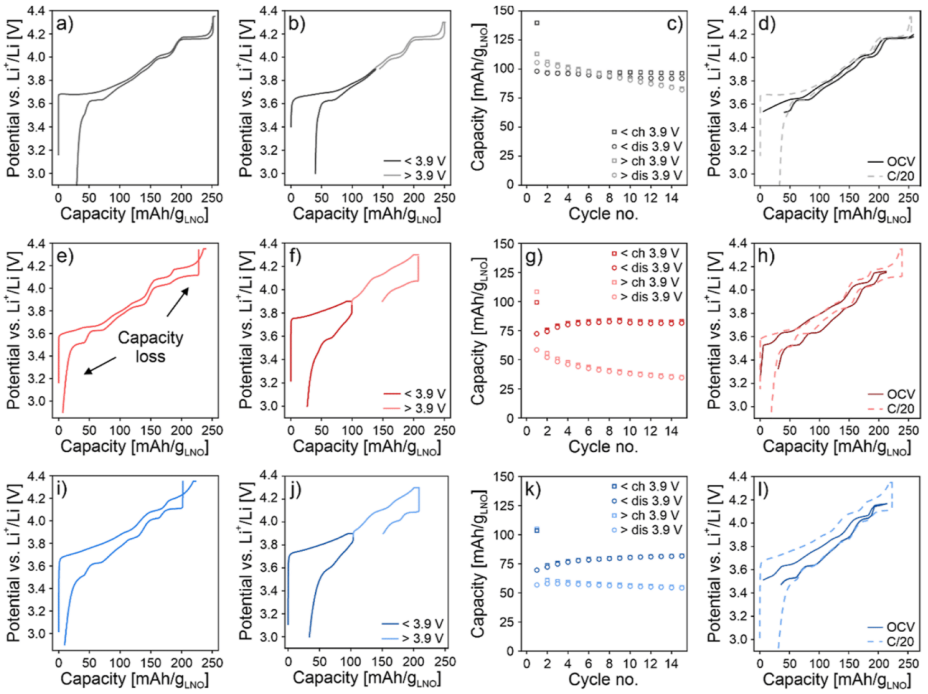

Figure 7. (a,e,i) Aligned first-cycle charge/discharge curves of (a, black) PC-LNO, (e, red) IE-LNO-2.0W-PC, and (i, blue) IE-LNO-2.0W-PC-Mg at C/20 rate (2.9−4.35 V vs Li^+/Li). (b,f,j) First-cycle charge/discharge curves for cycling in the potential windows of 3.0−3.9 and 3.9−4.3 V vs Li^+/Li at C/10 rate and (c,g,k) corresponding capacity retentions. (d,h,l) OCV curves (solid line) extracted from GITT measurements performed at an effective rate of C/100 shown together with the as-measured cycling data (dashed line) from panels (a,e,i).

vs Li^+/Li, and the *C*-rate was lowered to *C*/20. Under these conditions, initial specific capacities of q_{ch} = 255 and 239 mA h/g_{LNO} and q_{dis} = 222 and 221 mA h/g_{LNO} were achieved with PC-LNO and IE-LNO-2.0W-PC, respectively, corresponding to 13 and 8% first-cycle loss. Because of the polycrystalline morphology, the IE-LNO is able to deliver capacities similar to those of conventional LNO despite water washing. This could indicate that a pristine, defect-free LNO would perform even better, but such a material cannot be produced at present. The IE-LNO-2.0W-PC-Mg sample achieved q_{ch} = 223 mA h/g_{LNO} and q_{dis} = 192 mA h/g_{LNO} (14% first-cycle loss). The capacity loss separation was conducted on all three samples, as seen in Figure 7a,e,i. As mentioned previously, PC-LNO shows mainly KH loss, while the IE-LNO materials exhibit contributions from both loss features.

Next, the capacity retention in the regions of interest was examined by galvanostatic cycling in the potential windows of 3.0−3.9 V for the KH loss and 3.9−4.3 V to study the loss associated with high states of charge. The initial voltage profiles and capacity retentions over 15 cycles of LIB half-cells using the different samples are shown in Figure 7b,c,f,g,j,k. Cycling below 3.9 V leads to a large initial capacity loss of 17% (with respect to the specific charge capacity delivered between 3.0 and 4.3 V vs Li^+/Li) and then stable behavior for PC-LNO, whereas for both ion-exchanged samples, the first-cycle loss is followed by a capacity creep toward higher discharge capacities. This could point to changes in the surface structure upon consecutive cycling, e.g., by removing carbonates. If the highest capacity that is achieved after a few cycles is considered as the true value, overall low capacity losses of about 8 and 10% are observed for IE-LNO-2.0W-PC and IE-LNO-2.0W-PC-Mg, respectively. The latter sample therefore falls between the two extremes of no pillaring as in IE-LNO-2.0W-PC and $Ni^{\bullet}_{Li}$ defect-pillaring in PC-LNO.

Cycling to high potentials, on the other hand, leads to larger relative first-cycle losses of 24 and 23% for the ion-exchanged material without and with magnesium, respectively, whereas 4% capacity loss is observed for PC-LNO. All values here are somewhat larger than what is achieved by the separation method used above. This is due to the narrower potential window and large overpotentials for the ion-exchanged samples. This systematically excludes full discharge at 3.9 V and causes an apparently larger first-cycle loss in the high-voltage region. The consecutive cycles show continuous capacity decay to such an extent that 29% of the discharge capacity is lost after 15 cycles in the case of PC-LNO. For IE-LNO-2.0W-PC and IE-LNO-2.0W-PC-Mg, capacity losses of 45 and 7%, respectively, are found. This indicates an increase in long-term stability that is reintroduced into the material by incorporation of Mg^{2+} ions and further suggests that $Ni^{\bullet}_{Li}$-free LNO can even surpass the intrinsic stability of PC-LNO (if stabilized by other means). This result is also corroborated by

https://doi.org/10.1021/acs.chemmater.3c02727
Chem. Mater. XXXX, XXX, XXX−XXX

Table 6. Le Bail Refinement Results for the Charged PC-LNO, IE-LNO-2.0W-PC, and IE-LNO-2.0W-PC-Mg Samples

sample	R_{wp} [%]	phase	fraction [%]	a [Å]	c [Å]	V [Å^3]	$\Delta V/V_0$ [%]
PC-LNO	10.5	H2	81.4	2.820(1)	14.400(4)	99.16(1)	−6.2
		H3	18.6	2.818(4)	13.528(30)	93.05(6)	
IE-LNO-2.0W-PC	13.9	H2	80.6	2.819(1)	14.505(2)	99.80(2)	−9.2
		H3	19.4	2.819(2)	13.177(7)	90.66(11)	
IE-LNO-2.0W-PC-Mg	12.6	H2	98.1	2.827(1)	14.476(1)	100.21(2)	−9.0
		H3	1.9	2.824(6)	13.200(12)	91.16(42)	

long-term cycling data (Figure S7, Supporting Information), revealing 45, 52, and 60% capacity retention for PC-LNO, IE-LNO-2.0W-PC, and IE-LNO-2.0W-PC-Mg, respectively, after 100 cycles at C/3 rate in the potential window of 2.9−4.35 V vs Li^+/Li.

To gain more insight into the role that diffusion plays in the observed behaviors, galvanostatic intermittent titration technique (GITT) measurements were performed (Figure S8, Supporting Information). The extracted open-circuit voltage (OCV) curves are presented in Figure 7d,h,l. For PC-LNO, almost no difference to cycling at C/20 is observed at high potentials, whereas at the end of discharge, a divergence of the curves is apparent. This stands in contrast to IE-LNO-2.0W-PC, for which a large overpotential at high states of charge and striking similarity between the OCV curve and the first-cycle voltage profile in the KH region are observed. This is indicative of facilitated diffusion at the end of discharge and seems to be due to the removal of $Ni_{Li}^{\bullet}$ as a physical barrier and the increase in vacancy concentration, which would otherwise be trapped by the point defects. Again, IE-LNO-2.0W-PC-Mg shows an intermediate behavior of these two extremes, further validating that substitutional defects are directly linked to the observed cyclability.

High-Voltage Degradation. The origin of the high-voltage degradation was further analyzed by ex situ PXRD measurements and in situ gas analysis. Specifically, all three materials were charged to 4.3 V vs Li^+/Li and kept at this potential until the specific current dropped below 2.0 mA/g_{LNO} (C/100), after which the coin cells were opened in an argon atmosphere and the cathodes probed using PXRD. The corresponding charge curves and experimental patterns are shown in Figures S7 and S9 (Supporting Information), respectively. The diffraction data indicate the presence of two phases. The main phase can be assigned to H2, and the other likely corresponds to the collapsed H3 phase. The unpillared material (IE-LNO-2.0W-PC) exhibits the strongest contribution from the H3 phase with 19%, compared to 18% in PC-LNO and 2% in IE-LNO-2.0W-PC-Mg. The phases were further analyzed using the Le Bail method, the results of which are shown in Table 6. Both phases are assumed to be hexagonal in nature ($R\bar{3}m$ space group), although it has been hypothesized previously that O1 stacking can occur in LNO due to layer gliding. The latter was also observed for Ni-rich NCMs, yet the process of O1 formation is apparently very slow.[13,28,36,39,40] This phase is believed to appear below a lithiation degree of 7%, but the substitutional defects are expected to prevent gliding at high states of charge.[16,18] Nevertheless, it could be facilitated in IE-LNO due to the lack of $Ni_{Li}^{\bullet}$ defects, which has been predicted to result in lower activation energies for gliding.[41] The presence of the O1 phase, compared to O3, would only be visible by a slight peak broadening, which is inherent in the IE-LNO materials. Therefore, we cannot conclusively discern the two phases. Upon phase transition from H2 to H3, a large anisotropic volume change occurs, leading to a decrease in cell volume by about 6% for PC-LNO. For the ion-exchanged samples, this collapse is much more severe at ∼9%. The interlayer spacing is slightly increased for the H3 phase when magnesium is introduced, which is likely a sign of the pillaring functionality. Also, the H3 contribution is less pronounced, suggesting that the pillar ions mitigate to some extent the phase transformation to the collapsed state. Overall, these results point to an increase in the formation of the H3 phase under comparable charging conditions and larger volume variation for the unpillared IE-LNO relative to that for PC-LNO. If magnesium is introduced into the structure, the interlayer collapse is accompanied by slightly less volume change, and the fraction of the H3 phase is significantly reduced.

Finally, differential electrochemical mass spectrometry (DEMS) measurements were performed to examine the differences in the gassing behavior, which has also been linked to the degradation of LNO at high potentials.[27,42] At the cathode side, CO_2 is the most prominently evolved gas, for which there are three main sources.[42−46] First, surface carbonate impurities formed by exposure of the cathode material to humidity and atmospheric CO_2 decompose under CO_2 evolution, especially in the initial cycle.[44−48] Second, oxygen, which subsequently leads to chemical oxidation of the electrolyte, results mostly in CO_2 and, to a lesser extent, O_2 evolution.[45,49,50] Lastly, electrochemical oxidation of the electrolyte also leads to the decomposition of the solvent molecules under the CO_2 evolution. However, for ethylene carbonate (EC) as the most common electrolyte solvent, the onset of this decomposition has been determined to be around 4.6 V vs Li^+/Li.[51−53] Figure 8a−c shows the CO_2 evolution profiles for the three materials previously discussed, as obtained via DEMS during cycling of LIB half-cells at C/10 rate between 3.0 and 4.5 V. Table S2 (Supporting Information) reports the specific capacities and CO_2 amounts obtained in each cycle and for each material.

Strong differences in the CO_2 evolution of the materials are evident and will be discussed in the following. However, while a slightly delayed CO_2 evolution for PC-LNO in the initial cycle is in accordance with previous reports,[27,54,55] the low overall amount and the unusual evolution curve require further considerations. The gas evolution profiles are affected by the use of a rather large volume of electrolyte, which is unfortunately sometimes required for the reliable cycling of DEMS cells in an open-headspace configuration. The reason is that the electrolyte is constantly purged out, and the cells therefore tend to dry out during the experiment. Figure S10 (Supporting Information) shows the gas evolution profiles for PC-LNO and IE-LNO-2.0W-PC obtained with a much lower volume of electrolyte (350 vs 750 μL). For the IE-LNO-2.0W-PC-Mg sample, no such measurement could be successfully performed. Two main effects can be observed when using less

https://doi.org/10.1021/acs.chemmater.3c02727
Chem. Mater. XXXX, XXX, XXX−XXX

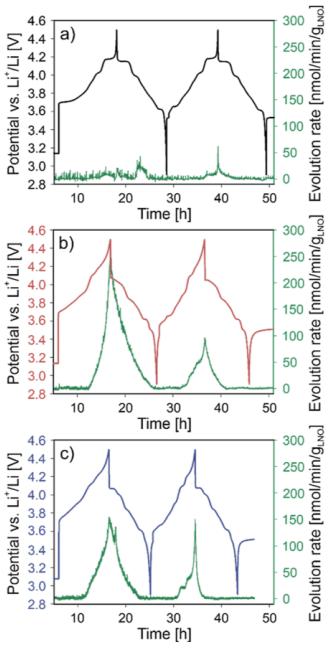

Figure 8. CO_2 evolution as measured by DEMS (3.0−4.5 vs Li^+/Li, C/10 rate). (a) PC-LNO, (b) IE-LNO-2.0W-PC, and (c) IE-LNO-2.0W-PC-Mg.

electrolyte. First, the gas evolution profile for IE-LNO-2.0W-PC reveals a higher maximum rate but a narrower peak, resulting in similar total gas amounts after two cycles (82 vs 88 μmol/g_{LNO}). A likely explanation is the reduced amount of CO_2 dissolved into the electrolyte, leading to less tailing in the evolution peaks. Second, a slightly higher gas evolution and a clearer profile are observed for PC-LNO (10 vs 21 μmol/g_{LNO}). The total CO_2 amount is in good agreement with those in previous literature reports of NCM and LNO outgassing under consideration of surface purity and upper cutoff potential.[27,31,49,56,57] The detection of additional shoulder peaks or plateaus of gas evolution at lower states of charge or during early discharge, such as for PC-LNO, IE-LNO-2.0W-PC with less electrolyte, and IE-LNO-2.0W-PC-Mg (second cycle), has been previously reported for LNO, although there is still uncertainty in whether increased gas evolution is associated with mono- or biphasic delithiation.[27,57] As shown in Figure S10 (Supporting Information) for PC-LNO, these shoulders mainly correspond to monophasic regions.

The main contribution to outgassing of the materials obtained by ion exchange as well as the main difference from the gas evolution of PC-LNO obtained via solid-state synthesis is the presence of surface carbonate impurities, likely as remnants of the post-treatment procedure. An onset of CO_2 evolution between 3.8 and 4.0 V, as found in this study, is commonly observed for the decomposition of surface carbonates, yet the contribution of the underlying degradation mechanisms is disputed.[42,46,58] The presence of surface carbonates is further confirmed by attenuated total reflection infrared spectroscopy (ATR IR) data collected from the materials (Figure S7, Supporting Information).[45,59,60] Unlike IE-LNO-2.0W-PC and IE-LNO-2.0W-PC-Mg, only weak bands are visible for PC-LNO, as expected for a dry-room-processed and optimized material. While IE-LNO-2.0W-PC-Mg exhibits the strongest surface carbonate signal, more gas evolution is observed for IE-LNO-2.0W-PC, opening room for discussion of further contributions to gas evolution.

For PC-LNO, the majority of the capacity above 4.1 V is obtained during the H2-H3 phase transition, and the cathode is only at high potentials for a relatively short period of time. By contrast, IE-LNO-2.0W-PC and IE-LNO-2.0W-PC-Mg show similar voltage profiles with a less pronounced plateau and a rather linear increase of potential over time during charge above 4.1 V, resulting in a longer time spent at high potentials, accompanied by high gas evolution rates. However, because no significant electrochemical electrolyte oxidation is expected in this potential range, a contribution involving lattice oxygen release (chemical electrolyte oxidation) can be assumed. This could also explain the higher gas evolution seen for IE-LNO-2.0W-PC than that for IE-LNO-2.0W-PC-Mg, even though the latter likely has more surface carbonates, and both materials contain tungsten and are of similar particle size. Considering the lattice collapse in the materials, a possible explanation for higher lattice oxygen release in IE-LNO-2.0W-PC might be the higher H3 phase content and stronger *c*-parameter decrease due to the absence of the pillaring ions. If adjacent NiO_2 layers come closer to each other, the formation of oxygen dimers between them may be facilitated, a mechanism suggested by Kong et al. for the (104) facet of LNO and under nickel migration into the lithium layer, i.e., rock-salt-type NiO formation.[61] Yet, Genreith-Schriever et al. suggest dimer formation from oxygen atoms of the same layer and under assistance of H_2O, while also pointing to the predominance of the (012) facet and arguing that oxygen, not nickel, is the main redox contributor to LNO capacity.[62] The required peroxo-like intermediates have not been observed (via titration-mass spectrometry) by Kaufman et al., which instead link surface crack formation resulting from parasitic reactions with the electrolyte to gas evolution of layered Ni-rich oxide cathodes.[63] This provides further support for the assumption that larger volume variations, due to the absence of pillaring ions, lead to stronger gas evolution. Furthermore, various facets of different stability are found in LNO, and the presence of electrolyte solvent, especially EC, has also been shown to affect the activation energy for lattice oxygen release.[64−66] The lack of pillaring ions is the main difference between the materials and is likely to affect lattice oxygen release and nickel reduction, which go hand in hand.

Overall, we find increased oxygen evolution from the ion-exchanged materials compared to that in the reference LNO. This is due in part to the presence of surface carbonates. Nevertheless, lattice oxygen release is strongly increased for both materials, with the unpillared system showing the most severe release. These findings underpin the observations made for all size-tailored samples. Upon removing the $Ni_{Li}^{\bullet}$ point defects, the balance between kinetic hindrance and structural stabilization tilts toward improved kinetics and decreased stability accompanied by common signs of degradation, such as oxygen release, which is described by the metaphor of a seesaw.

https://doi.org/10.1021/acs.chemmater.3c02727
Chem. Mater. XXXX, XXX, XXX−XXX

■ CONCLUSIONS

Sodium-to-lithium ion exchange is an effective method to prepare high-quality $LiNiO_2$ and represents an ideal platform to study the effect that the $Ni_{Li}^{\bullet}$ point defects have on the electrochemical behavior of layered Ni-rich oxide cathode materials. However, small particle (grain) sizes are necessary to ensure full conversion of $NaNiO_2$ to $LiNiO_2$. In this work, three different methods for tailoring the particle size of $NaNiO_2$ were employed, and the charge-storage properties of the ion-exchanged materials were probed by galvanostatic cycling. For all samples, improvement of lithium diffusion and reduction in first-cycle capacity loss are associated with decreasing particle size, allowing in the case of polycrystalline morphology to lower the irreversible capacity loss on the initial cycle below that of conventional $LiNiO_2$ prepared by solid-state synthesis. Upon removal of the $Ni_{Li}^{\bullet}$ point defects, the highly charged state is rendered less stable, leading to electrochemical degradation accompanied by an increase in oxygen evolution from the crystal lattice. The decrease in interlayer spacing likely accounts for the more severe gassing and thus also for the loss of capacity at high states of charge. However, the formation of stacking faults, due to a lack of $Ni_{Li}^{\bullet}$ preventing layer gliding, may occur simultaneously and may lead to intragranular cracking, thereby causing the observed degradation independent of the exposed surface(s). Introduction of Mg^{2+} ions as a substitute for $Ni_{Li}^{\bullet}$ defects can not only restore some of the stabilization but also negatively affects kinetics. We therefore hypothesize a "seesaw effect" of nickel substitutional defects and related pillaring agents, emphasizing the need for an optimal balance between diffusivity and structural stability to optimize first-cycle efficiency and battery performance.

■ EXPERIMENTAL SECTION

Synthesis of $NaNiO_2$. $NaNiO_2$ was prepared by a solid-state reaction from $Ni(OH)_2$ (d_{50} = 4 μm, BASF SE) or NiO nanoparticles (d_{50} = 50 nm, BASF SE) and NaOH (Sigma-Aldrich) or Na_2O_2 (Sigma-Aldrich), and optionally APT (Sigma-Aldrich), as indicated. The reactants were homogenized in a laboratory blender (Kinematica) under an Ar atmosphere for 5 min with 10 mol % excess of $NaOH/Na_2O_2$ [i.e., n(Ni)/n(Na) = 1/1.1]. The precursor mixtures were then heated in an Al_2O_3 crucible under an oxygen flow (~2 volume exchanges per h) in a tube furnace (Nabertherm P330) at 300 °C for 10 h with 3 K/min heating and cooling rates. After cooling, the reactant mixtures were homogenized again for 5 min, and in one instance, APT was added to produce the polycrystalline material. The resulting mixtures were transferred to an Al_2O_3 crucible for calcination at 450−700 °C for 12 h under an oxygen flow (~2 volume exchanges per h) and with 3 K/min heating and cooling rates. The products were sieved using a 32 μm steel mesh.

Synthesis of Mg-Doped $NaNiO_2$. Doping magnesium into the $NaNiO_2$ structure was attempted by addition of $Mg(OH)_2$ nanoparticles (10 nm, US Research Nanomaterials Inc.) to the synthesis outlined for $NaNiO_2$ above, with the amounts indicated in the main text and in Figure S6 (Supporting Information).

Synthesis of Reference $LiNiO_2$. Reference (polycrystalline) $LiNiO_2$ was prepared by a solid-state reaction from $Ni(OH)_2$ (d_{50} = 14 μm, BASF SE) and $LiOH{\cdot}H_2O$ (10−20 μm, BASF SE). The reactants were dry mixed in a blender (Kinematica) under an Ar atmosphere for 5 min in the required ratios with 1 mol % excess of $LiOH{\cdot}H_2O$. The precursor mixture was then calcined in an Al_2O_3 crucible under oxygen flow (~2 volume exchanges per h) in a tube furnace (Nabertherm P330) at 700 °C for 8 h with 3 K/min heating and cooling rates and with a preheating step at 400 °C for 4 h. The product was sieved using a 32 μm steel mesh.

Ball Milling of $NaNiO_2$. $NaNiO_2$ was milled in a planetary ball mill (Fritsch) with a 20/1 ball-to-powder weight ratio using 2 mm ZrO_2 balls at the indicated rotational speed of 300−600 rpm for 10 min. The product was directly used for ion exchange.

Synthesis of Mg-Containing $LiNO_3$. A mixture of 90 mol % $LiNO_3$ and 10 mol % $Mg(NO_3)_2$ (Sigma-Aldrich) was liquefied at 350 °C, followed by quenching to room temperature. Subsequently, it was homogenized and used as a dry mixture with $LiNO_3$ at a ratio of 1/10 Mg/Li/Li.

Ion-Exchange Protocol. 1 g of $NaNiO_2$ and 1 g of $LiNO_3$ (Sigma-Aldrich) or 1 mol % Mg-containing $LiNO_3$ were mixed in a mortar and pestle and filled into an Al_2O_3 crucible. The powder mixtures were heated at 300 °C for 6 h and left to cool to room temperature. A PTFE-coated magnetic stir bar and 50 mL of LiOH solution (pH = 12.5, 0.025 M) were used to dissolve the remaining nitrate salt, and the resulting materials were washed with 50 mL of LiOH solution, 10 mL of ethanol, and 10 mL of acetone. The products were dried in vacuum at 65 °C and sieved using a 32 μm steel mesh.

Electrochemical Testing. Electrode tapes were prepared by casting an *N*-methyl-pyrrolidone (NMP)-based slurry with 96 wt % cathode material, 3 wt % Super C65 carbon additive, and 3 wt % polyvinylidene difluoride binder (Solef 5130, Solvay) onto a 0.03 mm Al foil as the current collector. The slurry was prepared freshly by combining all the constituents with 20 wt % additional NMP in a planetary mixer (ARE250, Thinky) and stirring using a two-step program (3 min at 2000 rpm, 3 min at 400 rpm). The slurry was spread at a casting thickness of 140 μm and at a rate of 5 mm/s using an Erichsen Coatmaster 510 coating machine with a stainless-steel blade. The obtained tapes were dried overnight in vacuum at 120 °C and calendared at 14 N/mm (Sumet Messtechnik). Individual circular cathodes of 13 mm diameter were cut, and LIB half-cells containing LP57 electrolyte (1 M $LiPF_6$ in a mixture of EC and ethyl methyl carbonate [3/7 ratio]), a GF/D separator, and a Li−metal anode were assembled in an Ar glovebox.

SEM. Morphological and compositional insights into the as-prepared samples were obtained from field-emission SEM and EDXS analyses using a LEO-1530 microscope (Carl Zeiss AG).

FIB. Electron-transparent specimens for the TEM investigation were prepared by the lift-out technique using an FEI Strata 400 S dual-beam system. Gallium-ion-beam-induced sample damage and amorphization were minimized by stepwise reduction of the acceleration voltage, from 30 to 2 keV, during the final thinning of the lamella. Specimen preparation was immediately followed by a TEM investigation to reduce possible oxidation during sample storage.

(S)TEM. (S)TEM images were acquired at 300 keV using a probe aberration-corrected Thermo Fisher Scientific Themis Z microscope. EDXS maps were collected with a Super-X EDX detector.

ICP-OES. The composition of the products was determined by ICP-OES using a Thermo Fisher Scientific ICAP 7600 DUO. To this end, powder samples were dissolved in an acid digester in a graphite furnace. Mass fractions were obtained from three independent measurements for each sample. About 10 mg of the material of interest was dissolved in 6 mL of hydrochloric acid and 2 mL of nitric acid at 353 K for 4 h. The digested samples were diluted, and an analysis of the elements was conducted with four different calibration solutions and an internal standard (Sc). The range of the calibration solutions did not exceed a decade. Two or three wavelengths of the elements were used for analysis. The oxygen content was analyzed by carrier gas hot extraction using a commercial TC600 oxygen/nitrogen analyzer (LECO). The oxygen content was calibrated with the certified standard KED 1025, a steel powder from ALPHA. The standards and samples were weighed with a mass in the range of 1−2 mg, in addition to 5 mg of graphite, in Sn crucibles (9−10 mm) and wrapped. Together with a Sn pellet, the wrapped samples were placed in a Ni crucible and loaded in an outgassed double-graphite crucible. Evolving CO_2 and CO were swept out by He carrier gas and measured by infrared detectors.

https://doi.org/10.1021/acs.chemmater.3c02727
Chem. Mater. XXXX, XXX, XXX−XXX

Capillary PXRD. PXRD patterns were collected on a STADI P (STOE) diffractometer in Debye–Scherrer geometry with monochromatic Mo $K\alpha_1$ radiation (λ = 0.7093 Å, 50 kV, 40 mA) and a Mythen 1K detector (Dectris). The diffraction data sets were analyzed using TOPAS Academic v7. LeBail fitting was done first, in which background correction was applied by a set of Chebyshev polynomials (10 terms), and lattice parameters, zero-shift, axial divergence, and crystallite size were extracted as Gaussian and Lorentzian contributions. The phenomenological model by Stephens was used to describe *hkl*-dependent microstrain.[67] During Rietveld refinement, the parameters from LeBail fitting were first fixed, and the oxygen coordinate(s) z_O ($LiNiO_2$) and z_{O_1} and z_{O_2} ($NaNiO_2$), site occupancies, and Debye–Waller factors were refined while applying an absorption correction. Lastly, all parameters were refined in parallel until convergence was achieved. The confidence intervals were three times the estimated standard deviations as obtained from TOPAS Academic.

ATR-IR Spectroscopy. Spectra were measured in an Ar glovebox using an ALPHA FT-IR spectrometer equipped with an Eco ATR sampling module. The data were Fourier transformed using the OPUS software (Bruker) and background subtracted with Origin Pro 2021.

DEMS. Cells consisting of a 30 mm diameter cathode with a 4 mm hole in the center, a 40 mm diameter GF/D separator, a 32 mm Li–metal anode, and 750 μL of LP57 electrolyte were assembled in a customized housing. In a variation, only 350 μL of electrolyte was used. The cells were cycled at 0.1C rate between 3.0 and 4.5 V vs Li^+/Li for two cycles, while a stream of He carrier gas (2.5 mL/min, purity 6.0) was constantly passed through. After passing a cold trap (−30 °C) to condense the extracted electrolyte solvent, the gas mixture was analyzed by a mass spectrometer (GSD320, Pfeiffer Vacuum GmbH). A calibration curve was obtained from measuring various dilutions of a gas of a known composition. A more detailed description of the setup and method is available in the literature.[42,68,69]

■ ASSOCIATED CONTENT

Supporting Information

The Supporting Information is available free of charge at https://pubs.acs.org/doi/10.1021/acs.chemmater.3c02727.

PXRD patterns and refinement plots/results, electrochemical testing data (including cycling and GITT), TEM/EDXS analysis, ATR-IR spectra, and DEMS results (PDF)

■ AUTHOR INFORMATION

Corresponding Authors

Jürgen Janek − *Battery and Electrochemistry Laboratory (BELLA), Institute of Nanotechnology, Karlsruhe Institute of Technology (KIT), 76344 Eggenstein-Leopoldshafen, Germany; Institute of Physical Chemistry & Center for Materials Research (ZfM/LaMa), Justus-Liebig-University Giessen, 35392 Giessen, Germany;* orcid.org/0000-0002-9221-4756; Email: juergen.janek@kit.edu

Torsten Brezesinski − *Battery and Electrochemistry Laboratory (BELLA), Institute of Nanotechnology, Karlsruhe Institute of Technology (KIT), 76344 Eggenstein-Leopoldshafen, Germany;* orcid.org/0000-0002-4336-263X; Email: torsten.brezesinski@kit.edu

Authors

Leonhard Karger − *Battery and Electrochemistry Laboratory (BELLA), Institute of Nanotechnology, Karlsruhe Institute of Technology (KIT), 76344 Eggenstein-Leopoldshafen, Germany*

Svetlana Korneychuk − *Institute of Nanotechnology and Karlsruhe Nano Micro Facility (KNMFi), Karlsruhe Institute of Technology (KIT), 76344 Eggenstein-Leopoldshafen, Germany*

Wessel van den Bergh − *Battery and Electrochemistry Laboratory (BELLA), Institute of Nanotechnology, Karlsruhe Institute of Technology (KIT), 76344 Eggenstein-Leopoldshafen, Germany*

Sören L. Dreyer − *Battery and Electrochemistry Laboratory (BELLA), Institute of Nanotechnology, Karlsruhe Institute of Technology (KIT), 76344 Eggenstein-Leopoldshafen, Germany;* orcid.org/0000-0001-8867-4787

Ruizhuo Zhang − *Battery and Electrochemistry Laboratory (BELLA), Institute of Nanotechnology, Karlsruhe Institute of Technology (KIT), 76344 Eggenstein-Leopoldshafen, Germany*

Aleksandr Kondrakov − *Battery and Electrochemistry Laboratory (BELLA), Institute of Nanotechnology, Karlsruhe Institute of Technology (KIT), 76344 Eggenstein-Leopoldshafen, Germany; BASF SE, 67056 Ludwigshafen, Germany*

Complete contact information is available at: https://pubs.acs.org/10.1021/acs.chemmater.3c02727

Notes

The authors declare no competing financial interest.

■ ACKNOWLEDGMENTS

This work was partially supported by BASF SE. The authors are grateful to the Federal Ministry of Education and Research (Bundesministerium für Bildung und Forschung, BMBF) for funding within the project UNIKAM (03XP0484B). Thomas Bergfeldt is acknowledged for conducting the ICP-OES measurements and Philipp Müller for TEM analysis of NNO. The authors also thank Damian Goonetilleke and Nikolai Bartnick for experimental support. The authors acknowledge the support from the Karlsruhe Nano Micro Facility (KNMFi, http://www.knmf.kit.edu), a Helmholtz research infrastructure at Karlsruhe Institute of Technology (KIT, http://www.kit.edu).

■ REFERENCES

(1) Xiao, J.; Chernova, N. A.; Whittingham, M. S. Layered Mixed Transition Metal Oxide Cathodes with Reduced Cobalt Content for Lithium Ion Batteries. *Chem. Mater.* **2008**, *20*, 7454–7464.

(2) Hoang, K.; Johannes, M. Defect Physics and Chemistry in Layered Mixed Transition Metal Oxide Cathode Materials: (Ni,Co,Mn) vs (Ni,Co,Al). *Chem. Mater.* **2016**, *28*, 1325–1334.

(3) Chernova, N. A.; Nolis, G. M.; Omenya, F. O.; Zhou, H.; Li, Z.; Whittingham, M. S. What Can We Learn about Battery Materials from Their Magnetic Properties? *J. Mater. Chem.* **2011**, *21*, 9865–9875.

(4) Bianchini, M.; Roca-Ayats, M.; Hartmann, P.; Brezesinski, T.; Janek, J. There and Back Again—The Journey of $LiNiO_2$ as a Cathode Active Material. *Angew. Chem., Int. Ed.* **2019**, *58*, 10434–10458.

(5) Kanno, R.; Kubo, H.; Kawamoto, Y.; Kamiyama, T.; Izumi, F.; Takeda, Y.; Takano, M. Phase Relationship and Lithium Deintercalation in Lithium Nickel Oxides. *J. Solid State Chem.* **1994**, *110*, 216–225.

(6) Li, W.; Reimers, J. N.; Dahn, J. R. Crystal Structure of $Li_xNi_{2-x}O_2$ and a Lattice-Gas Model for the Order-Disorder Transition. *Phys. Rev. B* **1992**, *46*, 3236–3246.

(7) Goonetilleke, D.; Schwarz, B.; Li, H.; Fauth, F.; Suard, E.; Mangold, S.; Indris, S.; Brezesinski, T.; Bianchini, M.; Weber, D. Stoichiometry Matters: Correlation between Antisite Defects, Micro-

structure and Magnetic Behavior in the Cathode Material $Li_{1-z}Ni_{1+x}O_2$. *J. Mater. Chem. A* **2023**, *11*, 13468−13482.
(8) Pokle, A.; Weber, D.; Bianchini, M.; Janek, J.; Volz, K. Probing the $Ni(OH)_2$ Precursor for $LiNiO_2$ at the Atomic Scale: Insights into the Origin of Structural Defect in a Layered Cathode Active Material. *Small* **2023**, *19*, 2205508.
(9) Bianchini, M.; Fauth, F.; Hartmann, P.; Brezesinski, T.; Janek, J. An In Situ Structural Study on the Synthesis and Decomposition of $LiNiO_2$. *J. Mater. Chem. A* **2020**, *8*, 1808−1820.
(10) Wei, H.; Tang, L.; Huang, Y.; Wang, Z.; Luo, Y.; He, Z.; Yan, C.; Mao, J.; Dai, K.; Zheng, J. Comprehensive Understanding of Li/Ni Intermixing in Layered Transition Metal Oxides. *Mater. Today* **2021**, *51*, 365−392.
(11) Kurzhals, P.; Riewald, F.; Bianchini, M.; Sommer, H.; Gasteiger, H. A.; Janek, J. The $LiNiO_2$ Cathode Active Material: A Comprehensive Study of Calcination Conditions and Their Correlation with Physicochemical Properties. Part I. Structural Chemistry. *J. Electrochem. Soc.* **2021**, *168*, 110518.
(12) Riewald, F.; Kurzhals, P.; Bianchini, M.; Sommer, H.; Janek, J.; Gasteiger, H. A. The $LiNiO_2$ Cathode Active Material: A Comprehensive Study of Calcination Conditions and Their Correlation with Physicochemical Properties Part II. Morphology. *J. Electrochem. Soc.* **2022**, *169*, 020529.
(13) Quisbert, E. B.; Fauth, F.; Abakumov, A. M.; Blangero, M.; Guignard, M.; Delmas, C. Understanding the High Voltage Behavior of $LiNiO_2$ Through the Electrochemical Properties of the Surface Layer. *Small* **2023**, *19*, 2300616.
(14) Karger, L.; Weber, D.; Goonetilleke, D.; Mazilkin, A.; Li, H.; Zhang, R.; Ma, Y.; Indris, S.; Kondrakov, A.; Janek, J.; Brezesinski, T. Low-Temperature Ion Exchange Synthesis of Layered $LiNiO_2$ Single Crystals with High Ordering. *Chem. Mater.* **2023**, *35*, 648−657.
(15) Peres, J. P.; Delmas, C.; Rougier, A.; Broussely, M.; Perton, F.; Biensan, P.; Willmann, P. The Relationship between the Composition of Lithium Nickel Oxide and the Loss of Reversibility during the First Cycle. *J. Phys. Chem. Solids* **1996**, *57*, 1057−1060.
(16) Croguennec, L.; Pouillerie, C.; Mansour, A. N.; Delmas, C. Structural Characterisation of the Highly Deintercalated $Li_xNi_{1.02}O_2$ Phases (with $x \leq 0.30$). *J. Mater. Chem.* **2001**, *11*, 131−141.
(17) Tarascon, J. M.; Vaughan, G.; Chabre, Y.; Seguin, L.; Anne, M.; Strobel, P.; Amatucci, G. In Situ Structural and Electrochemical Study of $Ni_{1-x}Co_xO_2$ Metastable Oxides Prepared by Soft Chemistry. *J. Solid State Chem.* **1999**, *147*, 410−420.
(18) Croguennec, L.; Pouillerie, C.; Delmas, C. Structural Characterisation of New Metastable NiO_2 Phases. *Solid State Ionics* **2000**, *135*, 259−266.
(19) Arai, H.; Okada, S.; Ohtsuka, H.; Ichimura, M.; Yamaki, J. Characterization and Cathode Performance of $Li_{1-x}Ni_{1+x}O_2$ Prepared with the Excess Lithium Method. *Solid State Ionics* **1995**, *80*, 261−269.
(20) Delmas, C.; Pérès, J. P.; Rougier, A.; Demourgues, A.; Weill, F.; Chadwick, A.; Broussely, M.; Perton, F.; Biensan, Ph.; Willmann, P. On the Behavior of the Li_xNiO_2 System: An Electrochemical and Structural Overview. *J. Power Sources* **1997**, *68*, 120−125.
(21) Bianchi, V.; Bach, S.; Belhomme, C.; Farcy, J.; Pereira-Ramos, J. P.; Caurant, D.; Baffier, N.; Willmann, P. Electrochemical Investigation of the Li Insertion-Extraction Reaction as a Function of Lithium Deficiency in $Li_{1-x}Ni_{1+x}O_2$. *Electrochim. Acta* **2001**, *46*, 999−1011.
(22) Xu, Z.; Wang, Z.; Tan, X.; Guo, H.; Peng, W.; Li, X.; Wang, J.; Yan, G. Correlating Morphological and Structural Evolution with the Electrochemical Performance of Nickel-Rich Cathode Materials: From Polycrystal to Single Crystal. *J. Electrochem. Soc.* **2022**, *169*, 090520.
(23) Sicolo, S.; Sadowski, M.; Vettori, K.; Bianchini, M.; Janek, J. Off-Stoichiometry, Vacancy Trapping and Pseudo-Irreversible First-Cycle Capacity in $LiNiO_2$. *Theor. Comput. Chem.* **2023**. (accessed 31.09.2023)
(24) van den Bergh, W.; Karger, L.; Murugan, S.; Janek, J.; Kondrakov, A.; Brezesinski, T. Single Crystal Layered Oxide Cathodes: The Relationship between Particle Size, Rate Capability, and Stability. *ChemElectroChem* **2023**, *10*, e202300165.
(25) Rougier, A.; Gravereau, P.; Delmas, C. Optimization of the Composition of the $Li_{1-z}Ni_{1+x}O_2$ Electrode Materials: Structural, Magnetic, and Electrochemical Studies. *J. Electrochem. Soc.* **1996**, *143*, 1168−1175.
(26) Li, H.; Zhang, N.; Li, J.; Dahn, J. R. Updating the Structure and Electrochemistry of Li_xNiO_2 for $0 \leq x \leq 1$. *J. Electrochem. Soc.* **2018**, *165*, A2985−A2993.
(27) de Biasi, L.; Schiele, A.; Roca-Ayats, M.; Garcia, G.; Brezesinski, T.; Hartmann, P.; Janek, J. Phase Transformation Behavior and Stability of $LiNiO_2$ Cathode Material for Li-Ion Batteries Obtained from In Situ Gas Analysis and Operando X-Ray Diffraction. *ChemSusChem* **2019**, *12*, 2240−2250.
(28) Mock, M.; Bianchini, M.; Fauth, F.; Albe, K.; Sicolo, S. Atomistic Understanding of the $LiNiO_2$-NiO_2 Phase Diagram from Experimentally Guided Lattice Models. *J. Mater. Chem. A* **2021**, *9*, 14928−14940.
(29) Liu, A.; Phattharasupakun, N.; Cormier, M. M. E.; Zsoldos, E.; Zhang, N.; lyle, E.; Arab, P.; Sawangphruk, M.; Dahn, J. R. Factors That Affect Capacity in the Low Voltage Kinetic Hindrance Region of Ni-Rich Positive Electrode Materials and Diffusion Measurements from a Reinvented Approach. *J. Electrochem. Soc.* **2021**, *168*, 070503.
(30) Rueß, R.; Gomboso, D.; Ulherr, M.; Trevisanello, E.; Ma, Y.; Kondrakov, A.; Brezesinski, T.; Janek, J. Single-Crystalline $LiNiO_2$ as High-Capacity Cathode Active Material for Solid-State Lithium-Ion Batteries. *J. Electrochem. Soc.* **2023**, *170*, 020533.
(31) Oswald, S.; Pritzl, D.; Wetjen, M.; Gasteiger, H. A. Novel Method for Monitoring the Electrochemical Capacitance by In Situ Impedance Spectroscopy as Indicator for Particle Cracking of Nickel-Rich NCMs: Part II. Effect of Oxygen Release Dependent on Particle Morphology. *J. Electrochem. Soc.* **2021**, *168*, 120501.
(32) Pritzl, D.; Teufl, T.; Freiberg, A. T. S.; Strehle, B.; Sicklinger, J.; Sommer, H.; Hartmann, P.; Gasteiger, H. A. Editors' Choice—Washing of Nickel-Rich Cathode Materials for Lithium-Ion Batteries: Towards a Mechanistic Understanding. *J. Electrochem. Soc.* **2019**, *166*, A4056−A4066.
(33) Goonetilleke, D.; Mazilkin, A.; Weber, D.; Ma, Y.; Fauth, F.; Janek, J.; Brezesinski, T.; Bianchini, M. Single Step Synthesis of W-Modified $LiNiO_2$ Using an Ammonium Tungstate Flux. *J. Mater. Chem. A* **2022**, *10*, 7841−7855.
(34) Kasnatscheew, J.; Evertz, M.; Streipert, B.; Wagner, R.; Klöpsch, R.; Vortmann, B.; Hahn, H.; Nowak, S.; Amereller, M.; Gentschev, A.-C.; Lamp, P.; Winter, M. The Truth about the 1st Cycle Coulombic Efficiency of $LiNi_{1/3}Co_{1/3}Mn_{1/3}O_2$ (NCM) Cathodes. *Phys. Chem. Chem. Phys.* **2016**, *18*, 3956−3965.
(35) Bae, C.; Dupre, N.; Kang, B. Further Improving Coulombic Efficiency and Discharge Capacity in $LiNiO_2$ Material by Activating Sluggish ∼ 3.5 V Discharge Reaction. *ACS Appl. Mater. Interfaces* **2021**, *13*, 23760−23770.
(36) Bi, Y.; Tao, J.; Wu, Y.; Li, L.; Xu, Y.; Hu, E.; Wu, B.; Hu, J.; Wang, C.; Zhang, J.-G.; Qi, Y.; Xiao, J. Reversible Planar Gliding and Microcracking in a Single-Crystalline Ni-Rich Cathode. *Science* **2020**, *370*, 1313−1317.
(37) Shannon, R. D. Revised Effective Ionic Radii and Systematic Studies of Interatomic Distances in Halides and Chalcogenides. *Acta Crystallogr.* **1976**, *32*, 751−767.
(38) Weber, D.; Lin, J.; Pokle, A.; Volz, K.; Janek, J.; Brezesinski, T.; Bianchini, M. Tracing Low Amounts of Mg in the Doped Cathode Active Material $LiNiO_2$. *J. Electrochem. Soc.* **2022**, *169*, 030540.
(39) Ruff, Z.; Coates, C. S.; Märker, K.; Mahadevegowda, A.; Xu, C.; Penrod, M. E.; Ducati, C.; Grey, C. P. O3 to O1 Phase Transitions in Highly Delithiated NMC811 at Elevated Temperatures. *Chem. Mater.* **2023**, *35*, 4979−4987.
(40) Wang, C.; Zhang, R.; Kisslinger, K.; Xin, H. L. Atomic-Scale Observation of O1 Faulted Phase-Induced Deactivation of $LiNiO_2$ at High Voltage. *Nano Lett.* **2021**, *21*, 3657−3663.
(41) Sadowski, M.; Koch, L.; Albe, K.; Sicolo, S. Planar Gliding and Vacancy Condensation: The Role of Dislocations in the Chemo-

https://doi.org/10.1021/acs.chemmater.3c02727
Chem. Mater. XXXX, XXX, XXX−XXX

mechanical Degradation of Layered Transition-Metal Oxides. *Chem. Mater.* **2023**, *35*, 584−594.
(42) Dreyer, S. L.; Kondrakov, A.; Janek, J.; Brezesinski, T. In Situ Analysis of Gas Evolution in Liquid- and Solid-Electrolyte-Based Batteries with Current and Next-Generation Cathode Materials. *J. Mater. Res.* **2022**, *37*, 3146−3168.
(43) Salomez, B.; Grugeon, S.; Armand, M.; Tran-Van, P.; Laruelle, S. Review—Gassing Mechanisms in Lithium-Ion Battery. *J. Electrochem. Soc.* **2023**, *170*, 050537.
(44) Renfrew, S. E.; McCloskey, B. D. Residual Lithium Carbonate Predominantly Accounts for First Cycle CO_2 and CO Outgassing of Li-Stoichiometric and Li-Rich Layered Transition-Metal Oxides. *J. Am. Chem. Soc.* **2017**, *139*, 17853−17860.
(45) Hatsukade, T.; Schiele, A.; Hartmann, P.; Brezesinski, T.; Janek, J. Origin of Carbon Dioxide Evolved during Cycling of Nickel-Rich Layered NCM Cathodes. *ACS Appl. Mater. Interfaces* **2018**, *10*, 38892−38899.
(46) Freiberg, A. T. S.; Sicklinger, J.; Solchenbach, S.; Gasteiger, H. A. Li_2CO_3 Decomposition in Li-Ion Batteries Induced by the Electrochemical Oxidation of the Electrolyte and of Electrolyte Impurities. *Electrochim. Acta* **2020**, *346*, 136271.
(47) Sicklinger, J.; Metzger, M.; Beyer, H.; Pritzl, D.; Gasteiger, H. A. Ambient Storage Derived Surface Contamination of NCM811 and NCM111: Performance Implications and Mitigation Strategies. *J. Electrochem. Soc.* **2019**, *166*, A2322−A2335.
(48) Fang, Z.; Confer, M. P.; Wang, Y.; Wang, Q.; Kunz, M. R.; Dufek, E. J.; Liaw, B.; Klein, T. M.; Dixon, D. A.; Fushimi, R. Formation of Surface Impurities on Lithium-Nickel-Manganese-Cobalt Oxides in the Presence of CO_2 and H_2O. *J. Am. Chem. Soc.* **2021**, *143*, 10261−10274.
(49) Streich, D.; Erk, C.; Guéguen, A.; Müller, P.; Chesneau, F.-F.; Berg, E. J. Operando Monitoring of Early Ni-Mediated Surface Reconstruction in Layered Lithiated Ni-Co-Mn Oxides. *J. Phys. Chem. C* **2017**, *121*, 13481−13486.
(50) Wandt, J.; Freiberg, A. T. S.; Ogrodnik, A.; Gasteiger, H. A. Singlet Oxygen Evolution from Layered Transition Metal Oxide Cathode Materials and Its Implications for Lithium-Ion Batteries. *Mater. Today* **2018**, *21*, 825−833.
(51) Metzger, M.; Walke, P.; Solchenbach, S.; Salitra, G.; Aurbach, D.; Gasteiger, H. A. Evaluating the High-Voltage Stability of Conductive Carbon and Ethylene Carbonate with Various Lithium Salts. *J. Electrochem. Soc.* **2020**, *167*, 160522.
(52) Metzger, M.; Marino, C.; Sicklinger, J.; Haering, D.; Gasteiger, H. A. Anodic Oxidation of Conductive Carbon and Ethylene Carbonate in High-Voltage Li-Ion Batteries Quantified by On-Line Electrochemical Mass Spectrometry. *J. Electrochem. Soc.* **2015**, *162*, A1123−A1134.
(53) Jung, R.; Metzger, M.; Maglia, F.; Stinner, C.; Gasteiger, H. A. Chemical versus Electrochemical Electrolyte Oxidation on NMC111, NMC622, NMC811, LNMO, and Conductive Carbon. *J. Phys. Chem. Lett.* **2017**, *8*, 4820−4825.
(54) Misiewicz, C.; Lundström, R.; Ahmed, I.; Lacey, M. J.; Brant, W. R.; Berg, E. J. Online Electrochemical Mass Spectrometry on Large-Format Li-Ion Cells. *J. Power Sources* **2023**, *554*, 232318.
(55) Lundström, R.; Berg, E. J. Design and Validation of an Online Partial and Total Pressure Measurement System for Li-Ion Cells. *J. Power Sources* **2021**, *485*, 229347.
(56) Dreyer, S. L.; Kurzhals, P.; Seiffert, S. B.; Müller, P.; Kondrakov, A.; Brezesinski, T.; Janek, J. The Effect of Doping Process Route on $LiNiO_2$ Cathode Material Properties. *J. Electrochem. Soc.* **2023**, *170*, 060530.
(57) Oswald, S.; Gasteiger, H. A. The Structural Stability Limit of Layered Lithium Transition Metal Oxides Due to Oxygen Release at High State of Charge and Its Dependence on the Nickel Content. *J. Electrochem. Soc.* **2023**, *170*, 030506.
(58) Kaufman, L. A.; McCloskey, B. D. Surface Lithium Carbonate Influences Electrolyte Degradation via Reactive Oxygen Attack in Lithium-Excess Cathode Materials. *Chem. Mater.* **2021**, *33*, 4170−4176.
(59) Kim, A.-Y.; Strauss, F.; Bartsch, T.; Teo, J. H.; Hatsukade, T.; Mazilkin, A.; Janek, J.; Hartmann, P.; Brezesinski, T. Stabilizing Effect of a Hybrid Surface Coating on a Ni-Rich NCM Cathode Material in All-Solid-State Batteries. *Chem. Mater.* **2019**, *31*, 9664−9672.
(60) Busca, G.; Lorenzelli, V. Infrared Spectroscopic Identification of Species Arising from Reactive Adsorption of Carbon Oxides on Metal Oxide Surfaces. *Mater. Chem.* **1982**, *7*, 89−126.
(61) Kong, F.; Liang, C.; Wang, L.; Zheng, Y.; Perananthan, S.; Longo, R. C.; Ferraris, J. P.; Kim, M.; Cho, K. Kinetic Stability of Bulk $LiNiO_2$ and Surface Degradation by Oxygen Evolution in $LiNiO_2$-Based Cathode Materials. *Adv. Energy Mater.* **2019**, *9*, 1802586.
(62) Genreith-Schriever, A. R.; Banerjee, H.; Menon, A. S.; Bassey, E. N.; Piper, L. F. J.; Grey, C. P.; Morris, A. J. Oxygen Hole Formation Controls Stability in $LiNiO_2$ Cathodes. *Joule* **2023**, *7*, 1623−1640.
(63) Kaufman, L. A.; Huang, T.-Y.; Lee, D.; McCloskey, B. D. Particle Surface Cracking Is Correlated with Gas Evolution in High-Ni Li-Ion Cathode Materials. *ACS Appl. Mater. Interfaces* **2022**, *14*, 39959−39964.
(64) Su, C.-C.; He, M.; Amine, R.; Chen, Z.; Yu, Z.; Rojas, T.; Cheng, L.; Ngo, A. T.; Amine, K. Unveiling Decaying Mechanism through Quantitative Structure-Activity Relationship in Electrolytes for Lithium-Ion Batteries. *Nano Energy* **2021**, *83*, 105843.
(65) Garcia, J. C.; Bareño, J.; Yan, J.; Chen, G.; Hauser, A.; Croy, J. R.; Iddir, H. Surface Structure, Morphology, and Stability of $Li(Ni_{1/3}Mn_{1/3}Co_{1/3})O_2$ Cathode Material. *J. Phys. Chem. C* **2017**, *121*, 8290−8299.
(66) Dose, W. M.; Temprano, I.; Allen, J. P.; Björklund, E.; O'Keefe, C. A.; Li, W.; Mehdi, B. L.; Weatherup, R. S.; De Volder, M. F. L.; Grey, C. P. Electrolyte Reactivity at the Charged Ni-Rich Cathode Interface and Degradation in Li-Ion Batteries. *ACS Appl. Mater. Interfaces* **2022**, *14*, 13206−13222.
(67) Stephens, P. W. Phenomenological Model of Anisotropic Peak Broadening in Powder Diffraction. *J. Appl. Crystallogr.* **1999**, *32*, 281−289.
(68) Berkes, B. B.; Jozwiuk, A.; Sommer, H.; Brezesinski, T.; Janek, J. Simultaneous Acquisition of Differential Electrochemical Mass Spectrometry and Infrared Spectroscopy Data for In Situ Characterization of Gas Evolution Reactions in Lithium-Ion Batteries. *Electrochem. Commun.* **2015**, *60*, 64−69.
(69) Berkes, B. B.; Jozwiuk, A.; Vračar, M.; Sommer, H.; Brezesinski, T.; Janek, J. Online Continuous Flow Differential Electrochemical Mass Spectrometry with a Realistic Battery Setup for High-Precision, Long-Term Cycling Tests. *Anal. Chem.* **2015**, *87*, 5878−5883.

https://doi.org/10.1021/acs.chemmater.3c02727
Chem. Mater. XXXX, XXX, XXX−XXX

3.3 Publication III: Decoupling Substitution Effects from Defects in Ni-rich CAMs

Publication III describes the transfer of findings from studying IE-LNO to the related Ni-rich NCM materials. A series of samples with varying nickel contents from 88-100 mol% were synthesized *via* solid-state synthesis of the parent sodium NCMs and subsequent ion exchange in molten salt. During ion exchange, Na-NCM synthesized at 700 °C does not fully react due to its large primary particle size. Therefore, the anti-sintering-based size tailoring, developed in Publication II, was exploited to obtain samples with comparable grain sizes throughout the study. The obtained IE-NCM materials were studied by galvanostatic charge/discharge and *operando* XRD during the first cycle. The results implicate a stabilizing effect of substituting nickel with manganese and cobalt, because the abrupt unit-cell parameter change becomes smoother and changes to solid-solution behavior for IE-NCM with 88 mol% nickel. Regarding the lithium diffusion, transition-metal substitution causes loss of capacity due to kinetic hindrance, which is assigned to pinning of lithium vacancies, particularly by manganese introduction, as corroborated by DFT simulations.

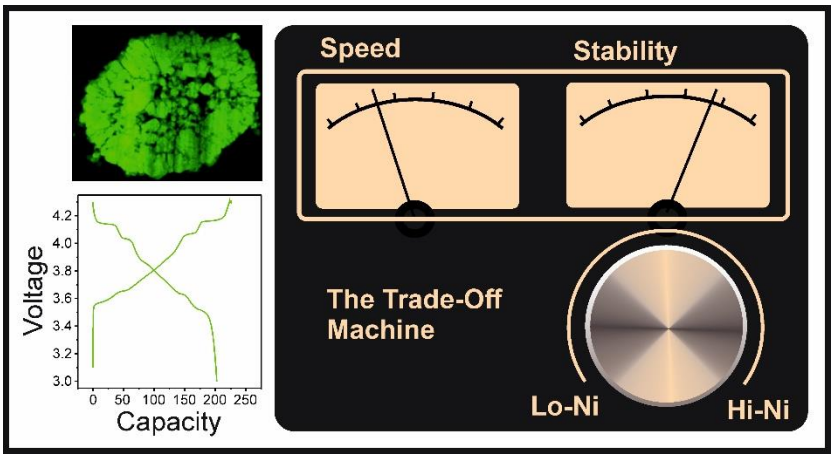

Figure 9. Graphical table of content of publication III [313].

The experiments were planned and designed by the first author under the supervision of A. Kondrakov, J. Janek and T. Brezesinski. The first author developed and optimized the size-tailoring methods for sodium NCMs and carried out the ion exchange procedures. The first author carried out the electrochemical experiments and data analysis. S. Korneychuk performed the TEM investigation and interpreted the results together with the first author. S. Sicolo performed DFT calculations according to the hypothesis from the experimental results and discussed the results with the first author. H. Li performed MAS NMR spectroscopy experiments under the supervision of S. Indris and discussed the results with the first author. W. van den Bergh carried out some syntheses of large sodium NCM particles. R. Zhang conducted the SEM experiments, and the data were analyzed by the first author. The manuscript was written by the first author and edited by all coauthors.

Submitted Manuscript of Publication III

Decoupling Substitution Effects from Point Defects in Layered Ni-rich Oxide Cathode Materials for Lithium-ion Batteries

Leonhard Karger,[a] Svetlana Korneychuk,[b,c] Sabrina Sicolo,[d] Hang Li,[e,†] Wessel van den Bergh,[a] Ruizhuo Zhang,[a] Sylvio Indris,[e] Aleksandr Kondrakov,[a,d] Jürgen Janek[a,f,*] and Torsten Brezesinski[a,*]

[a] L. Karger, W. van den Bergh, R. Zhang, A. Kondrakov, J. Janek, T. Brezesinski

Battery and Electrochemistry Laboratory (BELLA), Institute of Nanotechnology, Karlsruhe Institute of Technology (KIT), Herrmann-von-Helmholtz-Platz 1, 76344 Eggenstein-Leopoldshafen, Germany

E-mail: juergen.janek@kit.edu, torsten.brezesinski@kit.edu

[b] S. Korneychuk

Institute of Nanotechnology, Karlsruhe Institute of Technology (KIT), Herrmann-von-Helmholtz-Platz 1, 76344 Eggenstein-Leopoldshafen, Germany

[c] S. Korneychuk

Karlsruhe Nano Micro Facility (KNMFi), Karlsruhe Institute of Technology (KIT), Herrmann-von-Helmholtz-Platz 1, 76344 Eggenstein-Leopoldshafen, Germany

[d] S. Sicolo, A. Kondrakov

BASF SE, Carl-Bosch-Str. 38, 67056 Ludwigshafen, Germany

[e] H. Li, S. Indris

Institute for Applied Materials – Energy Storage Systems (IAM-ESS), Karlsruhe Institute of Technology (KIT), Hermann-von-Helmholtz-Platz 1, 76344 Eggenstein-Leopoldshafen, Germany

J. Janek

[f] Institute of Physical Chemistry & Center for Materials Research (ZfM/LaMa), Justus-Liebig-University Giessen, Heinrich-Buff-Ring 17, 35392 Giessen, Germany

† Current Affiliation: School of Advanced Materials, Peking University, Shenzhen Graduate School, Shenzhen 518055, China

Keywords: Ni-rich cathode, first-cycle capacity loss, ion exchange, point defects

Abstract: Ni-rich $LiNi_xCo_yMn_zO_2$ cathode materials offer high practical capacities and good rate capability, but are notorious for being unstable at high state of charge. Here, a series of such layered oxides with nickel contents ranging from 88 to 100 mol% was fabricated by sodium-to-lithium ion exchange, yielding materials devoid of $Ni_{Li}^{\bullet}$ substitutional defects. Examining the initial charge/discharge cycle reveals effects that are specifically caused by transition-metal substitution, which would otherwise be obscured by changes in lithium-site defect concentration. Lowering the nickel content helps to stabilize the high-voltage regime while simultaneously adversely affecting lithium diffusion. *Operando* X-ray diffraction indicates mitigation of volume variation during cycling and transition towards solid-solution behavior with sufficiently high cobalt and manganese contents, thus providing an explanation for the increased stability. The interplay between transition-metal substitution, kinetic hindrance, and solid-solution behavior may be a result of local inhomogeneities due to lithium-vacancy pinning, which was further elucidated through density functional theory calculations. Overall, this work sheds new light on the effects of manganese and cobalt incorporation into the transition-metal layer and their conjunction with $Ni_{Li}^{\bullet}$ defects.

Introduction

Ni-rich cathode active materials (CAMs) of $LiNi_xCo_yMn_zO_2$ (NCM/NMC) or $LiNi_xCo_yAl_zO_2$ (NCA) type are at the forefront of commercial high-energy-density lithium-ion batteries (LiBs).[1] Although similar capacities can be achieved with different generations of NCMs, increasing the nickel content lowers the cutoff potential at which high specific capacities (> 200 mAh/g) are attainable.[2] However, these Ni-rich CAMs, and particularly $LiNiO_2$ (LNO), are notorious for their instability, especially due to degradation at high state of charge (SOC). The latter has been linked to mechanical degradation resulting from anisotropic volume changes, oxygen release, and surface degradation upon cycling.[3–10]

Intrinsic to all Ni-rich NCMs produced by solid-state synthesis are $Ni_{Li}^{\bullet}$ substitutional defects, sometimes also termed off-stoichiometry, lithium deficiency,[11,12] or “Ni/Li intermixing”, referring to antisite defects, which can occur in the presence of manganese but not in close-to-stoichiometric LNO.[13,14] The origin of these defects lies in the similar ionic radii of Ni^{2+} (r = 0.69 Å) and Li^{+} (r = 0.76 Å),[15] along with the need for strongly oxidizing conditions, causing incomplete layer separation.[16,17] For charge compensation, each $Ni_{Li}^{\bullet}$ defect is accompanied by the presence of a reduced nickel cation in the transition-metal layer, which according to Kröger-Vink notation is represented by Ni_{Ni}'.[18] However, hereafter, for simplicity we only mention $Ni_{Li}^{\bullet}$ when referring to the combination of $Ni_{Li}^{\bullet}$ and Ni_{Ni}' defects.

The extent to which these point defects occur is related to the chemical composition. For example, upon increasing the nickel content from 80 to 100 mol% in the solid solution $LiNi_xCo_yO_2$, Delmas *et al.* found an increase in lithium deficiency from 6 to

10%.[12] Although improvements have been made to the calcination protocols, such that even $Ni_{Li}^{\bullet}$ defect concentrations as low as 1.6% are accessible by conventional solid-state synthesis,[19,20] the problem of convolution of Ni-site substitution with cobalt, manganese, or other metal species with changes in the fraction of $Ni_{Li}^{\bullet}$ defects persists. This makes the correlation between transition-metal-site substitution (or doping) and diffusion properties (kinetics) ambiguous, as the effects seen may also originate from differences in $Ni_{Li}^{\bullet}$ concentration.[12] For example, Manthiram *et al.* faced this problem when studying individual effects of modifying LNO with 5% of cobalt, manganese, or aluminum. They found poor diffusivity after manganese incorporation and fast lithium diffusion in the case of cobalt, which increases and decreases the fraction of $Ni_{Li}^{\bullet}$ defects, respectively.[21] Therefore, it is experimentally very challenging to separate substitution effects in the transition-metal site from those induced by $Ni_{Li}^{\bullet}$ defects.[22] Nevertheless, understanding the individual contributions to key properties, such as lithium diffusion, lattice parameter changes, and (electro-)chemical stability, independent of other factors, such as particle size or $Ni_{Li}^{\bullet}$ defects, is crucial for designing new generations of advanced CAMs. Especially with the emergence of single-crystalline cathodes for improving stability and tap density, the search for sufficiently fast lithium diffusion (mobility) gains momentum.[23–26]

Herein, we attempt to separate the contribution due to cobalt and manganese substitution from $Ni_{Li}^{\bullet}$ defects by employing a recently developed ion-exchange synthesis, yielding $Ni_{Li}^{\bullet}$-free CAM.[27,28] Specifically, a series of NCM materials with varying nickel content was synthesized by sodium-to-lithium ion exchange with the objective to prevent $Ni_{Li}^{\bullet}$ defect formation. Substitution with cobalt and manganese helps to stabilize the high-voltage regime by smoothening the structural transition at high SOC and lowering the overall volume variation. However, there is a trade-off, as lowering the nickel content proves detrimental to the lithium diffusion, causing capacity loss due to incomplete relithiation of CAM. With regards to first-cycle efficiency, ion-exchanged NCM95 (with Ni:Co:Mn molar ratio of 95:4:1) is found to exhibit the lowest cumulative capacity loss among all materials tested in this work.

Results and Discussion

The ion-exchange method relies on a perfectly layered “parent” sodium metal oxide. In the case of LNO, this material is $NaNiO_2$ (NNO), which adopts a distorted (monoclinic) *C*2/*m* phase at room temperature. In contrast, $NaNi_xCo_yMn_zO_2$ (Na-NCM) materials with $x \leq 0.8$ have been reported to adopt an *R*−3*m* structure.[29] The synthesis of Ni-rich Na-NCMs is conducted according to an adaption of a previously reported method.[27] In short, co-precipitated hydroxide precursor CAM (pCAM) particles and NaOH are heated at 300 °C in oxygen atmosphere to remove crystal water and improve wetting, followed by calcination of the premix at 700 °C.

Sodium Trapping in Single-Crystalline, Ion-Exchanged NCM

The as-synthesized Na-NCM90 (with Ni:Co:Mn molar ratio of 90:5:5) was investigated by powder X-ray diffraction (PXRD), as shown in **Figure 1a**. Corresponding structural parameters determined by Rietveld refinement analysis are given in **Table 1**. PXRD indicates the presence of two phases with space groups *C*2/*m* and *R*−3*m* in a ratio of 84:16 by weight. The structural parameters of the individual phases agree with those reported in the literature (see **Table 1**).[27,30] However, *β* is slightly smaller compared to NNO, and the *a* and *b* lattice parameters of the monoclinic phase are decreased and increased, respectively. As has been published for Co-doping of NNO, for example, this is indicative of less monoclinic distortion with transition-metal substitution.[31] Therefore, the presence of two phases is not necessarily a sign of separation into Na-NCM and NNO, but rather suggests local inhomogeneities. With regards to the hexagonal phase of Na-NCM90, we find an overall larger unit-cell volume compared to Na-NCM85 (reference from literature).[30]

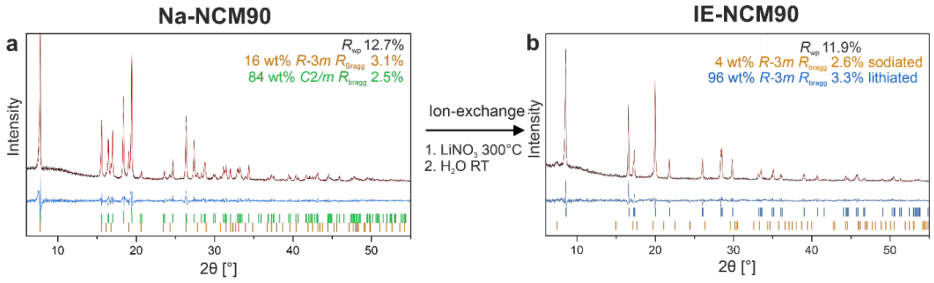

Figure 1. PXRD patterns and Rietveld refinement plots for (a) Na-NCM90 and (b) IE-NCM90.

Table 1. Structural parameters determined by Rietveld refinement for Na-NCM90, NNO, Na-NCM811, and IE-NCM90.

Sample	Phase	wt.%	R_{wp} [%]	R_{Bragg} [%]	*a* [Å]	*b* [Å]	*c* [Å]	*β* [°]	*V* [Å^3]
Na-NCM90	*C*2/*m*	84	12.7	3.1	5.2847(3)	2.8536(2)	5.5686(4)	110.100(9)	78.86(1)
	R−3*m*	16		2.5	2.9510(4)	-	15.7024(56)	-	118.42(5)
NNO[27]	*C*2/*m*	100	-	2. 7	5.3173(1)	2.8424(1)	5.5789(1)	110.485(1)	78.99(1)
Na-NCM811[30]	*R*−3*m*	100	12.6	-	2.9309(1)	-	15.776(8)	-	117.36(7)
IE-NCM90	*R*−3*m*	96	11.9	3.3	2.8763(2)	-	14.1915(10)	-	101.68(1)
	R−3*m*	4		2.6	2.8617(15)	-	16.3245(333)	-	115.77(47)

Next, the Na-NCM90 was subject to ion exchange and probed again using PXRD. As shown in **Figure 1b**, two phases are observed, both of which can be indexed to the *R*−3*m* space group. The main phase corresponds to the ion-exchanged material (IE-

NCM90), and the lattice parameters agree well with literature results for IE-NCM and NCM obtained from solid-state synthesis.[29,32] The second phase exhibits a peak at the 003 (*R*−3*m*) or 001 position (*C*2/*m*) of Na-NCM90, and we therefore assign it to sodium-containing (only partially ion-exchanged) domains, likely located in the particle bulk. However, the interlayer spacing is slightly expanded compared to the parent material, which agrees with our previous *in situ* analysis of the reaction mechanism.[27] The refined weight ratio of these two phases is 95:5, indicating incomplete conversion when using Na-NCM90 as the precursor. This could be a result of too large a size of the primary particles (grains) and sodium trapping due to poor diffusion.

The morphology and structural attributes of the as-synthesized IE-NCM90 were studied by (scanning) transmission electron microscopy [(S)TEM] of a focused-ion beam (FIB)-cut lamella. The high angle annular dark field (HAADF) image in **Figure 2a** reveals the presence of monolithic particles with sizes ranging from 1 to 8 µm in diameter. Some particles show signs of cracking, which appears to occur parallel to the sodium/lithium layer, as can be seen from **Figure 2b**, **c**, **h**, **i**. Small (~1 µm, see **Figure 2b**-**g**) and large particles (~8 µm, **Figure 2h**-**m**) were examined by energy-dispersive X-ray spectroscopy (EDS). Those imaged in **Figure 2** reveal a uniform distribution of nickel and cobalt, while manganese is present in the bulk but also segregates at the surface. This could be due to formation of Mn^{4+} during the pre-annealing. Because of the high oxidation state, Mn^{4+} is expected to diffuse slower in a solid-state reaction. In the following, the atmosphere in this step of the synthesis was thus changed from oxygen to argon. In the large particle, residual sodium is clearly observed by EDS, which is not evenly distributed in the bulk but is present in enriched domains of several hundred nanometers in size. Within such a domain, layer bending is apparent, as can be seen in **Figure 2i.** This is probably a result of high strain due to co-presence of lithium and sodium in adjacent phases. These sodium-enriched domains are likely visible—in the form of the 5% impurity phase—in the PXRD pattern in **Figure 1b**. Contrary to previous findings on IE-LNO particles, no cracking parallel to the stacking direction is observed.[27] This points towards an increase in mechanical stability resulting from the transition-metal substitution. The small particle, on the other hand, also contains some residual sodium. As evident from **Figure 2g**, it is located within a small volume fraction of the particle. This means that the bulk is largely free of sodium, and further suggests that smaller particles allow for more efficient sodium-to-lithium ion exchange.[28]

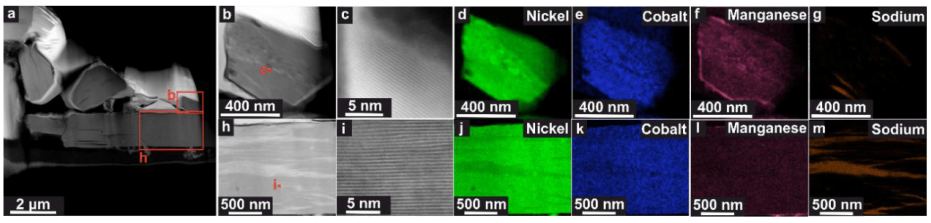

Figure 2. (S)TEM analysis of FIB-prepared IE-NCM90 with areas probed by EDS indicated by red rectangles in (a). (b, h) Higher-magnification HAADF images of the regions of interest, and (c, i) high-resolution TEM images of the areas highlighted in

red in panels (b) and (h). (d-g, j-m) EDS maps for nickel, cobalt, manganese, and sodium.

IE-NCM90 was also tested electrochemically in LIB half-cells at C/10 rate in the potential window of 3.0-4.3 V vs. Li^+/Li (see **Figure S1**, Supporting Information). Specific capacities of q_{ch} = 209 mAh/g_{CAM} and q_{dis} = 163 mAh/g_{CAM} were achieved, similar to literature results for IE-NCM85,[29] but much lower than expected from a Ni-rich NCM.[32] For increasing the specific capacity, the residual sodium within the structure, which is connected to the particle size, needs to be eliminated from the CAM. This can likely be achieved by lowering the particle size and reducing the sodium diffusion path lengths, as we have shown recently for size-tailored IE-LNO.[28]

Full Ion Exchange by Reducing Grain Size

The particle size of layered oxide CAMs can be reduced by addition of surface segregating species, such as ammonium paratungstate.[28,33,34] Here, 2 mol% were added to prevent the growth/sintering of Na-NCM grains. The tungsten-doped sample (Na-NCM90-W) also consists of two phases with space groups *C*2/*m* and *R*−3*m* in a ratio of 20:80 by weight (see Rietveld refinement results in **Table S1**, Supporting Information), thus being less Jahn-Teller distorted than Na-NCM90. This points towards introduction of tungsten into the bulk structure, leading to an overall larger fraction of the hexagonal phase. After ion exchange, we find 0.52 mol% tungsten relative to the sum of the other transition metals by inductively coupled plasma-optical emission spectroscopy (ICP-OES), as shown in **Table 2**. From this result, it can be concluded that the majority of tungsten segregates on the particle surface and is removed during the ion-exchange process.

Structural analysis of Na-NCM90-W revealed the presence of a single phase with *R*−3*m* space group; the Rietveld refinement results are given in **Table 3**. The parameters indicate good layering with a slightly larger unit-cell volume than reported in the literature,[2] which could be due to the residual sodium. Indeed, Rietveld analysis suggests 2.4% $\mathrm{Na}_{\mathrm{Li}}^{\times}$ defects, while the sodium content determined by ICP-OES is only 1.2 mol%. This is in agreement with previously reported data on tungsten-based size tailoring, indicating apparently increased electron density in the lithium slab, an effect likely caused by rock salt-type surface layer formation due to tungsten doping.[28] Overall, these results are indicative of a phase-pure material, as opposed to that obtained after ion exchange of the much larger Na-NCM90 particles.

Nickel Concentration Series – Microstructural Analysis

A series of IE-NCMs with nickel contents ranging from 88 to 100 mol% was synthesized by means of tungsten-based size tailoring. Hereafter, the samples are referred to as IE-LNO-W, IE-NCM95-W, IE-NCM90-W, and IE-NCM88-W for 100, 95, 90, and 88 mol% nickel content, respectively. The materials were probed using PXRD and ICP-

OES, and the corresponding results are shown in **Tables 2** and **3**. All materials crystallize in the *R*−3*m* space group and are obtained in single-phase form. They exhibit similar lattice parameters and unit-cell volume (with some minor increase with decreasing nickel content). IE-LNO-W also follows this trend, but the *c* lattice parameter is smaller, with ~14.18 Å compared to ~14.20 Å for the IE-NCM-W materials. This could be related to the relatively low residual sodium content, providing less pillaring to uphold the increased interlayer spacing from the parent NNO phase. However, by ICP-OES, we find 1.2 mol% sodium in IE-LNO-W and 1.2-1.9 mol% in the IE-NCM-W materials, indicating that Rietveld refinement systematically overestimates the residual sodium content. The lithium content is ~93 mol% for all samples, suggesting some lithium loss during the ion-exchange procedure, most likely upon water washing, which is known to have a more deleterious effect with increasing nickel content. Chemical oxidation of the samples during ion exchange could be a reason too. However, this would be evident from nuclear magnetic resonance (NMR) spectroscopy experiments and has not been observed previously.[27] Lastly, some of the lithium loss may also be due to formation of rock salt-type surface impurities upon tungsten addition.[28]

Table 2. Results from ICP-OES (normalized to the cumulative amount of nickel, cobalt, and manganese).

Sample	Li [%]	Na [%]	Ni [%]	Co [%]	Mn [%]	W [%]	O [%]
IE-LNO-W	93.1	1.2	100	0	0	0.40	208.5
IE-NCM95-W	92.9	1.9	93.5	4.5	2.0	0.50	219.1
IE-NCM90-W	93.2	1.2	90.1	4.9	5.0	0.52	217.7
IE-NCM88-W	93.7	1.4	87.3	4.7	8.0	1.06	219.2

Table 3. Structural parameters determined by Rietveld refinement for IE-LNO-W, IE-NCM95-W, IE-NCM90-W, and IE-NCM88-W.

Sample	Phase	wt.%	R_{wp} [%]	R_{Bragg} [%]	*a* [Å]	*c* [Å]	*V* [Å^3]	$Na_{Li}^{\times}$
IE-LNO-W	*R*−3*m*	100	16.3	3.7	2.8775(12)	14.1768(156)	101.679(150)	3.8(22)
IE-NCM95-W	*R*−3*m*	100	20.3	4.2	2.8775(4)	14.2023(12)	101.836(45)	3.7(32)
IE-NCM90-W	*R*−3*m*	100	12.9	3.3	2.8778(3)	14.1992(25)	101.837(30)	2.4(26)
IE-NCM88-W	*R*−3*m*	100	11.7	2.1	2.8789(2)	14.2094(9)	102.055(20)	4.0(7)

To gain insight into the elemental distribution in the size-tailored materials, IE-NCM88-W was examined by TEM. The results obtained are shown in **Figure 3**. The imaging data indeed reveal a polycrystalline morphology, with the secondary particles appearing less dense in the center (see **Figure 3a**). As can be seen from the higher-magnification HAADF images in **Figure 3b**, **c**, the grain (primary particle) size is on the

order of 50-400 nm. Regarding elemental distribution (see **Figure 3d**, **e**, **g**, **h**, **j**, **l**), the altered pre-annealing atmosphere seems effective in mitigating manganese segregation near the primary particle surface. Nevertheless, regions of higher concentration are still visible. Similarly, tungsten appears to be locally concentrated in some of the particles. The presence of small amounts of sodium is also apparent but not in the form of domains, as observed for IE-NCM90. Lithium localization was achieved by electron energy loss spectroscopy (EELS) mapping, see **Figure 3k**, **l**, suggesting uniform distribution throughout the primary grains. However, the specific grain examined was located in the center of the secondary particle and thus may not have been exposed to water during the washing step after ion exchange. High-resolution TEM analysis (see **Figure 3 f**, **i**, **m**) further indicates that the surfaces oriented parallel to the stacking direction are more disordered (~5 nm thick layer) than those oriented parallel to the layering direction. This may suggest preferential migration of tungsten depending on the crystal facet. However, the observed amorphization could also be related to damage induced by the electron beam.

Overall, the TEM results provide evidence that size tailoring is effective in removing sodium from the lattice and corroborate the ICP-OES and PXRD data. Furthermore, they demonstrate that changing the pre-annealing atmosphere from oxygen to argon is beneficial for improving the distribution of transition-metal species. The location of tungsten could not be conclusively analyzed, but the formation of a disordered surface layer points towards preferential accumulation at the surfaces oriented parallel to the stacking direction.

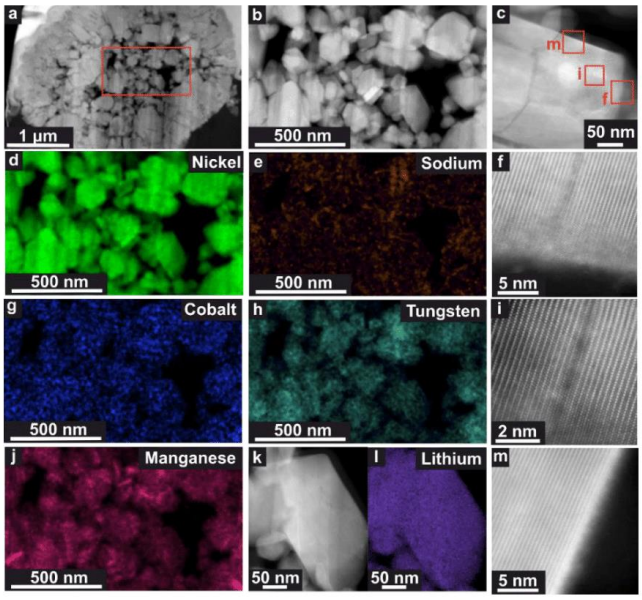

Figure 3. (S)TEM analysis of FIB-prepared IE-NCM88-W with the area probed by EDS indicated by a red rectangle in (a). (b) Higher-magnification HAADF image of the region of interest and (d, e, g, h, j) corresponding EDS maps for nickel, sodium, cobalt,

tungsten, and manganese. (c) HAADF image of a single grain with the areas probed by high-resolution TEM (f, i, m) indicated by red rectangles. (k) HAADF image of primary particles used for EELS mapping of lithium (l).

NMR Spectroscopy

The samples were also probed by ^{7}Li magic-angle spinning (MAS) NMR spectroscopy (see **Figure 4**). Compared to the spectrum of large-sized IE-LNOs,[27] the size-tailored IE-LNO-W reveals several distinct lithium environments. The most pronounced peak centered at 702 ppm is relatively narrow and no signal is detected beyond 800 ppm, evidencing the $Ni_{Li}^{\bullet}$-free nature of material.[27] Additional smaller and shoulder peaks are visible at 640, 665, 734, and 795 ppm. Also, clusters of peaks are observed at 487 and 511 ppm. Recently, the presence of twin and antiphase boundaries has been associated with peaks in that region.[35] Specifically, the shifts that were calculated to be in the ranges 542-690 ppm, 794-954 ppm, and 484-590 ppm for lithium atoms located away, close to, and at the antiphase boundary, respectively, agree well with the aforementioned additional peaks. Furthermore, the presence of W^{6+} may cause charge compensation effects in the transition-metal substructure, thus leading to Ni^{2+} formation. This would result in higher shifts, i.e., ppm values for the described lithium environments. Some of the signal could also originate from the disordered surface regions having high tungsten content or from tungsten substitution in the bulk structure. Nevertheless, the main signal displays no shift to higher ppm values, which would otherwise be characteristic of the presence of $Ni_{Li}^{\bullet}$ defects.[27,35,36]

With decreasing nickel content, the main peak becomes broadened, as expected due to the multiple Ni/Mn/Co environments (resulting in Ni^{2+} formation) around lithium. While for IE-NCM95-W, the peak pattern of the undoped material is still somewhat visible, it vanishes completely for the other two samples due to extreme peak broadening. Therefore, not much information can be gathered for both IE-NCM90-W and IE-NCM88-W by NMR spectroscopy other than the fact that the main peak position is shifting to lower ppm values for IE-NCM88-W (to ~665 ppm). Additionally, the spinning sideband of lithium residuals in diamagnetic environment at 710 ppm makes analysis more challenging.

Taken together, the data confirm the lack of $Ni_{Li}^{\bullet}$ defects for samples prepared by ion-exchange synthesis. A contribution to peak broadening may be structural disorder, i.e. variations in bond length/angle, induced by the additional transition metals (Co/Mn) or the grain size.[37] However, the materials also contain lithium in considerable amounts in defective sites, which are likely introduced by tungsten addition. A signal is observed at 0 ppm, which can be linked to diamagnetic lithium salts present on the particle surface.[38] Interestingly, for the IE-NCM-W CAMs, this signal increases with increasing degree of substitution. As shown in **Figure 5e**, the particle size decreases in the same direction and the specific surface area increases. Hence, variations in surface area could account for the increase in lithium residuals (originating from leaching upon water exposure during washing).

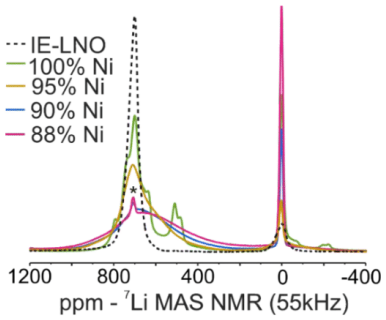

Figure 4. Normalized ^{7}Li MAS NMR spectra (55 kHz) of large-sized IE-LNO[27] and the IE-LNO/NCM-W samples. The spinning sideband of the 0 ppm peak is marked with an asterisk.

Morphology

The morphology of the ion-exchanged materials was investigated by scanning electron microscopy (SEM, see **Figure 5a**-**d**). Relatively small primary particles sizes in the range of d_{50} = 132-226 nm are observed for all samples (see **Figure 5e**). This finding corroborates the successful mitigation of sintering due to tungsten addition, as already described for IE-NCM88-W in **Figure 3**. The grain size decreases slightly with decreasing nickel content, which is likely related to reduced growth caused by the presence of cobalt and manganese. Regardless, the primary particle sizes are representative of those typically achieved in Ni-rich CAMs prepared by solid-state synthesis.[20,39] The degree of agglomeration, or in other words, the retention of the original polycrystalline morphology, differs between the samples. This seems to point towards higher mechanical stability of the secondary particle structure with lower nickel content, although IE-NCM-90-W does not perfectly fit this trend. Nevertheless, the particle sizes do not differ much among the polycrystalline samples, thus allowing for reasonable comparison of the electrochemical performance.

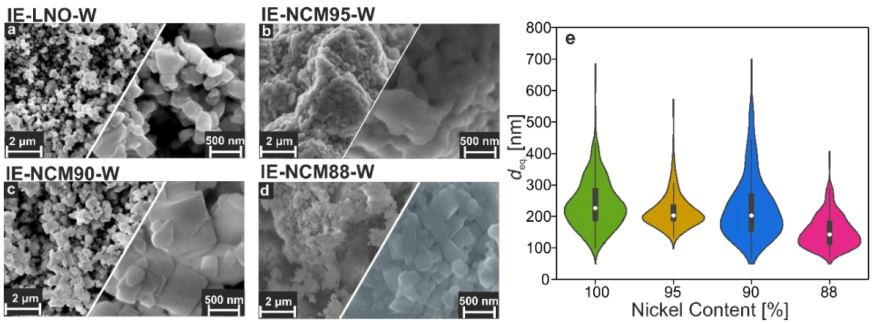

Figure 5. SEM images of (a) IE-LNO-W, (b) IE-NCM95-W, (c) IE-NCM90-W, and (d) IE-NCM88. (e) Corresponding size analysis (see Supporting Information for details).

Electrochemistry

The materials were electrochemically tested by galvanostatic cycling in LIB half-cells at C/10 rate in the potential window of 3.0-4.3 V vs. Li^+/Li. As can be seen from the first-cycle voltage profiles in **Figure 6a**-**d**, the specific charge capacities increase with decreasing nickel content, from q_{ch} = 200 mAh/g_{CAM} for IE-LNO-W to q_{ch} = 235 mAh/g_{CAM} for IE-NCM88-W. Similarly, the specific discharge capacities increase from q_{dis} = 173 mAh/g_{CAM} (IE-LNO-W) to 202 mAh/g_{CAM} (IE-NCM95-W), 183 mAh/g_{CAM} (IE-NCM90-W), and 199 mAh/g_{CAM} (IE-NCM88-W). Clearly, transition-metal substitution helps to increase the extractable charge. This may be due to the more reactive surface of LNO compared to the Ni-rich NCMs, causing more severe detrimental side reactions.[40] During water washing, LNO is known to undergo lithium-to-proton exchange, leading to some degradation of the material.[41] As mentioned above, ICP-OES analysis indicates lack of lithium, however independent of the nickel content. Since the extent of lithium deficiency is similar for the different CAMs, it is likely not responsible for the lower specific capacity of IE-LNO-W. Nevertheless, the stability of the partially protonated surface is expected to differ among the samples and is believed to cause capacity loss, specifically in the case of IE-LNO-W.

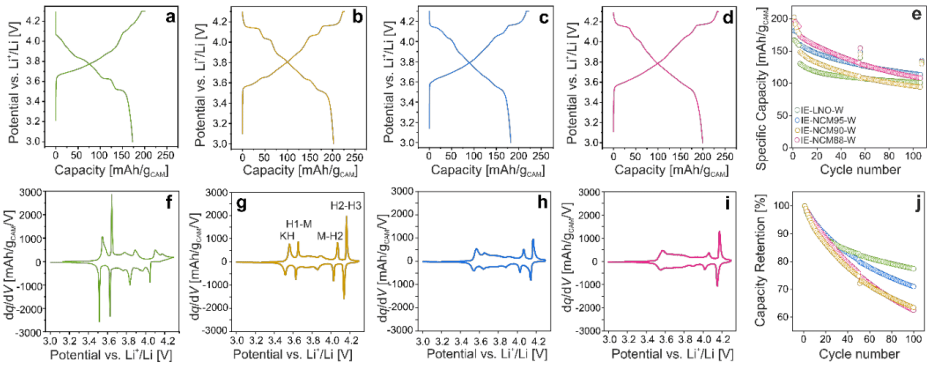

Figure 6. First-cycle voltage profiles and second-cycle differential capacity curves for (a, f) IE-LNO-W, (b, g) IE-NCM95-W, (c, h) IE-NCM90-W, and (d, i) IE-NCM88-W. (e) Long-term cycling performance with 5 cycles at C/10, 50 cycles at 1C charge and C/2 discharge, 1 cycle at C/10, and 50 cycles at 1C charge and C/2 discharge in the potential window of 3.0-4.3 V vs. Li^+/Li. (j) Capacity retention relative to the 6th cycle at 1C charge and C/2 discharge. Note that the 56th cycle at C/10 is omitted for clarity.

The first-cycle capacity loss does not show a linear relation with nickel content. Interestingly, IE-NCM95-W performs best, with only 24 mAh/g_{CAM} or 10.6% capacity loss, while the other materials exhibit losses exceeding 14%. The first-cycle loss was separated into kinetic hindrance and degradation at high potentials by aligning the charge and discharge curves in the region corresponding to $Li_{2/5}Ni_xCo_yMn_zO_2$, as shown in **Figure 7a**-**c**.[42] This phase is chosen specifically, as it is most clearly recognizable as a single-phase region in all of the first-cycle voltage profiles while being in a range that is likely more stable than the high-voltage H2 and H3 phases.

The results from this analysis are presented in **Figure 7d**. With decreasing nickel content, an increase in capacity loss due to kinetic hindrance is observed, from 2.5% in IE-LNO to 10.3% in IE-NCM88-W. This could be attributed to sluggish lithium diffusion in the bulk or degradation of the materials' surface. Regarding surface stability, the opposite trend would be expected from the available literature, as Ni-rich NCMs tend to release less lattice oxygen than LNO, suggesting that surfaces and interfaces are more stable/robust.[40] This, in turn, means that the degraded surface of LNO would add more to losses associated with lithium diffusion than that of a Ni-rich CAM. But, as indicated by (S)TEM of IE-NCM-88 in **Figure 3**, which is substituted most, manganese does not segregate at the surface if the pre-annealing step is performed in an inert atmosphere. The stability at high SOC follows the opposite trend. With decreasing nickel content, the reversibility in the high-voltage range increases. This observation agrees well with the increased surface stability of NCMs.[40] As for polarization, no differences that would be indicative of facilitated lithium diffusion at low potentials are observed with decreasing nickel content. In fact, polarization is more pronounced in the case of IE-LNO.

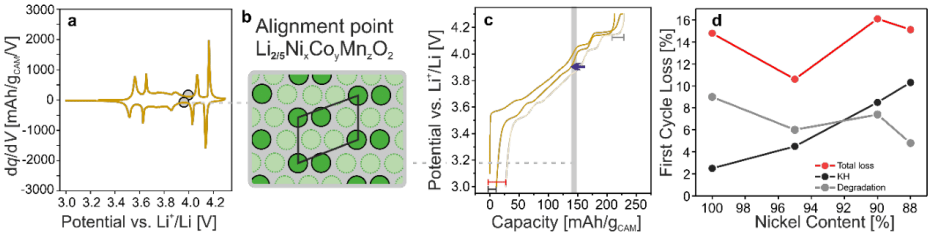

Figure 7. (a) Second-cycle differential capacity curve of IE-NCM95-W with indication of the alignment points. (b) Schematic representation of lithium/vacancy ordering in the phase corresponding to the alignment points. (c) Aligned first-cycle charge and discharge curves of IE-NCM95-W. (d) Results from first-cycle capacity loss analysis.

Trends in Stability, Diffusion, and Jahn-Teller Distortion

To gain more insight into the impact of cobalt and manganese substitution on lithium diffusion, the differential capacity (d*q*/d*V*) curves shown in **Figure 6f-i** were compared. The peaks seen for IE-LNO-W have previously been assigned to the same transitions occurring in LNO prepared by conventional solid-state synthesis,[27] and similar peaks are apparent for the IE-NCM-W samples. In short, when going from low to high potential, the observed peaks correspond to the so-called "kinetic hindrance" (KH), H1-M, M-H2, and H2-H3 transitions (see also **Figure 6g** for peak assignments). In the case of IE-LNO-W, the kinetic hindrance and H1-M transition are characterized by the presence of distinct peaks. However, the M-H2 and H2-H3 transitions appear broadened and shifted compared to IE-LNO. This may be caused by hysteresis at high SOC, which has been hypothesized to be due to sluggish (de-)lithiation of a surface rock salt-type phase.[43] The formation of such a phase could be facilitated by lithium-to-proton exchange, a process known to occur when subjecting LNO to water washing

(and subsequent thermal decomposition of the resulting NiO(OH) phase during drying of the electrode).[41] An alternative explanation for the increased polarization is provided by the theoretical work of Xiao *et al*. They hypothesize that lithium diffusion from the H2 phase into the H3 phase is rate limiting during charging, causing a nucleation barrier for the formation of (collapsed) NiO_2.[44] Specifically, the free surface is assumed to facilitate phase transitions by affecting Li-Li interactions. In a similar fashion, substitutional defects in the transition-metal site may also facilitate the H2-H3 transition, as indicated by the decrease in polarization. This observation falls in line with the emergence of solid-solution behavior (see below).

As evident from the data in **Figure 6**, the KH and H1-M peaks decrease with decreasing nickel content. This indicates slower lithium diffusion at the end of discharge, as well as a lowering in the degree of monoclinic distortion. The latter can be explained by reduced interplay between lithium/vacancy ordering and Jahn-Teller activity of Ni^{3+} ions.[42,45] Also, the lower nickel content and change in oxidation state caused by Mn^{4+} residing on the transition-metal site[46] contribute towards mitigating Jahn-Teller distortion. At high SOC, the peaks related to the M-H2 and H2-H3 transitions become more pronounced for IE-NCM95-W, and they are less shifted compared to those of IE-LNO-W. However, further increase in nickel content seems to broaden and diminish the H2-H3 peak. The M-H2 peak, on the other hand, clearly decreases with decreasing nickel content, similar to the H1-M peak, which is due to loss of Jahn-Teller active species and disruption of lithium/vacancy ordering, as explained above.

Regarding cycling stability (see **Figure 6e**, **j**), the polycrystalline samples, IE-NCM95-W and IE-NCM88-W, deliver the highest specific capacities, but also exhibit the most severe fading, which is likely caused by intergranular cracking. By contrast, the more isolated particles of IE-LNO-W and IE-NCM90-W deliver lower specific capacities, but cells using these materials show better capacity retention. No clear correlation between capacity or capacity retention and degree of substitution is observed, as the effects of processing likely outweigh the fine differences between the stoichiometries tested.

Overall, the results achieved by reducing the nickel content seem to be threefold. First, stabilization of the high-voltage regime is apparent, similar to conventionally synthesized NCM CAMs.[40] Second, slower lithium diffusion is observed upon decreasing the nickel content. This is somewhat surprising, as Manthiram *et al*. reported that manganese incorporation negatively affects lithium diffusion, while cobalt has a beneficial effect.[21] However, the authors commented on the possibility of variations in cation intermixing being the cause of differences in diffusivity. In the present work, the active materials do not contain any $Ni_{Li}^{\bullet}$ defects. Another factor that can affect the capacity in the KH region is primary particle (grain) size. The expected trend for this would be a decrease in capacity loss with decreasing size. However, the opposite is observed here. Therefore, an additional mechanism is believed to be responsible for the faster lithium diffusion with increasing nickel content. One explanation is pinning of lithium vacancies, which would slow down diffusion and has

been shown to occur in the vicinity of $Ni_{Li}^{\bullet}$ defects.[47] Lastly, the data indicate changes to the degree of monoclinic distortion, which may have several reasons. Loss of Jahn-Teller active species upon substituting nickel with cobalt and manganese and reduction of the average nickel oxidation state due to manganese incorporation are expected. Another reason could be the disruption of lithium/vacancy ordering due to pinning of lithium vacancies induced by the altered composition, as already mentioned with regards to the trends in lithium diffusion.

Operando XRD

Several factors were shown to contribute to the Coulomb efficiency in the first cycle. In short, a combination of kinetic hindrance and material degradation yields the overall capacity loss. For the kinetic hindrance, a clear inverse correlation with nickel content is observed (the higher the nickel content, the lower the KH loss), while the loss related to high-voltage degradation follows the opposite trend. For the CAMs studied here, IE-NCM95-W is found to exhibit the lowest first-cycle capacity loss.

To compare the structural evolution of IE-LNO-W, IE-NCM95-W, and IE-NCM88-W during cycling, *operando* XRD measurements were conducted on LIB half-cells. The data acquired and the corresponding refinement results (details in Experimental section and Supporting Information, see **Figures S2** and **S3**) are shown in **Figure 8**. The cells were cycled in the potential window of 2.9-4.5 V vs. Li^+/Li at C/20, and the PXRD patterns collected during discharge were analyzed by sequential Le Bail refinement. Due to thermal noise problems of the detector, some of the patterns could not be used for reliable refinement. As can be seen from the contour plot in **Figure 8a**, IE-LNO-W shows clearly two-phase behavior in the high-voltage regime. The latter causes minor variations in the *a* lattice parameter, with −0.5% difference between H2 and H3, while the *c* lattice parameter and the unit-cell volume undergo relative changes of −8.4% and −9.1%, respectively. For IE-NCM95-W, two-phase behavior in the H2-H3 region is still apparent, however decreasing the nickel content further leads to solid-solution behavior (see **Figure 8b**, **c**). The volume change during phase transition decreases to −5.2% for IE-NCM95-W. Also, the overall volume change from discharged to charged state decreases from −12.7% for IE-LNO-W to −9.6% for IE-NCM95-W (−9.3% for IE-NCM88-W). This result indicates that increasing the nickel content from 88% or 95% to 100% has a profound effect on the volume variation during cycling and may help explain why CAMs with a very high nickel content typically experience stronger fading and oxygen evolution,[40] even though the absolute volume change of NCMs is not much affected by the nickel content.[2] Especially the abrupt volume variation and the co-existence of two, increasingly different phases, as opposed to solid-solution behavior, are believed to negatively affect stability. Furthermore, the results indicate a stabilizing effect of $Ni_{Li}^{\bullet}$ substitutional defects on the high-voltage H2-H3 transition. This is consistent with the calculated linear relationship between the potential of the phase transition and the $Ni_{Li}^{\bullet}$ fraction.[42] With 95% nickel content, two-phase behavior is observed (i.e. presence of two distinct layered phases), while literature data indicate a smoother transition for NCM95.[48] Hence, the results

stress the importance of intrinsic $Ni_{Li}^{\bullet}$ defects for achieving long-term stability of state-of-the-art Ni-rich NCM and LNO CAMs. Accordingly, $Ni_{Li}^{\bullet}$ defects should be thought of as a functional modification to the CAM, which can have beneficial and/or detrimental effects on the cycling performance.

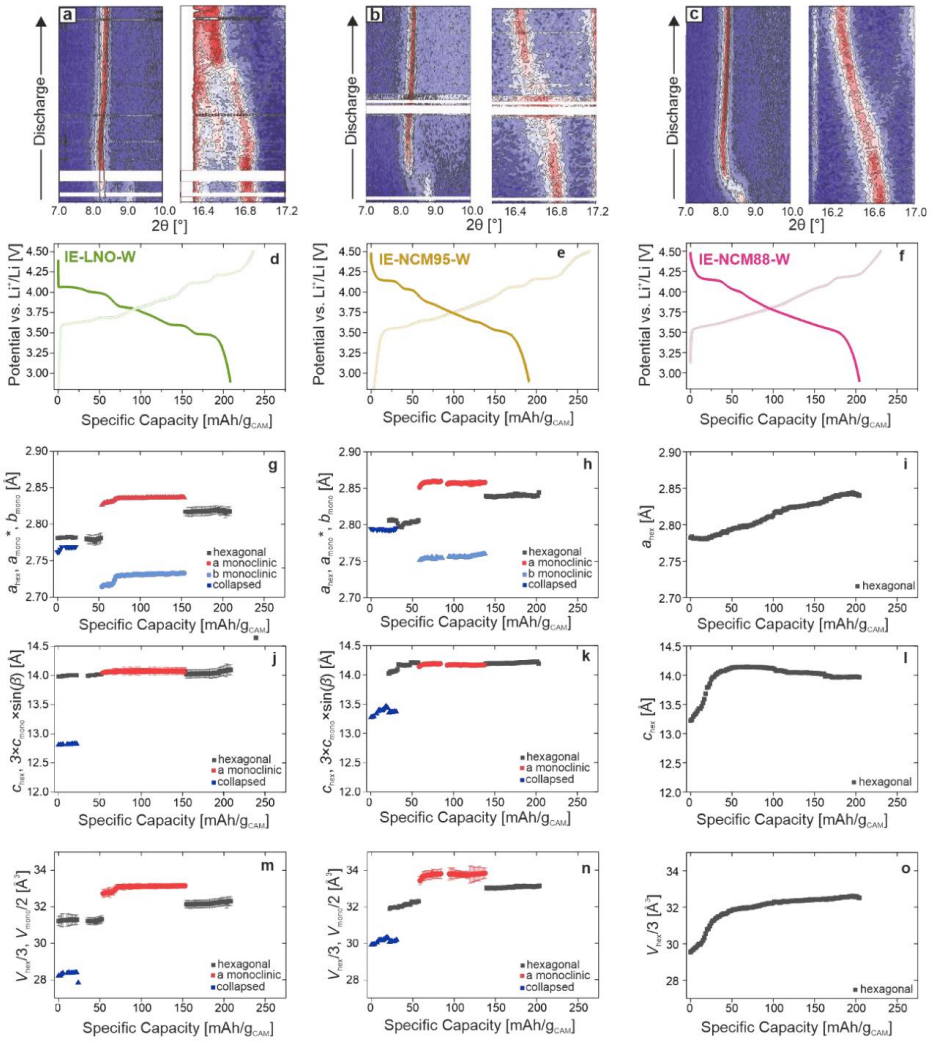

Figure 8. Contour plots of *operando* XRD data collected from (a) IE-LNO-W, (b) IE-NCM95-W, and (c) IE-NCM88-W during discharge from 4.5 to 2.9 V vs. Li^+/Li at a rate of C/20. (d-f) Corresponding voltage profiles and results from sequential Le Bail analysis for (g, j, m) IE-LNO-W, (h, k, n) IE-NCM95-W, and (i, l, o) IE-NCM88-W.

Regarding the monoclinic distortion region, ranging from 3.6 to 3.9 V vs. Li^+/Li, distinct peak separation is observed for IE-LNO-W, while IE-NCM95-W exhibits diffuse peaks

and IE-NCM88-W reveals single-phase behavior (in the range of 3.45-3.90 V). Because monoclinic distortion is caused by the coupling of lithium/vacancy ordering and Jahn-Teller active Ni^{3+}, it is expected that cobalt and/or manganese incorporation reduces the degree of distortion by altering the overall nickel content, the nickel oxidation state (only Mn^{4+}), and the lithium distribution. Nevertheless, we find clear signs of monoclinic distortion in the 95% nickel sample. Note that this may be more pronounced due to the lack of $Ni_{Li}^{\bullet}$ defects, which disrupt the lithium/vacancy ordering and introduce Ni_{Ni}' defects (get oxidized quickly upon charging though).[18,42,47] The monoclinic distortion in IE-NCM95-W is smaller than that of IE-LNO-W, which is evident from the difference between the a^* and b lattice parameters and the angle β (see **Figure S4**, Supporting Information).

Taken together, the *operando* XRD analysis reveals the presence of two-phase regions with relatively large changes in unit-cell volume at high SOC, as well as a distinct monoclinic distortion for IE-LNO. Upon cobalt and manganese substitution, the phase transitions become less apparent. However, in comparison to results available in the literature,[48] less solid-solution behavior is observed. The absence of $Ni_{Li}^{\bullet}$ defects seems to intensify the differences between crystallographic phases and to lead to a more biphasic behavior. Intrinsic point defects likely stabilize LNO and state-of-the-art Ni-rich CAMs against degradation, an effect that should be considered when assessing the cycling performance of such materials.

Vacancy-Pinning Hypothesis

We recently showed that $Ni_{Li}^{\bullet}$ defects can slow down the kinetics of LNO both by diminishing the number of ionic charge carriers and increasing the length of diffusion paths.[18,42,47] The positive charge of excess nickel in the lithium layer, along with the accompanying local chemo-mechanical strain, creates an attractive potential for lithium vacancies that also considerably lowers the migration barrier for a lithium vacancy to approach the defect, effectively making $Ni_{Li}^{\bullet}$ defects sinks for lithium vacancies. Following the same line of thought, we conducted a similar study to investigate the thermodynamics of lithium-vacancy formation in the vicinity of isolated cobalt and manganese dopants in the nickel layer, corresponding to a concentration of 1.6% per layer or 0.8% per cell. We calculated the vacancy-stabilization energy for individual lithium vacancies with respect to the energy of the farthest vacancy from the dopant.

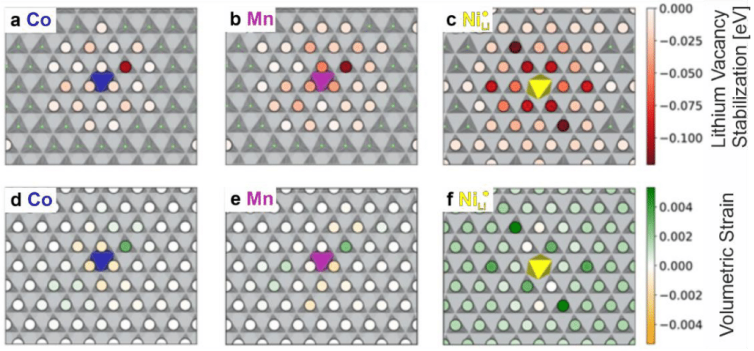

Figure 9. (a, b, c) Lithium-vacancy stabilization energies and (d, e, f) volumetric strains in the presence of dilute amounts of cobalt (blue) and manganese substitutional dopants (purple) and $Ni_{Li}^{\bullet}$ point defects (yellow). The underlying Ni-O lattice is depicted as gray polyhedra. Lithium sites in the Li layer are indicated by small green points, with circular markers representing explicitly calculated points. The Li layer underneath the Ni-O layer shows similar patterns, with the transition metal acting as an inversion center.

Figure 9 illustrates the top view of the Ni layer with the dopant, where lithium sites in the Li layer are represented as small green points. Superimposed on this view are color maps that depict the vacancy-stabilization energy (see **Figure 9a**, **b**) and the volumetric strain experienced by each lithium ion (see **Figure 9d**, **e**) resulting from the substitution of nickel with cobalt and manganese. The effect of $Ni_{Li}^{\bullet}$ defects[18,42,47] is shown in **Figure 9c**, **f** as a comparison. Upon initial observation, it becomes apparent that the vacancy-stabilization energies are predominantly negative for both cobalt and manganese, suggesting a vacancy-pinning effect akin to $Ni_{Li}^{\bullet}$. This effect is more pronounced in the proximity of manganese than cobalt, evident in both the magnitude of stabilization (energy scale) and the spatial extent of the trapping pattern. The weaker influence of cobalt is consistent with findings by Dahn *et al.*[49] The stabilization of specific lithium sites can be partially explained by the volumetric strain that occurs when cobalt or manganese substitutes nickel. Notably, the lithium site connected to the dopant through the previously elongated Jahn-Teller distorted Ni-O bond experiences the highest strain. It is evident that substituting Ni^{3+} with a non-Jahn-Teller active ion inevitably introduces non-negligible local strain. It is important to note that both strain and stabilization energy exhibit centrosymmetry relative to the dopant's position. This indicates that similar pinning effects will also be observed in the Li layer below the dopant. Therefore, the number of affected lithium vacancies is twice what is shown in **Figure 9**. Delmas linked the pinning of six lithium ions to each $Ni_{Li}^{\bullet}$ defect,[50] and we have explicitly computed that this is a realistic estimate.[47] Based on a visual inspection, manganese and especially cobalt seem to be less effective vacancy traps than $Ni_{Li}^{\bullet}$. In the past, we have calculated the effects of vacancy pinning on the smoothing of voltage profiles and the suppression of phase transitions and compared

them to experimental results,[42] concluding that the major effect of substitutional strategies is the disruption of lithium/vacancy orderings, which in turn results in the establishment of solid solutions and the progressive elimination of phase transitions.

However, in NCMs, both dopants are present simultaneously and in greater concentrations, which means their strain fields are bound to overlap and could lead to unexpected trapping patterns in these configurations. To gain a qualitative understanding, we conducted the strain analysis on a relaxed NCM88 model ($Li_{128}Ni_{112}Co_8Mn_8O_{256}$) with uniformly distributed cobalt and manganese. Although an even distribution of dopants is reasonable, it may not be realistic if the substituents have a tendency to cluster or segregate. The strain analysis is presented in **Figure S5** (Supporting Information), clearly illustrating overlapping effects in close proximity to the substituents, as well as in the regions between them.

Conclusion

LNO and the related Ni-rich NCMs intrinsically contain $Ni_{Li}^{\bullet}$ substitutional defects, which are generally believed to be detrimental by impeding lithium diffusion. Herein, we successfully studied a series of Ni-rich cathodes synthesized by sodium-to-lithium ion exchange. In contrast to state-of-the-art positive electrode materials, the ion-exchanged samples are devoid of $Ni_{Li}^{\bullet}$ defects and thus serve as an ideal platform to examine the intrinsic role of transition-metal site dopants, without intermingling effects induced by substitution and point defects. We find that the nickel content affects the first-cycle specific capacity, with higher contents allowing for faster diffusion, particularly at the end of discharge. We hypothesize a mechanism involving lithium-vacancy pinning to be responsible for this observation and confirm the results by DFT calculations. However, lower nickel contents are associated with increased stability at high state of charge. The latter was studied in some more detail by *operando* XRD, which reveals more severe phase transitions during cycling upon approaching 100 mol% nickel content. Furthermore, we demonstrate that point defects help to mitigate the negative effects of electrode breathing (volume variation) and suggest that the $Ni_{Li}^{\bullet}$ fraction should be considered more carefully when studying Ni-rich NCM and NCA cathode materials, as the stabilizing effects of cobalt, manganese, and $Ni_{Li}^{\bullet}$ emerge simultaneously.

Experimental Section

Synthesis of NNO and Na-NCMs: $Ni(OH)_2$ or co-precipitated NCM hydroxide pCAM particles (BASF SE; d_{50} = 4.0 µm with 100:0:0, 95:4:1, 90:5:5, and 88:5:7 Ni:Co:Mn molar ratios) were mixed with 1.1 eq. NaOH (Sigma-Aldrich) and, if stated, with 0.02 eq. ammonium paratungstate (Sigma-Aldrich) using a laboratory grade blender. The powder mixtures were first pre-annealed at 300 °C for 10 h in argon (unless stated otherwise in the main text) with two atmosphere exchanges per hour. Subsequently, the samples were mixed again under an inert atmosphere, followed by calcination at

700 °C for 12 h in oxygen with two atmosphere exchanges per hour and 3 K/min heating and cooling rates.

Ion-Exchange Procedure: Sodium-to-lithium ion exchange was accomplished by mixing NNO or Na-NCMs with $LiNO_3$ (1:1 by weight) in a mortar and pestle. The powder mixtures were then filled into alumina crucibles and heated at 300 °C for 6 h without control over atmosphere. After cooling to room temperature, the samples were washed twice with 1:10 by weight of CAM to 0.025 M LiOH solution in DI water for a total of 30 min. Residual water was removed by washing with ethanol and acetone, followed by drying in a vacuum at 70 °C. Prior to electrochemical testing, the samples were sieved with a 32 µm stainless-steel mesh.

Electrochemical Testing: The CAM particles were first mixed with polyvinylidene difluoride binder (PVDF; Solef 5130, Solvay) and Super C65 carbon additive (TIMCAL Ltd.) in a ratio of 94:3:3 by weight and then cast onto 0.03 mm thick aluminum foil using a stainless-steel blade with a slit thickness of 140 and 200 µm for electrochemical and *operando* XRD testing, respectively, using an Erichsen Coatmaster 510 applicator (resulting in areal loadings of ~10 and ~14 mg/cm^2, respectively). The as-prepared electrode tapes were dried in a vacuum at 120 °C, calendared at 14 N/mm (Sumet Messtechnik), and cut into circular 13 mm diameter discs. Coin cells were assembled using a glass fiber GF/D separator, LP57 electrolyte (1 M $LiPF_6$ in a 3:7 by weight of ethylene carbonate and ethyl methyl carbonate), and a lithium-metal anode in an argon glovebox.

SEM: Sample imaging/mapping was carried out using a LEO-1530 microscope (Carl Zeiss AG).

FIB Cutting: Electron-transparent samples were produced by the lift-out technique using an FEI Strata 400 S dual-beam system. Sample damage and amorphization from the gallium-ion beam were minimized by stepwise reduction of the acceleration voltage from 30 to 2 keV during final thinning of the lamellae. Specimen preparation was immediately followed by TEM investigation.

(S)TEM: Measurements were carried out on a probe aberration corrected Thermo Fisher Scientific Themis Z microscope at 300 kV. EDS maps were acquired using a Super-X EDX detector.

ICP-OES: A Thermo Fisher Scientific ICAP 7600 DUO was used for ICP-OES analysis. Specifically, the samples were dissolved in an acid digester in a graphite furnace. Mass fractions were obtained from three independent measurements. About 10 mg of material was dissolved in hydrochloric acid and nitric acid at 353 K for 4 h. The digested samples were diluted for analysis. The range of calibration solutions did not exceed a decade. Two or three wavelengths of the elements were used for quantitative analysis.

PXRD: Patterns were collected on a STADI P (STOE) diffractometer in Debye-Scherrer geometry using monochromatic Mo-$K_{\alpha1}$ radiation (λ = 0.7093 Å, 50 kV, 40 mA) and a Mythen 1K detector (DECTRIS AG). The data sets were analyzed using the TOPAS-Academic v7 software. Le Bail fitting was done first, in which background correction was applied by a set of Chebyshev polynomials, and lattice parameters,

zero-shift, axial divergence, and crystallite size were extracted as Gaussian and Lorentzian contributions. During Rietveld refinement, the parameters from Le Bail fitting were first fixed, and the oxygen coordinates z_O (LNO) and z_{O_1} and z_{O_2} (NNO), site occupancies, and Debye-Waller factors were refined while applying an absorption correction. Eventually, all parameters were refined in parallel until convergence was achieved. The confidence intervals were three times the estimated standard deviations as obtained from TOPAS-Academic v7 software.

Solid-State NMR Spectroscopy: ^{7}Li MAS NMR spectroscopy measurements were carried out on a Bruker AVANCE NEO instrument at a magnetic field of 4.7 T, corresponding to a resonance frequency of 77.8 MHz. Spinning was performed in 1.3 mm rotors at 55 kHz. NMR spectra were acquired with a Hahn echo pulse sequence, a $\pi/2$ pulse length of 0.85 µs, and a recycle delay of 1 s. The ^{7}Li chemical shifts were referenced to a 1 M LiCl solution at 0 ppm.

Operando XRD: The positive/negative caps and spacers of the coin-cell casing were modified by electro-erosion to have a hole of 5 mm diameter in the middle, sealed with Kapton foil of 6 mm diameter and 160 µm thickness. The cells were cycled at a rate of C/20 using a Gamry Interface 1000 potentiostat, while patterns were collected simultaneously using a STOE Stadi-P diffractometer with a Mo anode. Data were acquired in the range $5° < 2\theta < 37°$ with a collection time of 10.3 min per pattern. Le Bail fitting was carried out sequentially on the diffraction data using the TOPAS-Academic v7 software. The zero offset was refined for each cell component individually, and the instrumental contribution to peak broadening was determined by measurement of a LaB_6 660b standard.

Theory: The Vienna Ab initio Simulation Package (VASP)[51,52] was used to perform spin-polarized DFT calculations with projector augmented wave pseudopotentials[53,54] and the optB86b-VdW exchange-correlation functional[55] that has recently been used to model intercalation compounds.[36,42,56,57] Isolated cobalt and manganese dopants were inserted in a 2·8·4 supercell of the $P2_1/c$ cell of LNO, allowing for the proper Jahn-Teller distortion caused by Ni^{3+} ions.[58,59] Structural models have been fully relaxed by releasing all degrees of freedom (ionic positions, cell shape, and volume) with a cutoff energy of 600 eV and a *k*-point spacing of 0.5 $Å^{-1}$ until the forces were lower than 10^{-2} eV/Å. The convergence criterion for the electronic self-consistent cycles was set to 10^{-5} eV; the minimum number of electronic self-consistency steps was set to 6, which occasionally enforced tighter convergence. Atomic volumetric strains have been calculated using OVITO[60].

Supporting Information

Supporting Information is available from the Wiley Online Library or from the author.

Rietveld refinement results for NNO-W and Na-NCM-W, details on the size analysis, electrochemistry of IE-NCM90, additional data from *operando* XRD, and volumetric strain at the Li positions calculated for an NCM88 model.

Acknowledgements

This work was partially supported by the BASF SE. Dr. Thomas Bergfeldt and team (IAM-AWP, KIT) are acknowledged for performing the ICP-OES measurements. The authors are grateful to the Federal Ministry of Education and Research (Bundesministerium für Bildung und Forschung, BMBF) for funding within the project UNIKAM (03XP0484A, 03XP0484B).

Conflict of Interest

The authors declare no conflict of interest.

Data Availability Statement

The data that support the findings of this study are available from the corresponding author upon reasonable request.

References

[1] G. E. Blomgren, *J. Electrochem. Soc.* **2017**, *164*, A5019.

[2] W. Li, H. Y. Asl, Q. Xie, A. Manthiram, *J. Am. Chem. Soc.* **2019**, *141*, 5097.

[3] S. Schweidler, M. Bianchini, P. Hartmann, T. Brezesinski, J. Janek, *Batter. Supercaps* **2020**, *3*, 1021.

[4] K. Y. Park, Y. Zhu, C. G. Torres-Castanedo, H. J. Jung, N. S. Luu, O. Kahvecioglu, Y. Yoo, J. W. T. Seo, J. R. Downing, H. D. Lim, M. J. Bedzyk, C. Wolverton, M. C. Hersam, *Adv. Mater.* **2022**, *34*, 2106402.

[5] L. De Biasi, A. O. Kondrakov, H. Geßwein, T. Brezesinski, P. Hartmann, J. Janek, *J. Phys. Chem. C* **2017**, *121*, 26163.

[6] H. H. Ryu, B. Namkoong, J. H. Kim, I. Belharouak, C. S. Yoon, Y. K. Sun, *ACS Energy Lett.* **2021**, *6*, 2726.

[7] B. You, Z. Wang, F. Shen, Y. Chang, W. Peng, X. Li, H. Guo, Q. Hu, C. Deng, S. Yang, G. Yan, J. Wang, *Small Methods* **2021**, *5*, 2100234.

[8] U.-H. Kim, E.-J. Lee, C. S. Yoon, S.-T. Myung, Y.-K. Sun, *Adv. Energy Mater.* **2016**, *6*, 1601417.

[9] F. Lin, I. M. Markus, D. Nordlund, T.-C. Weng, M. D. Asta, H. L. Xin, M. M. Doeff, *Nat. Commun.* **2014**, *5*, 3529.

[10] H.-H. Ryu, N.-Y. Park, T.-C. Noh, G.-C. Kang, F. Maglia, S.-J. Kim, C. S. Yoon, Y.-K. Sun, *ACS Energy Lett.* **2021**, *6*, 216.

[11] M. Bianchini, M. Roca-Ayats, P. Hartmann, T. Brezesinski, J. Janek, *Angew. Chem. Int. Ed.* **2019**, *58*, 10434.

[12] D. Caurant, N. Baffier, B. Garcia, J. P. Pereira-Ramos, *Solid State Ionics* **1996**,

91, 45.

[13] E. Rossen, C. D. W. Jones, J. R. Dahn, *Solid State Ionics* **1992**, *57*, 311.

[14] D. Goonetillke, B. Schwarz, H. Li, F. Fauth, E. Suard, S. Mangold, S. Indris, T. Brezesinski, M. Bianchini, D. Weber, *J. Mater. Chem. A* **2023**, *11*, 13468.

[15] R. D. Shannon, *Acta Crystallogr.* **1976**, *A32*, 751.

[16] M. Bianchini, J. Wang, R. J. Clément, B. Ouyang, P. Xiao, D. Kitchaev, T. Shi, Y. Zhang, Y. Wang, H. Kim, M. Zhang, J. Bai, F. Wang, W. Sun, G. Ceder, *Nat. Mater.* **2020**, *19*, 1088.

[17] M. Bianchini, F. Fauth, P. Hartmann, T. Brezesinski, J. Janek, *J. Mater. Chem. A* **2020**, *8*, 1808.

[18] K. Hoang, M. Johannes, *Chem. Mater.* **2016**, *28*, 1325.

[19] P. Kurzhals, F. Riewald, M. Bianchini, H. Sommer, H. A. Gasteiger, J. Janek, P. Kurzhals, M. Bianchini, H. Sommer, J. Janek, H. A. Gasteiger, *J. Electrochem. Soc.* **2021**, *168*, 110518.

[20] F. Riewald, P. Kurzhals, M. Bianchini, H. Sommer, J. Janek, H. A. Gasteiger, *J. Electrochem. Soc.* **2022**, *169*, 020529.

[21] Z. Cui, Z. Guo, A. Manthiram, *Adv. Energy Mater.* **2023**, *12*, 2203853.

[22] Y. Song, Y. Cui, L. Geng, B. Li, L. Ge, L. Zhou, Z. Qiu, J. Nan, W. Wu, H. Xu, X. Li, Z. Yan, Q. Xue, Y. Tang, W. Xing, *Adv. Energy Mater.* **2023**, DOI: 10.1002/aenm.202303207.

[23] W. van den Bergh, L. Karger, S. Murugan, J. Janek, A. Kondrakov, T. Brezesinski, *ChemElectroChem* **2023**, *10*, 202300165.

[24] J. Langdon, A. Manthiram, *Energy Storage Mater.* **2021**, *37*, 143.

[25] R. Ruess, D. Gomboso, M. A. Ulherr, E. Trevisanello, Y. Ma, A. Kondrakov, T. Brezesinski, J. Janek, *J. Electrochem. Soc.* **2023**, *170*, 020533.

[26] A. Liu, N. Zhang, J. E. Stark, P. Arab, H. Li, J. R. Dahn, *J. Electrochem. Soc.* **2021**, *168*, 040531.

[27] L. Karger, D. Weber, D. Goonetilleke, A. Mazilkin, H. Li, R. Zhang, Y. Ma, S. Indris, A. Kondrakov, J. Janek, T. Brezesinski, *Chem. Mater.* **2023**, *35*, 648.

[28] L. Karger, S. Korneychuk, W. Van Den Bergh, S. L. Dreyer, R. Zhang, A. Kondrakov, J. Janek, T. Brezesinski, Chem. Mater. **2023**, DOI: 10.1021/acs.chemmater.3c02727.

[29] J. Z. Yu-hong Luo, Qing-lin Pan, Han-xin Wei, Ying-de Huang, Lin-bo Tang, Zhen-yu Wang, Zhen-jiang He, Cheng Yan, Jing Mao, Ke-hua Dai, Xia-hui Zhang, *Nano Energy* **2022**, *102*, 107626.

[30] J. Y. Hwang, C. S. Yoon, I. Belharouak, Y. K. Sun, *J. Mater. Chem. A* **2016**, *4*, 17952.

[31] C. Delmas, I. Saadoune, P. Dordor, *Mol. Cryst. Liq. Cryst. Sci. Technol. Sect. A. Mol. Cryst. Liq. Cryst.* **1994**, *244*, 337.

[32] W. Liu, P. Oh, X. Liu, M. J. Lee, W. Cho, S. Chae, Y. Kim, J. Cho, *Angew. Chem. Int. Ed.* **2015**, *54*, 4440.

[33] D. Goonetilleke, A. Mazilkin, D. Weber, Y. Ma, F. Fauth, J. Janek, T. Brezesinski, M. Bianchini, *J. Mater. Chem. A* **2022**, *10*, 7841.

[34] H. Kim, Y. Kong, W. M. Seong, A. Manthiram, *ACS Appl. Mater. Interfaces* **2023**, *15*, 26585.

[35] H. Nguyen, R. Silverstein, A. Zaveri, W. Cui, P. Kurzhals, S. Sicolo, M. Bianchini, K. Seidel, R. J. Clément, *Adv. Funct. Mater.* **2023**, DOI: 10.1002/adfm.202306168.

[36] H. Li, W. Hua, X. Liu-Théato, Q. Fu, M. Desmau, A. Missyul, M. Knapp, H. Ehrenberg, S. Indris, *Chem. Mater.* **2021**, *33*, 9546.

[37] S. Indris, M. Scheuermann, S. M. Becker, V. Šepelák, R. Kruk, J. Suffner, F. Gyger, C. Feldmann, A. S. Ulrich, H. Hahn, *J. Phys. Chem. C* **2011**, *115*, 6433.

[38] H. Li, W. Hua, M. Etter, S. Mangold, G. Melinte, N. Pietro, M. Casati, H. Ehrenberg, S. Indris, **2022**, *34*, 8163.

[39] L. Wang, A. Mukherjee, C. Y. Kuo, S. Chakrabarty, R. Yemini, A. A. Dameron, J. W. DuMont, S. H. Akella, A. Saha, S. Taragin, H. Aviv, D. Naveh, D. Sharon, T. S. Chan, H. J. Lin, J. F. Lee, C. Te Chen, B. Liu, X. Gao, S. Basu, Z. Hu, D. Aurbach, P. G. Bruce, M. Noked, *Nat. Nanotechnol.* **2023**, DOI 10.1038/s41565-023-01519-8.

[40] S. Oswald, H. A. Gasteiger, *J. Electrochem. Soc.* **2023**, *170*, 30506.

[41] D. Pritzl, T. Teufl, A. T. S. Freiberg, B. Strehle, J. Sicklinger, H. Sommer, P. Hartmann, H. A. Gasteiger, *J. Electrochem. Soc.* **2019**, *166*, A4056.

[42] M. Mock, M. Bianchini, F. Fauth, K. Albe, S. Sicolo, *J. Mater. Chem. A* **2021**, *9*, 14928.

[43] E. B. Quisbert, F. Fauth, A. M. Abakumov, M. Blangero, M. Guignard, C. Delmas, *Small* **2023**, *19*, 2300616.

[44] P. Xiao, N. Zhang, H. S. Perez, M. Park, arXiv **2023**, DOI: 10.48550/arXiv.2311.06140 (accessed online on 10.01.2024).

[45] M. E. Arroyo y de Dompablo, G. Ceder, *J. Power Sources* **2003**, *119–121*, 654.

[46] M. Yi, Z. Cui, H. Celio, A. Manthiram, *Chem. Mater.* **2023**, *35*, 9352.

[47] S. Sicolo, M. Sadowski, K. Vettori, M. Bianchini, J. Janek, Chem. Mater. **2023**, 36, 492.

[48] H. H. Ryu, K. J. Park, C. S. Yoon, Y. K. Sun, *Chem. Mater.* **2018**, *30*, 1155.

[49] H. Li, M. Cormier, N. Zhang, J. Inglis, J. Li, J. R. Dahn, *J. Electrochem. Soc.* **2019**, *166*, A429.

[50] C. Delmas, J. P. Pérès, A. Rougier, A. Demourgues, F. Weill, A. Chadwick, M. Broussely, F. Perton, P. Biensan, P. Willmann, *J. Power Sources* **1997**, *68*, 120.

[51] G. Kresse, J. Furthmüller, *Phys. Rev. B* **1996**, *54*, 11169.

[52] G. Kresse, J. Furthmüller, *Comput. Mater. Sci.* **1996**, *6*, 15.

[53] G. Kresse, D. Joubert, *Phys. Rev. B* **1999**, *59*, 1758.

[54] P. E. Blöchl, *Phys. Rev. B* **1994**, *50*, 17953.

[55] J. Klimeš, D. R. Bowler, A. Michaelides, *J. Phys. Condens. Matter* **2010**, *22*, 22201.

[56] J. L. Kaufman, J. Vinckevičiūtė, S. Krishna Kolli, J. Gabriel Goiri, A. Van der Ven, *Philos. Trans. R. Soc. A Math. Phys. Eng. Sci.* **2019**, *377*, 20190020.

[57] J. Vinckevičiūtė, M. D. Radin, N. V Faenza, G. G. Amatucci, A. Van der Ven, *J. Mater. Chem. A* **2019**, *7*, 11996.

[58] M. D. Radin, J. C. Thomas, A. Van der Ven, *Phys. Rev. Mater.* **2020**, *4*, 43601.

[59] S. Sicolo, M. Mock, M. Bianchini, K. Albe, *Chem. Mater.* **2020**, *32*, 10096.

[60] A. Stukowski, *Model. Simul. Mater. Sci. Eng.* **2010**, *18*, 15012.

ToC Entry

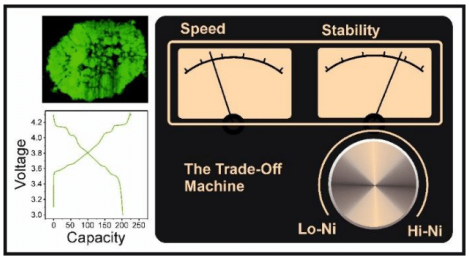

Nickel substitution strongly impacts on the electrochemistry of layered Ni-rich oxide cathode materials. In particular, changes in composition alter the defect concentration, rendering substitution-based structure-property relationships ambiguous. In this work, the nickel content is varied while maintaining defect-free character, thus allowing for selective study of substitution effects.

4 Conclusions

The trend towards ever higher nickel contents, in an effort to maximize the capacity of layered lithium metal oxide CAMs, is opposed by the unfavorable trends of material (in)stability and defect formation with increasing nickel content. LNO can be almost fully delithiated in the initial charge, but the corresponding discharge capacity is lower. This so-called "first-cycle capacity loss" limits the capability of LNO as a CAM. Because of the relatively low cut-off potential used for testing LNO, almost no capacity is lost due to irreversible side reactions, and only slow diffusion at the end of discharge is contributing to the FCCL in sst-LNO.[58] The energy barrier for lithium diffusion increases with decreasing lithium vacancy concentration and thus directly with the degree of lithiation. However, the gross lithium content is not the only variable affecting the concentration of mobile vacancies. Intrinsically present $Ni_{Li}^{\bullet}$ substitutional defects in LNO can also trap lithium vacancies due to their energetically more favorable localization in the vicinity of such defects.[189] Another but equally important factor for the FCCL is the grain size of the LNO particles. With increasing particle size, the lithium diffusion path length increases and thus the onset of a slower lithium diffusion affects these particles more strongly. Lastly, the influence of the transition-metal composition on the electrochemical performance, particularly on stability and lithium diffusion has been the subject of numerous investigations.[53,210,250] Prior to this work, correlations between the stated factors, $Ni_{Li}^{\bullet}$ defect density, transition-metal content and particle size, and the FCCL have been proposed, singling out different factors to be the key in addressing this problem. However, in the employed solid-state synthesis of LNO, and by the same token also of the related NCM and NCA CAMs, the individual contributions cannot be varied independently and thus, in many cases, only an ambiguous structure-property relationship can be drawn.

For this reason, new synthetic protocols were developed to enable the synthesis of LNO without the characteristic $Ni_{Li}^{\bullet}$ substitutional defects. The novel method utilizes the larger size of sodium ions, compared to lithium, to develop fully separated layers of nickel oxide and sodium in a precursor material with proper particle size by means of solid-state synthesis. This material can be synthesized in a larger temperature range as LNO and still be obtained phase pure due to the inability to form partially sodiated structures in the form of electrochemically inactive rock-salt materials. This in turn allows for tailoring of the primary particle (grain) size by temperature while preventing $Ni_{Li}^{\bullet}$ defect formation. The advantage of this approach lies in the absence of $Ni_{Li}^{\bullet}$, which was previously not attained in any reported synthesis. The successful mitigation of $Ni_{Li}^{\bullet}$ is demonstrated by MAS NMR spectroscopy and XRD measurements, and is further evident from the electrochemical behavior. By XRD, conversion of the *C*2/*m* phase to a hexagonal *R*–3*m* structure was demonstrated. For larger particle sizes, the XRD refinement still yields residual electron density, which however originates from residual sodium in the material, as indicated by ICP-OES and TEM. For smaller

particles, the XRD/Rietveld analysis demonstrates the absence of this residual electron density, because the particles are small enough to completely ion exchange. The effectiveness of ion exchange with smaller particles was then demonstrated by focused ion beam (FIB)-cut EDS. In MAS NMR, the main signal is very narrow and lacks a characteristic shoulder at higher ppm values, which could be correlated with an increase in defect density. Furthermore, an additional feature originating from twin boundaries[72] is also absent in the IE-LNO, demonstrating that truly SC material is obtained. The mechanism of ion exchange was further investigated by variable temperature XRD, demonstrating an onset of the reaction at around 180 °C and the formation of an intermediate with larger interlayer spacing before full conversion to LNO. The microstructure of larger grains showed an abundance of cracks in the center of the particle, which certainly impede the diffusion of lithium ions, as well as sodium during the ion exchange process. It was therefore attempted to heal these cracks out by a second calcination step to obtain SC-LNO. However, upon annealing the materials, $Ni_{Li}^{\bullet}$ defects reformed in large amounts (> 5%). Addition of $LiOH{\cdot}H_2O$ to the second annealing step helps to reduce the defect density to values comparable to PC-LNO (after heating the material for 40 h), but the electrochemistry of the obtained material improved only slightly.

Alternatively, the problem of residual sodium and microcracking can be addressed by lowering the particle size. NNO was synthesized in the temperature range of 450-750 °C, and after ion exchange, a series of size-tailored LNO particles could be obtained. The materials were probed by XRD, SEM and galvanostatic cycling. With decreasing particle size, the unit cell volume decreased and the residual sodium content in the lithium site decreased. In electrochemical testing, no clear correlation of the discharge capacity with particle size was found; however, the FCCL clearly correlated with particle size. The analysis was repeated for two other methods of grain-size tailoring. The first method was high-energy ball milling with varying rotation speeds, which proved to be not optimal, as the obtained materials were size tailored, but the particle-size distribution was broad due to chipping of the primary grains. Furthermore, disorder and amorphization of the material could be demonstrated by HR-TEM. Nevertheless, the obtained particles followed the same trend outlined by the temperature-based size tailoring, albeit with poorer overall electrochemical performance. The third method for size tailoring followed previous results from our group, which is now also adopted by other groups to control the microstructure through anti-sintering agents.[125,284] Herein, 0.1-2.0 mol% ammonium paratungstate was used, which proved successful to control the microstructure of NNO calcined at 700 °C. Depending on whether ammonium paratungstate is added before or after the pre-annealing step of NNO, PC or SC materials can be obtained. From the SC size series, the same findings as in the other two size-tailoring methods were made. However, the XRD/Rietveld refinement analysis proved less successful in determining a decrease of defect densities with lower particle sizes, most likely due to the formation of rock-salt type impurities resulting from the introduction of tungsten. Again, no clear size trend of specific discharge capacities was found, while for the FCCL a clear

correlation with size was observed in all size-tailored samples. The FCCL was still relatively high, even though the low-potential regime showed almost full reversibility for the smaller particles, as was evident from differential capacity analysis. To delve deeper into this new loss phenomenon, an analysis method for LNO charge profiles was developed, which allows extracting degradation (high SOC) and KH (low potential) losses directly. The method relies on aligning the first-cycle charge and discharge curves in a stable regime, which is the monoclinic range at around 3.9 V vs. Li^+/Li with a lithium-lithium/vacancy ordered state corresponding to $Li_{2/5}NiO_2$. KH losses showed a strong correlation with grain size, while the high-voltage degradation appeared to be more or less constant with respect to grain size. This is counterintuitive to the expected surface dependence of the degradation reaction, as most degradation-induced losses are assumed to be due to surface side reactions and loss of active material. The validity of this analysis was demonstrated with a reference $Ni_{Li}^{\bullet}$-containing sst-LNO, which showed only KH loss and negligible high-voltage loss, likely due to the presence of pillaring defects. The high-SOC loss could be caused by the ion exchange process, or it could be related to the absence of $Ni_{Li}^{\bullet}$, which would otherwise hinder severe volume collapse and oxygen evolution, as was shown by ex-situ XRD and DEMS measurements. Furthermore, GITT results revealed that the high-potential region of ion-exchanged material exhibits much larger polarization, which may be due to the more pronounced difference in H2-H3 region causing impeded diffusion. This would agree with the findings by Xiao and co-workers,[56] who propose that defect sites, such as $Ni_{Li}^{\bullet}$ point defects, can facilitate lithium diffusion at high SOC by funneling lithium ions from the H2 to the H3 state. The observed capacity loss could also be related to irreversible side reactions in the bulk material, such as layer gliding and irreversible formation of stacking faults. Because of the large inherent strain of material obtained *via* ion exchange, the oxygen stacking sequence at high SOC could not be assigned unambiguously, which leaves the correlation between $Ni_{Li}^{\bullet}$ pillaring and H4 phase formation open.

When the PC-IE material was tested, it was evident that this material performs much better and that most likely the larger surface of the smaller primary particles in SC morphology is detrimental to the specific capacity. Since the samples have to be washed with water, which is known to negatively affect the charge/discharge capacities of Ni-rich materials and LNO in particular, this comes as no surprise. In the PC morphology, however, the interior grains are protected and the material quality retention during washing is better. This PC IE-CAM was then compared to PC reference LNO as well as to a magnesium-doped IE-LNO. Magnesium doping was first attempted in the NNO synthesis step, which proved unsuccessful, because Mg was inserted into the nickel rather than the sodium site. Therefore, a novel dual ion exchange method was devised, which simultaneously exchanges sodium for lithium and magnesium in the desired ratio. The materials were compared in a variety of electrochemical tests, such as cycling in low-and high-potential regions and GITT measurements. The results corroborated the hypotheses stated above. In short, the effect of lithium-site

substitution, whether inherent as in $Ni_{Li}^{\bullet}$ or deliberate as in the inclusion of Mg, was demonstrated to be ambivalent with respect to the capacity of layered oxide CAMs. Lithium-site substitution helps to stabilize CAMs at high SOC against oxygen release, while at the same time the diffusivity, particularly at the end of discharge, is affected negatively. This raises the question what an ideal concentration of pillaring ions might be, as well as whether pillaring ions are only locally needed, *e.g.* on the particle surface. The developed methodology of ion exchange and novel dual ion exchange may help in elucidating that question, particularly for the defect range below 1.6 mol%, which prior to this work was not accessible experimentally.

Additionally, the usually complex interplay between $Ni_{Li}^{\bullet}$ and transition-metal-site dopant could be separated by the ion exchange method. By doing so, materials with variable nickel content were synthesized *via* ion exchange. Similar to IE-LNO, the grain size had to be adjusted to allow full conversion to the lithium analogs. Furthermore, the annealing conditions had to be adapted to prevent dopant segregation. The obtained material series was investigated by FCCL analysis and *operando* XRD.

For the FCCL, a trade-off between stability and optimal lithium diffusion was observed, similar to the function of $Ni_{Li}^{\bullet}$ sites. By *operando* XRD, it could be shown that transition-metal substitution helps to mitigate abrupt volume changes and to induce solid-solution behavior, even in the absence of $Ni_{Li}^{\bullet}$ defects. Also, the interlayer distance collapse at high SOC proved to be most severe for the 100% nickel-containing material. From these results, it was hypothesized that transition-metal substitution may also cause pinning of vacancies close to the substituents' location. DFT calculations revealed that this is in fact feasible and that manganese in particular has a strong affinity to lithium vacancies. This may explain the smoothening of the voltage curves and the emergence of solid-solution behavior, as the pinned vacancies disrupt the ordering of lithium and lithium vacancies.

The complex interplay between stability and diffusion for the common dopants, cobalt and manganese, as well as for the ever-present $Ni_{Li}^{\bullet}$ substitution, was investigated with a novel ion exchange approach. With this synthesis method otherwise inaccessibly low defect densities can be probed. However, the method relies on water washing, which is one of the main drawbacks. Nevertheless, the results generated herein raise new questions as to what the optimal pillar ion density might be and whether this value also depends on the CAM particle size and the nature of the pillar ion. Particularly for the emerging SC morphology, for which diffusion properties play a crucial role, these questions need to be addressed. Furthermore, the independent study of doping effects is paramount to identify the best candidates, which ideally stabilize the structure and improve diffusion. Due to the normally intrinsic convolution of $Ni_{Li}^{\bullet}$ formation and nickel substitution, ion exchange synthesis offers a unique approach to understand transition-metal-site dopants and lithium-site dopants at a more fundamental level.

5 Bibliography

[1] M. S. Whittingham, *J. Chem. Soc. Chem. Commun.* 1974, *9*, 328–329.

[2] M. S. Whittingham, *Science* 1976, *192*, 1126–1127.

[3] K. Mizushima, P. C. Jones, P. J. Wiseman, J. B. Goodenough, *Mater. Res. Bull.* 1980, *15*, 783–789.

[4] A. Fujisawa, K. Sanechika, T. Nakajima, Secondary Battery. US Patent, 1985.

[5] The Royal Swedish Academy of Sciences. The Nobel Prize in Chemistry 2019. 2019. [Online]; Available: https://www.nobelprize.org/prizes/chemistry/2019/press-release/ (accessed 08.01.2024)

[6] Editorial, *Nat. Energy* 2019, *4*, 893.

[7] N. Nitta, F. Wu, J. T. Lee, G. Yushin, *Mater. Today* 2015, *18*, 252–264.

[8] C. Xu, Q. Dai, L. Gaines, M. Hu, A. Tukker, B. Steubing, *Commun. Mater.* 2020, *1*, DOI: 10.1038/s43246-020-00095-x.

[9] M. M. Titirici, *Adv. Energy Mater.* 2021, *11*, 2003700.

[10] U.S. Department of Energy, Energy Stoage Grand Challenge: Energy Storage Market Report. 2020. [Online]; https://www.energy.gov/sites/prod/files/2020/12/f81/Energy%20Storage%20Market%20Report%202020_0.pdf (accessed 08.01.2024)

[11] A. Thielmann, *AIP Conf. Proc.* 2016, *1765*, 020001.

[12] C. Xu, P. Behrens, P. Gasper, K. Smith, M. Hu, A. Tukker, B. Steubing, *Nat. Commun.* 2023, *14*, 119.

[13] C. Niu, H. Lee, S. Chen, Q. Li, J. Du, W. Xu, J. G. Zhang, M. S. Whittingham, J. Xiao, J. Liu, *Nat. Energy* 2019, *4*, 551–559.

[14] R. Weber, M. Genovese, A. J. Louli, S. Hames, C. Martin, I. G. Hill, J. R. Dahn, *Nat. Energy* 2019, *4*, 683–689.

[15] G. A. Umeda, E. Menke, M. Richard, K. L. Stamm, F. Wudl, B. Dunn, *J. Mater. Chem.* 2011, *21*, 1593–1599.

[16] R. Mukherjee, A. V. Thomas, D. Datta, E. Singh, J. Li, O. Eksik, V. B. Shenoy, N. Koratkar, *Nat. Commun.* 2014, *5*, 3710.

[17] Y. G. Lee, S. Fujiki, C. Jung, N. Suzuki, N. Yashiro, R. Omoda, D. S. Ko, T. Shiratsuchi, T. Sugimoto, S. Ryu, J. H. Ku, T. Watanabe, Y. Park, Y. Aihara, D. Im, I. T. Han, *Nat. Energy* 2020, *5*, 299–308.

[18] H. Huo, J. Janek, Nat. Sci. Rev. 2023, *10*, DOI: 10.1093/nsr/nwad098.

[19] S. Choudhury, A. Agrawal, S. Wei, E. Jeng, L. A. Archer, *Chem. Mater.* 2016, *28*, 2147–2157.

[20] J. Billaud, F. Bouville, T. Magrini, C. Villevieille, A. R. Studart, *Nat. Energy* 2016, *1*, 16097.

[21] Y. Son, J. Ma, N. Kim, T. Lee, Y. Lee, J. Sung, S. H. Choi, G. Nam, H. Cho, Y. Yoo, J. Cho, *Adv. Energy Mater.* 2019, *9*, 1803480.

[22] C. M. Park, J. H. Kim, H. Kim, H. J. Sohn, *Chem. Soc. Rev.* 2010, *39*, 3115–3141.

[23] H. Huo, J. Janek, *ACS Energy Lett.* 2022, *7*, 4005–4016.

[24] S. Chae, S. H. Choi, N. Kim, J. Sung, J. Cho, *Angew. Chemie - Int. Ed.* 2020, *59*, 110–135.

[25] E. Rossen, C. D. W. Jones, J. R. Dahn, *Solid State Ionics* 1992, *57*, 311–318.

[26] Q. Zhong, U. v. Sacken, *J. Power Sources* 1995, *3*, 794–794.

[27] Y. Nitta, K. Okamura, K. Haraguchi, S. Kobayashi, A. Ohata, *J. Power Sources* 1995, *54*, 511–515.

[28] R. Stoyanova, E. Zhecheva, L. Zarkova, *Solid State Ionics* 1994, *73*, 233–240.

[29] Y. Makimura, T. Ohzuku, *J. Power Sources* 2003, *119–121*, 156–160.

[30] Z. Liu, A. Yu, J. Y. Lee, *J. Power Sources* 1999, *81–82*, 416–419.

[31] M. M. Thackeray, C. Johnson, K. Amine, J. Kim, Lithium Metal Oxide Electrodes for Lithium Cells and Batteries,

US Patent, 2004.

[32] Z. Lu, J. Dahn, Cathode Compositions for Lithium-Ion Batteries, US Patent, 2005.

[33] N. Yabuuchi, T. Ohzuku, *J. Power Sources* 2003, *119–121*, 171–174.

[34] C. Vogler, R. Hemmer, G. Arnold, A. Trépo, M. Wohlfahrt-Mehrens, *Ionics* 1999, *5*, 421–425.

[35] C. Masquelier, A. K. Padhi, K. S. Nanjundaswamy, J. B. Goodenough, *J. Solid State Chem.* 1998, *135*, 228–234.

[36] B. Starke, S. Seidlmayer, O. Dolotko, R. Gilles, K. H. Pettinger, *Energies* 2017, *10*, 1–15.

[37] M. M. Thackeray, P. J. Johnson, L. A. de Picciotto, P. G. Bruce, J. B. Goodenough, Mat. Res. Bull. 1984, *19*, 179–187.

[38] K. Amine, H. Tukamoto, H. Yasuda, Y. Fujita, *J. Power Sources* 1997, *68*, 604–608.

[39] J. Huang, P. Zhong, Y. Ha, D. H. Kwon, M. J. Crafton, Y. Tian, M. Balasubramanian, B. D. McCloskey, W. Yang, G. Ceder, *Nat. Energy* 2021, *6*, 706–714.

[40] H. Ji, J. Wu, Z. Cai, J. Liu, D. H. Kwon, H. Kim, A. Urban, J. K. Papp, E. Foley, Y. Tian, M. Balasubramanian, H. Kim, R. J. Clément, B. D. McCloskey, W. Yang, G. Ceder, *Nat. Energy* 2020, *5*, 213–221.

[41] D. Herbert, J. Ulam, Electric Dry Cells and Storage Batteries, US Patent, 1962.

[42] K. J. Griffith, K. M. Wiaderek, G. Cibin, L. E. Marbella, C. P. Grey, *Nature* 2018, *559*, 556–563.

[43] I. Konuma, D. Goonetilleke, N. Sharma, T. Miyuki, S. Hiroi, K. Ohara, Y. Yamakawa, Y. Morino, H. B. Rajendra, T. Ishigaki, N. Yabuuchi, *Nat. Mater.* 2023, *22*, 225–234.

[44] G. E. Blomgren, *J. Electrochem. Soc.* 2017, *164*, A5019–A5025.

[45] M. Li, T. Liu, X. Bi, Z. Chen, K. Amine, C. Zhong, J. Lu, *Chem. Soc. Rev.* 2020, *49*, 1688–1705.

[46] E. Hu, X. Yu, R. Lin, X. Bi, J. Lu, S. Bak, K. W. Nam, H. L. Xin, C. Jaye, D. A. Fischer, K. Amine, X. Q. Yang, *Nat. Energy* 2018, *3*, 690–698.

[47] H. Peng, H. Zhuo, F. Xia, W. Zeng, C. Sun, J. Wu, *Adv. Funct. Mater.* 2023, *51*, 2306804.

[48] N. Yabuuchi, K. Kubota, M. Dahbi, S. Komaba, *Chem. Rev.* 2014, *114*, 11636–11682.

[49] Y. E. Durmus, H. Zhang, F. Baakes, G. Desmaizieres, H. Hayun, L. Yang, M. Kolek, V. Küpers, J. Janek, D. Mandler, S. Passerini, Y. Ein-Eli, *Adv. Energy Mater.* 2020, *10*, 2000089.

[50] Chris Randall, First sodium-ion battery EVs go into serial production in China, 2024, [Online]; Available: https://www.electrive.com/2024/01/02/first-sodium-ion-battery-evs-go-into-serial-production-in-china/ (accessed 08.01.2024)

[51] Y. Ding, Z. P. Cano, A. Yu, J. Lu, Z. Chen, *Electrochem. Energy Rev.* 2019, *2*, 1–28.

[52] M. Tran, A. DaCosta, A. Mevawalla, S. Panchal, M. Fowler, *Batteries* 2021, *7*, 51.

[53] L. De Biasi, A. O. Kondrakov, H. Geßwein, T. Brezesinski, P. Hartmann, J. Janek, *J. Phys. Chem. C* 2017, *121*, 26163–26171.

[54] W. Li, H. Y. Asl, Q. Xie, A. Manthiram, *J. Am. Chem. Soc.* 2019, *141*, 5097–5101.

[55] J. Kasnatscheew, M. Evertz, B. Streipert, R. Wagner, R. Klöpsch, B. Vortmann, H. Hahn, S. Nowak, M. Amereller, A. C. Gentschev, P. Lamp, M. Winter, *Phys. Chem. Chem. Phys.* 2016, *18*, 3956–3965.

[56] P. Xiao, N. Zhang, H. S. Perez, M. Park, ChemRxiv 2023, (accessed on 08.01.2024) DOI: 10.48550/arXiv.2311.06140.

[57] P. Kurzhals, F. Riewald, M. Bianchini, H. Sommer, H. A. Gasteiger, J. Janek, P. Kurzhals, M. Bianchini, H. Sommer, J. Janek, H. A. Gasteiger, *J. Electrochem. Soc.* 2021, *169*, 020529.

[58] C. Bae, N. Dupre, B. Kang, *ACS Appl. Mater. Interfaces* 2021, *13*, 23760–23770.

[59] F. Riewald, P. Kurzhals, M. Bianchini, H. Sommer, J. Janek, H. A. Gasteiger, *J. Electrochem. Soc.* 2022, *169*, 020529.

[60] W. van den Bergh, L. Karger, S. Murugan, J. Janek, A. Kondrakov, T. Brezesinski, *ChemElectroChem* 2023, *10*, e202300165.

[61] R. D. Shannon, *Acta Crystallogr.* 1976, *A32*, 751.

[62] M. Bianchini, M. Roca-Ayats, P. Hartmann, T. Brezesinski, J. Janek, *Angew. Chemie - Int. Ed.* 2019, *58*, 10434–10458.

[63] P. Kalyani, N. Kalaiselvi, *Sci. Technol. Adv. Mater.* 2005, *6*, 689.

[64] C. Delmas, C. Fouassier, P. Hagenmuller, *Phys. B+C* 1980, *99*, 81–85.

[65] S. Sicolo, M. Mock, M. Bianchini, K. Albe, *Chem. Mater.* 2020, *32*, 10096–10103.

[66] J. Sugiyama, Y. Ikedo, K. Mukai, H. Nozaki, M. Månsson, O. Ofer, M. Harada, K. Kamazawa, Y. Miyake, J. H. Brewer, E. J. Ansaldo, K. H. Chow, I. Watanabe, T. Ohzuku, *Phys. Rev. B.* 2010, *82*, 1–11.

[67] J. H. Chung, T. Proffen, S. Shamoto, A. M. Ghorayeb, L. Croguennec, W. Tian, B. C. Sales, R. Jin, D. Mandrus, T. Egami, *Phys. Rev. B - Condens. Matter Mater. Phys.* 2005, *71*, 8–11.

[68] D. G. Kellerman, *Russ. Chem. Rev.* 2001, *70*, 777.

[69] A. Rougier, C. Delmas, A. V Chadwick, *Solid State Commun.* 1995, *94*, 123–127.

[70] I. Nakai, K. Takahashi, Y. Shiraishi, T. Nakagome, F. Nishikawa, *J. Solid State Chem.* 1998, *140*, 145–148.

[71] M. Reynaud, J. Serrano-Sevillano, M. Casas-Cabanas, *Chem. Mater.* 2022, *35,* 3345-3363.

[72] H. Nguyen, R. Silverstein, A. Zaveri, W. Cui, P. Kurzhals, S. Sicolo, M. Bianchini, K. Seidel, R. J. Clément, *Adv. Funct. Mater.* 2023, *n/a*, 2306168, DOI: 10.1002/adfm.202306168.

[73] A. Pokle, D. Weber, M. Bianchini, J. Janek, K. Volz, *Small* 2023, *19*, 2205508.

[74] R. Kanno, H. Kubo, Y. Kawamoto, T. Kamiyama, F. Izumi, Y. Takeda, M. Takano, *J. Solid State Chem.* 1994, *110*, 216–225.

[75] S. P. Lin, K. Z. Fung, Y. M. Hon, M. H. Hon, *J. Cryst. Growth* 2002, *234*, 176–183.

[76] L. Hartmann, D. Pritzl, H. Beyer, H. A. Gasteiger, *J. Electrochem. Soc.* 2021, *168*, 070507.

[77] J. Sicklinger, M. Metzger, H. Beyer, D. Pritzl, H. A. Gasteiger, *J. Electrochem. Soc.* 2019, *166*, A2322–A2335.

[78] H. S. Liu, Z. R. Zhang, Z. L. Gong, Y. Yang, *Electrochem. Solid-State Lett.* 2004, *7*, A190.

[79] X. H. Meng, T. Lin, H. Mao, J. L. Shi, H. Sheng, Y. G. Zou, M. Fan, K. Jiang, R. J. Xiao, D. Xiao, L. Gu, L. J. Wan, Y. G. Guo, *J. Am. Chem. Soc.* 2022, *144*, 11338–11347.

[80] Y. Bi, J. Tao, Y. Wu, L. Li, Y. Xu, E. Hu, B. Wu, J. Hu, C. Wang, J. G. Zhang, Y. Qi, J. Xiao, *Science* 2020, *370*, 1313–1318.

[81] L. Li, J. Chen, H. Huang, L. Tan, L. Song, H. H. Wu, C. Wang, Z. Zhao, H. Yi, J. Duan, T. Dong, *ACS Appl. Mater. Interfaces* 2021, *13*, 42554–42563.

[82] D. Goonetillke, B. Schwarz, H. Li, F. Fauth, E. Suard, S. Mangold, S. Indris, T. Brezesinski, M. Bianchini, D. Weber, *J. Mater. Chem. A* 2023, *11*, 13468-13482.

[83] C. Delmas, J. P. Pérès, A. Rougier, A. Demourgues, F. Weill, A. Chadwick, M. Broussely, F. Perton, P. Biensan, P. Willmann, *J. Power Sources* 1997, *68*, 120–125.

[84] C. Delmas, M. Ménétrier, L. Croguennec, I. Saadoune, A. Rougier, C. Pouillerie, G. Prado, M. Grüne, L. Fournès, *Electrochim. Acta* 1999, *45*, 243–253.

[85] L. Yin, G. S. Mattei, Z. Li, J. Zheng, W. Zhao, F. Omenya, C. Fang, W. Li, J. Li, Q. Xie, J.-G. Zhang, M. S. Whittingham, Y. S. Meng, A. Manthiram, P. G. Khalifah, *Rev. Sci. Instrum.* 2018, *89*, 93002.

[86] C. Pouillerie, E. Suard, C. Delmas, *J. Solid State Chem.* 2001, *158*, 187–197.

[87] K. Hoang, M. Johannes, *Chem. Mater.* 2016, *28*, 1325–1334.

[88] A. Hirano, R. Kanno, Y. Kawamoto, Y. Takeda, K. Yamaura, M. Takano, K. Ohyama, M. Ohashi, Y. Yamaguchi, *Solid*

State Ionics 1995, *78*, 123–131.

[89] J. R. Dahn, U. von Sacken, C. A. Michal, *Solid State Ionics* 1990, *44*, 87–97.

[90] J. B. Goodenough, D. G. Wickham, W. J. Croft, *J. Appl. Phys.* 2004, *29*, 382–383.

[91] A. Rougier, P. Gravereau, C. Delmas, *J. Electrochem. Soc.* 1996, *143*, 1168–1175.

[92] I. J. Pickering, J. T. Lewandowski, A. J. Jacobson, J. A. Goldstone, *Solid State Ionics* 1992, *53–56*, 405–412.

[93] W. Bronger, H. Bade, W. Klemm, *Zeitschrift für Anorg. und Allg. Chemie* 1964, *333*, 188–200.

[94] A. Genreith-Schriever, A. Alexei, C. Coates, G. Phillips, C. Grey, ChemRxiv. 2023, (accessed on 08.01.2024) DOI: 10.26434/chemrxiv-2023-q3cmz

[95] L. de Biasi, B. Schwarz, T. Brezesinski, P. Hartmann, J. Janek, H. Ehrenberg, *Adv. Mater.* 2019, *31*, 1900985.

[96] L. D. Dyer, B. S. Borie, G. P. Smith, *J. Am. Chem. Soc.* 1954, *76*, 1499–1503.

[97] M. D. L. Garayt, N. Zhang, S. Yu, J. J. Abraham, A. Murphy, R. Omessi, Z. Ye, S. Azam, M. B. Johnson, C. Yang, J. R. Dahn, *J. Electrochem. Soc.* 2023, *170*, 060529.

[98] C.-H. Lu, L. Wei-Cheng, *J. Mater. Chem.* 2000, *10*, 1403–1407.

[99] K. S. Park, S. H. Park, Y. K. Sun, K. S. Nahm, Y. S. Lee, M. Yoshio, *J. Appl. Electrochem.* 2002, *32*, 1229–1233.

[100] M. Bianchini, A. Schiele, S. Schweidler, S. Sicolo, F. Fauth, E. Suard, S. Indris, A. Mazilkin, P. Nagel, S. Schuppler, M. Merz, P. Hartmann, T. Brezesinski, J. Janek, *Chem. Mater.* 2020, *32*, 9211–9227.

[101] M. Bianchini, F. Fauth, P. Hartmann, T. Brezesinski, J. Janek, *J. Mater. Chem. A* 2020, *8*, 1808–1820.

[102] C. C. Chang, P. N. Kumta, *Mater. Sci. Eng. B* 2005, *116*, 341–345.

[103] T. Ohzuku, A. Ueda, M. Nagayama, *J. Electrochem. Soc.* 1993, *140*, 1862–1870.

[104] S. Mallick, A. Patel, X. G. Sun, M. P. Paranthaman, M. Mou, J. H. Mugumya, M. Jiang, M. L. Rasche, H. Lopez, R. B. Gupta, *J. Mater. Chem. A* 2023, *11*, 3789–3821.

[105] J. Välikangas, P. Laine, M. Hietaniemi, T. Hu, P. Tynjälä, U. Lassi, *Appl. Sci.* 2020, *10*, 8988.

[106] S. L. Dreyer, P. Kurzhals, S. B. Seiffert, P. Müller, A. Kondrakov, T. Brezesinski, J. Janek, *J. Electrochem. Soc.* 2023, *170*, 60530.

[107] P. Hou, H. Zhang, Z. Zi, L. Zhang, X. Xu, *J. Mater. Chem. A* 2017, *5*, 4254–4279.

[108] H. Dong, G. M. Koenig, *CrystEngComm* 2020, *22*, 1514–1530.

[109] C. S. Yoon, D. W. Jun, S. T. Myung, Y. K. Sun, *ACS Energy Lett.* 2017, *2*, 1150–1155.

[110] C. S. Yoon, U. H. Kim, G. T. Park, S. J. Kim, K. H. Kim, J. Kim, Y. K. Sun, *ACS Energy Lett.* 2018, *3*, 1634–1639.

[111] P. Kurzhals, F. Riewald, A. M. Kern, F. Walther, J. Janek, M. Bianchini, S. Ahmed, H. Sommer, K. Volz, J. Electrochem. Soc. 2022, *169*, 050526.

[112] C. C. Chang, N. Scarr, R. N. Kumta, *Solid State Ionics* 1998, *112*, 329–344.

[113] M. Y. Song, R. Lee, *J. Power Sources* 2002, *111*, 97–103.

[114] Y. Lee, Y. Sun, K. Nahm, *Solid State Ionics* 1999, *118*, 159–168.

[115] J. P. Peres, C. Delmas, A. Rougier, M. Broussely, F. Perton, P. Biensan, P. Willmann, *J. Phys. Chem. Solids* 1996, *57*, 1057–1060.

[116] R. Stoyanova, E. Zhecheva, R. Alcántara, J. L. Tirado, G. Bromiley, F. Bromiley, T. Boffa Ballaran, *Solid State Ionics* 2003, *161*, 197–204.

[117] D. Goonetilleke, E. Suard, B. Bergner, J. Janek, T. Brezesinski, M. Bianchini, J. Hajdu, *J. Appl. Crystallogr.* 2023, *56*, 1066–1075.

[118] R. Weber, H. Li, W. Chen, C.-Y. Kim, K. Plucknett, J. R. Dahn, *J. Electrochem. Soc.* 2020, *167*, 100501.

[119] H. Arai, S. Okada, H. Ohtsuka, M. Ichimura, J. Yamaki, *Solid State Ionics* 1995, *80*, 261–269.

[120] E. McCalla, G. H. Carey, J. R. Dahn, *Solid State Ionics* 2012, *219*, 11–19.

[121] S. P. Ong, L. Wang, B. Kang, G. Ceder, *Chem. Mater.* 2008, *20*, 1798–1807.

[122] T. Sata, *J. Ceram. Soc. Japan* 1998, *106*, 660–664.

[123] A. Liu, N. Zhang, J. E. Stark, P. Arab, H. Li, J. R. Dahn, *J. Electrochem. Soc.* 2021, *168*, 040531.

[124] H. Kaneda, Y. Furuichi, A. Ikezawa, H. Arai, *ACS Appl. Mater. Interfaces* 2022, *14*, 52766–52778.

[125] D. Goonetilleke, A. Mazilkin, D. Weber, Y. Ma, F. Fauth, J. Janek, T. Brezesinski, M. Bianchini, *J. Mater. Chem. A* 2022,*10*, 7841.

[126] R. Ruess, D. Gomboso, M. A. Ulherr, E. Trevisanello, Y. Ma, A. Kondrakov, T. Brezesinski, J. Janek, *J. Electrochem. Soc.* 2023, *170*, 020533.

[127] A. Mesnier, A. Manthiram, *J. Power Sources* 2023, *586*, 233681.

[128] A. Mesnier, A. Manthiram, *ACS Appl. Mater. Interfaces* 2023, *15*, 12895–12907.

[129] J. Kim, H. Lee, H. Cha, M. Yoon, M. Park, J. Cho, *Adv. Energy Mater.* 2018, *8*, 1–25.

[130] J. Marchand-Brynaert, N. Jongen, J.-L. Dewez, *J. Polym. Sci. Part A Polym. Chem.* 1997, *35*, 1227–1235.

[131] F. Strauss, S. Payandeh, A. Kondrakov, T. Brezesinski, *Mater. Futur.* 2022, *1*, 023501.

[132] D. Weber, Đ. Tripković, K. Kretschmer, M. Bianchini, T. Brezesinski, *Eur. J. Inorg. Chem.* 2020, *2020*, 3117–3130.

[133] Y. Kim, H. Park, J. H. Warner, A. Manthiram, *ACS Energy Lett.* 2021, *6*, 941–948.

[134] W. M. Seong, Y. Kim, A. Manthiram, *Chem. Mater.* 2020, *32*, 9479–9489.

[135] J. Kim, Y. Hong, K. S. Ryu, M. G. Kim, J. Cho, *Electrochem. Solid-State Lett.* 2005, *9*, A19.

[136] Y. Kim, *J. Solid State Electrochem.* 2013, *17*, 1961–1965.

[137] R. Jung, R. Morasch, P. Karayaylali, K. Phillips, F. Maglia, C. Stinner, Y. Shao-Horn, H. A. Gasteiger, *J. Electrochem. Soc.* 2018, *165*, A132–A141.

[138] N. V. Faenza, L. Bruce, Z. W. Lebens-Higgins, I. Plitz, N. Pereira, L. F. J. Piper, G. G. Amatucci, *J. Electrochem. Soc.* 2017, *164*, A3727–A3741.

[139] I. A. Shkrob, J. A. Gilbert, P. J. Phillips, R. Klie, R. T. Haasch, J. Bareño, D. P. Abraham, *J. Electrochem. Soc.* 2017, *164*, A1489–A1498.

[140] T. Toma, R. Maezono, K. Hongo, *ACS Appl. Energy Mater.* 2020, *3*, 4078–4087.

[141] D. Pritzl, T. Teufl, A. T. S. Freiberg, B. Strehle, J. Sicklinger, H. Sommer, P. Hartmann, H. A. Gasteiger, *J. Electrochem. Soc.* 2019, *166*, A4056–A4066.

[142] R. Fantin, E. Trevisanello, R. Ruess, A. Pokle, G. Conforto, F. H. Richter, K. Volz, J. Janek, *Chem. Mater.* 2021, *33*, 2624–2634.

[143] L. You, B. Chu, G. Li, T. Huang, A. Yu, *J. Power Sources* 2021, *482*, 228940.

[144] X. Li, C. Zhao, J. He, Y. Li, Y. Wang, L. Liu, J. Huang, C. Li, D. Wang, J. Duan, Y. Zhang, *Electrochim. Acta* 2022, *406*, 139879.

[145] H. H. Ryu, H. W. Lim, S. G. Lee, Y. K. Sun, *Nat. Energy* 2023, DOI: 10.1038/s41560-023-01403-8.

[146] R. S. Negi, Y. Yusim, R. Pan, S. Ahmed, K. Volz, R. Takata, F. Schmidt, A. Henss, M. T. Elm, *Adv. Mater. Interfaces* 2022, *9*, 2101428.

[147] R. S. Negi, E. Celik, R. Pan, R. Stäglich, J. Senker, M. T. Elm, *ACS Appl. Energy Mater.* 2021, *4*, 3369–3380.

[148] N. Kalaiselvi, A. V. Raajaraajan, B. Sivagaminathan, N. G. Renganathan, N. Muniyandi, M. Ragavan, *Ionics* 2003, *9*, 382–387.

[149] M. Song, I. Kwon, H. Kim, S. Shim, D. R. Mumm, *J. Appl. Electrochem.* 2006, *36*, 801–805.

[150] M. Y. Song, I. H. Kwon, H. R. Park, D. R. Mumm, *Ceram. Int.* 2012, *38*, 2443–2448.

[151] M. M. Rao, C. Liebenow, M. Jayalakshmi, H. Wulff, U. Guth, F. Scholz, *J. Solid State Electrochem.* 2001, *5*, 348–354.

[152] P. Kalyani, N. Kalaiselvi, N. G. Renganathan, M. Raghavan, *Ionics Kiel* 2003, *9*, 417–427.

[153] A. Vandenberg, A. Hintennach, *Russ. J. Electrochem.* 2015, *51*, 310–317.

[154] K. Palanichamy, N. G. Renganathan, *J. Power Sources* 2003, *123*, 53–60.

[155] M. Mock, M. Bianchini, F. Fauth, K. Albe, S. Sicolo, *J. Mater. Chem. A* 2021, *9*, 14928–14940.

[156] J. Xie, X. Huang, Z. Zhu, J. Dai, *Ceram. Int.* 2011, *37*, 665–668.

[157] J.-M. T. M. R. Palacin, D. Larcher, A. Audemer, N. Sac-Epee, G. G. Amatucci, *J. Electrochem. Soc.* 1997, *144*, 4226–4236.

[158] Y. Sun, P. Wan, J. Pan, C. Xu, X. Liu, *Solid State Ionics* 2006, *177*, 1173–1177.

[159] D. Larcher, M. R. Palacín, G. G. Amatucci, J. -M. Tarascon, *J. Electrochem. Soc.* 1997, *144*, 408–417.

[160] C. Delmas, Y. Borthomieu, C. Faure, A. Delahaye, M. Figlarz, *Solid State Ionics* 1989, *32–33*, 104–111.

[161] J. Z. Yu-hong Luo, Qing-lin Pan, Han-xin Wei, Ying-de Huang, Lin-bo Tang, Zhen-yu Wang, Zhen-jiang He, Cheng Yan, Jing Mao, Ke-hua Dai, Xia-hui Zhang, *Nano Energy* 2022, *102*, 107626.

[162] G. C. Kisuk Kang, Ying Shirley Meng, Julien Bréger, Clare P. Grey, *Science* 2006, *311*, 977–981.

[163] M. Tsuda, H. Arai, M. Takahashi, H. Ohtsuka, Y. Sakurai, K. Sumitomo, H. Kageshima, *J. Power Sources* 2005, *144*, 183–190.

[164] X. Cao, Y. Qiao, M. Jia, P. He, H. Zhou, *Adv. Energy Mater.* 2022, *12*, 1–14.

[165] X. Lai, D. Gao, J. Bi, Y. Li, P. Cheng, C. Xu, D. Lin, *J. Alloys Compd.* 2009, *487*, 30–32.

[166] M. Yoshimura, K. S. Han, S. Tsurimoto, *Solid State Ionics* 1998, *106*, 39–44.

[167] M. Rubin, S. J. Wen, T. Richardson, J. Kerr, K. Von Rottkay, J. Slack, *Sol. Energy Mater. Sol. Cells* 1998, *54*, 59–66.

[168] M. A. Eleruja, G. O. Egharevba, O. A. Abulude, O. O. Akinwunmi, C. Jeynes, E. O. B. Ajayi, *J. Mater. Sci.* 2007, *42*, 2758–2765.

[169] M. S. El-Bana, I. M. El Radaf, S. S. Fouad, G. B. Sakr, *J. Alloys Compd.* 2017, *705*, 333–339.

[170] L. de Biasi, A. Schiele, M. Roca-Ayats, G. Garcia, T. Brezesinski, P. Hartmann, J. Janek, *ChemSusChem* 2019, *12*, 2240–2250.

[171] H. Li, N. Zhang, J. Li, J. R. Dahn, *J. Electrochem. Soc.* 2018, *165*, A2985–A2993.

[172] M. E. Arroyo y de Dompablo, G. Ceder, *J. Power Sources* 2003, *119–121*, 654–657.

[173] L. Croguennec, C. Pouillerie, C. Delmas, *Solid State Ionics* 2000, *135*, 259–266.

[174] J. M. Tarascon, G. Vaughan, Y. Chabre, L. Seguin, M. Anne, P. Strobel, G. Amatucci, *J. Solid State Chem.* 1999, *147*, 410–420.

[175] E. B. Quisbert, F. Fauth, A. M. Abakumov, M. Blangero, M. Guignard, C. Delmas, 2023, *19,* 2300616.

[176] N. Ikeda, I. Konuma, H. B. Rajendra, T. Aida, N. Yabuuchi, *J. Mater. Chem. A* 2021, *9*, 15963–15967.

[177] C. Wang, R. Zhang, K. Kisslinger, H. L. Xin, *Nano Lett.* 2021, *21*, 3657–3663.

[178] M. Sadowski, L. Koch, K. Albe, S. Sicolo, *Chem. Mater.* 2022, *35*, 584-594.

[179] K. Y. Park, Y. Zhu, C. G. Torres-Castanedo, H. J. Jung, N. S. Luu, O. Kahvecioglu, Y. Yoo, J. W. T. Seo, J. R. Downing, H. D. Lim, M. J. Bedzyk, C. Wolverton, M. C. Hersam, *Adv. Mater.* 2022, *34*, 2106402.

[180] Y. Huang, Y. Zhu, H. Fu, M. Ou, C. Hu, S. Yu, Z. Hu, C. Chen, G. Jiang, H. Gu, H. Lin, W. Luo, Y. Huang, *Angew. Chemie* 2021, *133*, 4732–4738.

[181] M. Zou, M. Yoshio, S. Gopukumar, J. I. Yamaki, *Electrochem. Solid-State Lett.* 2004, *7*, A176.

[182] M. E. Arroyo y de Dompablo, A. Van der Ven, G. Ceder, *Phys. Rev. B - Condens. Matter Mater. Phys.* 2002, *66*, 064112.

[183] H. Das, A. Urban, W. Huang, G. Ceder, *Chem. Mater.* 2017, *29*, 7840–7851.

[184] H. Li, W. Hua, X. Liu-Théato, Q. Fu, M. Desmau, A. Missyul, M. Knapp, H. Ehrenberg, S. Indris, *Chem. Mater.* 2021, *33*, 9546–9559.

[185] K. Märker, P. J. Reeves, C. Xu, K. J. Griffith, C. P. Grey, *Chem. Mater.* 2019, *31*, 2545–2554.

[186] J. P. Peres, F. Weill, C. Delmas, *Solid State Ionics* 1999, *116*, 19–27.

[187] C. Chazel, M. Ménétrier, L. Croguennec, C. Delmas, *Inorg. Chem.* 2006, *45*, 1184–1191.

[188] C. Delmas, M. Ménétrier, L. Croguennec, S. Levasseur, J. P. Pérès, C. Pouillerie, G. Prado, L. Fournès, F. Weill, *Int. J. Inorg. Mater.* 1999, *1*, 11–19.

[189] S. Sicolo, M. Sadowski, K. Vettori, M. Bianchini, J. Janek, *Chem. Mater.* 2023, DOI: 10.1021/acs.chemmater.3c02534.

[190] A. Van Der Ven, J. C. Thomas, Q. Xu, B. Swoboda, D. Morgan, *Phys. Rev. B - Condens. Matter Mater. Phys.* 2008, *78*, 104306.

[191] A. Van Der Ven, G. Ceder, Electrochem. Solid-State Lett. 2000, *3*, 301.

[192] A. Grenier, P. J. Reeves, H. Liu, I. D. Seymour, K. Märker, K. M. Wiaderek, P. J. Chupas, C. P. Grey, K. W. Chapman, *J. Am. Chem. Soc.* 2020, *142*, 7001–7011.

[193] D. Lee, M. Avdeev, D. Kim, W. H. Shin, J. Hong, M. Kim, ACS Appl. Energy Mater. 2023, *6*, 5309-5317.

[194] M. Weiss, R. Ruess, J. Kasnatscheew, Y. Levartovsky, N. R. Levy, P. Minnmann, L. Stolz, T. Waldmann, M. Wohlfahrt-Mehrens, D. Aurbach, M. Winter, Y. Ein-eli, J. Janek, 2021, *11*, 2101126.

[195] D. D. MacNeil, Z. Lu, J. R. Dahn, *J. Electrochem. Soc.* 2002, *149*, A1332.

[196] J. R. Dahn, E. W. Fuller, M. Obrovac, U. von Sacken, *Solid State Ionics* 1994, *69*, 265–270.

[197] S. L. Dreyer, A. Kondrakov, J. Janek, T. Brezesinski, *J. Mater. Res.* 2022, *37*, 3146–3168.

[198] H. Baltruschat, *J. Am. Soc. Mass Spectrom.* 2004, *15*, 1693–1706.

[199] T. Herl, Methodical developments for hyphenation of electrochemistry and mass spectrometry coupled to different separation techniques, Universität Regensburg, 2020, DOI: 10.5283/epub.43514.

[200] R. Sim, Z. Cui, A. Manthiram, *ACS Energy Lett.* 2023, 5143–5148.

[201] B. Salomez, S. Grugeon, M. Armand, P. Tran-Van, S. Laruelle, *J. Electrochem. Soc.* 2023, *170*, 050537.

[202] S. E. Renfrew, B. D. McCloskey, *J. Am. Chem. Soc.* 2017, *139*, 17853–17860.

[203] J. Wandt, A. T. S. Freiberg, A. Ogrodnik, H. A. Gasteiger, *Mater. Today* 2018, *21*, 825–833.

[204] T. Hatsukade, A. Schiele, P. Hartmann, T. Brezesinski, J. Janek, *ACS Appl. Mater. Interfaces* 2018, *10*, 38892–38899.

[205] D. Streich, C. Erk, A. Guéguen, P. Müller, F.-F. Chesneau, E. J. Berg, *J. Phys. Chem. C* 2017, *121*, 13481–13486.

[206] M. Metzger, P. Walke, S. Solchenbach, G. Salitra, D. Aurbach, H. A. Gasteiger, *J. Electrochem. Soc.* 2020, *167*, 160522.

[207] M. Metzger, C. Marino, J. Sicklinger, D. Haering, H. A. Gasteiger, *J. Electrochem. Soc.* 2015, *162*, A1123.

[208] R. Jung, M. Metzger, F. Maglia, C. Stinner, H. A. Gasteiger, *J. Phys. Chem. Lett.* 2017, *8*, 4820–4825.

[209] A. T. S. Freiberg, J. Sicklinger, S. Solchenbach, H. A. Gasteiger, *Electrochim. Acta* 2020, *346*, 136271.

[210] S. Oswald, H. A. Gasteiger, *J. Electrochem. Soc.* 2023, *170*, 30506.

[211] R. Pan, E. Jo, Z. Cui, A. Manthiram, *Adv. Funct. Mater.* 2023, *33*, 2211461.

[212] J. K. Papp, N. Li, L. A. Kaufman, A. J. Naylor, R. Younesi, W. Tong, B. D. McCloskey, *Electrochim. Acta* 2021, *368*, 137505.

[213] F. Kong, C. Liang, L. Wang, Y. Zheng, S. Perananthan, R. C. Longo, J. P. Ferraris, M. Kim, K. Cho, *Adv. Energy Mater.* 2019, *9*, 1802586.

[214] K.-W. Nam, S.-M. Bak, E. Hu, X. Yu, Y. Zhou, X. Wang, L. Wu, Y. Zhu, K.-Y. Chung, X.-Q. Yang, *Adv. Funct. Mater.* 2013, *23*, 1047–1063.

[215] S. Hwang, W. Chang, S. M. Kim, D. Su, D.-H. Kim, J. Y. Lee, K. Y. Chung, E. A. Stach, *Chem. Mater.* 2014, *26*, 1084–1092.

[216] S. Hwang, S. M. Kim, S. M. Bak, K. Y. Chung, W. Chang, *Chem. Mater.* 2015, *27*, 6044–6052.

[217] L. Wang, T. Maxisch, G. Ceder, *Chem. Mater.* 2007, *19*, 543–552.

[218] F. Kong, C. Liang, L. Wang, Y. Zheng, S. Perananthan, R. C. Longo, J. P. Ferraris, M. Kim, K. Cho, *Adv. Energy Mater.* 2019, *9*, 1802586.

[219] L. Terborg, S. Weber, F. Blaske, S. Passerini, M. Winter, U. Karst, S. Nowak, *J. Power Sources* 2013, *242*, 832–837.

[220] N. V. Faenza, Z. W. Lebens-Higgins, P. Mukherjee, S. Sallis, N. Pereira, F. Badway, A. Halajko, G. Ceder, F. Cosandey, L. F. J. Piper, G. G. Amatucci, *Langmuir* 2017, *33*, 9333–9353.

[221] H. R. Morin, D. G. Graczyk, Y. Tsai, S. Lopykinski, H. Iddir, J. C. Garcia, N. Dietz Rago, S. Trask, L. R. Flores, S. B. Son, Z. Zhang, N. M. Johnson, I. Bloom, *ACS Appl. Energy Mater.* 2020, *3*, 2565–2575.

[222] J. A. Gilbert, I. A. Shkrob, D. P. Abraham, *J. Electrochem. Soc.* 2017, *164*, A389–A399.

[223] A. Jarry, S. Gottis, Y. S. Yu, J. Roque-Rosell, C. Kim, J. Cabana, J. Kerr, R. Kostecki, *J. Am. Chem. Soc.* 2015, *137*, 3533–3539.

[224] R. Zhang, F. Strauss, L. Jiang, L. Casalena, L. Li, J. Janek, A. Kondrakov, T. Brezesinski, *Chem. Commun.* 2023, *59*, 4600–4603.

[225] S. Schweidler, M. Bianchini, P. Hartmann, T. Brezesinski, J. Janek, *Batter. Supercaps* 2020, *3*, 1021–1027.

[226] K. Dokko, M. Nishizawa, S. Horikoshi, T. Itoh, M. Mohamedi, I. Uchida, *Electrochem. Solid-State Lett.* 2000, *3*, 125.

[227] S. Schweidler, L. De Biasi, G. Garcia, A. Mazilkin, P. Hartmann, T. Brezesinski, J. Janek, *ACS Appl. Energy Mater.* 2019, *2*, 7375–7384.

[228] S. Oswald, M. Bock, H. A. Gasteiger, *J. Electrochem. Soc.* 2022, *169*, 050501.

[229] S. Oswald, D. Pritzl, M. Wetjen, H. A. Gasteiger, *J. Electrochem. Soc.* 2021, *168*, 120501.

[230] S. Lee, W. Li, A. Dolocan, H. Celio, H. Park, J. H. Warner, A. Manthiram, *Adv. Energy Mater.* 2021, *11*, 2100858.

[231] H. Liu, M. Wolfman, K. Karki, Y.-S. Yu, E. A. Stach, J. Cabana, K. W. Chapman, P. J. Chupas, *Nano Lett.* 2017, *17*, 3452–3457.

[232] Z. Cheng, B. Zhao, Y. J. Guo, L. Yu, B. Yuan, W. Hua, Y. X. Yin, S. Xu, B. Xiao, X. Han, P. F. Wang, Y. G. Guo, *Adv. Energy Mater.* 2022, *12*, 2103461.

[233] F. Wu, S. Fang, M. Kuenzel, G. Kim, F. Wu, S. Fang, M. Kuenzel, A. Mullaliu, J. Kim, X. Gao, *Joule* 2021, *5*, 2177–2194.

[234] J. Langdon, Z. Cui, A. Manthiram, *ACS Energy Lett.* 2021, *6*, 3809–3816.

[235] L. Su, K. Jarvis, H. Charalambous, A. Dolocan, A. Manthiram, *Adv. Funct. Mater.* 2023, *33*, 2213675.

[236] S. Lee, L. Su, A. Mesnier, Z. Cui, A. Manthiram, *Joule* 2023, *7*, 2430–2444.

[237] M. Kim, L. Zou, S.-B. Son, I. D. Bloom, C. Wang, G. Chen, *J. Mater. Chem. A* 2022, *10*, 12890-12899.

[238] H. H. Ryu, B. Namkoong, J. H. Kim, I. Belharouak, C. S. Yoon, Y. K. Sun, *ACS Energy Lett.* 2021, *6*, 2726–2734.

[239] F. Zhang, S. Lou, S. Li, Z. Yu, Q. Liu, A. Dai, C. Cao, M. F. Toney, M. Ge, X. Xiao, W. K. Lee, Y. Yao, J. Deng, T. Liu, Y. Tang, G. Yin, J. Lu, D. Su, J. Wang, *Nat. Commun.* 2020, *11*, 3050.

[240] L. A. Kaufman, T.-Y. Huang, D. Lee, B. D. McCloskey, *ACS Appl. Mater. Interfaces* 2022, *14*, 39959–39964.

[241] S. Ahmed, A. Pokle, S. Schweidler, A. Beyer, M. Bianchini, F. Walther, A. Mazilkin, P. Hartmann, T. Brezesinski, J. Janek, K. Volz, *ACS Nano* 2019, *13*, 10694–10704.

[242] L. Wang, J. Wang, X. Zhang, Y. Ren, P. Zuo, G. Yin, J. Wang, *Nano Energy* 2017, *34*, 215–223.

[243] D. Caurant, N. Baffier, B. Garcia, J. P. Pereira-Ramos, *Solid State Ionics* 1996, *91*, 45–54.

[244] A. Rougier, I. Saadoune, P. Gravereau, P. Willmann, C. Delmasa, *Solid State Ionics* 1996, *90*, 83–90.

[245] T. Ohzuku, A. Ueda, M. Nagayama, Y. Iwakoshi, H. Komori, *Electrochim. Acta* 1993, *38*, 1159–1167.

[246] C. Marichal, J. Hirschinger, P. Granger, M. Menetrier, A. Rougier, C. Delmas, *Inorg. Chem.* 1995, *34*, 1773–1778.

[247] W. Li, J. C. Currie, *J. Electrochem. Soc.* 1997, *144*, 2773–2779.

[248] S. 1996, *J. Mater. Chem. A* 1996, *6*, 193–199.

[249] J. Cho, B. Park, *J. Power Sources* 2001, *92*, 35–39.

[250] Z. Cui, Z. Guo, A. Manthiram, *Adv. Energy Mater.* 2023, *13*, 2203853.

[251] A. R. Armstrong, P. G. Bruce, *Nature* 1996, *381*, 499–500.

[252] H. Zhou, Y. Li, J. Zhang, W. Kang, D. Y. W. Yu, *J. Alloys Compd.* 2016, *659*, 248–254.

[253] M. Jansen, R. Hoppe, *Zeitschrift für Anorg. und Allg. Chemie* 1973, *397*, 279–289.

[254] D. Goonetilleke, F. Riewald, A. O. Kondrakov, J. Janek, T. Brezesinski, M. Bianchini, *J. Phys. Chem. C* 2022, *126*, 16952–16964.

[255] H. Arai, S. Okada, Y. Sakurai, J. Yamaki, *J. Electrochem. Soc.* 1997, *144*, 3117–3125.

[256] M. Yi, Z. Cui, H. Celio, A. Manthiram, *Chem. Mater.* 2023, *35*, 9352–9361.

[257] M. Guilmard, A. Rougier, M. Grüne, L. Croguennec, C. Delmas, *J. Power Sources* 2003, *115*, 305–314.

[258] Z. Liu, H. Zhen, Y. Kim, C. Liang, *J. Power Sources* 2011, *196*, 10201–10206.

[259] S. N. Kwon, M. Y. Song, H. R. Park, *Ceram. Int.* 2014, *40*, 14141–14147.

[260] C. Julien, G. A. Nazri, A. Rougier, *Solid State Ionics* 2000, *135*, 121–130.

[261] H. R. Park, *J. Ind. Eng. Chem.* 2010, *16*, 698–702.

[262] L. Croguennec, Y. Shao-Horn, A. Gloter, C. Colliex, M. Guilmard, F. Fauth, C. Delmas, *Chem. Mater.* 2009, *21*, 1051–1059.

[263] W. Liu, P. Oh, X. Liu, M. J. Lee, W. Cho, S. Chae, Y. Kim, J. Cho, *Angew. Chemie - Int. Ed.* 2015, *54*, 4440–4457.

[264] G.-T. Park, S.-B. Kim, B. Namkoong, N.-Y. Park, H. Kim, C. S. Yoon, Y.-K. Sun, *Mater. Today* 2023, *71*, 38-49.

[265] S. Ho Chang, S.-G. Kang, S.-W. Song, J.-B. Yoon, J.-H. Choy, *Solid State Ionics* 1996, *86–88*, 171–175.

[266] R. Kanno, T. Shirane, Y. Inaba, Y. Kawamoto, *J. Power Sources* 1997, *68*, 145–152.

[267] J. N. Reimers, E. Rossen, C. D. Jones, J. R. Dahn, *Solid State Ionics* 1993, *61*, 335–344.

[268] B. Fuchs, S. Kemmler-Sack, *Solid State Ionics* 1994, *68*, 279–285.

[269] J. Kim, K. Amine, *J. Power Sources* 2002, *104*, 33–39.

[270] L. Yu, T. Liu, R. Amine, J. Wen, J. Lu, K. Amine, *ACS Appl. Mater. Interfaces* 2022, *14*, 23056-23065.

[271] R. Zhang, C. Wang, P. Zou, R. Lin, L. Ma, L. Yin, T. Li, W. Xu, H. Jia, Q. Li, S. Sainio, K. Kisslinger, S. E. Trask, S. N. Ehrlich, Y. Yang, A. M. Kiss, M. Ge, B. J. Polzin, S. J. Lee, W. Xu, Y. Ren, H. L. Xin, *Nature* 2022, *610*, 67–73.

[272] M. Bonda, M. Holzapfel, S. De Brion, C. Darie, T. Feher, P. J. Baker, T. Lancaster, S. J. Blundell, F. L. Pratt, *Phys.*

Rev. B. 2008, *78*, 104409.

[273] C. Pouillerie, L. Croguennec, P. Biensan, P. Willmann, C. Delmas, *J. Electrochem. Soc.* 2000, *147*, 2061.

[274] Q. Xie, W. Li, A. Manthiram, *Chem. Mater.* 2019, *31*, 938–946.

[275] D. Weber, J. Lin, A. Pokle, K. Volz, J. Janek, T. Brezesinski, *J. Electrochem. Soc.* 2022, *169*, 030540.

[276] D. Kitsche, S. Schweidler, A. Mazilkin, H. Geßwein, F. de Fauth, E. Suard, P. Hartmann, T. Brezesinski, J. Janek, M. Bianchini, *Mater. Adv* 2020, *1*, 639.

[277] Q. Liu, X. Su, D. Lei, Y. Qin, J. Wen, F. Guo, Y. A. Wu, Y. Rong, R. Kou, X. Xiao, F. Aguesse, J. Bareño, Y. Ren, W. Lu, Y. Li, *Nat. Energy* 2018, *3*, 936–943.

[278] M. Zhang, C. Wang, J. Zhang, G. Li, L. Gu, *ACS Omega* 2021, *6*, 16465–16471.

[279] L. Ni, H. Chen, J. Gao, Y. Mei, H. Wang, F. Zhu, J. Huang, B. Zhang, W. Xu, B. Song, Y. Zhang, W. Deng, G. Zou, H. Hou, Y. Zhou, X. Ji, *Nano Energy* 2023, *115*, 108743.

[280] T. Sattar, B.-S. Jin, H.-S. Kim, *ECS Meet. Abstr.* 2020, *MA2020-02*, 258.

[281] L. Li, L. Xia, H. Yang, X. Zhan, J. Chen, Z. Chen, J. Duan, *J. Alloys Compd.* 2020, *832*, 154959.

[282] G. Sun, X. Yin, W. Yang, J. Zhang, Q. Du, Z. Ma, G. Shao, Z.-B. Wang, *Electrochim. Acta* 2018, *272*, 11–21.

[283] V. Bianchi, S. Bach, C. Belhomme, J. Farcy, J. P. Pereira-Ramos, D. Caurant, N. Baffier, P. Willmann, *Electrochim. Acta* 2001, *46*, 999–1011.

[284] H. Kim, Y. Kong, W. M. Seong, A. Manthiram, *ACS Appl. Mater. Interfaces* 2023, *15*, 26585–26592.

[285] Z. Sun, Y. Lai, N. Lv, Y. Hu, B. Li, S. Jing, L. Jiang, M. Jia, J. Li, S. Chen, F. Liu, *Adv. Mater. Interfaces* 2021, *8*, 1–8.

[286] F. Reissig, M. A. Lange, L. Haneke, T. Placke, W. G. Zeier, M. Winter, R. Schmuch, A. Gomez-Martin, *ChemSusChem* 2022, *15*, e202102220.

[287] Y. Li, L. Ben, H. Yu, W. Zhao, X. Liu, X. Huang, *Inorganics* 2022, *10*, 111.

[288] W. Li, J. Zhang, Y. Zhou, W. Huang, X. Liu, Z. Li, M. Gao, Z. Chang, N. Li, J. Wang, S. Lu, X. Li, W. Wen, D. Zhu, Y. Lu, W. Zhuang, *ACS Appl. Mater. Interfaces* 2020, *12*, 47513–47525.

[289] S. Liu, Z. Dang, D. Liu, C. Zhang, T. Huang, A. Yu, *J. Power Sources* 2018, *396*, 288–296.

[290] D. Kitsche, F. Strauss, Y. Tang, N. Bartnick, A. Y. Kim, Y. Ma, C. Kübel, J. Janek, T. Brezesinski, *Batter. Supercaps* 2022, *5*, e202100397.

[291] K. Min, K. Park, S. Y. Park, S.-W. Seo, B. Choi, E. Cho, *J. Electrochem. Soc.* 2018, *165*, A79–A85.

[292] Z. Xue, X. Qi, L. Li, W. Li, L. Xu, Y. Xie, X. Lai, G. Hu, Z. Peng, Y. Cao, K. Du, *ACS Appl. Mater. Interfaces* 2018, *10*, 27141–27149.

[293] F. Lin, I. M. Markus, D. Nordlund, T.-C. Weng, M. D. Asta, H. L. Xin, M. M. Doeff, *Nat. Commun.* 2014, *5*, 3529.

[294] B. Han, S. Xu, S. Zhao, G. Lin, Y. Feng, L. Chen, D. G. Ivey, P. Wang, W. Wei, *ACS Appl. Mater. Interfaces* 2018, *10*, 39599–39607.

[295] Y. Cho, P. Oh, J. Cho, *Nano Lett.* 2013, *13*, 1145–1152.

[296] P. Vassilaras, X. Ma, X. Li, G. Ceder, *J. Electrochem. Soc.* 2013, *160*, A207–A211.

[297] M. Holzapfel, C. Darie, P. Bordet, E. Chappel, M. D. Núñez-Regueiro, S. Diaz, S. De Brion, G. Chouteau, P. Strobel, *Solid State Sci.* 2005, *7*, 497–506.

[298] T. Matsumura, R. Kanno, R. Gover, Y. Kawamoto, T. Kamiyama, B. J. Mitchell, *Solid State Ionics* 2002, *152–153*, 303–309.

[299] M. H. Han, E. Gonzalo, M. Casas-Cabanas, T. Rojo, *J. Power Sources* 2014, *258*, 266–271.

[300] E. Chappel, F. Dupont, G. Chouteau, C. Darie, A. Sulpice, *Eur. Phys. J. B* 2000, *17*, 609–614.

[301] M. Sofin, M. Jansen, Z. f. Naturforschung B 2005, *60*, 701–704.

[302] E. Chappel, M. D. Núñez-Regueiro, G. Chouteau, O. Isnard, C. Darie, *Eur. Phys. J. B* 2000, *17*, 615–622.

[303] C. Zhao, Q. Wang, Z. Yao, J. Wang, B. Sánchez-Lengeling, F. Ding, X. Qi, Y. Lu, X. Bai, B. Li, H. Li, A. Aspuru-Guzik, X. Huang, C. Delmas, M. Wagemaker, L. Chen, Y. S. Hu, *Science* 2020, *370*, 708–712.

[304] R. Kaushalya, P. Iyngaran, N. Kuganathan, A. Chroneos, *Energies* 2018, *12*, 3094.

[305] C. Delmas, I. Saadoune, P. Dordor, *Mol. Cryst. Liq. Cryst. Sci. Technol. Sect. A. Mol. Cryst. Liq. Cryst.* 1994, *244*, 337–342.

[306] L. Zheng, R. Fielden, J. C. Bennett, M. N. Obrovac, *J. Power Sources* 2019, *433*, 226698.

[307] H. Kim, A. Choi, S. W. Doo, J. Lim, Y. Kim, K. T. Lee, *J. Electrochem. Soc.* 2018, *165*, A201–A205.

[308] A. J. Toumar, S. P. Ong, W. D. Richards, S. Dacek, G. Ceder, *Phys. Rev. Appl.* 2015, *4*, 064002.

[309] J. Y. Hwang, C. S. Yoon, I. Belharouak, Y. K. Sun, *J. Mater. Chem. A* 2016, *4*, 17952–17959.

[310] G. Li, W. Zhu, W. Liu, *J. Indian Chem. Soc.* 2022, *99*, 100424.

[311] L. Karger, D. Weber, D. Goonetilleke, A. Mazilkin, H. Li, R. Zhang, Y. Ma, S. Indris, A. Kondrakov, J. Janek, T. Brezesinski, *Chem. Mater.* 2022, *35*, 648-657.

[312] L. Karger, S. Korneychuk, W. Van Den Bergh, S. L. Dreyer, R. Zhang, A. Kondrakov, J. Janek, T. Brezesinski, *Chem. Mater.* 2023, DOI: 10.1021/acs.chemmater.3c02727.

[313] L. Karger, Korneychuk, S. Sicolo, H. Li, W. van den Bergh, R. Zhang, S. Indris, A. Kondrakov, J. Janek, T. Brezesinski, *submitted to peer-reviewed journal.*

[314] L. Karger, B.N. Nunes, Y. Yusim, A. Mazilkin, R. Zhang, W. Zhao, A. Henss, A. Kondrakov, J. Janek, T. Brezesinski, *submitted to peer-reviewed journal.*

6 Appendix

6.1 Publication IV: Protective Nanosheet Coatings for Thiophosphate-Based All-Solid-State Batteries

Publication IV describes the initial project of this doctoral work, aimed at using so-called nanosheet materials as protective barrier between cathode material and argyrodite-type thiophosphate solid electrolyte. Without such a barrier, oxidation and decomposition of the electrolyte would occur during cycling. Nanosheets, in principle, offer ideal properties, such as high mechanical strength and atomic thickness, for such an application. Therefore, several methods were tested for the deposition of nanosheets. While dry coating provided good surface coverage, the secondary particle structure could not withstand the ball-milling conditions. Therefore, deposition from organic solvents was chosen for the testing of three different nanosheet types. The respective materials were WS_2, h-BN and exfoliated $((CH_3(CH_2)_3)_4N)_4Nb_6O_{17}$ nanosheets. Stabilization was only observed in solid-state batteries, most likely due to the partial coating that allows liquid electrolyte to bypass the barrier. The transformation of WS_2 to partially oxidized material was observed and the stabilization mechanism was investigated. From the results, we infer a stabilization due to prevention of contact loss instead of solid electrolyte degradation (electrochemical oxidation).

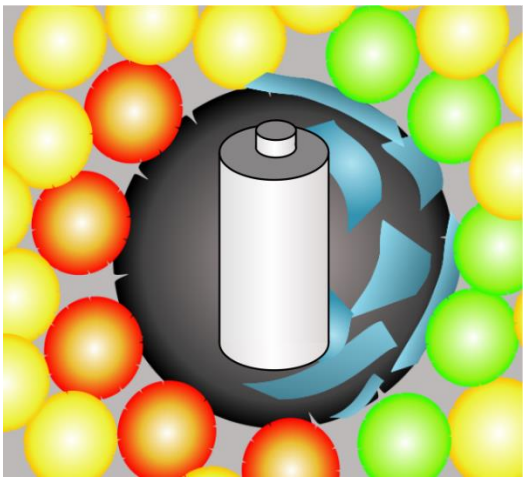

Figure 10. Graphical table of content of publication IV [314].

The experiments were planned and designed by the first author under the supervision of A. Kondrakov, J. Janek and T. Brezesinski. The first author developed and optimized the deposition method, and applied it to h-BN and WS_2 nanosheets. The first author carried out the electrochemical measurements in LIBs and solid-state batteries on those materials, as well as a reference material. Synthesis and coating of the niobate nanosheet, as well as testing in LIBs, was carried out by B. Nunes. Y. Yusim carried out the ToF-SIMS measurements and analysis under the supervision of A. Henss and J. Janek and discussed the data with the first author. A. Mazilkin carried out the TEM analysis and discussed the data with the first author. R. Zhang conducted the SEM experiments, and the data were analyzed by the first author. W. Zhao carried out electrochemical tests in solid-state batteries for the niobate-coated material. The manuscript was written by the first author and edited by all coauthors.

Submitted Manuscript of Publication IV

Protective Nanosheet Coatings for Thiophosphate-Based All-Solid-State Batteries

Leonhard Karger, Barbara Nascimento Nunes, Yuriy Yusim, Andrey Mazilkin, Ruizhuo Zhang, Wengao Zhao, Anja Henss, Aleksandr Kondrakov, Jürgen Janek* and Torsten Brezesinski*

L. Karger, Dr. B. N. Nunes, Dr. A. Mazilkin, R. Zhang, Dr. W. Zhao, Dr. A. Kondrakov, Prof. J. Janek, Dr. T. Brezesinski

Battery and Electrochemistry Laboratory (BELLA), Institute of Nanotechnology, Karlsruhe Institute of Technology (KIT), Hermann-von-Helmholtz-Platz 1, 76344 Eggenstein-Leopoldshafen, Germany

E-mail: torsten.brezesinski@kit.edu

Y. Yusim, Dr. A. Henss, Prof. J. Janek

Institute of Physical Chemistry & Center for Materials Research (ZfM/LaMa), Justus-Liebig-University Giessen, Heinrich-Buff-Ring 17, 35392 Giessen, Germany

E-mail: juergen.janek@phys.Chemie.uni-giessen.de

Dr. A. Mazilkin

Karlsruhe Nano Micro Facility (KNMFi), Karlsruhe Institute of Technology (KIT), Herrmann-von-Helmholtz-Platz 1, 76344 Eggenstein-Leopoldshafen, Germany

Dr. A. Kondrakov

BASF SE, Carl-Bosch-Str. 38, 67056 Ludwigshafen, Germany

Abstract

Superionic sulfide solid electrolytes (SEs) are of considerable interest for application in solid-state batteries, but suffer from limited stability. When in combination with state-of-the-art cathode active materials (CAMs), severe degradation at the CAM/SE interface occurs during electrochemical cycling. To improve upon the interfacial stability, inert coatings can be applied to the CAM particles, with the goal of preventing direct contact to the SE. In this study, different methods of depositing coatings, including hexagonal boron nitride, tungsten sulfide and exfoliated $((CH_3(CH_2)_3)_4N)_4Nb_6O_{17}$, in the form of nanosheets onto the free surface of a Ni-rich $LiNi_xCo_yMn_zO_2$ (NCM) CAM are examined and compared with one another. While dry coating is shown to produce relatively uniform coatings (good surface coverage), the secondary particle morphology of the NCM makes ball milling as a mechanical deposition method less attractive. In contrast, deposition from dispersions in organic solvents yields protective coatings with a lower degree of surface coverage. The different materials are electrochemically tested in liquid- and solid-electrolyte-based lithium-ion batteries. A stabilizing effect from nanosheet coating is only observed for the cells with lithium thiophosphate SE.

1. Introduction

Engineering of stable interfaces at both anode and cathode is one of the main challenges in making bulk-type solid-state batteries (SSBs) competitive with the established lithium-ion battery (LIB) technology.[1–3] Among the existing superionic conductors, lithium thiophosphates stand out due to high ionic conductivity at room temperature and favorable mechanical properties for electrode/separator manufacturing and battery operation.[4] When used as a catholyte, their reactivity toward energy-dense cathode active materials (CAMs), such as layered $LiNi_xCo_yMn_zO_2$ (NCM or NMC) or $LiNi_xCo_yAl_zO_2$ (NCA), necessitates protective barriers to prevent degradation upon electrochemical cycling.[5–7] Coating of the CAM particles is a promising strategy to achieve stable cathode interfaces (i.e., between NCMs and lithium thiophosphates).[6,8]

Commonly employed coatings for SSB application are (lithiated) metal oxides of niobium or zirconium, which can be applied by different techniques, such as sol-gel chemistry,[9–14] dry coating,[15] nanoparticle deposition[16–18] or atomic layer deposition.[19,20] Nanosheet coatings consisting of single or few atomic layers combine various beneficial properties, including high mechanical strength,[21] chemical stability[22] and gas blocking ability.[23] Furthermore, nanosheets are extremely thin (down to the theoretical limit of a single layer),[24,25] thus barely affecting the battery's energy density (by introducing additional mass in the form of inactive material).

In recent years, some nanosheet materials have already been tested as CAM coatings in LIBs.[26–30] Graphene takes a prominent position owing to its high stability and thoroughly researched properties and processing (including synthesis). Reduced graphene oxide is typically used to produce such carbon coatings due to facile

deposition upon reduction, although some authors argue that surface modification or gaseous reducing agents are required, making the techniques experimentally challenging.[31–34] Alternative methods relying on surfactant-stabilized graphene dispersions and allowing for controlled deposition have been reported.[35] Hersam and coworkers elaborate on this approach by employing Pickering emulsions for preparing conformal graphene shells, ultimately aiming at high volumetric density cathodes by avoiding low-density carbon black and decreasing porosity.[26] Graphene coating is found, among others, to attenuate oxygen release from the cathode with cycling to high cutoff potentials (note: in the SSB case, oxygen loss would contribute to the decomposition of the thiophosphate solid electrolyte).[27,36,37]

Apart from graphene, other nanosheet coatings and preparation methods have been reported. For example, layered double hydroxides were deposited from aqueous dispersions onto NCM and NCA both before and after calcination.[28,38] Graphitic carbon nitride can also be deposited from aqueous dispersions or by chemical vapor deposition (CVD).[39] Transition-metal chalcogenides, such as MoS_2 and WSe_2, have been shown to increase the stability of CAMs.[29] Recently, Maiti *et al.* utilized CVD-grown WSe_2 for improving the cycling performance of NCM851005 (85% Ni content) and high-voltage $LiNi_{0.5}Mn_{1.5}O_4$ (LNMO). Stabilization is ascribed to reduced transition-metal leaching from the CAM particles, while the coating apparently dissolves to some degree into the electrode, which in turn helps to form a protective layer on the anode.[29] Overall, nanosheet coatings have been employed successfully in LIBs and shown to facilitate charge transport[26] and/or mitigate cathode and electrolyte degradation.[29,31] Consequently, they may also have advantageous properties for application in SSBs. However, to date, no such studies have been performed that examine nanosheet-coated CAMs in batteries using superionic solid electrolytes.

Herein, we investigate the coating of polycrystalline $LiNi_{0.85}Co_{0.1}Mn_{0.05}O_2$ (NCM851005 with 85% Ni content, referred to as NCM in the following) with commercially available nanosheet materials. The focus is on improving the protective properties while avoiding the synthesis of conductive materials, such as graphene. This precautionary measure is taken to mitigate (electro)chemical degradation (oxidation) of the solid electrolyte. We first concentrate on establishing a coating method for hexagonal boron nitride (h-BN), which is isostructural to graphite/graphene, but electronically insulating.[40] h-BN is attractive as a coating material because of its high chemical stability, reacting only under extreme conditions (e.g., boiling sulfuric acid).[22] Dry- and liquid-phase deposition routes are compared with regards to coating content and distribution on the particle surface, as well as structural integrity of the CAM. Specifically, h-BN coating is compared to that achieved with WS_2 and exfoliated $((CH_3(CH_2)_3)_4N)_4Nb_6O_{17}$. The latter materials are known as functional coatings and can be readily obtained in nanosheet format.[41–45] WS_2 is found to undergo side reactions with the NCM particles upon mild annealing, and electrochemical testing shows that nanosheet coating leads to stability improvements in SSBs, but not in LIB cells. This highlights the differences in stabilization strategies for batteries with liquid and solid electrolytes and emphasizes the need for further studies.

2. Results and Discussion

2.1. Coating Methods

Liquid-phase stabilization of h-BN (e.g., from liquid-phase exfoliation) can be achieved with similar solvents or solvent-dispersant systems as for graphene.[42,46,47] Much of the work on h-BN stabilization has been focused on aqueous dispersions.[46,48] However, water is known to leach lithium from layered Ni-rich oxide CAMs and to adversely affect their surface structure and electrochemical properties (formation of rock salt-type NiO, etc.).[49,50] Furthermore, the dispersant may decompose and lead to the formation of surface carbonates during the annealing process after coating. Note that hybrid coatings containing carbonate species have recently been shown to have a profound effect on the cycling performance of thiophosphate-based SSBs.[11,12,51–54] To avoid false interpretation of carbonate coating rather than stabilization induced by the nanosheet materials, we focus on methods that do not rely on aqueous dispersions and organic dispersants.

Dry coating is a facile approach to avoid solvent exposure and dispersant chemistry altogether. Ball milling at a rotational speed of 100 rpm and with small ZrO_2 balls was chosen to limit the overall energy input. Further exfoliation of the nanosheets may be achieved under ball-milling conditions, since the CAM particles, in principle, can act as an abrasive agent, as reported for the exfoliation of nanosheet materials with common salts.[55,56] The material obtained was probed using scanning electron microscopy (SEM), see **Figure 1b**, **g** and **l** [**Figure 1a**, **f** and **k** is showing the pristine (uncoated) NCM]. Investigation of the surface of the secondary particles revealed the deposition of small circular nanosheets and, in some instances, shearing of individual sheets. This is sometimes observed during exfoliation of individual nanosheets and suggests that low-energy ball milling helps to further increase the available surface by shearing of few-layer sheets.[57] However, the secondary particle structure was only partially retained, as there was clearly chipping and fracturing of the NCM CAM.

To improve the mixing of nanosheets and NCM and reduce mechanical strain, it was attempted to perform wet milling using acetonitrile (with NCM:acetonitrile = 1:1 by weight). As seen in **Figure 1c**, **h** and **m**, this exacerbated the problem of particle disintegration, which may be due to dissolution of residual lithium from the polycrystalline sample. It was also attempted to mechanically mix the materials using a laboratory grade blender (Kinematica), but they tended to stick to the sides of the jar and agglomerate rather than being mixed uniformly. Therefore, although there is some decent deposition, the particle disintegration does not allow employing mechanical mixing for nanosheet coating of polycrystalline CAMs.

While water is detrimental when working with Ni-rich cathodes,[49] organic solvents may be used to suspend the nanosheets and deposit them onto the particles. Two methods of attaching nanosheets to the surface were tested, namely evaporation under agitation and spontaneous aggregation. In the first case, 10 mg of h-BN nanosheets were dispersed in 10 mL of acetonitrile via sonication for 30 min, after which 1.0 g of

CAM was added. The mixture was then vigorously stirred for 10 min at room temperature, followed by removal of the solvent in vacuo with continuous stirring. In the second approach, the h-BN nanosheets were suspended as described. Afterwards, NCM was added, and the mixture was vigorously stirred overnight to allow the nanosheets to spontaneously adhere to the particle surface. The suspension was then left to separate, and the modified CAM was harvested as the sediment. Lastly, the residual solvent was decanted, and the powder was dried again under vacuum. The coated samples were also probed using SEM, as shown in **Figure 1d**, **e**, **i**, **j**, **n** and **o**. As evident, in both samples, the secondary particle structure was retained, and there are no signs of deagglomeration or chipping. Aggregates of nanosheets are clearly visible on the particle surface. However, in the case of “evaporation under agitation”, the nanosheet content appears to be slightly higher. This is also corroborated by the observation that even after stirring overnight the supernatant was still somewhat turbid, indicating that not all of the nanosheets attach to the surface. Furthermore, the evaporation-based processing takes less time, and the sample is exposed to solvent for a shorter duration, which is why this route was used in the following coating experiments.

Taken together, the “evaporation under agitation” approach worked best with this specific set of materials. However, dry coating also yields high loadings (good surface coverage). In addition, the nanosheets appear to attach closely to the particle surface, whereas more fluffy aggregates are formed upon wet processing. For CAM morphologies that have a higher mechanical strength, such as single- or quasi single-crystalline, dry coating may indeed be the better choice, as particle (surface) integrity plays a crucial role in the cyclability.[58,59] As a preliminary test, we have examined the dry coating of a single-crystalline NCM831205 (83% Ni content). The results indicate that h-BN deposition onto the CAM surface is indeed possible. However, the coating coverage was not very uniform (see **Figure S1**, Supporting Information), and determining the optimal process parameters would require further study. Nevertheless, dry coating as such seems promising for the emerging single-crystal CAMs, for which surface-based degradation is also a major contributor to capacity fading.[59]

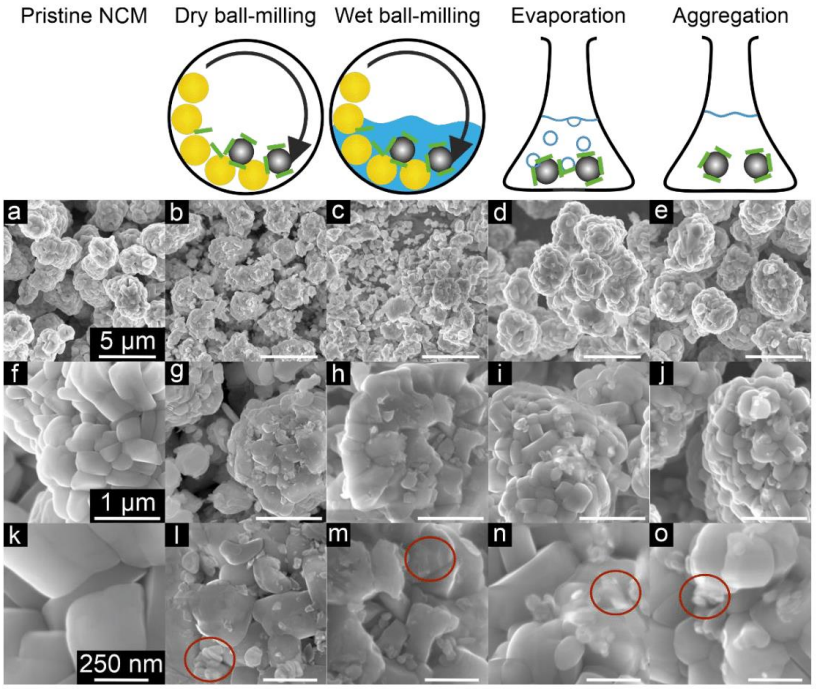

Figure 1. Schematic representation of nanosheet coating by dry ball-milling, wet ball-milling, solvent evaporation and spontaneous adsorption. (a-o) Low- and high-magnification SEM images for the comparison of coating attempts using h-BN nanosheets (highlighted by red circles). (a, f, k) Uncoated NCM particles, (b, g, l) dry ball-milling assisted coating, (c, h, m) wet ball-milling assisted coating, (d, i, n) solvent evaporation-based coating and (e, j, o) spontaneous adsorption-based coating.

2.2. Comparison of h-BN, WS_2 and Niobate-Type Nanosheet Coatings

To study a broader range of materials, the "evaporation under agitation" approach discussed above was applied to coating of the NCM CAM with 1 wt.% of h-BN, WS_2 and exfoliated $((CH_3(CH_2)_3)_4N)_4Nb_6O_{17}$ nanosheets (hereafter referred to as hBN-NCM, WS_2-NCM and Nb-NCM, respectively). For ensuring good contact with the secondary particle structure, the samples were heated at 400 °C in oxygen, which has been shown previously to be an optimal post-deposition treatment temperature for oxide coatings[10,19,20] in thiophosphate-based SSB cells. The organic cation in $((CH_3(CH_2)_3)_4N)_4Nb_6O_{17}$ decomposes during heating, yielding some kind of lithiated niobate-type (Li_xNbO_y) coating.[60]

The hBN-NCM, WS_2-NCM and Nb-NCM samples were investigated by SEM, inductively coupled plasma-optical emission spectroscopy (ICP-OES) and powder X-ray diffraction (PXRD), as shown in **Table 1** and **Figure 2a-h**. The pristine NCM as a reference was treated under the same conditions as the other samples, but in absence

of nanosheets. Structural analysis indicated that all materials are single phase and the lattice parameters do not change much with coating. Exemplary PXRD patterns collected from WS_2-NCM and hBN-NCM and Rietveld fits to the patterns are shown in **Figure S2** (Supporting Information). The greatest difference to the reference CAM was found for Nb-NCM, which exhibits slightly larger lattice parameters and unit-cell volume. This could point towards structural degradation, since an increase in lattice parameters is typically associated with the formation of $Ni_{Li}^{\bullet}$ point defects (cation intermixing). This, in turn, may be due to lithium loss from the NCM and possibly "absorption" by the niobate-type coating. ICP-OES revealed that the coating content is lowest for h-BN, with only about half of the nominal amount deposited onto the CAM particles. However, for both WS_2-NCM and Nb-NCM, it was close to the targeted content, indicating effective coating (note: 0.91 wt.% would theoretically correspond to 0.97 wt.% $LiNbO_3$). For the WS_2 nanosheets, it was even higher than the targeted loading, which may be because of the presence of oxygen impurities, as the nanosheets can readily oxidize at room temperature. In such a case, the actual stoichiometry to be considered would be $WS_{2-x}O_x$, causing excessive tungsten content when aiming for 1 wt.% WS_2 coating due to the lower molecular weight. The low- and high-magnification SEM images in **Figure 2c**-**h** confirm successful deposition of nanosheets onto the surface of the secondary particles, with h-BN having a relatively lower affinity to the CAM. As expected, the different nanosheet materials were attached in a surface-parallel manner.

Table 1. Structural parameters from Rietveld refinement for the uncoated and nanosheet-coated NCMs and corresponding ICP-OES analysis of the coating content.

Sample	**NCM**	**hBN-NCM**	**WS_2-NCM**	**Nb-NCM**
R_{wp} [%]	11.74	10.18	10.63	8.75
R_{Bragg} [%]	1.67	1.51	1.39	1.47
V [Å^3]	101.01(1)	101.04(1)	101.05(6)	101.32(2)
a [Å]	2.8682(1)	2.8683(6)	2.8687(1)	2.8712(1)
c [Å]	14.1770(9)	14.1782(12)	14.1787(10)	14.1897(12)
Sample		**hBN-NCM**	**WS_2-NCM**	**Nb-NCM**
Probed element		B	W	Nb
Assumed stoichiometry		BN	WS_2	$Nb_6O_{17}^{4-}$
Coating content [wt.%]		0.45(6)	1.11(2)	0.91(3)

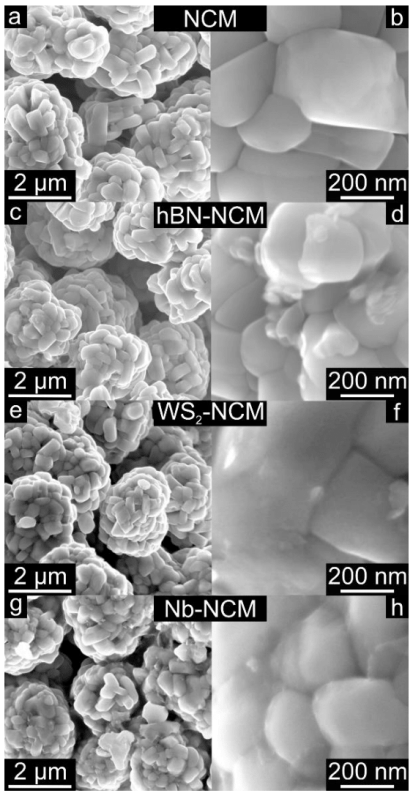

Figure 2. SEM images at different magnifications of (a, b) uncoated NCM, (c, d) hBN-NCM, (e, f) WS_2-NCM and (g, h) Nb-NCM.

2.3. Electrochemical Testing in Battery Cells

The electrochemical properties of the uncoated and nanosheet-coated NCM samples were evaluated in LIB half-cells and pellet-stack SSB cells. With regards to the cells with LP57 electrolyte, the tests were conducted in the potential window of 3.0-4.3 V vs. Li^+/Li at a constant temperature of 25 °C and at C-rates ranging from C/10 to 10C. The first-cycle charge/discharge curves at C/10 were similar for the different CAMs, as can be seen from **Figure 3a**, suggesting that surface coating has no notable effect on the original NCM structure/morphology. In addition, except for Nb-NCM (q_{dis} = 195 mAh g^{-1}), all cells delivered a similar first-cycle specific discharge capacity of q_{dis} = 208 (±2) mAh g^{-1}. As indicated by PXRD analysis, this observation may be attributed to a larger fraction of nickel substitutional defects in Nb-NCM due to formation of lithium niobate during post-deposition anneal. It should be noted that the latter may also add to the cell resistance (impedance buildup).[60]

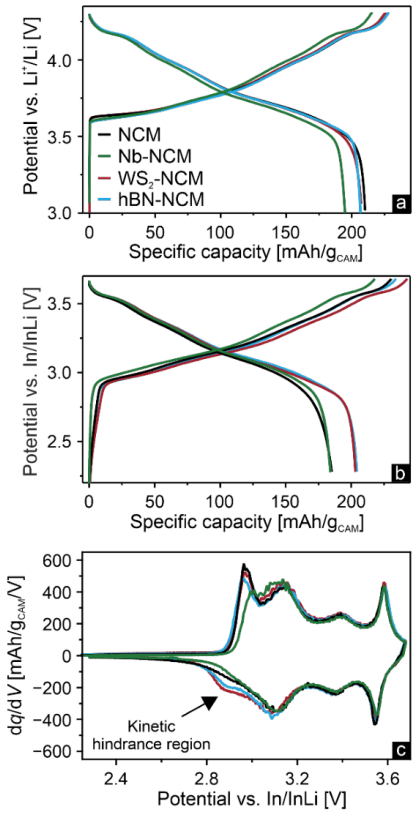

Figure 3. First-cycle charge/discharge curves of the uncoated and nanosheet-coated NCM CAMs (a) in LIB half-cells with LP57 electrolyte and (b) in SSB cells with LPSCl electrolyte at a rate of C/10. (c) Differential capacity curves of the cells shown in (b). For each material, three (LIB) or two cells (SSB) were tested and the data averaged.

Unlike LIBs, the SSB cells with argyrodite Li_6PS_5Cl (referred to as LPSCl) electrolyte were tested at 45 °C in a potential range between 2.28 and 3.68 V vs. In/InLi (approx. 2.9-4.3 V vs. Li^+/Li). As expected based on the LIB data, the different CAMs revealed similar electrochemical behaviors in the initial cycle at C/10 rate (see **Figure 3b**). Except for Nb-NCM (q_{dis} = 184 mAh g^{-1}), the coated samples achieved a higher initial specific discharge capacity that the uncoated NCM [q_{dis} = 204 (±1) mAh g^{-1} vs. 185 mAh g^{-1}]. As shown in **Figure 2c-h**, the nanosheets did not fully cover the particle surface, especially when considering areas where the primary grains meet, resulting in a somewhat non-uniform coating. When tested in LIBs, liquid electrolyte can easily access the exposed surfaces and penetrate into microcracks, leading to minor or even no improvements in cycling performance (see also **Figure S3**, Supporting Information). By contrast, when tested in SSBs, the coatings strongly reduce the contact area

between the bare CAM and the LPSCl electrolyte, which helps to prevent interfacial side reactions from occurring, and therefore positively affects cyclability.

Differential capacity plots can provide thorough information about the phase transitions occurring during cycling. As seen from **Figure 3c**, the only difference between the uncoated and WS_2/h-BN nanosheet-coated samples is an additional feature at the end of discharge (at ~2.9 V vs. In/InLi). This is commonly referred to as the so-called "kinetic hindrance" region, and is more apparent for Ni-rich CAMs exhibiting a high lithium diffusivity (e.g., because of low $Ni_{Li}^{\bullet}$ defect concentration or cycling at elevated temperatures).[61–63] However, in the present work, the primary particle (grain) size and defect concentration are similar for the different materials tested. The same holds for the temperature during cycling. This leaves the protective coating as a reason for the facilitated lithium diffusion (by preventing unfavorable side reactions and impedance buildup during cycling). Additional features that may originate from redox activity and/or degradation of the nanosheets upon battery operation were not observed. By contrast, Nb-NCM revealed smaller peaks, which is indicative of a different mechanism of improved capacity retention and further agrees with the lower specific capacity compared to the uncoated NCM.

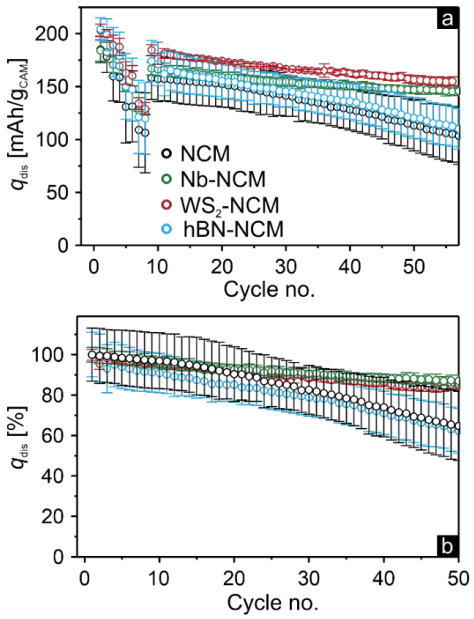

Figure 4. Cyclability of uncoated and nanosheet-coated NCM CAMs in SSB cells with LPSCl electrolyte. (a) Rate performance testing with two cycles each at C/10, C/5, C/2 and 1C, followed by 50 cycles at C/5. (b) Relative stability (capacity retention) with 100% referring to the first cycle at C/5 after the rate capability test. The error bars represent the standard deviation from two independent cells.

Figure 4a shows the cyclability of the uncoated and nanosheet-coated NCM CAMs in SSB cells at different C-rates. In agreement with the results from SEM imaging and ICP-OES analysis regarding surface coverage, WS_2-NCM and Nb-NCM exhibited much improved cycling performance and relative stability (see **Figure 4b** and **Figure S4**, Supporting Information). After 50 cycles at C/5, hBN-NCM, WS_2-NCM and Nb-NCM showed capacity retentions of 63%, 85% and 87%, respectively, compared to 64% for the uncoated CAM. Interestingly, the niobate-type coating also resulted in increased Coulomb efficiency, from 80% for the uncoated material to 85% for Nb-NCM, in the initial cycle (see **Figure 3b**). As mentioned previously, residual lithium is probably being consumed to some degree by the nanosheets during post-processing in the formation of Li_xNbO_y, which itself is a well-established coating material in LIBs and SSBs.[45] For that reason, this kind of coating will be investigated in more detail in the future.

2.4. Analysis of WS_2-NCM

From the electrochemical testing, WS_2-NCM was found to deliver the highest specific capacities (note: similar stabilization was achieved with the niobate-type nanosheets in SSB cells). Since WS_2 is reactive toward ambient oxygen,[64–67] it is necessary to characterize the actual coating species given that the nanosheets may transform into some oxidized state during deposition and/or post-deposition anneal.

Figure 5a-**h** shows results from high-angle annular dark-field scanning transmission electron microscopy (HAADF STEM) and energy-dispersive X-ray spectroscopy (EDS) of a focused ion beam (FIB)-cut lamella of the WS_2-NCM sample. HAADF STEM imaging (see **Figure 5a**) indicated sparse distribution of nanosheets on the particle (apparent from the large differences in contrast). Upon closer inspection (see **Figure 5b**), the nanosheets were found to not perfectly follow the curvature of the substrate, unlike conformal coatings, but instead they seem to have relatively loose contact with the CAM surface. Despite post-annealing in oxygen, WO_3 formation was not clearly recognizable from the EDS maps presented in **Figure 5c**-**h**. However, some minor oxygen signal appeared in the area of the nanosheet coating, which points towards partial WS_2 oxidation. Apart from that, when probing other areas of the particle surface using fast Fourier transform (FFT) analysis of TEM lattice fringes (see **Figure S5**, Supporting Information), some of the reflections matched with the tetragonal WO_3 phase, thus confirming oxidation of WS_2.

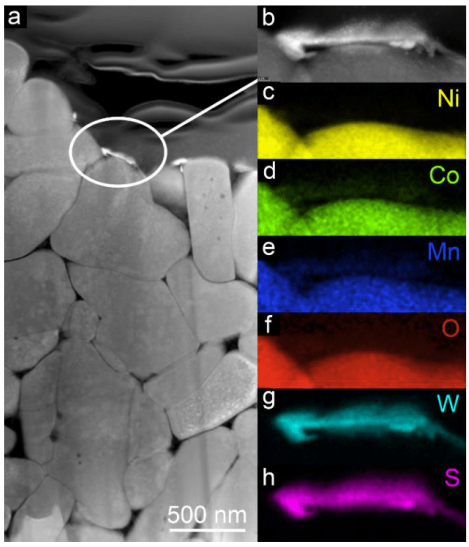

Figure 5. EDS analysis of FIB-cut WS_2-NCM with (a) overview and (b) zoomed-in HAADF STEM images and (c-h) corresponding elemental maps from EDS analysis.

To further elucidate the interfacial stabilization mechanism, the uncoated NCM and WS_2-NCM composite cathodes—before and after 50 cycles in SSB cells—were studied by time-of-flight secondary ion mass spectrometry (TOF-SIMS). Surface analysis via TOF-SIMS enables the detection of decomposition products, such as phosphates and sulfates, which has been described in detail by Walther and coworkers.[5,36,68] Because the WS_2 coating contains sulfur, the analysis of sulfate/sulfite fragments can lead to misinterpretation of data, and therefore they were not considered here. Representative mass spectra collected before and after cycling are shown in **Figure 6a**. To ensure good statistics and data reliability, 10 mass spectra per sample were measured and summarized in box plots (see **Figure 6b**). As evident, the amount of PO_x^- fragments (PO_2^- and PO_3^-) after 50 cycles was significantly higher for WS_2-NCM compared to the uncoated sample. This result is somewhat surprising and not in apparent agreement with the cycling performance in **Figure 4**, showing that uncoated NCM suffers from much faster capacity fading than the coated counterpart. Rather, the data suggest that the decomposition interphase [similar to the cathode electrolyte interphase (CEI) in liquid-electrolyte-based batteries), which is formed by side reactions at the interface between the NCM (oxygen source) and the LPSCl (phosphorus source), is not necessarily detrimental to the cyclability of the thiophosphate-based SSBs. A possible explanation for this finding may be that the decomposition interphase exhibits favorable transport properties, especially with regards to partial ionic conductivity. According to Homma *et al.*,[69] the ionic conductivity of a mixture of different materials depends on the actual composition. Consequently, it can be inferred that the coating directly affects the mixing ratio of degradation products

and/or WS_2 catalyzes the formation of other species. Additionally, a signal of low intensity appeared at m/z = 78.96 in the pristine state. This feature has been previously linked to the presence of PSO^- fragments.[5] Upon cycling, the electrolyte undergoes some (electro)chemical degradation, accompanied by the formation of oxygenated sulfur and phosphorus species, among others. The reliability of the presented data (i.e., trend in signal intensities) was also verified by another normalization technique (see **Figure S6**, Supporting Information). In this case, the intensities were not normalized to the total ion signal, but rather to the NiO_2^- fragment, the latter representing the NCM.

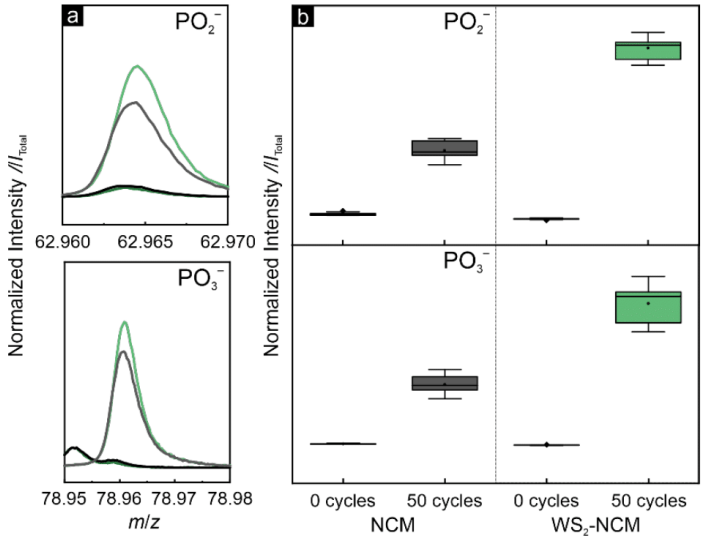

Figure 6. ToF-SIMS data for fragments (PO_2^- and PO_3^-) characteristic of interfacial degradation products. (a) Representative mass spectra collected from the uncoated NCM and WS_2-NCM composite cathodes before and after cycling. (b) Corresponding boxplots of normalized intensities containing 10 data points each.

Overall, the results hint at an underlying stabilization mechanism that is distinct from the classical “inert” cathode interface/interphase associated with oxide nanocoatings.[12] Another explanation that would be consistent with the observations would be mitigation of transition-metal dissolution, as proposed by Maiti *et al.* for WSe_2 coating (LIB application).[29] Indeed, leaching is not limited to liquid electrolytes, but has also been reported recently for thiophosphate-based SSBs.[70] Regardless, higher surface coverage of the NCM particles would likely help to unravel the mechanism more easily. However, in this work, we were limited to partial surface coverage due to mechanical stability issues of the CAM secondary particles, as discussed above. Nevertheless, these relatively poorly coated materials demonstrated substantial improvements in cycling performance, which renders the tailoring of nanosheet

coatings, e.g. by focusing on mechanically more robust single-crystalline CAMs, all the more intriguing.

3. Conclusion

Lithium thiophosphate solid electrolytes are promising superionic materials for use in solid-state batteries owing to their high room-temperature ionic conductivity that is readily accessible by cold-pressing. However, their enhanced reactivity toward oxidation necessitates the application of protective coatings to stabilize the cathode/electrolyte interface. Here, we have examined whether nanosheet materials lend themselves as protective coating agents in liquid- and solid-electrolyte-based lithium-ion batteries. First, we have evaluated various coating methods and found that deposition from dispersions in organic solvents is best suited for surface modification without harming the cathode active material. Next, we have compared different kinds of nanosheets in conventional and solid-state batteries. Our findings demonstrate that significant stabilization through nanosheet coating can only be achieved in thiophosphate-based solid-state cells, which is likely related to the relative immobility of the solid electrolyte when compared to organic liquid electrolytes. However, for the chemically inert coating, h-BN, no stabilization was observed, while the “more reactive” coatings, WS_2 and Li_xNbO_y, had a major effect on cycling performance. Overall, the concept of nanosheet coating may be a promising addition to established surface-modification strategies, especially in the context of solid-state batteries. Nevertheless, the main challenge that needs to be addressed is achieving uniform and conformal surface coverage.

4. Experimental Section

Coating Procedure: The CAM was received from BASF SE (NCM851005, $d_{50} \approx 4$ µm) and the coating materials, h-BN (90 nm) and WS_2 (200 nm), from Sigma-Aldrich as commercial products. The latter materials were used without further processing, while the niobate-type nanosheets were synthesized in house. 10 mg (in case of Nb, for $[K_{4-x}H_xNb_6O_{17}]$) of nanosheet precursor was weighed into 10 mL of dry isopropanol (WS_2, h-BN) or dry ethanol (Nb) and sonicated for 30 min in an ultrasonication bath. To this mixture, 1 g of CAM was added, followed by stirring for 10 min, after which the solvent was removed under vacuum with continuous agitation. The obtained powders were calcined in a tube furnace under flowing oxygen atmosphere (two atmosphere exchanges per hour) at 400 °C for 1 h and then sieved using a 32 µm stainless steel mesh.

Preparation of $((CH_3(CH_2)_3)_4N)_4Nb_6O_{17}$: First, bulk $K_4Nb_6O_{17}\cdot 3H_2O$ was prepared by a solid-state method, in which Nb_2O_5 and K_2CO_3 (2:3 molar ratio) were ground and heated at 1100 °C for 10 h.[71,72] The material was then subject to ion exchange (K^+ to H^+) by stirring 3.0 g of $K_4Nb_6O_{17}\cdot 3H_2O$ in 150 mL of 0.2 mol L^{-1} H_2SO_4 for 3 d. Next, the solid was filtered, washed with water and dried at 70 °C. The nanosheets were obtained by exfoliation of bulk $K_{4-x}H_xNb_6O_{17}$ (0.5 g) using 100 mL of $8\cdot 10^{-3}$ mol L^{-1}

tetrabutylammonium hydroxide for 7 d (see **Figure S7**, Supporting Information).[73,74] Once the stirring is suspended, the non-exfoliated material tends to precipitate out, while the exfoliated layers remain in the form of a stable suspension. The suspension of nanosheets was collected, followed by drying at 70 °C.

Microscopy: SEM imaging of the as-prepared samples was performed using a LEO-1530 microscope (Carl Zeiss AG).

TEM was performed on a Themis Z (Thermo Fisher Scientific) double-corrected transmission electron microscope operated at an acceleration voltage of 300 kV. Lift-out samples were prepared on a STRATA (FEI) dual-beam system equipped with a gallium-ion source. The samples were milled at 30 kV, followed by final polishing at 2 kV to reduce surface damage. Prior to milling, the sample surface was protected by deposition of a carbon layer. STEM images were recorded using a HAADF detector. Elemental analysis was performed by EDS employing a Super-X detector. JEMS software was used to index the FFT patterns.
The TEM image presented in **Figure S7** (Supporting Information) was acquired on a Tecnai G2 F20 TMP equipped with a field emission gun operating at 200 kV (featuring TWIN objective lenses and a point resolution of 0.27 nm).

Powder XRD and Pattern Refinement: XRD data were collected from powder samples in 0.03 mm glass capillaries (Hilgenberg) on a STADI P (STOE) diffractometer in Debye-Scherrer geometry with monochromatic Mo-$K_{\alpha 1}$ radiation (λ = 0.7093 Å, 50 kV, 40 mA) and a Mythen 1K detector (DECTRIS). The different datasets were analyzed using TOPAS Academic V7. First, Le Bail fitting was done (Chebyshev polynomial with 10 terms for background correction); lattice parameters, zero-shift, axial divergence and crystallize size were extracted as Gaussian and Lorentzian contributions. The results of the Le Bail analysis were used as initial parameters for Rietveld refinement, during which the site occupancies, Debye-Waller factors and oxygen coordinates were refined in parallel until convergence was achieved.

Chemical Analysis: ICP-OES measurements were conducted using a Thermo Fisher Scientific ICAP 7600 DUO. The CAMs were dissolved in an acid digester using a graphite furnace. Mass fractions were obtained from three independent measurements per sample. About 10 mg of material was dissolved in a mixture of hydrochloric acid and nitric acid at 353 K for 4 h. The digested samples were diluted prior to analysis, which was done with four different calibration solutions and an internal standard (Sc). The concentration range of the calibration solutions did not exceed a decade. Two or three wavelengths of each element were used for quantitative analysis.

Electrochemical Testing: The sieved CAMs were mixed with Super C65 carbon black additive and polyvinylidene difluoride binder (PVDF, Solef 5130, Solvay) in a ratio of 94:3:3 by weight and cast onto a 0.03 mm-thick aluminum foil using an Erichsen Coatmaster 510 film applicator (140 µm slit thickness of the stainless-steel doctor blade). The electrodes were dried under vacuum at 120 °C for at least 10 h, calendared at 14 N mm^{-1} (Sumet Messtechnik) and cut into circular 13 mm-diameter discs. LIB coin cells were assembled using the cathodes, a glass fiber GF/D separator, LP57

electrolyte (1 M $LiPF_6$ in a 3:7 mixture of ethylene carbonate and ethyl methyl carbonate) and a lithium-metal anode in an Ar-filled glovebox with a crimping pressure of 1 t. The uncoated and coated CAMs (~10 mg cm^{-2} areal loading) were tested electrochemically at 25 °C and at C-rates ranging from C/10 to 10C (with 1C = 190 mA g^{-1}).

SSB cells were assembled according to a previously described procedure.[10] For the cathode, 10-12 mg of a composite containing 69 wt.% CAM (~10 mg cm^{-2} areal loading), 1 wt.% Super C65 and 30 wt.% LPSCl solid electrolyte was used. LPSCl (100 mg) and In/InLi were used as separator and anode, respectively. InLi alloy was prepared *in situ* by pressing In and Li foils together, with the In foil initially facing the separator layer. The cells were cycled under constant current mode at 45 °C while maintaining a uniaxial stack pressure of 81 MPa. An initial rate test of five cycles at C/10, C/5, C/2 and 1C was followed by 50 cycles at C/5.

SIMS Analysis: ToF-SIMS was conducted using a M6 Hybrid SIMS (IONTOF GmbH) equipped with a 30 kV Bi-cluster primary ion gun for analysis. In general, during ToF-SIMS measurements, charged fragments are obtained as a result of a collision cascade that results from the impact of the high-energy primary ion beam. All samples were prepared in the same way and under the same conditions in a glovebox, attached to the sample holder using non-conductive adhesive tape and transferred to the instrument using the LEICA EM VCT500 shuttle (Leica Microsystems). Accordingly, composite cathodes with WS_2-coated NCM were compared to those using uncoated material. The samples were analyzed before and after cycling. To probe the interfaces in the composite cathodes, the current collector was removed. The instrument was operated in spectrometry mode using Bi_3^+ as primary ions (0.60 pA) in negative mode, providing high mass resolution [FWHM $m/\Delta m$ > 13000 @m/z = 62.97 (PO_2^-)]. The analysis area was set to 100·100 μm^2, which was rasterized with 128·128 pixels and a primary ion dose of $1.0 \cdot 10^{12}$ ions cm^{-2}. To ensure data reliability, 10 mass spectra were measured per sample. Evaluation of the ToF-SIMS data was done with the software SurfaceLab 7.2 (IONTOF GmbH).

Supporting Information

Supporting Information is available from the Wiley Online Library or from the author.

Acknowledgements

This work was partly supported by BASF SE. The authors are grateful to the Federal Ministry of Education and Research (Bundesministerium für Bildung und Forschung, BMBF) for funding within the projects SUSTRAB (03XP0415D) and FestBatt (03XP0430A, 03XP0433D). The authors acknowledge the support from the Karlsruhe Nano Micro Facility (KNMFi, www.knmf.kit.edu), a Helmholtz research infrastructure at Karlsruhe Institute of Technology (KIT, www.kit.edu). The authors also thank Thomas Bergfeldt and team for conducting the ICP-OES analysis, Matteo Bianchini for helpful

discussions and the Laboratory of Nano and Quantum Engineering (LNQE, Leibniz University Hannover) for collecting the TEM imaging data in **Figure S7** (Supporting Information).

Conflict of Interest

The authors declare no conflict of interest.

Data Availability Statement

The data that support the findings of this study are available from the corresponding author upon reasonable request.

Keywords

Lithium-ion battery; solid-state battery; layered Ni-rich cathode; nanosheet coating; interface stability

[1] J. Janek, W. G. Zeier, *Nat. Energy* **2016**, *1*, 16141.

[2] Y. Yusim, E. Trevisanello, R. Ruess, F. H. Richter, A. Mayer, D. Bresser, S. Passerini, J. Janek, A. Henss, *Angew. Chem., Int. Ed.* **2023**, *62*, e202218316.

[3] J. Janek, W. G. Zeier, *Nat. Energy* **2023**, *8*, 230.

[4] F. P. McGrogan, T. Swamy, S. R. Bishop, E. Eggleton, L. Porz, X. Chen, Y.-M. Chiang, K. J. Van Vliet, *Adv. Energy Mater.* **2017**, *7*, 1602011.

[5] F. Walther, R. Koerver, T. Fuchs, S. Ohno, J. Sann, M. Rohnke, W. G. Zeier, J. Janek, *Chem. Mater.* **2019**, *31*, 3745.

[6] S. P. Culver, R. Koerver, W. G. Zeier, J. Janek, *Adv. Energy Mater.* **2019**, *9*, 1900626.

[7] P. Minnmann, F. Strauss, A. Bielefeld, R. Ruess, P. Adelhelm, S. Burkhardt, S. L. Dreyer, E. Trevisanello, H. Ehrenberg, T. Brezesinski, F. H. Richter, J. Janek, *Adv. Energy Mater.* **2022**, *12*, 2201425.

[8] B.-X. Shi, Y. Yusim, S. Sen, T. Demuth, R. Ruess, K. Volz, A. Henss, F. H. Richter, *Adv. Energy Mater.* **2023**, *13*, 2300310.

[9] Y. Ma, J. H. Teo, D. Kitsche, T. Diemant, F. Strauss, Y. Ma, D. Goonetilleke, J. Janek, M. Bianchini, T. Brezesinski, *ACS Energy Lett.* **2021**, *6*, 3020.

[10] D. Kitsche, F. Strauss, Y. Tang, N. Bartnick, A.-Y. Kim, Y. Ma, C. Kübel, J. Janek, T. Brezesinski, *Batter. Supercaps* **2022**, *5*, e202100397.

[11] S. Payandeh, F. Strauss, A. Mazilkin, A. Kondrakov, T. Brezesinski, *Nano Res. Energy* **2022**, *1*, 9120016.

[12] A.-Y. Kim, F. Strauss, T. Bartsch, J. H. Teo, T. Hatsukade, A. Mazilkin, J. Janek, P. Hartmann, T. Brezesinski, *Chem. Mater.* **2019**, *31*, 9664.

[13] K. Takada, N. Ohta, L. Zhang, K. Fukuda, I. Sakaguchi, R. Ma, M. Osada, T. Sasaki, *Solid State Ionics* **2008**, *179*, 1333.

[14] G. Oh, M. Hirayama, O. Kwon, K. Suzuki, R. Kanno, *Chem. Mater.* **2016**, *28*, 2634.

[15] R. S. Negi, Y. Yusim, R. Pan, S. Ahmed, K. Volz, R. Takata, F. Schmidt, A. Henss, M. T. Elm, *Adv. Mater. Interfaces* **2022**, *9*, 2101428.

[16] Y. Ma, R. Zhang, Y. Tang, Y. Ma, J. H. Teo, T. Diemant, D. Goonetilleke, J. Janek, M. Bianchini, A. Kondrakov, T. Brezesinski, *ACS Nano* **2022**, *16*, 18682.

[17] Y. Ma, J. H. Teo, F. Walther, Y. Ma, R. Zhang, A. Mazilkin, Y. Tang, D. Goonetilleke, J. Janek, M. Bianchini, T. Brezesinski, *Adv. Funct. Mater.* **2022**, *32*, 2111829.

[18] R. Zhang, Y. Ma, Y. Tang, D. Goonetilleke, T. Diemant, J. Janek, A. Kondrakov, T. Brezesinski, *Chem. Mater.* **2023**, *35*, 6835.

[19] D. Kitsche, Y. Tang, Y. Ma, D. Goonetilleke, J. Sann, F. Walther, M. Bianchini, J. Janek, T. Brezesinski, *ACS Appl. Energy Mater.* **2021**, *4*, 7338.

[20] D. Kitsche, Y. Tang, H. Hemmelmann, F. Walther, M. Bianchini, A. Kondrakov, J. Janek, T. Brezesinski, *Small Sci.* **2023**, *3*, 2200073.

[21] C. Lee, X. Wei, J. W. Kysar, J. Hone, *Science* **2008**, *321*, 385.

[22] N. I. Kovtyukhova, Y. Wang, R. Lv, M. Terrones, V. H. Crespi, T. E. Mallouk, *J. Am. Chem. Soc.* **2013**, *135*, 8372.

[23] S. Hu, M. Lozada-Hidalgo, F. C. Wang, A. Mishchenko, F. Schedin, R. R. Nair, E. W. Hill, D. W. Boukhvalov, M. I. Katsnelson, R. A. W. Dryfe, I. V Grigorieva, H. A. Wu, A. K. Geim, *Nature* **2014**, *516*, 227.

[24] Y. Huang, J. Wu, K. C. Hwang, *Phys. Rev. B* **2006**, *74*, 245413.

[25] C. Backes, R. J. Smith, N. McEvoy, N. C. Berner, D. McCloskey, H. C. Nerl, A. O'Neill, P. J. King, T. Higgins, D. Hanlon, N. Scheuschner, J. Maultzsch, L. Houben, G. S. Duesberg, J. F. Donegan, V. Nicolosi, J. N. Coleman, *Nat. Commun.* **2014**, *5*, 4576.

[26] K.-Y. Park, J.-M. Lim, N. S. Luu, J. R. Downing, S. G. Wallace, L. E. Chaney, H. Yoo, W. J. Hyun, H.-U. Kim, M. C. Hersam, *Adv. Energy Mater.* **2020**, *10*, 2001216.

[27] K.-Y. Park, Y. Zhu, C. G. Torres-Castanedo, H. J. Jung, N. S. Luu, O. Kahvecioglu, Y. Yoo, J.-W. T. Seo, J. R. Downing, H.-D. Lim, M. J. Bedzyk, C. Wolverton, M. C. Hersam, *Adv. Mater.* **2022**, *34*, 2106402.

[28] P. Xiao, Y. Cao, W. Li, G. Li, Y. Yu, Z. Dai, Z. Du, X. Chen, J. Sun, W. Yang, *ACS Appl. Mater. Interfaces* **2021**, *13*, 29714.

[29] S. Maiti, R. Konar, H. Sclar, J. Grinblat, M. Talianker, M. Tkachev, X. Wu, A. Kondrakov, G. D. Nessim, D. Aurbach, *ACS Energy Lett.* **2022**, *7*, 1383.

[30] R. Rojaee, R. Shahbazian-Yassar, *ACS Nano* **2020**, *14*, 2628.

[31] S. Sharifi-Asl, F. A. Soto, T. Foroozan, M. Asadi, Y. Yuan, R. Deivanayagam, R. Rojaee, B. Song, X. Bi, K. Amine, J. Lu, A. Salehi-khojin, P. B. Balbuena, R. Shahbazian-Yassar, *Adv. Funct. Mater.* **2019**, *29*, 1901110.

[32] Y. Shi, S.-L. Chou, J.-Z. Wang, D. Wexler, H.-J. Li, H.-K. Liu, Y. Wu, *J. Mater. Chem.* **2012**, *22*, 16465.

[33] M. A. Razmjoo Khollari, P. Paknahad, M. Ghorbanzadeh, *New J. Chem.* **2019**, *43*, 2766.

[34] J.-H. Shim, Y.-M. Kim, M. Park, J. Kim, S. Lee, *ACS Appl. Mater. Interfaces* **2017**, *9*, 18720.

[35] C. W. Park, J.-H. Lee, J. K. Seo, W. Y. Jo, D. Whang, S. M. Hwang, Y.-J. Kim, *Nat. Commun.* **2021**, *12*, 2145.

[36] F. Walther, F. Strauss, X. Wu, B. Mogwitz, J. Hertle, J. Sann, M. Rohnke, T. Brezesinski, J. Janek, *Chem. Mater.* **2021**, *33*, 2110.

[37] T. Bartsch, F. Strauss, T. Hatsukade, A. Schiele, A.-Y. Kim, P. Hartmann, J. Janek, T. Brezesinski, *ACS Energy Lett.* **2018**, *3*, 2539.

[38] W. Liu, F. Gao, Y. Zang, J. Qu, J. Xu, S. Ji, Y. Huo, J. Qiu, *J. Alloys Compd.* **2021**, *867*, 159079.

[39] S. She, Y. Zhou, Z. Hong, Y. Huang, Y. Wu, *ACS Omega* **2022**, *7*, 24851.

[40] G. Cassabois, P. Valvin, B. Gil, *Nat. Photonics* **2016**, *10*, 262.

[41] D. Becker, M. Börner, R. Nölle, M. Diehl, S. Klein, U. Rodehorst, R. Schmuch, M. Winter, T. Placke, *ACS Appl. Mater. Interfaces* **2019**, *11*, 18404.

[42] C. Backes, B. M. Szydłowska, A. Harvey, S. Yuan, V. Vega-Mayoral, B. R. Davies, P.-l. Zhao, D. Hanlon, E. J. G. Santos, M. I. Katsnelson, W. J. Blau, C. Gadermaier, J. N. Coleman, *ACS Nano* **2016**, *10*, 1589.

[43] S.-J. Sim, S.-H. Lee, B.-S. Jin, H.-S. Kim, *J. Power Sources* **2021**, *481*, 229037.

[44] C. Nico, T. Monteiro, M. P. F. Graça, *Prog. Mater. Sci.* **2016**, *80*, 1.

[45] B. N. Nunes, W. van den Bergh, F. Strauss, A. Kondrakov, J. Janek, T. Brezesinski, *Inorg. Chem. Front.* **2023**, *10*, 7126.

[46] C. Backes, T. M. Higgins, A. Kelly, C. Boland, A. Harvey, D. Hanlon, J. N. Coleman, *Chem. Mater.* **2017**, *29*, 243.

[47] R. J. Smith, P. J. King, M. Lotya, C. Wirtz, U. Khan, S. De, A. O'Neill, G. S. Duesberg, J. C. Grunlan, G. Moriarty, J. Chen, J. Wang, A. I. Minett, V. Nicolosi, J. N. Coleman, *Adv. Mater.* **2011**, *23*, 3944.

[48] A. Griffin, A. Harvey, B. Cunningham, D. Scullion, T. Tian, C.-J. Shih, M.

Gruening, J. F. Donegan, E. J. G. Santos, C. Backes, J. N. Coleman, *Chem. Mater.* **2018**, *30*, 1998.

[49] D. Pritzl, T. Teufl, A. T. S. Freiberg, B. Strehle, J. Sicklinger, H. Sommer, P. Hartmann, H. A. Gasteiger, *J. Electrochem. Soc.* **2019**, *166*, A4056.

[50] J. Sicklinger, M. Metzger, H. Beyer, D. Pritzl, H. A. Gasteiger, *J. Electrochem. Soc.* **2019**, *166*, A2322.

[51] H. Visbal, S. Fujiki, Y. Aihara, T. Watanabe, Y. Park, S. Doo, *J. Power Sources* **2014**, *269*, 396.

[52] F. Strauss, S. Payandeh, A. Kondrakov, T. Brezesinski, *Mater. Futures* **2022**, *1*, 023501.

[53] S. H. Jung, K. Oh, Y. J. Nam, D. Y. Oh, P. Brüner, K. Kang, Y. S. Jung, *Chem. Mater.* **2018**, *30*, 8190.

[54] F. Strauss, J. H. Teo, J. Maibach, A.-Y. Kim, A. Mazilkin, J. Janek, T. Brezesinski, *ACS Appl. Mater. Interfaces* **2020**, *12*, 57146.

[55] O. Y. Posudievsky, O. A. Khazieieva, V. G. Koshechko, V. D. Pokhodenko, *Theor. Exp. Chem.* **2014**, *50*, 103.

[56] O. Y. Posudievsky, O. A. Khazieieva, V. V. Cherepanov, G. I. Dovbeshko, A. G. Shkavro, V. G. Koshechko, V. D. Pokhodenko, *J. Mater. Chem. C* **2013**, *1*, 6411.

[57] K. R. Paton, E. Varrla, C. Backes, R. J. Smith, U. Khan, A. O'Neill, C. Boland, M. Lotya, O. M. Istrate, P. King, T. Higgins, S. Barwich, P. May, P. Puczkarski, I. Ahmed, M. Moebius, H. Pettersson, E. Long, J. Coelho, S. E. O'Brien, E. K. McGuire, B. M. Sanchez, G. S. Duesberg, N. McEvoy, T. J. Pennycook, C. Downing, A. Crossley, V. Nicolosi, J. N. Coleman, *Nat. Mater.* **2014**, *13*, 624.

[58] H.-H. Ryu, B. Namkoong, J.-H. Kim, I. Belharouak, C. S. Yoon, Y.-K. Sun, *ACS Energy Lett.* **2021**, *6*, 2726.

[59] W. van den Bergh, L. Karger, S. Murugan, J. Janek, A. Kondrakov, T. Brezesinski, *ChemElectroChem* **2023**, *10*, e202300165.

[60] Y. Kobayashi, H. Hata, T. E. Mallouk, *MRS Online Proc. Libr.* **2007**, *988*, 9880320.

[61] L. Karger, D. Weber, D. Goonetilleke, A. Mazilkin, H. Li, R. Zhang, Y. Ma, S. Indris, A. Kondrakov, J. Janek, T. Brezesinski, *Chem. Mater.* **2023**, *35*, 648.

[62] L. Karger, S. Korneychuk, W. van Den Bergh, S. L. Dreyer, R. Zhang, A. Kondrakov, J. Janek, T. Brezesinski, *Chem. Mater.* **2023**, DOI: 10.1021/acs.chemmater.3c02727.

[63] R. Rueß, D. Gomboso, M. Ulherr, E. Trevisanello, Y. Ma, A. Kondrakov, T. Brezesinski, J. Janek, *J. Electrochem. Soc.* **2023**, *170*, 020533.

[64] G. Mirabelli, C. McGeough, M. Schmidt, E. K. McCarthy, S. Monaghan, I. M. Povey, M. McCarthy, F. Gity, R. Nagle, G. Hughes, A. Cafolla, P. K. Hurley, R.

Duffy, *J. Appl. Phys.* **2016**, *120*, 125102.

[65] H. Liu, N. Han, J. Zhao, *RSC Adv.* **2015**, *5*, 17572.

[66] W. Jaegermann, D. Schmeisser, *Surf. Sci.* **1986**, *165*, 143.

[67] L. Karger, K. Synnatschke, S. Settele, Y. J. Hofstetter, T. Nowack, J. Zaumseil, Y. Vaynzof, C. Backes, *Adv. Mater.* **2021**, *33*, 2102883.

[68] F. Walther, S. Randau, Y. Schneider, J. Sann, M. Rohnke, F. H. Richter, W. G. Zeier, J. Janek, *Chem. Mater.* **2020**, *32*, 6123.

[69] K. Homma, Y. Liu, M. Sumita, R. Tamura, N. Fushimi, J. Iwata, K. Tsuda, C. Kaneta, *J. Phys. Chem. C* **2020**, *124*, 12865.

[70] R. Zhang, F. Strauss, L. Jiang, L. Casalena, L. Li, J. Janek, A. Kondrakov, T. Brezesinski, *Chem. Commun.* **2023**, *59*, 4600.

[71] M. A. Bizeto, V. R. L. Constantino, *Mater. Res. Bull.* **2004**, *39*, 1729.

[72] T. Nakato, K. Kuroda, C. Kato, *Chem. Mater.* **1992**, *4*, 128.

[73] A. L. Shiguihara, M. A. Bizeto, V. R. L. Constantino, *Colloids and Surfaces A: Physicochem. Eng. Aspect* **2007**, *295*, 123.

[74] C. H. B. Silva, N. A. Galiote, F. Huguenin, É. Teixeira-Neto, V. R. L. Constantino, M. L. A. Temperini, *J. Mater. Chem.* **2012**, *22*, 14052.

ToC Figure and Text

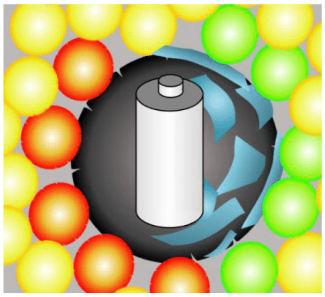

Various materials in the form of nanosheets are examined with regards to their use as protective coatings in liquid- and solid-electrolyte-based lithium-ion batteries. WS_2 and Li_xNbO_y nanosheets are found to have a profound effect on the cycling performance of thiophosphate-based solid-state batteries.

X (Twitter) Handles

@TBrezesinski

@Janek_Lab_JLU

@KITKarlsruhe

6.2 Supporting Information

6.2.1 Supporting Information of Publication I: Low-Temperature Ion Exchange Synthesis of Layered $LiNiO_2$ Single Crystals with High Ordering

Supporting Information

Low-Temperature Ion-Exchange Synthesis of Layered $LiNiO_2$ Single Crystals with High Ordering

Leonhard Karger,[a] Daniel Weber,[a,b*] Damian Goonetilleke,[a] Andrey Mazilkin,[a] Hang Li,[b] Ruizhuo Zhang,[a] Yuan Ma,[a] Sylvio Indris,[b,c] Aleksandr Kondrakov,[a,d] Jürgen Janek,[a,e*] and Torsten Brezesinski[a*]

[a] Battery and Electrochemistry Laboratory (BELLA), Institute of Nanotechnology, Karlsruhe Institute of Technology (KIT), Herrmann-von-Helmholtz-Platz 1, 76344 Eggenstein-Leopoldshafen, Germany.

[b] Institute for Applied Materials-Energy Storage Systems (IAM-ESS), Karlsruhe Institute of Technology (KIT), Herrmann-von-Helmholtz-Platz 1, 76344 Eggenstein-Leopoldshafen, Germany.

[c] Helmholtz Institute Ulm (HIU) Electrochemical Energy Storage, Helmholtzstr. 11, 89081 Ulm, Germany.

[d] BASF SE, Carl-Bosch-Str. 38, 67056 Ludwigshafen, Germany.

[e] Institute of Physical Chemistry & Center for Materials Research (ZfM/LaMa), Justus-Liebig-University Giessen, Heinrich-Buff-Ring 17, 35392 Giessen, Germany.

Email: daniel.weber3@kit.edu, juergen.janek@phys.chemie.uni-giessen.de, torsten.brezesinski@kit.edu

Synthesis

Reference $LiNiO_2$ and $Na_xLi_{1-x}NiO_2$ were synthesized by solid-state reaction from the starting materials $Ni(OH)_2$ (d_{50} = 14 µm, BASF SE), $LiOH \cdot H_2O$ (10 - 20 µm, BASF SE) and NaOH (Sigma-Aldrich). The reactants were dry mixed in a blender (Kinematica) under argon atmosphere for 5 min in the required ratios with 1 mol % excess of $LiOH \cdot H_2O$. The reactant mixtures were calcined in an alumina crucible under oxygen flow (2 atm h^{-1}) in a tube furnace (Nabertherm P330) at 700 °C for 8 h with 3 K min^{-1} heating and cooling rates and with a pre-heating step at 400 °C for 4 h.

Reference $NaNiO_2$ was synthesized from NiO (Sigma-Aldrich) with 10% excess Na_2O_2 (Sigma-Aldrich). Both materials were ground thoroughly in a mortar and then half of the powder was pressed into a pellet. The pellet was covered with the remaining powder (pellet under powder technique) and calcined under oxygen flow (2 atm h^{-1}) in a tube furnace (Nabertherm P330) at 700 °C for 12 h with 3 K min^{-1} heating and cooling rates.

Ion Exchange with $LiNO_3$ and Water-Free Washing

1 g NNO and 0.75 g $LiNO_3$ (1.2 eq.) were mixed and filled into a large Schlenk tube. The tube was connected to an Ar line and left open until the target temperature of 320 °C was reached. The tube was closed and left heating for 10 h, followed by cooling to room temperature. Next, a stir bar and 20 mL dry methanol or dry acetonitrile were added to the tube. The tube was equipped with a septum and heated to 65 or 110 °C, respectively, under stirring for 1 h, after which the sample was left to separate. The supernatant was removed with a syringe, and the procedure was repeated twice. The remaining solvent was removed in a vacuum. The product was sieved using a 45 µm steel mesh.

Ion Exchange with LiFSI and LiTFSI

1 g NNO and 1.99 g lithium bis(fluorosulfonyl)imide or 3.05 g lithium bis(trifluoromethanesulfonyl)imide (1.2 eq.) were mixed and filled into a large Schlenk tube. The tube was connected to an Ar line and left open until reaching the target temperature of 150 or 270 °C, respectively. The tube was closed and left heating for 10 h. After cooling, a stir bar and 10 mL dry methanol were added. The mixture was stirred for 30 min, after which the sample was left to separate. The supernatant was removed using a syringe. The procedure was repeated twice. The remaining solvent was removed in a vacuum and the product sieved with a 45 µm steel mesh.

Alternative Ion-Exchange Procedures

As the described route required an aqueous washing step that is known to be detrimental to the LNO, alternative reaction pathways for washing and ion exchange were investigated. First, it was attempted to wash away the residual salts using different organic solvents, of which methanol and acetonitrile were able to dissolve the nitrate salts at 65 and 110 °C, respectively. EELS analysis of the surface structure after washing with methanol revealed the growth of an interfacial layer with reduced nickel oxidation state. Methanol is most likely oxidized during the washing step, leading to

surface degradation of LNO. Similarly, the sample washed with acetonitrile was found to deliver low specific capacities.

As alternative methods, different lithium sources for the exchange reaction were tested. Other lithium salts can also be used to produce LNO (when exceeding their melting point). For the low-melting lithium bis(fluorosulfonyl)imide and lithium bis(trifluoromethanesulfonyl)imide salts, reduction of the LNO cathode material was observed, leading to violent decomposition for temperatures above 270 °C.

Solvothermal exchange in glyme ethers was also tested, but proved unsuccessful due to the oxidizing nature of LNO (evident from discoloration of the solvent and formation of rocksalt-type NiO by XRD).

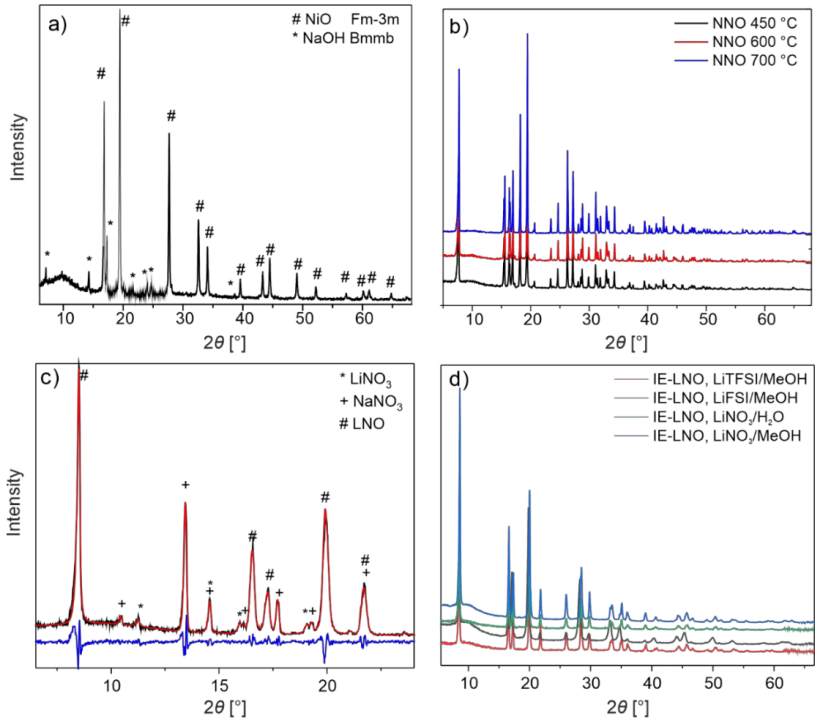

Figure S1. XRD patterns of a) NNO premix [$Ni(OH)_2$ and NaOH heated at 300 °C for 10 h], b) NNO prepared at 450, 600, and 700 °C for 6 h, c) IE-LNO from $LiNO_3$ before washing, and d) IE-LNO from LiFSI, LiTFSI, and $LiNO_3$ washed with water or methanol.

Table S1. Elemental analysis results for NNO and IE-LNO washed with water or hot methanol in molar fractions relative to nickel.

	NNO-600 [mol % rel. to Ni]	IE-LNO water-washed [mol % rel. to Ni]	IE-LNO methanol-washed [mol % rel. to Ni]
Lithium	-	0.92(1)	0.93(4)
Sodium	1.11(3)	0.094(3)	0.088(3)
Oxygen	2.09(19)	2.17(21)	2.22(22)
Nickel	1.00(1)	1.00(1)	1.00(1)

Table S2. Rietveld refinement results for IE-LNO and SS-LNO reference samples.

	a [Å]	*c* [Å]	*V* [Å^3]	z_O	Substitutional defects [%]	R_{Bragg} [%]
Water-washed	2.8748(2)	14.2001(2)	101.634(9)	0.2598(3)	5.0(8) Na_{Li}	1.75
Methanol-washed	2.8806(9)	14.2357(7)	102.300(8)	0.2610(2)	3.6(5) Na_{Li}	2.37
Water-washed & annealed (600 °C)	2.8798(4)	14.2032(4)	102.009(4)	0.2588(2)	4.9(2) Ni_{Li}	1.32
Exchanged once	2.8759(2)	14.1986(23)	101.757(16)	0.2586(3)	3.83(7) Na_{Li}	3.31
Exchanged twice	2.8784(6)	14.1990(67)	101.937(62)	0.2573(11)	2.87(8) Na_{Li}	4.13
Reference LNO	2.8732(3)	14.1853(3)	101.420(3)	0.2586(2)	1.7(2) Ni_{Li}	1.83
Reference LNO 1.0% Na	2.8775(3)	14.1976(2)	101.808(2)	0.2590(1)	2.5(1) Ni_{Li}	1.33
Reference LNO 2.5% Na	2.8779(2)	14.2024(2)	101.874(2)	0.2581(10)	2.8(1) Ni_{Li}	1.35

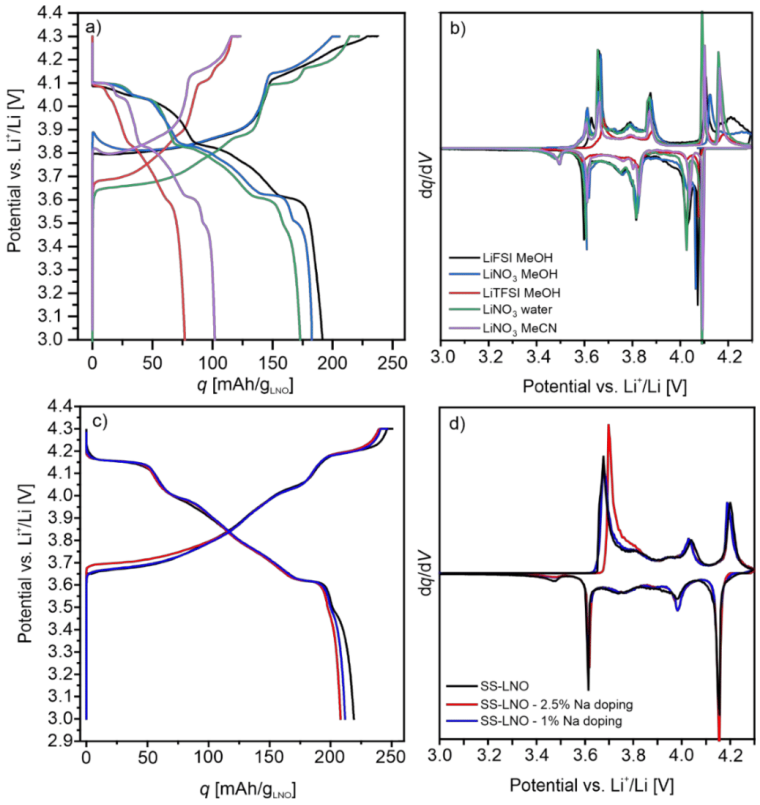

Figure S2. a) Initial charge/discharge curves at 0.1 C rate and b) corresponding second-cycle differential capacity curves for IE-LNO exchanged/washed with LiFSI/MeOH, LiTFSI/MeOH, $LiNO_3/H_2O$, $LiNO_3$/MeOH, and $LiNO_3$/MeCN. c) Initial charge/discharge curves at 0.1 C rate and d) first-cycle differential capacity curves for undoped and Na-doped SS-LNO reference samples.

Formula of d_{eq} and Related Description

To compare the size of the monolithic particles, both the length and width of 100 particles were determined from SEM images using ImageJ. The particles equivalent diameter was calculated by assuming a rectangular area using the following formula:

$$d_{\mathrm{eq}} = 2 \cdot \sqrt{\frac{\mathrm{A}}{\pi}},$$

probably leading to a systemic overestimation of the particle size.

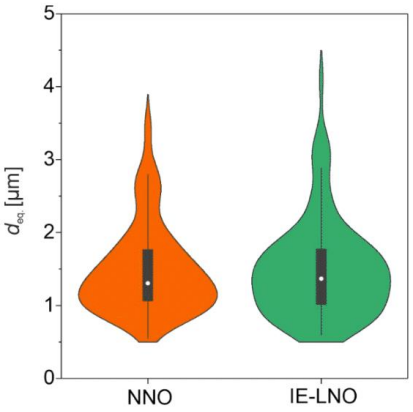

Figure S3. Violin and box-plot particle size analysis of NNO-600 and IE-LNO.

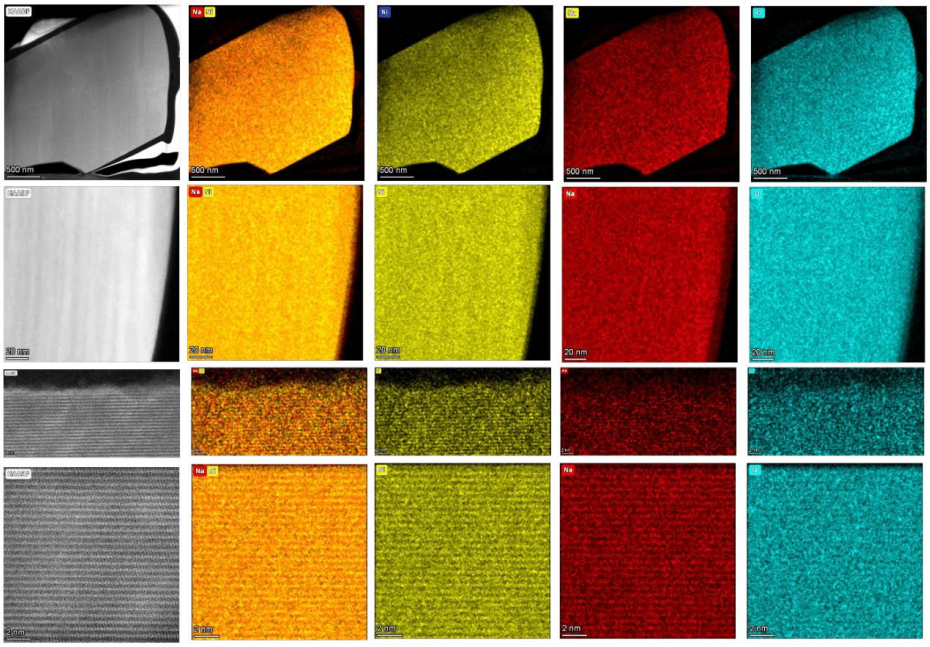

Figure S4. Low- and high-magnification STEM/EDX analysis of NNO-600. Elemental mapping results for Na/Ni (orange), Ni (green), Na (red), and O (blue).

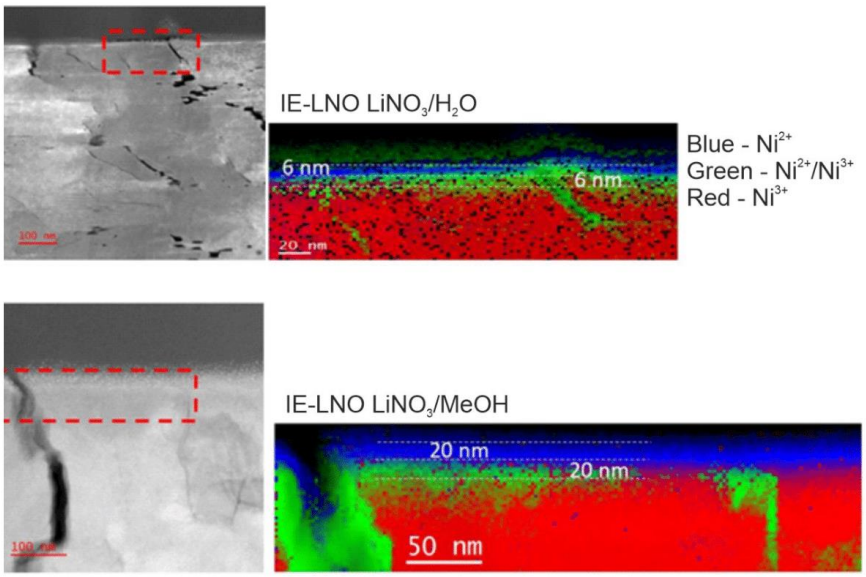

Figure S5. Surface analysis of IE-LNO washed with water or methanol. EELS analysis of oxidation state. The thickness of the layer containing reduced nickel species, possibly rocksalt-type NiO, increased when using methanol as washing medium.

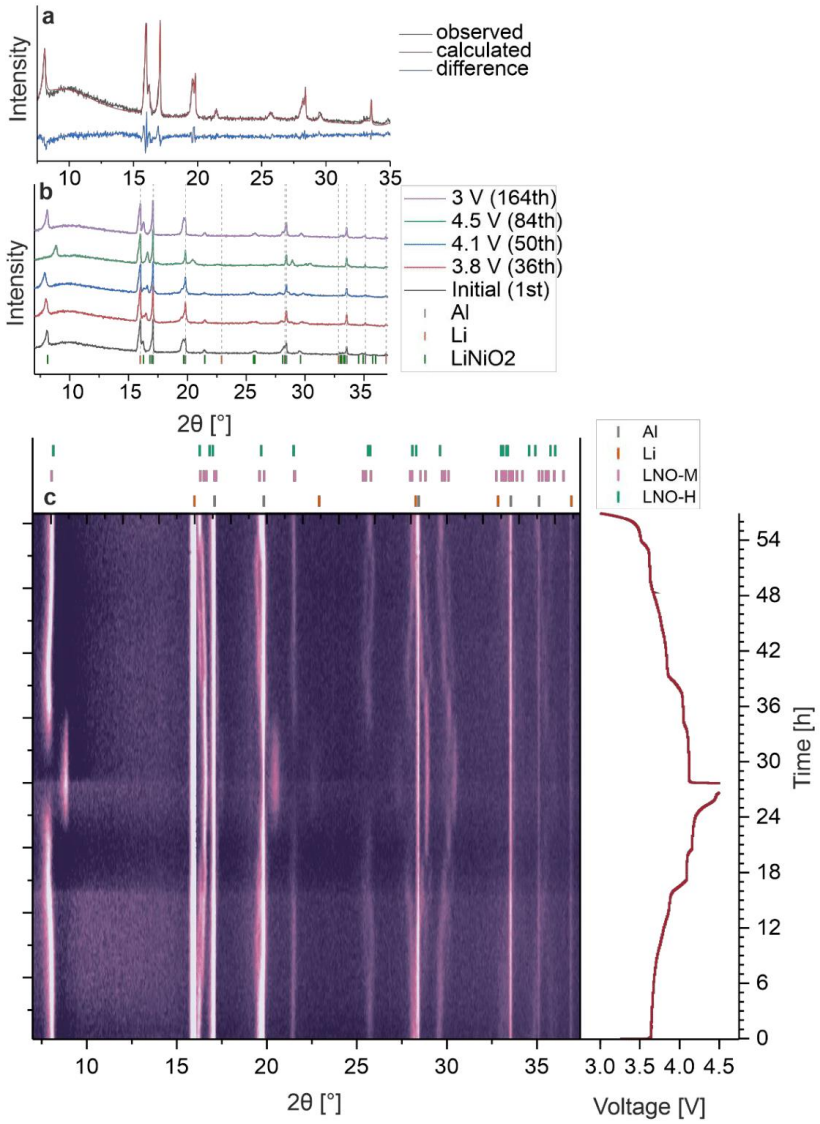

Figure S6. a) Refinement quality of *in situ* XRD data. b) Individual XRD patterns collected during the first charge cycle. c) Contour plot of *in situ* XRD data.

Analysis of d*q*/d*V* Phase Transitions

In order to analyze the characteristic potential vs Li^+/Li at which the H2-H3 transition occurs, a Lorentzian fit was applied to the corresponding peak both in the charge and discharge profiles of SS-LNO and IE-LNO. The mean value of charge and discharge for each sample [incl. deviation from Gaussian error propagation of the error of the fit]

was used in the present work. The same analysis was also done for the samples obtained using the alternative Li salts for ion exchange. The results were included to demonstrate the absence of $Ni_{Li}^{\bullet}$ defects for samples produced by ion exchange, independent of the lithium source and washing procedure.

6.2.2 Supporting Information of Publication II: Seesaw Effect of Substitutional Point Defects on the Electrochemical Performance of Single-Crystal $LiNiO_2$ Cathodes

Supporting Information

See-Saw Effect of Substitutional Point Defects on Electrochemical Performance in Single Crystal $LiNiO_2$ Cathodes

Leonhard Karger[a], Svetlana Korneychuk[b,c], Wessel van den Bergh[a], Sören L. Dreyer[a], Ruizhuo Zhang[a], Aleksandr Kondrakov[a,d], Jürgen Janek[a,e]*, and Torsten Brezesinski[a]*

[a]Battery and Electrochemistry Laboratory (BELLA), Institute of Nanotechnology, Karlsruhe Institute of Technology (KIT), Herrmann-von-Helmholtz-Platz 1, 76344 Eggenstein-Leopoldshafen, Germany

[b]Institute of Nanotechnology, Karlsruhe Institute of Technology (KIT), Herrmann-von-Helmholtz-Platz 1, 76344 Eggenstein-Leopoldshafen, Germany

[c]Karlsruhe Nano Micro Facility (KNMFi), Karlsruhe Institute of Technology (KIT), Herrmann-von-Helmholtz-Platz 1, 76344 Eggenstein-Leopoldshafen, Germany

[d]BASF SE, Carl-Bosch-Str. 38, 67056 Ludwigshafen, Germany

[e]Institute of Physical Chemistry & Center for Materials Research (ZfM/LaMa), Justus-Liebig-University Giessen, Heinrich-Buff-Ring 17, 35392 Giessen, Germany

*Email: juergen.janek@kit.edu, torsten.brezesinski@kit.edu

Table S1. Rietveld refinement results for the various NNO samples.

Sample	R_{wp} [%]	R_{Bragg} [%]	*a* [Å]	*b* [Å]	*c* [Å]	*β* [°]	*V* [Å^3]	Impurity
NNO-450	14.5	3.12	5.3140(1)	2.8421(1)	5.5770(2)	110.441(2)	78.92(1)	-
NNO-600	15.2	3.19	5.3158(1)	2.8419(1)	5.5779(2)	110.482(2)	78.94(1)	-
NNO-700	13.1	2.67	5.3173(1)	2.8424(1)	5.5789(1)	110.485(1)	78.99(1)	-
NNO-750	11.6	2.45	5.3193(1)	2.8429(1)	5.5800(1)	110.490(1)	79.04(1)	-
NNO-600rpm	15.9	4.37	5.3016(42)	2.8527(21)	5.5745(48)	110.237(60)	79.10(4)	-
NNO-0.1W	17.8	5.06	5.3210(6)	2.8451(3)	5.5833(9)	110.464(3)	79.19(2)	NiO
NNO-0.5W	12.2	3.61	5.3204(4)	2.8467(1)	5.5834(6)	110.442(2)	79.24(1)	-
NNO-1.0W	13.9	5.16	5.3179(12)	2.8523(6)	5.5891(12)	110.302(18)	79.51(1)	NiO
NNO-2.0W	12.0	4.66	5.3181(9)	2.8475(4)	5.5834(120)	110.439(2)	79.22(1)	NiO, WO_3
NNO-2.0W-PC	16.8	3.16	5.3096(15)	2.8433(8)	5.5744(21)	110.376(7)	78.89(2)	WO_3

Table S2. Specific capacities and gas amounts obtained in DEMS measurements.

	PC-LNO	IE-LNO-2.0W-PC	IE-LNO-2.0W-PC-Mg	PC-LNO (less electrolyte)	IE-LNO-2.0W-PC (less electrolyte)
1st-cycle q_{ch} [mAh/g_{LNO}]	242	218	210	241	232
1st-cycle q_{dis} [mAh/g_{LNO}]	207	192	172	206	206
2nd-cycle q_{ch} [mAh/g_{LNO}]	205	190	177	203	216
2nd-cycle q_{dis} [mAh/g_{LNO}]	201	185	176	195	204
1st-cycle CO_2 evolution [µmol/g_{LNO}]	6	64	40	11	76
2nd-cycle CO_2 evolution [µmol/g_{LNO}]	4	18	11	10	12
Total CO_2 evolution [µmol/g_{LNO}]	10	82	51	21	88

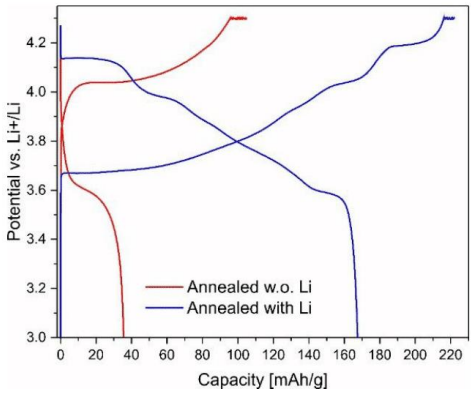

Figure S1. First-cycle voltage profiles of LIB half-cells using the IE-LNO cathode material calcined at 700 °C for 12 h (red) and 40 h with addition of 10 mol% $LiOH \cdot H_2O$ (blue).

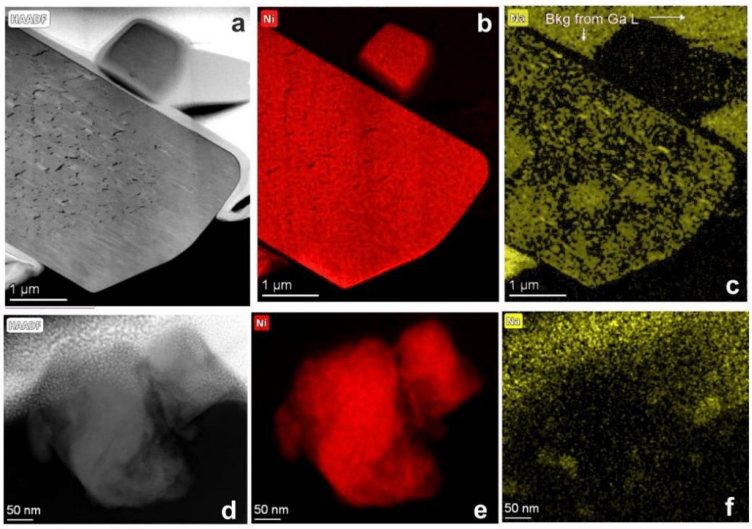

Figure S2. (a,d) STEM and (b,c,e,f) EDS results for FIB-cut IE-LNO-700 (a-c) and IE-LNO-600rpm (d-f).

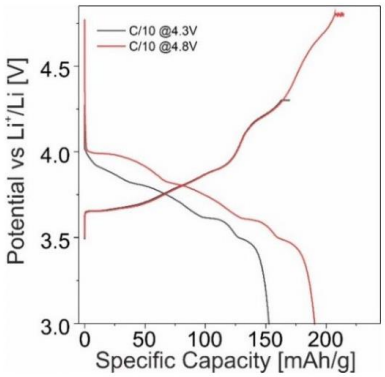

Figure S3. Voltage profiles of LIB half-cells using the IE-LNO-450 cathode material cycled in a potential window of 3.0-4.3 V vs. Li^+/Li (black) and 3.0-4.8 V vs. Li^+/Li (red) at C/10 rate.

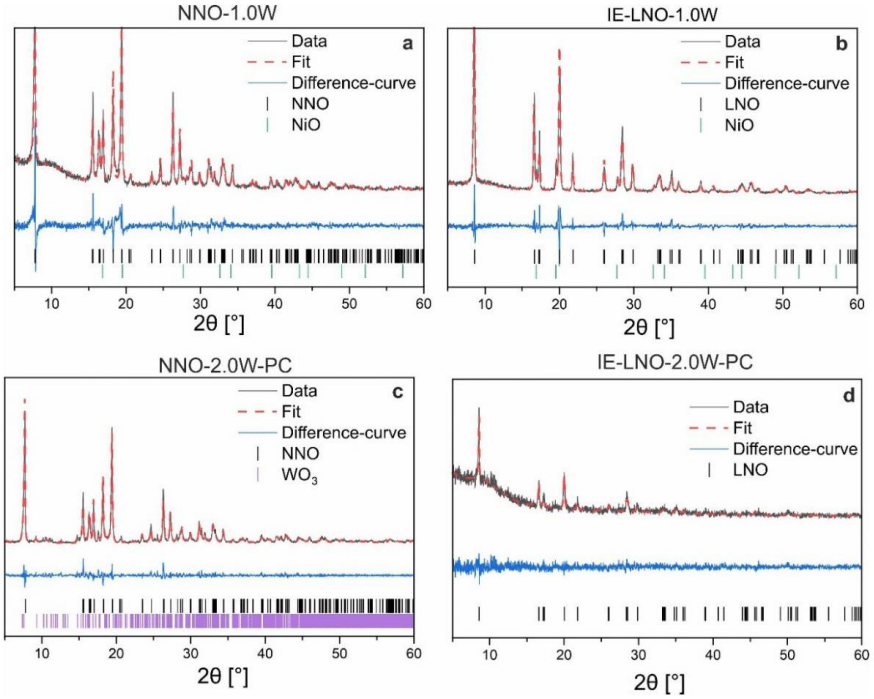

Figure S4. Examples of Rietveld analyses with representative impurities occasionally observed in NNO and LNO. (a) NNO-1.0W, (b) IE-LNO-1.0W, (c) NNO-2.0W-PC, and (d) IE-LNO-2.0W-PC.

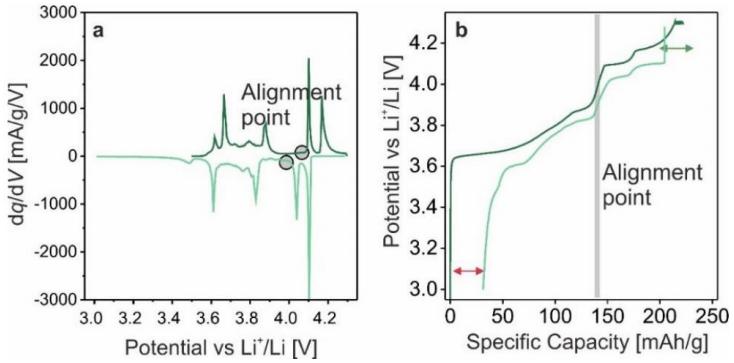

Figure S5. Example of loss separation into kinetic hindrance and high-voltage degradation. (a) Differential capacity curve for IE-LNO-700 with indication of the "alignment point" at ~3.9 V vs. Li^+/Li chosen for aligning charge and discharge profiles to extract the respective first-cycle capacity losses. (b) Aligned voltage profiles.

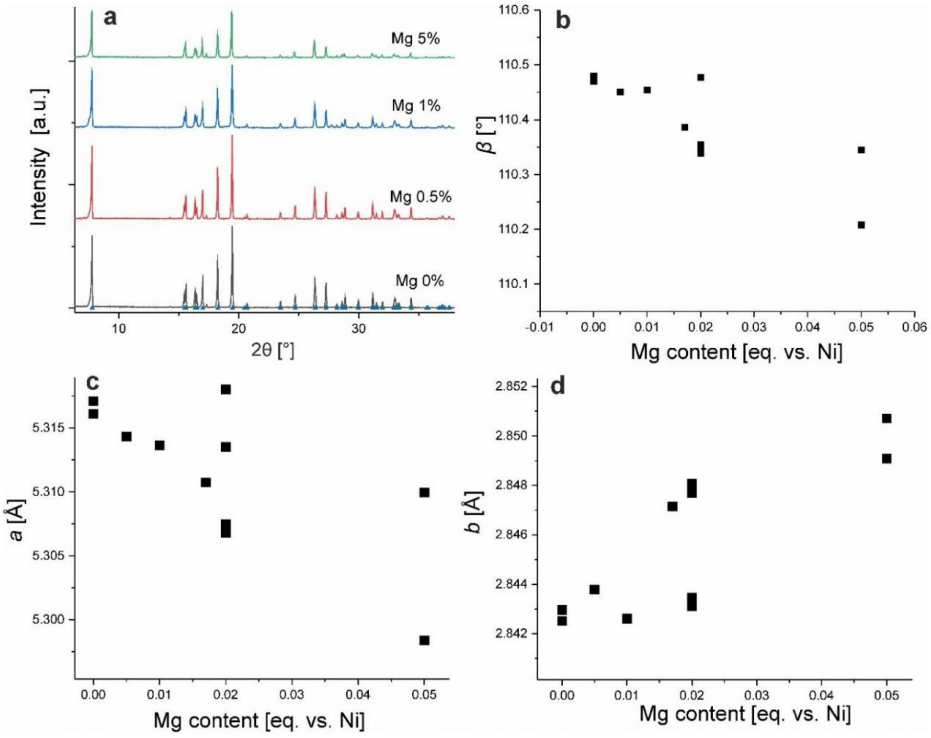

Figure S6. PXRD patterns and corresponding results from LeBail analysis for the Mg-doped NNO samples. (a) Selected patterns and LeBail fitting results for (b) *β*, (c) *a*, and (d) *b*.

It was attempted to produce a Na-site (Li-site for LNO) doped NNO material by introduction of Mg^{2+} ions. Magnesium-doping changes the lattice parameters of the parent NNO. Increasing amounts of doping reduce the monoclinic distortion. This behavior is in line with magnesium introduction into the transition-metal site (Ni-site), as opposed to the desired Na-site doping. Therefore, to introduce magnesium into the lithium site, a magnesium source was utilized in the ion-exchange process, as described in the main text.

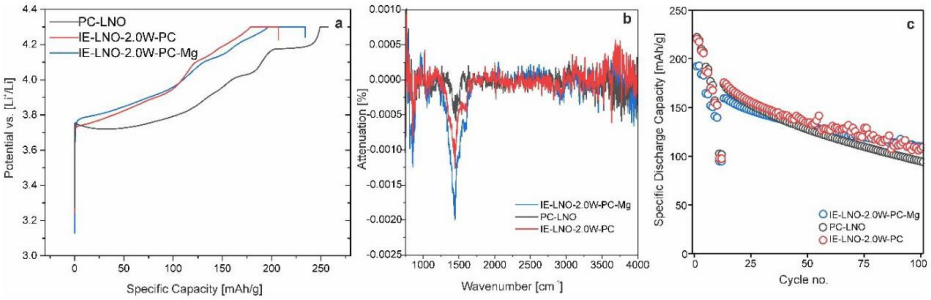

Figure S7. Additional information on the comparison of PC-LNO, IE-LNO-2.0W-PC, and IE-LNO-2.0W-PC-Mg. (a) Voltage profiles (for *ex-situ* PXRD analysis of charged materials). (b) Background-subtracted ATR-IR spectra collected from the as-prepared samples. (c) Specific discharge capacities in the potential window of 2.9-4.35 V vs. Li^+/Li with an initial rate test [C/20, C/10, C/3, 1C, 2C, and 5C (two cycles each)] and C/3 for long-term testing.

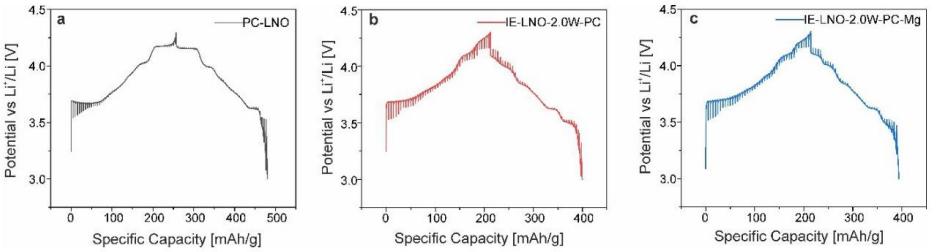

Figure S8. Results from GITT measurements conducted on LIB half-cells using (a) PC-LNO, (b) IE-LNO-2.0W-PC, and (c) IE-LNO-2.0W-PC-Mg with C/20 charge/discharge pulses for 30 min and 4 h rest time in between the pulses.

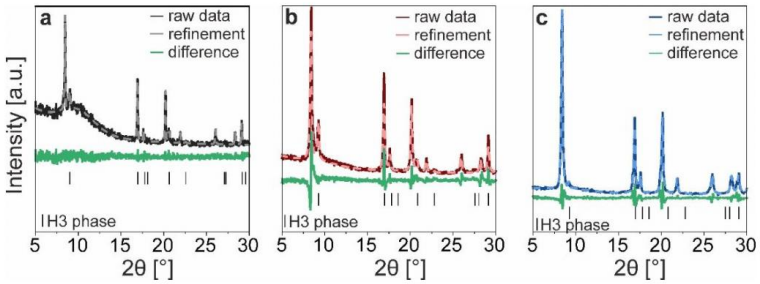

Figure S9. PXRD patterns and Le Bail plots for (a) charged PC-LNO, (b) IE-LNO-2.0W-PC, and (c) IE-LNO-2.0W-PC-Mg cathodes, with tick marks indicating the hexagonal H3 phase.

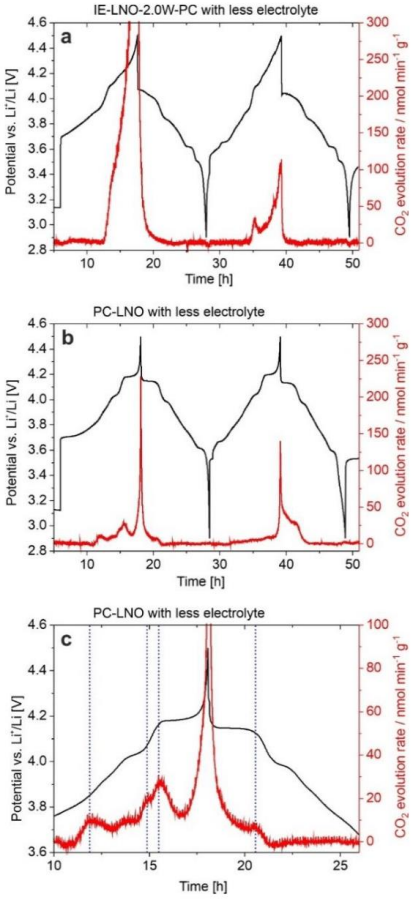

Figure S10. CO_2 evolution for (a) IE-LNO-2.0W-PC and (b,c) PC-LNO as measured via DEMS in LIB half-cells with less electrolyte volume resulting in sharper gas evolution peaks.

6.2.3 Supporting Information of Publication III: Decoupling Substitution Effects from Defects in Ni-rich CAMs

Supporting Information

Decoupling Substitution Effects from Point Defects in Layered Ni-rich Oxide Cathode Materials for Lithium-ion Batteries

Leonhard Karger,[a] Svetlana Korneychuk,[b,c] Sabrina Sicolo,[d] Hang Li,[e,†] Wessel van den Bergh,[a] Ruizhuo Zhang,[a] Sylvio Indris,[e] Aleksandr Kondrakov,[a,d] Jürgen Janek[a,f,*] and Torsten Brezesinski[a,*]

[a] L. Karger, W. van den Bergh, R. Zhang, A. Kondrakov, J. Janek, T. Brezesinski

Battery and Electrochemistry Laboratory (BELLA), Institute of Nanotechnology, Karlsruhe Institute of Technology (KIT), Herrmann-von-Helmholtz-Platz 1, 76344 Eggenstein-Leopoldshafen, Germany

E-mail: juergen.janek@kit.edu, torsten.brezesinski@kit.edu

[b] S. Korneychuk

Institute of Nanotechnology, Karlsruhe Institute of Technology (KIT), Herrmann-von-Helmholtz-Platz 1, 76344 Eggenstein-Leopoldshafen, Germany

[c] S. Korneychuk

Karlsruhe Nano Micro Facility (KNMFi), Karlsruhe Institute of Technology (KIT), Herrmann-von-Helmholtz-Platz 1, 76344 Eggenstein-Leopoldshafen, Germany

[d] S. Sicolo, A. Kondrakov

BASF SE, Carl-Bosch-Str. 38, 67056 Ludwigshafen, Germany

[e] H. Li, S. Indris

Institute for Applied Materials – Energy Storage Systems (IAM-ESS), Karlsruhe Institute of Technology (KIT), Hermann-von-Helmholtz-Platz 1, 76344 Eggenstein-Leopoldshafen, Germany

J. Janek

[f] Institute of Physical Chemistry & Center for Materials Research (ZfM/LaMa), Justus-Liebig-University Giessen, Heinrich-Buff-Ring 17, 35392 Giessen, Germany

† Current Affiliation: School of Advanced Materials, Peking University, Shenzhen Graduate School, Shenzhen 518055, China

Table S1. Rietveld refinement results for NNO-W and Na-NCM-W samples.

Sample	Phase	wt.%	R_{wp} [%]	R_{Bragg} [%]	a [Å]	b [Å]	c [Å]	β [°]	V [Å^3]
NNO-W	*C*2/*m*	100	12.0	4.66	5.3181(9)	2.8475(4)	5.5834(120)	110.439(2)	79.22(1)
Na-NCM95-W	*C*2/*m*	78	16.9	5.12	5.2700(8)	2.8547(4)	5.5499(7)	110.064(10)	78.43(2)
	R−3*m*	22		4.95	2.9503(8)	-	15.6751(92)	-	118.16(10)
Na-NCM90-W	*C*2/*m*	20	14.8	4.79	5.1163(19)	2.9565(12)	5.5163(10)	107.966(3)	79.37(5)
	R−3*m*	80		4.73	2.9570(4)	-	15.7244(30)	-	119.07(4)
Na-NCM88-W	*C*2/*m*	9	17.8	4.48	5.1262(20)	2.9520(12)	5.5248(11)	108.046(3)	79.49(5)
	R−3*m*	91		5.61	2.9560(5)	-	15.7271(49)	-	119.01(6)

Size Analysis

Size analysis was conducted as follows: For each material, length and width of 200 particles were determined from SEM images using the ImageJ software. The equivalent diameter was calculated as the diameter of a circle with the same area as the product of length and width.

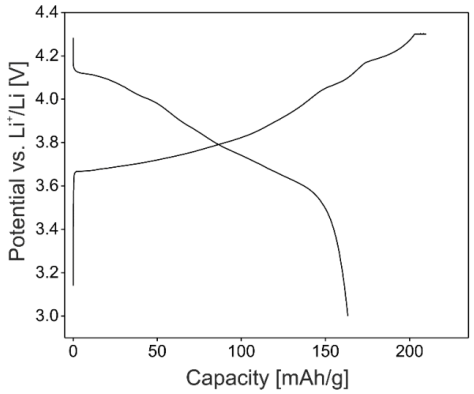

Figure S1. First-cycle charge/discharge curve of IE-NCM90 at C/10 in the potential window of 3.0-4.3 V vs. Li^+/Li.

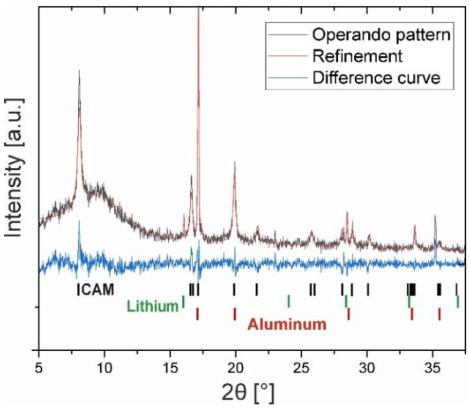

Figure S2. Example of refinement quality (for *operando* XRD results).

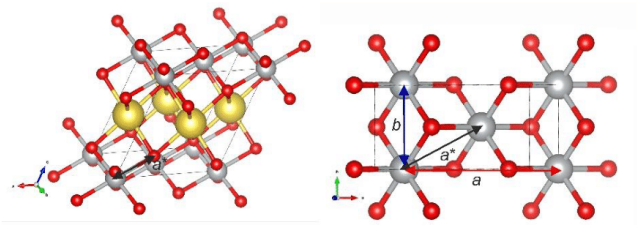

Figure S3. Scheme for the definition of *a** as calculated for the *operando* XRD refinement. For better comparison of the lattice parameters obtained for the refinement of the monoclinic (*C*2/*m*) phase, *a* was converted into *a**. As can be seen, *a** corresponds to the projection of *a* onto the next Ni atom in accordance with the definition in the hexagonal (*R*−3*m*) phase. The formula for calculating *a** is: $a^* = \frac{\sqrt{a^2+b^2}}{2}$.

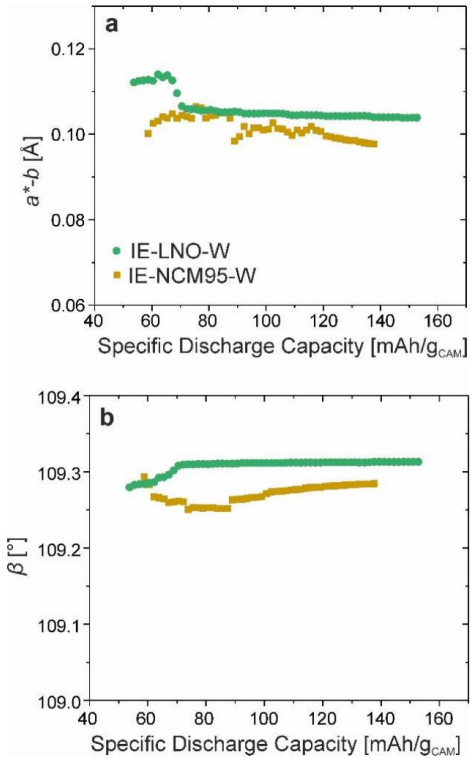

Figure S4. Comparison of monoclinic distortion parameters: (a) a^*-b and (b) β from *operando* XRD refinement of IE-LNO-W and IE-NCM95-W.

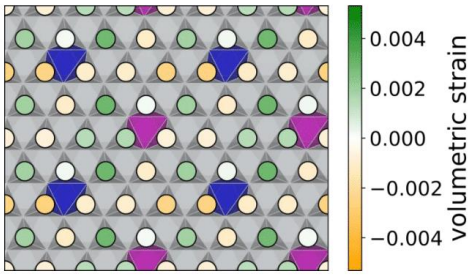

Figure S5. Volumetric strain at the lithium positions calculated for an NCM88 model. The underlying Ni-O lattice is depicted as gray polyhedra, while the lithium sites in the Li layer are indicated by circular markers that are colored according to the corresponding color map.

6.2.4 Supporting Information of Publication IV: Protective Nanosheet Coatings for Thiophosphate-Based All-Solid-State Batteries

Supporting Information

Protective Nanosheet Coatings for Thiophosphate-Based All-Solid-State Batteries

Leonhard Karger, Barbara Nascimento Nunes, Yuriy Yusim, Andrey Mazilkin, Ruizhuo Zhang, Wengao Zhao, Anja Henss, Aleksandr Kondrakov, Jürgen Janek* and Torsten Brezesinski*

L. Karger, Dr. B. N. Nunes, Dr. A. Mazilkin, R. Zhang, Dr. W. Zhao, Dr. A. Kondrakov, Prof. J. Janek, Dr. T. Brezesinski

Battery and Electrochemistry Laboratory (BELLA), Institute of Nanotechnology, Karlsruhe Institute of Technology (KIT), Hermann-von-Helmholtz-Platz 1, 76344 Eggenstein-Leopoldshafen, Germany

E-mail: torsten.brezesinski@kit.edu

Y. Yusim, Dr. A. Henss, Prof. J. Janek

Institute of Physical Chemistry & Center for Materials Research (ZfM/LaMa), Justus-Liebig-University Giessen, Heinrich-Buff-Ring 17, 35392 Giessen, Germany

E-mail: juergen.janek@phys.Chemie.uni-giessen.de

Dr. A. Mazilkin

Karlsruhe Nano Micro Facility (KNMFi), Karlsruhe Institute of Technology (KIT), Herrmann-von-Helmholtz-Platz 1, 76344 Eggenstein-Leopoldshafen, Germany

Dr. A. Kondrakov

BASF SE, Carl-Bosch-Str. 38, 67056 Ludwigshafen, Germany

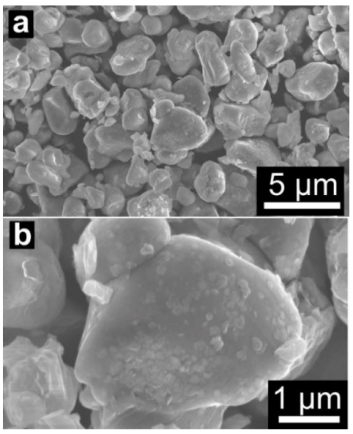

Figure S1. SEM analysis of the attempted nanosheet dry coating (1 wt.% h-BN) of single-crystalline NCM831205, as described in the main text. (a) Low- and (b) high-magnification images. The CAM was received from BASF SE.

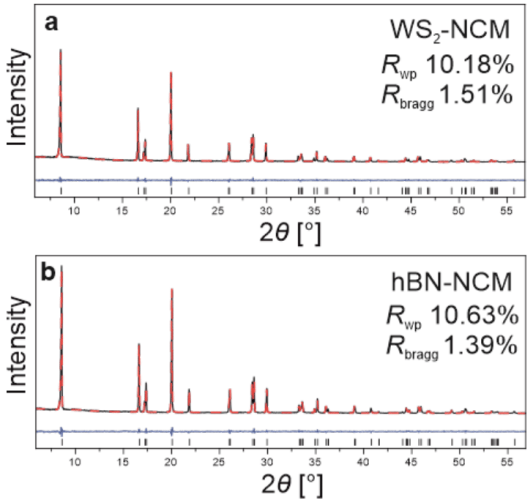

Figure S2. Examples of Rietveld refinement quality for (a) WS_2-NCM and (b) hBN-NCM. Experimental data are shown in black, fits in red and difference curves in blue.

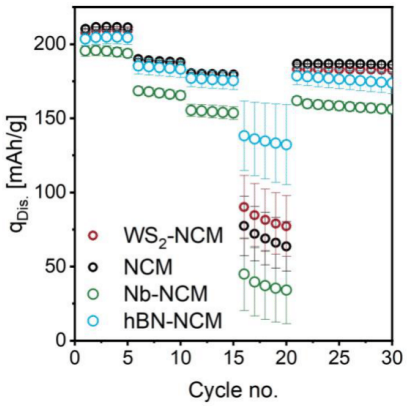

Figure S3. Cycling stability and rate performance testing of uncoated and nanosheet-coated NCM CAMs in LIB coin cells at 25 °C in the potential window of 3.0-4.3 V vs. Li^+/Li (five cycles at C/10, 1C, 2C, and 10C each, followed by 10 cycles at 1C). For each material, three cells were tested and the data averaged.

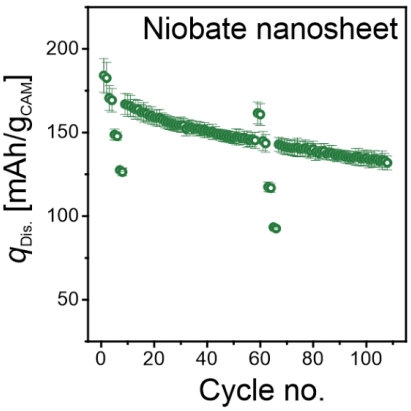

Figure S4. Long-term cyclability of Nb-NCM in SSB cells with LPSCl electrolyte. Rate performance testing with two cycles each at C/10, C/5, C/2, and 1C, followed by cycling at C/5. The error bars represent the standard deviation from two independent cells.

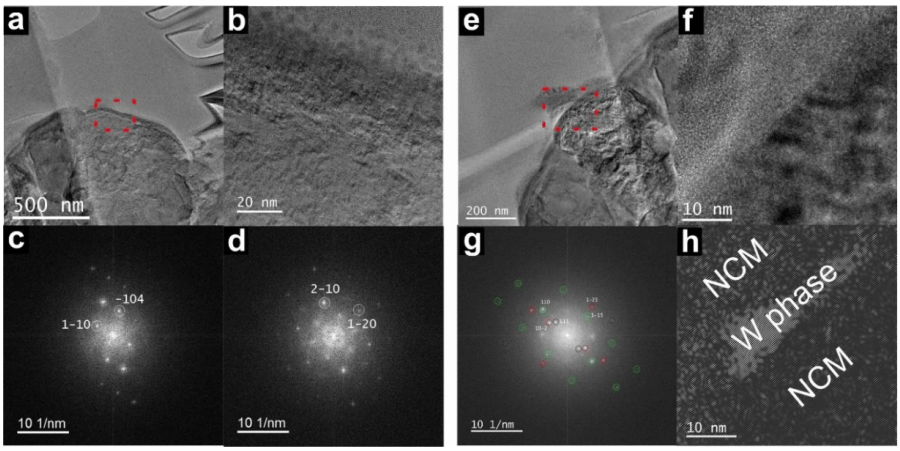

Figure S5. (a, e) Low-magnification TEM images of WS_2-NCM with areas chosen for further analysis indicated by dashed red squares. (b, f) HRTEM images and (c, d, g, h) FFT patterns.

Panel (a) shows a low-magnification TEM image, with the dashed red square denoting the area used for high-resolution imaging [HRTEM, see panel (b)]. The phases present in the sample were analyzed by fast Fourier transform (FFT). FFTs from both the subsurface and surface of the secondary particle are shown in panels (c) and (d). The FFT pattern of the subsurface can be indexed to layered NCM (*R*−3*m* space group), while that of the surface is indicative of hexagonal WS_2 with space group 194 (ICSD entry 202366). Another feature found in the structure is presented in panels (e-h). Panel (g) is the FFT of (e). The pattern contains several sets of reflections from different phases. The analysis revealed that two sets belong to the NCM phase; they are denoted by green and red circles. The “green” reflections originate from the grain at the bottom of the image with [122] zone axis. The “red” reflections stem from the grain at the top with $[\bar{5}52]$ zone axis. Additionally, two reflections, indicated by the blue circles, belong to the layer between the two NCM grains, as confirmed by the inverse FFT pattern shown in panel (h). The interplanar distance that corresponds to these reflections is ~2.7 Å, which best matches the (111) reflection of the tetragonal WO_3 phase (space group 129, ICSD entry 27962).

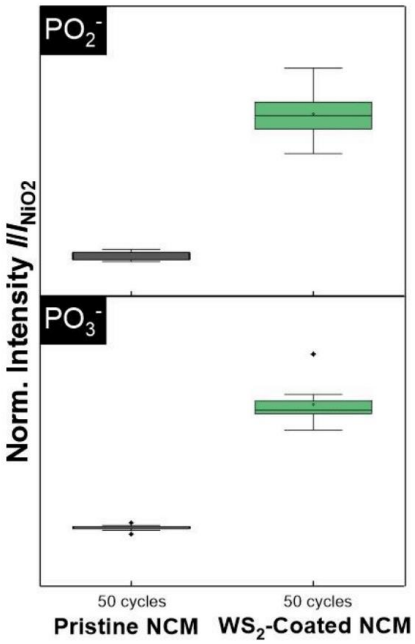

Figure S6. Comparison of normalized intensities of PO_2^- and PO_3^- fragments for cathodes using uncoated or WS_2-coated NCM after 50 cycles. The normalization was done relative to the NiO_2^- fragment.

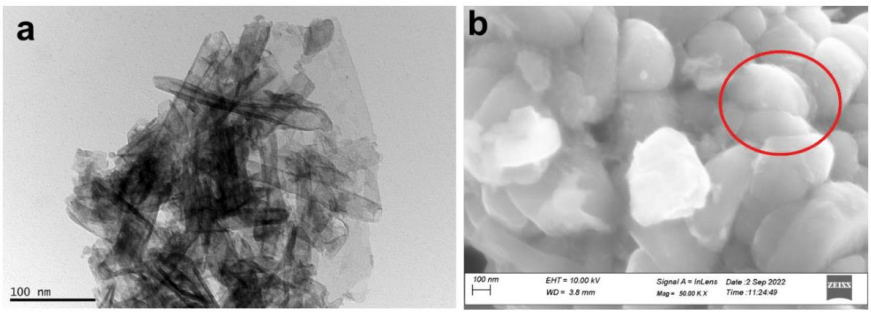

Figure S7. (a) TEM analysis of exfoliated $K_{4-x}H_xNb_6O_{17}$ nanosheets. (b) NCM coated with 5 wt.% $K_{4-x}H_xNb_6O_{17}$, with a nanosheet feature highlighted by the red circle.

6.3 Scientific Contributions

6.3.1 List of Publications during Doctoral Project

F. Strauss, J. Lin, L. Karger, D. Weber, T. Brezesinski, Probing the Lithium Substructure and Ionic Conductivity of the Solid Electrolyte Li_4PS_4I, *Inorganic Chemistry* 2022, *61*, 5885-5890.

L. Karger, D. Weber, D. Goonetilleke, A. Mazilkin, H. Li, R. Zhang, Y. Ma, S. Indris, A. Kondrakov, J. Janek, T. Brezesinski, Low-Temperature Ion Exchange Synthesis of Layered $LiNiO_2$ Single Crystals with High Ordering, *Chemistry of Materials* 2023, *35*, 648-657.

W. van den Bergh, L. Karger, S. Murugan, J. Janek, A Kondrakov, T. Brezesinski, Single crystal layered oxide cathodes: The relationship between particle size, rate capability, and stability, *ChemElectroChem* 2023, *10*, e202300165. (Highlighted on the Front Cover + Cover Profile (*ChemElectroChem* 2023, *10*, e202300430))

L. Karger, S. Korneychuk, W. van den Bergh, S. Dreyer, R. Zhang, A. Kondrakov, J. Janek, T. Brezesinski, Seesaw Effect of Substitutional Point Defects on the Electrochemical Performance of Single-Crystal $LiNiO_2$ Cathodes, *Chemistry of Materials* 2023, DOI: 10.1021/acs.chemmater.3c02727

L. Karger, B.N. Nunes, Y. Yusim, A. Mazilkin, R. Zhang, W. Zhao, A. Henss, A. Kondrakov, J. Janek, T. Brezesinski, Protective Nanosheet Coatings for Thiophosphate-Based All-Solid-State Batteries, *submitted*.

L. Karger, S. Korneychuk, S. Sicolo, H. Li, W. van den Bergh, R. Zhang, S. Indris, A. Kondrakov, J. Janek, T. Brezesinski, Decoupling Substitution Effects from Point Defects in Layered Ni-rich Oxide Cathode Materials for Lithium-ion Batteries, *submitted.*

6.3.2 List of Patents

1. “Process for Making a Coated Electrode Active Material, and Coated Electrode Active Material”
Appl. no.: EP 21203526.5; October 2021
L. Karger, T. Brezesinski, A. Kondrakov, X. Wu, R. Konar, S. Maiti, H. Sclar, D. Aurbach

2. “Cathode Active Materials and Process for their Manufacture”
(Single Crystal Ni Rich Cathode Active Material Obtained by Ion Exchange Method)
Appl. no.: EP22166397.4; April 2022
L. Karger, D. Weber, T. Brezesinski, A. Kondrakov

3. “Cathode Active Material and Its Use in Rechargeable Electrochemical Cells”
(Transition Metal Doped Sodium Containing Layered Oxide Cathode Active Material for Sodium Ion Battery)
Appl. no.: EP23174942.5; May 2023
L. Karger, S. An, W. van den Bergh Saarbergh, T. Brezesinski, A. Kondrakov

4. “Process for Making a Cathode Active Material, and Cathode Active Material”
(Cathode Active Material Made From an Overlithiated Precursor)
Appl. no.: EP23199014.4; September 2023
L. Karger, W. van den Bergh Saarbergh, T. Brezesinski, A. Kondrakov

6.3.3 List of Conference Contributions

773. WE-Heraeus-Seminar / Materials and Energy – New Directions for the "Energiewende"

Bad Honnef, Germany (2022)

Poster: Low-Temperature Ion Exchange Synthesis of Layered $LiNiO_2$ Single Crystals with High Ordering.

German-Israeli Battery School 2023

Ein Gedi, Israel (2023)

Poster: Understanding the Electrochemistry of Ion Exchanged $LiNiO_2$. The Interplay of Crystallinity and Particle Size.

BASF-Collaboration-Forum 2023

Ludwigshafen, Germany (2023)

Poster: Understanding Layered Cathode Active Materials, One Parameter at a Time *via* Ion-Exchange Synthesis.

Batterieforum Deutschland

Berlin, Germany (2024)

Poster: Towards Zero First-Cycle Loss: Impact of Lithium Site Defects in Nickel-Rich Cathode Active Material